University of California
Los Angeles

Development and Characterization of the QUartz Photon Intensifying Detector (QUPID), and Applications in Future Dark Matter and Neutrinoless Double Beta Decay Experiments

A dissertation submitted in partial satisfaction
of the requirements for the degree
Doctor of Philosophy in Physics

by

Artin Paul Teymourian

2011

The dissertation of Artin Paul Teymourian is approved.

William Newman

Jay Hauser

Edwin Schauble

Katsushi Arisaka, Committee Chair

University of California, Los Angeles

2011

To my parents

Table of Contents

List of Figures

LIST OF TABLES

Acknowledgments

I would like to offer special thanks to my advisor Professor Katsushi Arisaka, who has guided me throughout the past five years. I would not have been able to come this far without his help and encouragement. He taught me many valuable lessons and has shown me how to think like a true scientist. I would also like to thank Dr. Hanguo Wang for always being available to help me with nearly any issue and providing me with practical advice on any obstacle that I may have encountered.

The entire XENON collaboration has been of incredible help and I am forever indebted to them for giving me the knowledge I needed in dark matter research. The names are far too many to list here, however they have all been good collaborators and great friends throughout this journey. I would like to give my sincere thanks to Professor Elena Aprile for providing me with the opportunity to join a world class collaboration that is on the forefront of dark matter research.

I would also like to thank the UCLA dark matter group. Paolo Beltrame, Ethan Brown, Chamkaur Ghag, Chi Wai Lam, Kevin Lung, Yixiong Meng, Emilija Pantic, and Paul Scovell, along with Julie Rolla have all been there to help me with any issues I had and have been like a family to me.

I would like to offer my deep gratitude to all involved in the QUPID manufacturing, design, and testing at Hamamatsu Photonics. I am also indebted to Laura Baudis and Alfredo Ferella from the University of Zurich for performing the radioactivity screening of the QUPID in the Gator screening facility.

My mother, father, sister, and brother-in-law have all provided me with endless support through not only my time in graduate school, but throughout my entire life and I thank them from the bottom of my heart. I could not have made it here today without their undying encouragement.

Last but certainly not least, I would like to express my deepest gratitude to Nairi, who has been by my side throughout the past year and has changed my life for the better. She has given me the support I needed and has never failed to bring a smile to my face when I have needed it the most.

Furthermore, Ch. 8 is a version of our paper which has been published in Nuclear Instruments and Methods in Physics Research A [1].

VITA

1986	Born, Northridge, California, USA.
2006	B.A. (Astronomy), Cornell University, Ithaca, NY.
2006-Present	Research Assistant Physics and Astronomy Department, UCLA.
2007	M.S. (Physics), UCLA, Los Angeles, CA.
2008	Teaching Assistant Physics and Astronomy Department, UCLA.

PUBLICATIONS

R. Alarcon, et al., *MAX: Multi-Ton Argon and Xenon.* (2009), Fermilab Proposal 1001.

D. Alton, et al., *A Depleted Argon Dark Matter Search.* (2009), Fermilab Proposal 1000.

E. Aprile, et al., *Dark Matter Results from 100 Live Days of XENON100 Data.* (2011), arXiv:1104.2549.

E. Aprile, et al., *First Dark Matter Results from the XENON100 Experiment.* Physical Review Letters 105 (2010) 131302.

E. Aprile, et al., *Implications on Inelastic Dark Matter from 100 Live Days of XENON100 Data.* (2011), arXiv:1104.3121.

E. Aprile, et al., *Likelihood Approach to the First Dark Matter Results from XENON100.* (2011), arXiv:1103.0303.

E. Aprile, et al., *Material screening and selection for XENON100.* Astroparticle Physics 35 (2011) 43.

E. Aprile, et al., *Study of the electromagnetic background in the XENON100 experiment.* Physical Review D 83 (2011) 082001.

E. Aprile, et al., *The XENON100 Dark Matter Experiment.* (2011), arXiv:1107.2155.

K. Arisaka, et al., *XAX: A multi-ton, multi-target detection system for dark matter, double beta decay, and pp solar neutrinos.* Astroparticle Physics 31 (2009) 63.

K. Arisaka, et al., *Studies of a three-stage dark matter and neutrino observatory based on multi-ton combinations of liquid xenon and liquid argon detectors.* (2011), arXiv:1107.1295.

Y. Terzian and A. Teymourian, *The life and death of Planetary Nebulae.* 2005, in *The Initial Mass Function: 50 Years Later,* eds: E. Corbelli, F. Palla, and H. Zinnecker, 521.

A. Teymourian, et al., *Characterization of the QUartz Photon Intensifying Detector (QUPID) for use in Noble Liquid Detectors.* (2011), doi:10.1016/j.nima.2011.07.015.

Abstract of the Dissertation

Development and Characterization of the QUartz Photon Intensifying Detector (QUPID), and Applications in Future Dark Matter and Neutrinoless Double Beta Decay Experiments

by

Artin Paul Teymourian
Doctor of Philosophy in Physics
University of California, Los Angeles, 2011
Professor Katsushi Arisaka, Chair

Direct dark matter detection and neutrinoless double beta decay experiments require very low radioactivity in the detector construction materials. A new concept of photodetector called the QUartz Photon Intensifying Detector (QUPID) has been developed at UCLA in conjunction with Hamamatsu Photonics as a new photodetector with extremely low radioactivity to be used in future experiments. This thesis will discuss the concept of the liquid xenon Time Projection Chamber (TPC), used in the XENON100 dark matter detector, and the ability to use XENON100 for double beta decay detection, leading to a 90% confidence level lower limit on the half-life of two neutrino double beta decay in ^{136}Xe of $> 1.6 \times 10^{20}$ yr. This thesis will also discuss the importance of radioactivity concerns in the detector construction for dark matter and double beta decay detection experiments, and how the QUPID satisfies the radioactivity requirements for these detectors. The testing of various key parameters of the QUPID will also be discussed. The performance of the QUPID meets or exceeds the requirements

for current and future dark matter experiments, and as such the QUPID proves to be a good replacement for conventional photomultiplier tubes.

Finally, this thesis will introduce future dark matter detectors that will use the QUPID, namely the XENON1Ton and DARKSIDE50 experiments. These experiments are larger and cleaner than current generation detectors, which will increase the sensitivity for dark matter detection to the regions of theoretical predictions.

CHAPTER 1

Introduction

The past century has brought on a great increase in the understanding of the fundamental laws of physics, both at the smallest and largest scales. The Standard Model of Particle Physics [2] has been formulated to explain many of the phenomena observed at the quantum level, through the interactions of 17 particles. It has also made predictions on the existence of particles, along with predicting the values of several parameters, all of which have been confirmed. At the same time, the evolution of the Universe has been described by the Big Bang Cosmology [3, 4, 5]. This theory predicts that the Universe was created as an infinitely hot and dense state that expanded and cooled over the course of 13.7 billion years. During the cooling and expansion, the energy created all of the particles observed in the Universe today, which then combined to form baryons, followed by nuclei, neutral atoms, and eventually stars and galaxies. The Big Bang Cosmology predicted the existence of a Cosmic Microwave Background [6], which is a sea of microwave photons left over from the early stages of the evolution of the Universe. This Cosmic Microwave Background was observed in 1964 [7], and has been measured and mapped to increasing resolution ever since the discovery.

Although these models of the evolution of the Universe and the interactions of particles make precise predictions, there are some pitfalls to make physicists believe that the models are incomplete. In particular, 72% the Universe consists of "Dark Energy" which causes an acceleration in the expansion rate of the Universe [8], and 23% of the Universe is made of “Dark Matter” which appears to be a form of undetectable particle making up a majority of the mass of galaxies and galaxy clusters [9]. The Standard Model also describes the neutrinos as being massless, however measurements from the past four decades have hinted that neutrinos do indeed have mass [10, 11, 12].

Several experiments have been performed in recent years to better understand the nature of dark energy and dark matter. Observations have been made to survey and determine the velocities of distant galaxies [13, 14, 15], thereby characterizing the expansion rate and acceleration of the Universe, and other future experiments are in the planning stages.

The field of dark matter detection is also filled with many experiments designed to understand and detect the presence of dark matter (see Ch. 3). Every year, new results are presented from ongoing detection experiments and new proposals are submitted for larger and more sensitive detectors. Similarly, experiments focusing on the neutrino have been running for several decades. The mass differences between the different flavors of neutrinos have been measured through neutrino oscillation experiments [16, 17], however the absolute mass scale is still unknown. The coming years will bring on more experiments designed to determine the neutrino mass, either through direct observation of the endpoint of beta decays, or through the characterization of neutrinoless double beta decay whose lifetime depends on the mass of the neutrinos (See Ch. 4). These experiments will also be able to determine whether the neutrino is a Majorana particle (where the neutrino and antineutrino are the same particle) or a Dirac particle (the neutrino and antineutrino are different).

A breakthrough in any of these fields would signal a discovery of new physics beyond the Standard Model. The upcoming dark energy, dark matter, and neutrinoless double beta decay experiments will be able to probe areas in phase space where current theories predict discovery potential. It is important for each generation of experiment to be more sensitive than the last, and new advances must be made in the technologies used in these detectors. Research and development efforts for the future experiments are ongoing at many institutions, and UCLA is no exception. Much time and effort has been put into the development of a new type of photodetector to be used in the upcoming dark matter and double beta decay experiments. This thesis will discuss the challenges of dark matter and neutrinoless double beta decay detection, along with recent results. The creation, development, and testing of a new type of photodetector called the QUartz Photon Intensifying Detector, or QUPID will also be presented, and the implementation of the QUPID in future experiments will be discussed.

For this thesis, I have performed all of the analysis shown in Ch. 6 for obtaining a limit on the double beta decay half-life of ^{136}Xe. I have also worked on Monte Carlo simulations of the backgrounds expected in the XENON100 detector, and have taken several shifts at the Laboratori Nazionali del Gran Sasso (LNGS) where the XENON100 detector is housed. During these shifts, I helped with ensuring that the detector was running properly, performed calibration runs, and monitored the krypton distillation process. For the neutron calibartion runs for XENON100, I designed a lead shield used to block γ-rays from the neutron source in order to ensure that only neutrons enter the XENON100 detector, as explained in Ch. 5. Ch. 8 shows a systematic characterization of the QUPID photodetector. I performed nearly all of the tests done on the QUPID and designed and built the cooling system used for low temperature testing of the QUPID. Furthermore, I was involved in the development of a liquid xenon system used for QUPID operation, a uniformity scanner used to test the photocathode and anode uniformity of the QUPID, and a linearity system for testing the linear dynamic range of the

QUPID. Ch. 9 introduces my design for a modular QUPID holder and scalable support structure, which will be used to test seven QUPIDs simultaneously and can be scaled up for use in future experiments.

CHAPTER 2

Dark Matter

2.1 Experimental Evidence

2.1.1 Observations

Evidence for the existence of dark matter was first noted by Fritz Zwicky in 1933 during his observations of the Coma Cluster [18]. By observing the velocity dispersion of the galaxies in the cluster and the amount of visible matter, Zwicky noted that the cluster did not follow the virial theorem. The virial theorem states that in a gravitationally bound system, the total time averaged kinetic energy must be equal to one half of the gravitational potential energy. This is shown mathematically for a galaxy cluster by:

$$< v^2 >= \left\langle \frac{GM}{r} \right\rangle \tag{2.1}$$

Here, v is the average velocity of a galaxy, G is the gravitational constant, r is the radius of the cluster, and M is the mass of the cluster[1]. For the Coma Cluster, Zwicky noted that the equality in Eg. 2.1 was off by an order of magnitude. From this, it was inferred that there must be some form of invisible gravitating matter in the cluster. In 1970, Vera Rubin made the claim that the hydrogen gas in the Andromeda galaxy was rotating with velocities too high to be solely

---

[1] The angled brackets in Eq. 2.1 denote time averages.

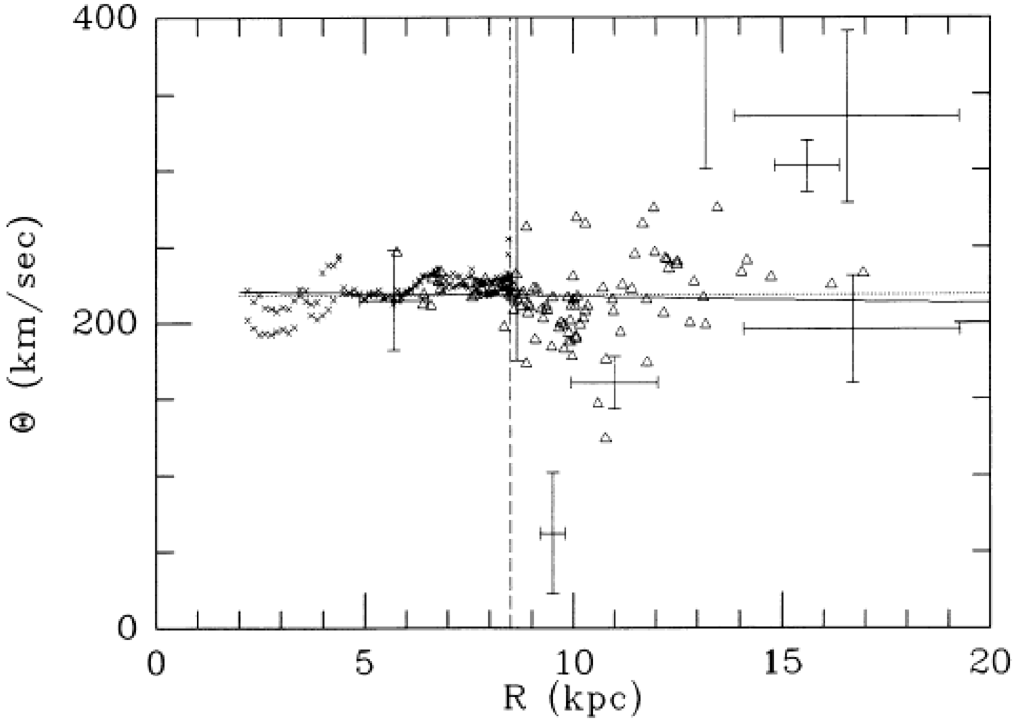

Figure 2.1: Rotation curve of the Milky Way galaxy [21]. The plot shows that the rotational velocity is relatively constant regardless of the radius from the center of the Milky Way. An $r^{-1/2}$ dependence is expected if the matter is concentrated in the center of the galaxy, but this is not the case.

due to the visible matter in the galaxy [19]. From these observations, and future observations, the theory of dark matter was developed.

Ever since the original claims of the existence of invisible gravitating matter, many other experiments have confirmed the need for dark matter. Further measurements of the velocity distributions of galaxies in clusters confirmed the observations of Zwicky [20]. Similarly, observations of the velocities of stars within galaxies consistently show a need for dark matter, just as Rubin had discovered. In most galaxies, the radial velocity of matter is constant and independent of radius [21]. Fig. 2.1 shows the rotational velocity of matter within the Milky Way galaxy as a function of distance. The mass distribution of a galaxy can be found from these rotation curves. For a spherical distribution of matter, the mass distribution will be

$$\frac{dM(r)}{dr} = 4\pi r^2 \rho(r) \tag{2.2}$$

where $M(r)$ is the amount of matter contained within a radius r and $\rho(r)$ is the density of matter. The potential Φ for a gravitational field is given by

$$\Phi = -\frac{GM(r)}{r} \tag{2.3}$$

and Poisson's equation states that

$$\nabla^2 \Phi = 4\pi G \rho \tag{2.4}$$

From this, the force generated at a position r is

$$F(r) = -\nabla\Phi(r) = -\frac{d\Phi}{dr} \tag{2.5}$$

and for a spherical distribution of matter, the force on a particle will be

$$F(r) = \frac{v^2(r)}{r} \tag{2.6}$$

From this, it can be determined that

$$v^2(r) = r\frac{d\Phi}{dr} = \frac{GM(r)}{r} \tag{2.7}$$

and thus, for a constant velocity distribution

$$M(r) = \frac{v^2 r}{G} \tag{2.8}$$

$$\rho(r) = \frac{1}{4\pi r^2}\frac{dM(r)}{dr} = \frac{1}{4\pi G}\frac{v^2}{r^2} \tag{2.9}$$

However, observations of the Milky Way and other galaxies show that the visible mass does not follow this distribution, and an $r^{-1/2}$ trend is expected in the velocity. There have been measurements of over 1100 spiral galaxies, all of which consistently show a deviation from the expected trend, indicating that a majority of the matter in these galaxies is in the form of dark matter [22].

Gravitational lensing measurements also give strong evidence for the existence of dark matter. As explained in General Relativity [23], large concentrations of mass can bend the trajectory of light around the mass. By measuring the bending angle of the light, one can infer the amount of gravitating matter which causes the bending in the trajectory of the light. Galaxy clusters have been observed that clearly cause gravitational lensing of light from distant galaxies. Fig. 2.2 shows an example of gravitational lensing due to the massive galaxy cluster Abell 2218 [24]. By inferring the gravitating mass from the bending angle of the light, and by comparing this to the visible matter in the cluster, one can see that a majority of the matter must be invisible, namely dark matter.

Finally, observations of the Cosmic Microwave Background Radiation give further proof for the existence of dark matter. In the early Universe, photons, electrons, baryons, and other particles were in equilibrium with one another. The photons were constantly undergoing Thomson scattering off of electrons and light nuclei. Eventually, as the Universe expanded and cooled, the average energy of the photons dropped below the binding energy of hydrogen. Because of this, electrons and protons became bound in neutral hydrogen, at which point the Universe became transparent to the photons. This occurred at 377,000 years after the Big Bang, when the temperature of the Universe was at 3000 K. As the Universe continued to expand, the now free streaming photons became redshifted to longer wavelengths, and are currently visible as a 2.75 K background radiation known as the Cosmic Microwave Background (CMB) [26]. The temperature of 2.75 K corresponds to the temperature of the blackbody spectrum that the CMB

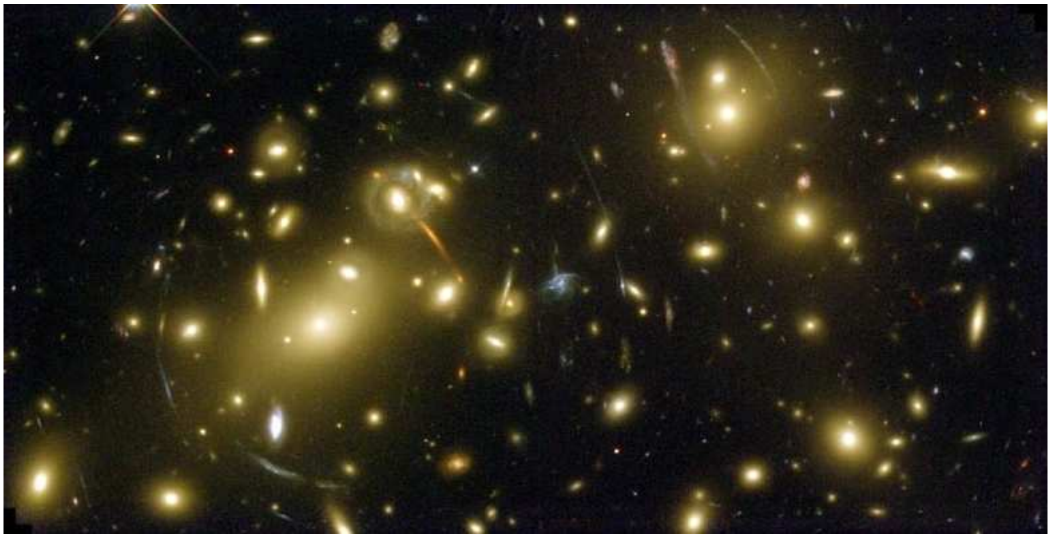

Figure 2.2: Gravitational lensing due to a large cluster of galaxies. The light originating from galaxies behind the cluster is bent around the large mass and creates distorted images on either side of the cluster. From the amount of distortion, the gravitating mass within the cluster can be determined. The amount of visible mass, as determined by X-Ray measurements, is much lower than the amount of gravitating mass in the galaxy cluster [24].

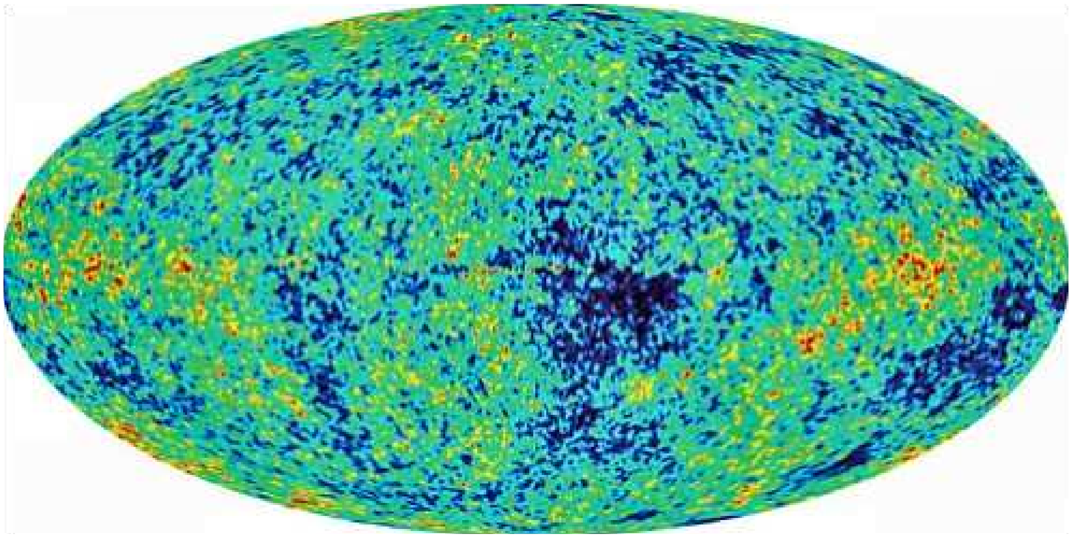

Figure 2.3: A map of the anisotropies of the Cosmic Microwave Background Radiation. The difference in temperature between the red and blue parts of the figure is 600 μK [25].

photons follow. Fig. 2.3 shows a map of the CMB anisotropies as measured by the WMAP satellite.

The Wilkinson Microwave Anisotropy Probe (WMAP) has mapped the CMB and has shown that it is extremely uniform. However, anisotropies do exist at the 10^{-5} level over angular scales of 0.9° [27]. These anisotropies are caused by the Integrated Sachs-Wolfe effect [28], which states that the gravitational potentials along the path of a CMB photon cause gravitational redshifting of these photons. In this way, understanding the anisotropies in the angular power spectrum of the CMB can lead to insight to the evolution of the mass-energy distribution of the Universe. Fig. 2.4 shows the angular power spectrum of the CMB, along with the best fit "ΛCDM" model of the Universe. This model assumes that the Universe is dominated by "dark energy" (Λ or the Cosmological Constant), which accounts for the acceleration of the Universe, and "cold dark matter" (CDM),

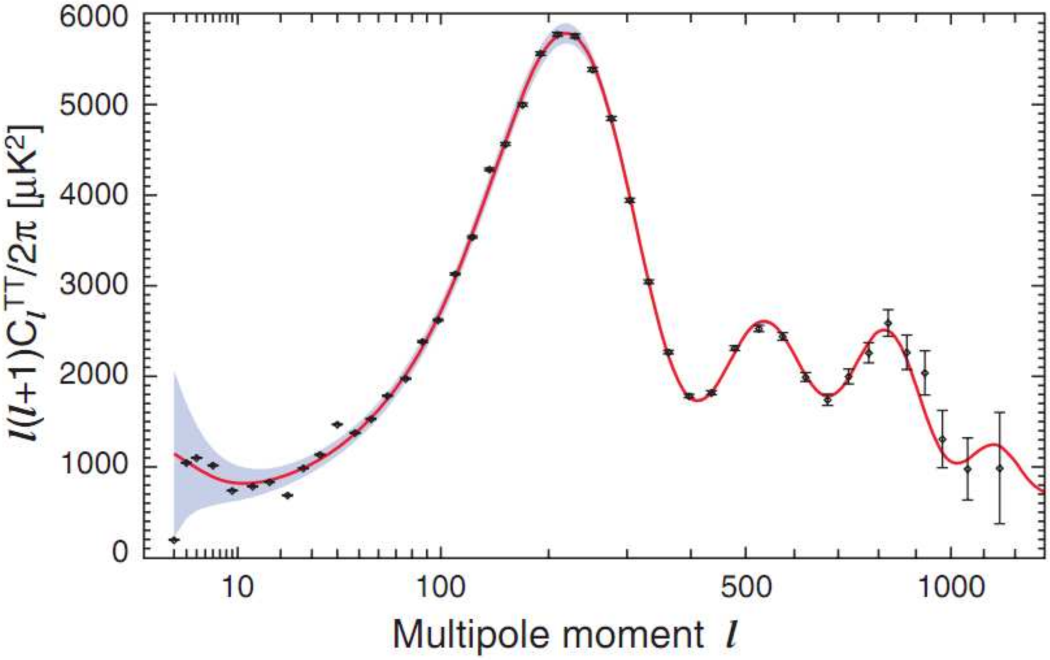

Figure 2.4: A plot of the power spectrum from the CMB map. The data points are from seven years of WMAP data. Theories that incorporate dark matter, such as ΛCDM, reproduce the data well. The ΛCDM model assumes that the Universe is dominated by dark energy along with a contribution from cold dark matter. The solid curve is the ΛCDM model best fit to the data [27].

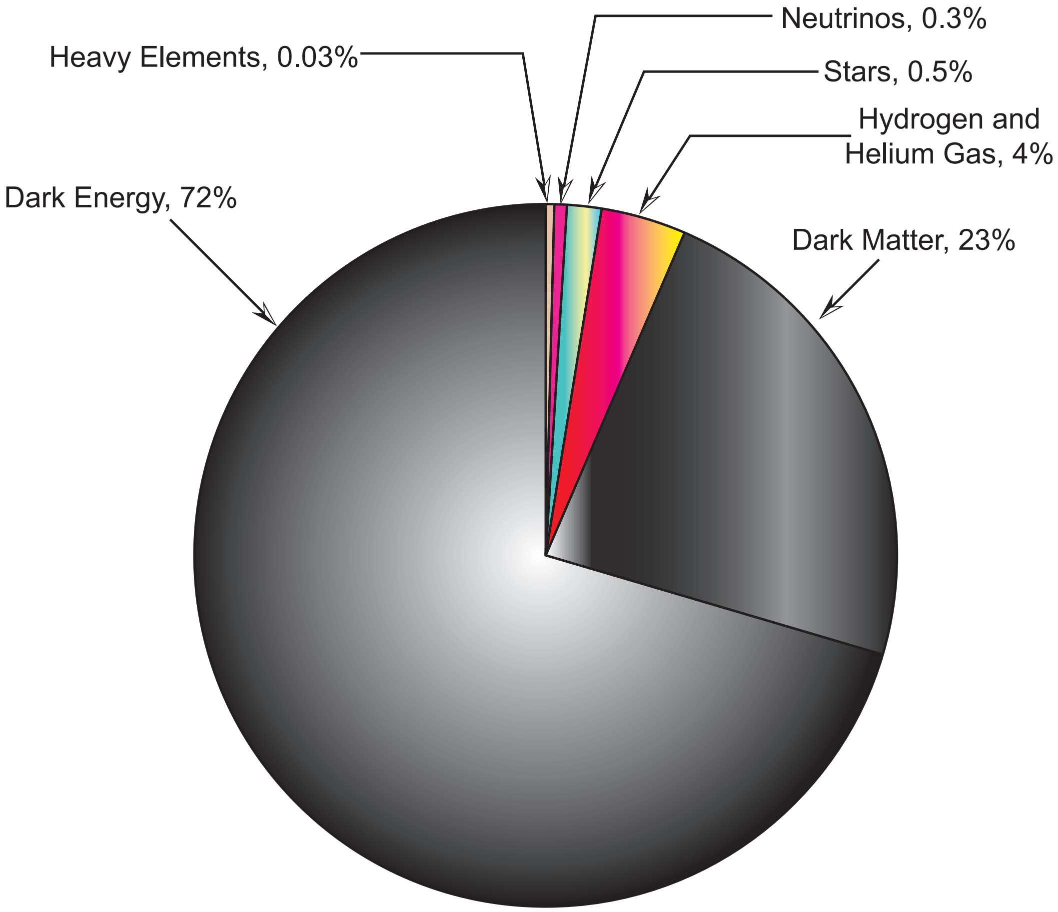

Figure 2.5: A drawing of the constituents of the mass-energy of the Universe. 72% of the Universe consists of dark energy, of which little is known. 23% of the Universe is dark matter, and only 5% of the mass-energy of the Universe consists of ordinary matter.

which accounts for 83% of matter. The best fit ΛCDM model characterizes the total mass-energy of the Universe as 72% dark energy and 23% dark matter [27]. Fig. 2.5 shows the overall constituents of all of the mass-energy of the Universe.

2.1.2 Simulations of Matter Clumping

Recent advances in computing power have allowed for N-Body simulations to be performed with a very large number of particles to simulate the creation of large scale structure in the Universe. By running these simulations only with ordinary baryonic matter, the large scale structure of the Universe was not formed. In order to get the filamentary structure seen in the distribution of galaxies and galaxy clusters on appropriate timescales, the simulation had to include some form of massive, slow moving, weakly interacting particles [29].

When the Weakly Interacting Massive Particles (or WIMPs) were included in the simulations, the slow moving nature of the particles seeded the clumping of baryonic matter around the concentrations of WIMPs. This in turn allowed for the creation of filamentary structures similar to the matter distribution in the present Universe. Fig. 2.6 shows the results of one such simulation called the Millennium Run [29]. The same WIMPs which allowed for the creation of large scale structure can also account for the CMB measurements, galactic rotation curves, and galaxy velocity distributions. It is therefore believed that dark matter should be in the form of WIMPs in order to explain these observations.

2.1.3 The Bullet Cluster

Perhaps the most compelling evidence for dark matter is in observations of the Bullet Cluster. The Bullet Cluster is the result of a collision of two galaxy clusters, as shown in Fig. 2.7. By observing the colliding clusters in X-Ray wavelengths,

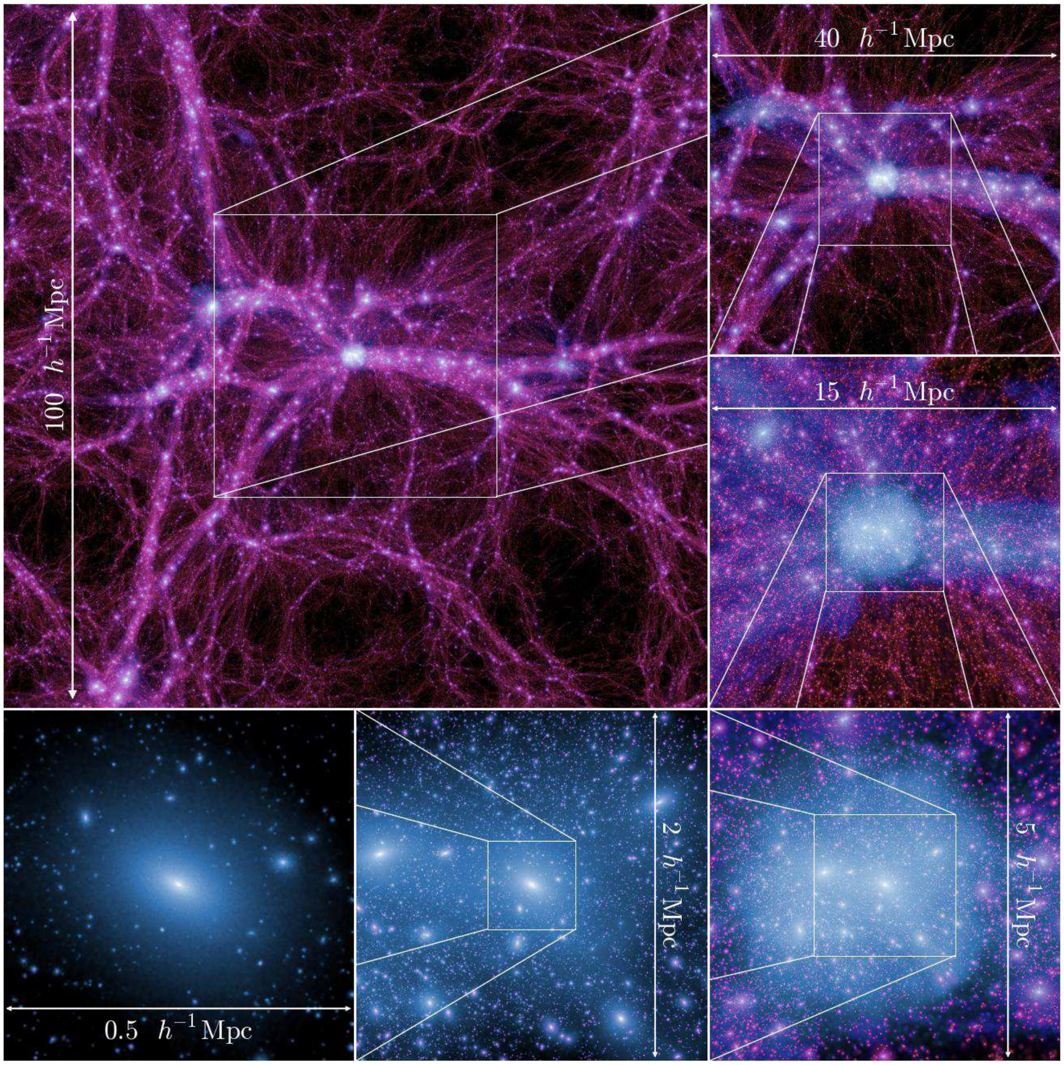

Figure 2.6: The dark matter distribution in the Universe, as simulated by the Millennium Run [29]. Clockwise from the top left, each figure zooms in further through the simulation. Much of the large scale structure matches what is observed in the Universe today.

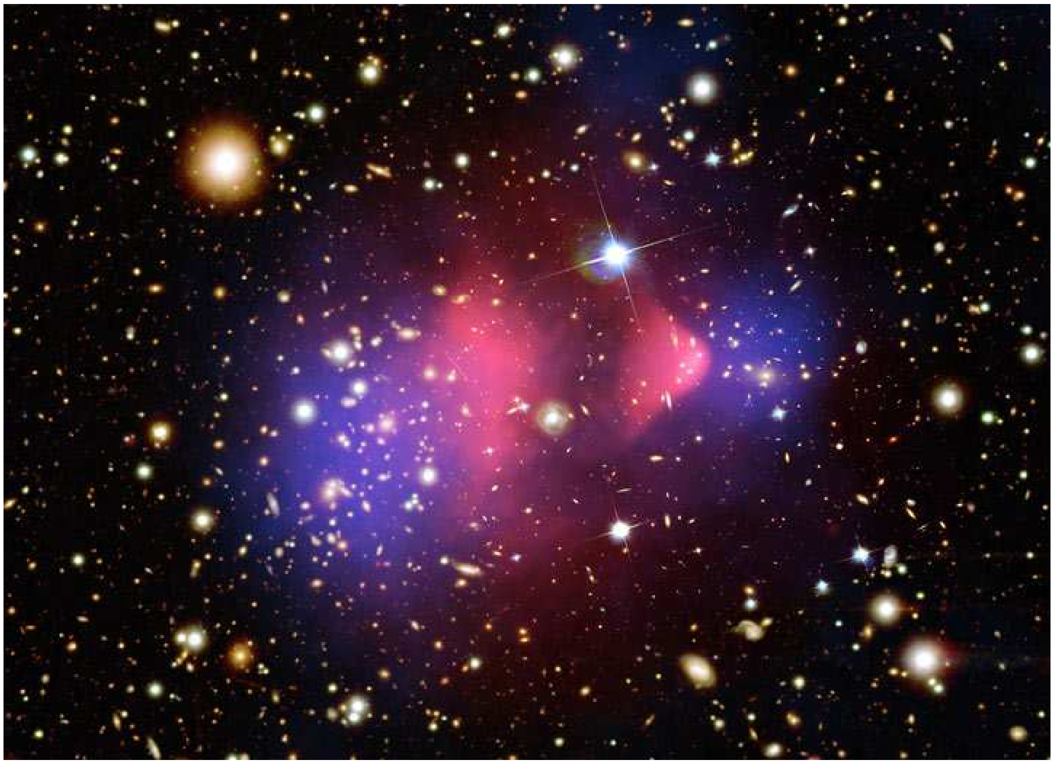

Figure 2.7: The Bullet Cluster showing evidence for the existence of dark matter in the form of WIMPs. The red areas are X-Ray emitting hot gases as observed by the Chandra Telescope, while the blue regions are the areas with the most gravitating matter, inferred by observations of gravitational lensing. Two galaxy clusters collided and continued to move away from one another. The strongly interacting gas, which makes up a majority of the visible matter, was slowed down during the collision, whereas a majority of the gravitating mass in the form of dark matter passed through each another with no resistance [30]. The stars and galaxies themselves are sparsely distributed and do not interact during the collision.

the mass distribution of the X-Ray emitting hot gas can be mapped. This gas makes up a majority of the visible matter in the cluster. Simultaneously, one can observe the effects of gravitational lensing in order to map the distribution of the gravitating matter in the cluster. Superimposing the two maps, it is clear that the X-Ray emitting hot gas has separated from the majority of gravitating matter [30].

Alternative explanations for the discrepancies observed in the CMB measurements, galactic rotation curves, galaxy velocity distributions, and large scale structure formation are theories which state that gravity behaves differently at large distance scales than was previously thought. These theories are known as Modified Newtonian Dynamics (MOND) or Modified Gravity (MOG) theories [31, 32]. However, MOND and MOG theories fail to explain the observations within the Bullet Cluster, which clearly shows how the ordinary baryonic matter from the two separate galaxy clusters collided and interacted, causing the matter to experience a frictional force which slowed it down. A majority of the gravitating matter however continued moving along unabated and separated from the visible matter. Only through the existence of dark matter can the X-Ray emitting matter and gravitating matter become separated the way it has in the Bullet Cluster.

2.2 Dark Matter Theories

2.2.1 The Makeup of the Universe

Cosmology predicts that the density of the total mass-energy of the Universe sets the overall geometry of the Universe. If the total amount of mass-energy is too low, the Universe is considered to be “open” with a negative curvature, and will continue to expand indefinitely. If the mass-energy is too high, the Universe is "closed" with a positive curvature and will eventually collapse in on itself. The third possibility is if the Universe is at the critical density ρ_c. Here, the Universe is flat and infinite. The value of ρ_c is given by the equations of General Relativity as [28]:

$$\rho_c(t) = \frac{3H^2(t)}{8\pi G} \tag{2.10}$$

where $t = 0$ is the current time and $H(t)$ is the Hubble parameter characterizing the expansion rate of the Universe, and the present value of the Hubble parameter is $H_0 = 73 \pm 3$ km s^{-1} Mpc^{-1} [33], where 1 parsec (pc) is equivalent to 3.26 light years, or 3.09×10^{16} m. The density of the mass-energy of the Universe ρ_{tot} can be broken up into various components:

$$\rho_{tot} = \rho_r + \rho_m + \rho_\Lambda \tag{2.11}$$

Here, ρ_r is the density of radiation, ρ_m is the density of matter, and ρ_Λ is the contribution from the Cosmological Constant. Then, one can define the density parameters Ω as:

$$\Omega_{tot} \equiv \frac{\rho_{tot}(0)}{\rho_c(0)} \tag{2.12}$$

$$\Omega_r \equiv \frac{\rho_r(0)}{\rho_c(0)} \qquad \Omega_m \equiv \frac{\rho_m(0)}{\rho_c(0)} \qquad \Omega_\Lambda \equiv \frac{\rho_\Lambda(0)}{\rho_c(0)} \tag{2.13}$$

$$\Omega_{tot} = \Omega_r + \Omega_m + \Omega_\Lambda \tag{2.14}$$

For the case that $\rho_{tot} = \rho_c$, $\Omega_{tot} = 1$. The present day contribution by Ω_r can be found from the CMB photons using Stefan's Law to be

$$\Omega_r = \frac{4\sigma T^4}{c^3\rho_c(0)} = 4.65 \times 10^{-5} \tag{2.15}$$

which makes up a very small contribution. In Eq. 2.15, σ is the StefanBoltzmann constant, T is the temperature of the CMB photons, and c is the speed of light. Observational evidence must be used to find the contributions from Ω_m and Ω_Λ.

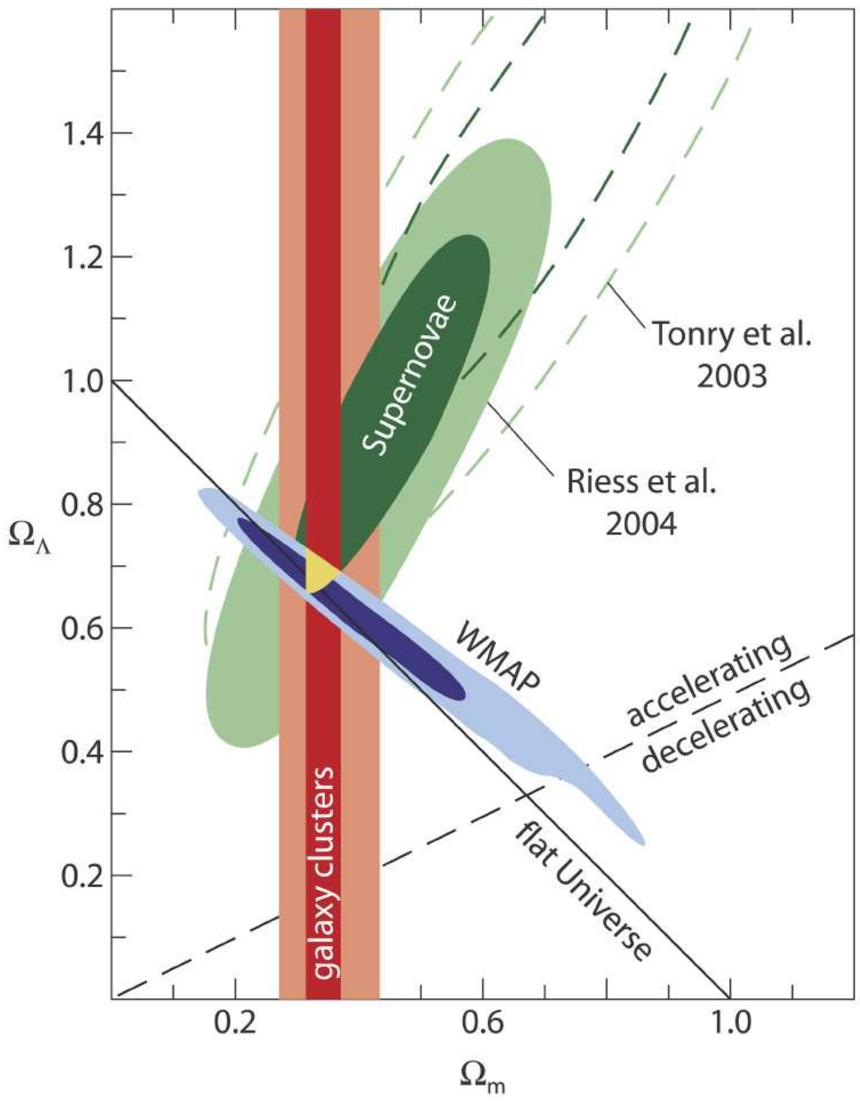

Figure 2.8: A plot of the measured values of Ω_Λ and Ω_m. The experimentally determined values come from supernova observations (green), galaxy cluster surveys (red) and WMAP measurements (blue). The solid diagonal line corresponds to $\Omega_{tot} = 1$, and the data converges around the point where $\Omega_\Lambda \simeq 0.73$ and $\Omega_m \simeq 0.27$ [34, 35, 36].

Different types of experiments have measured the values for these constituents of Ω_{tot}, and there is good evidence that the value is close to unity, as shown in Fig. 2.8.

2.2.2 MACHOs and Neutrinos

Some theories that have been formulated to describe the aforementioned observations have focused on more conventional explanations based on standard physics. One such theory is that dark matter consists of Brown Dwarfs, Black Holes, Neutron Stars, and other faint, massive objects which are difficult to detect. These objects are known collectively as Massive Compact Halo Objects, or MACHOs. The MACHOs can be a good explanation for dark matter, and can be found through searches of gravitational microlensing. In microlensing, a dim object (in this case a MACHO) becomes brighter when additional light from the object bends around a gravitational lens towards the observer [37]. However, observations of gravitational microlensing have almost completely ruled out this theory for dark matter [38]. These objects certainly do exist, and can act as a form of dark matter; however observations show that they only account for a fraction of the dark matter.

Another method of testing for large amounts of ordinary baryonic matter hidden in MACHOs is by considering the primordial abundance of light nuclei from Big Bang nucleosynthesis. By comparing the model predicted abundances of the light nuclei to currently measured values, one can deduce the total baryon density in the Universe, as the abundances of the light nuclei vary strongly with the baryon density [40]. Fig. 2.9 shows the model predicted abundances of various nuclei, along with the experimentally observed values. This corresponds to a baryon density of $\Omega_B = 0.038 \pm 0.002$ from deuterium measurements, and $\Omega_B =$

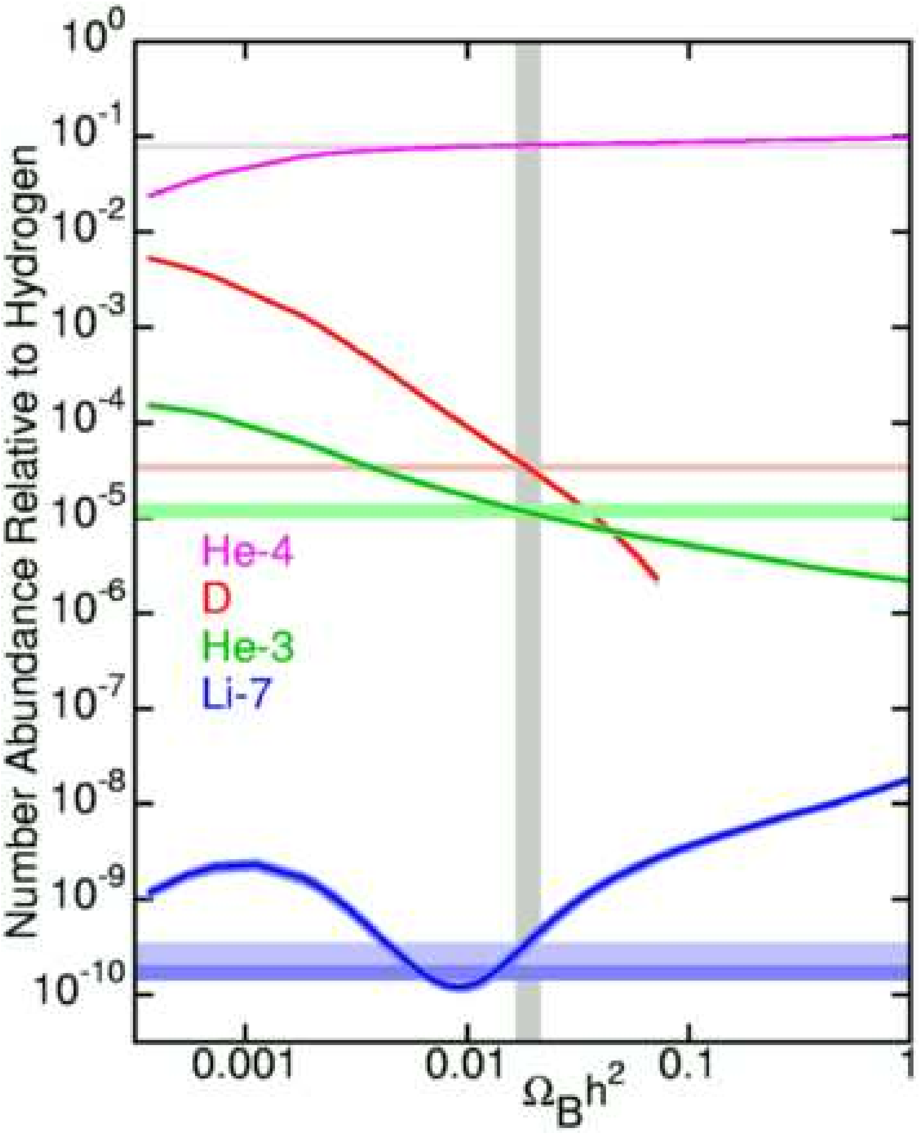

Figure 2.9: A plot of the predicted and observed abundances of various light nuclei. The dark, solid lines correspond to the predictions from Big Bang nucleosynthesis, whereas the lighter, horizontal lines are the experimentally observed values. The gray vertical bar represents the best fit for the total baryon density [39].

0.023 ± 0.007 from ^{4}He and ^{7}Li measurements [41, 42]. Both values are below the expected matter density in the Universe of $\Omega_m = 0.267$, and so baryonic matter cannot be a majority of the matter in the Universe. Since MACHOs consist of ordinary baryonic matter, they are not a good candidate for dark matter.

Other theories have been brought forth that focus on neutrinos as a dominant form of dark matter. Neutrinos are very light, weakly interacting particles predicted by the Standard Model (see Sec. 2.2.3). The weakly interacting aspect of neutrinos makes them a good candidate for dark matter, however neutrinos are moving at relativistic velocities, and would be a form of "hot dark matter." The fact that the neutrinos have high velocities means that they would not be able to seed the large scale structure visible in the current Universe. A chief requirement of dark matter candidates be that they are produced non-thermally and are non-relativistic, or "cold" during decoupling [43], and neutrinos do not satisfy this requirement. Similar to MACHOs, neutrinos do make up a fraction of the dark matter in the Universe, but there must still be some other form of dark matter.

2.2.3 The Standard Model

The leading model for particle physics is called the Standard Model. Having been developed through several decades of experimentation, the Standard Model describes all aspects of particle physics through a set of 17 particles and can make predictions to high accuracies. The particles of the Standard Model can be divided into two main sets, bosons, which have integer spins, and fermions, which have half-integer spins. In the current version of the Standard Model, there exist twelve fermions and four types of force mediating gauge bosons, as well as with the Higgs Boson, which has yet to be confirmed experimentally [44, 2].

A diagram of the particles in the Standard Model is shown in Fig. 2.10. The fermions include six quarks, which combine to make baryons such as the proton and neutron, and six leptons, which include particles such as the electron and neutrinos. These fermions make up the constituents of ordinary matter. The bosons however are responsible for the forces experienced between particles. The gluons are the particles which mediate the strong force, the W and Z bosons mediate the weak force, and the photon is responsible for the electromagnetic force. The electromagnetic and weak forces unify at energies above 246 GeV and become the electroweak force. The spontaneous symmetry breaking which separates these two forces is caused by the Higgs Boson, which is then responsible for the masses of the gauge bosons [2].

The Standard Model has been able to make many predictions, for example it predicted the existence of the W and Z bosons, the gluon, the top quark, and the charm quark before they were experimentally discovered. In the development of the Standard Model, the masses of the W and Z bosons were related to a parameter called the "Weak Mixing Angle" (or Weinberg Angle) θ_W as[2]:

$$M_{W^{\pm}} = \frac{37.4}{\sin\theta_W}\mathrm{GeV} \tag{2.16}$$

$$M_{Z^0} = \frac{M_{W^{\pm}}}{\cos\theta_W} = \frac{75}{\sin 2\theta_W}\mathrm{GeV} \tag{2.17}$$

The Weak Mixing Angle θ_W was determined through neutrino scattering and polarized electron scattering experiments, and the mass of the W boson, determined after discovery, helped to predict the mass of the Z boson. Using these parameters, the mass of the Z boson was predicted at 91.1874 ± 0.0021 GeV, while the experimentally measured mass was 91.1876 ± 0.0420 GeV [45]. However, despite the accurate predictions the Standard Model has made, there are

---

[2] Although GeV is a unit of energy, mass-energy equivalence states that $E = mc^2$ and so a mass can be described as energy scaled by a factor of $1/c^2$. Thus, the mass of a 1 GeV particle will be $m = \frac{1GeV}{c^2} = 1.78 \times 10^{-27}$ kg.

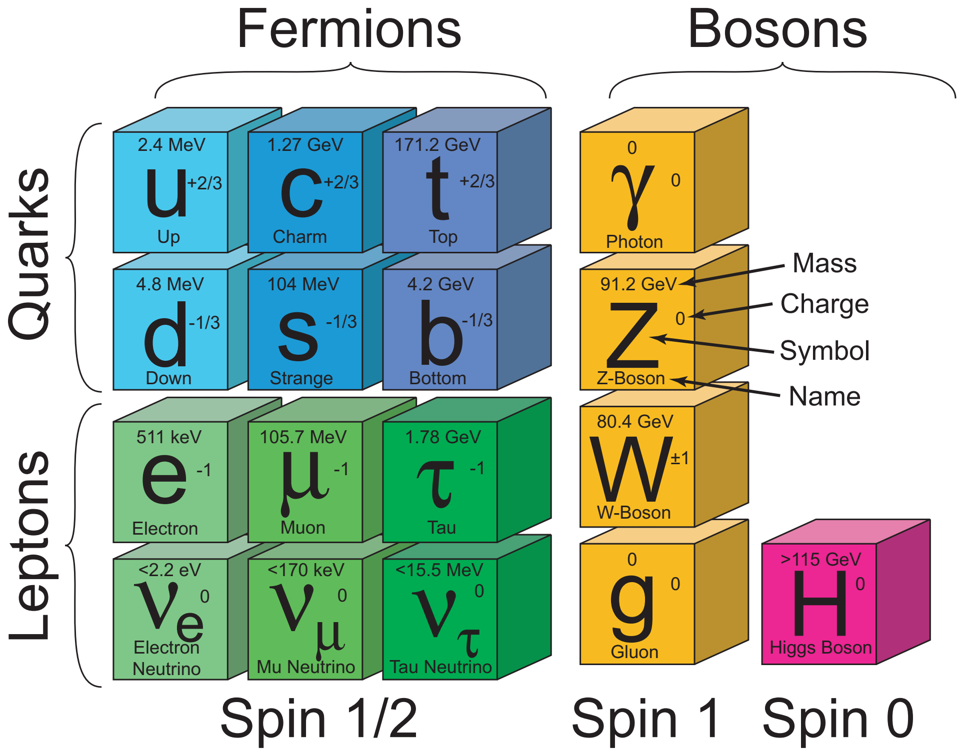

Figure 2.10: A diagram of all of the particles in the Standard Model. Fermions (particles with half-integer spins) are on the left, while bosons (particles with integer spins) are on the right. All of the particles have been experimentally confirmed except for the Higgs Boson.

several shortcomings which have led most physicists to believe that the Standard Model is incomplete.

2.2.4 Problems with the Standard Model

2.2.4.1 Neutrino Masses

The fermions of the Standard Model include six quarks and six leptons. Of the six leptons, three of them are the neutrinos, the electron neutrino, mu neutrino, and tau neutrino (ν_e, ν_μ and ν_τ). The Standard Model describes these neutrinos as massless, and only left-handed neutrinos (or right-handed antineutrinos) should interact with matter. However, recent experiments have shown compelling evidence that neutrinos do in fact have mass. The earliest experiment to show discrepancies in the understanding of neutrinos was performed by Ray Davis in the 1960's [10]. The experiment was designed to detect neutrinos originating from nuclear fusion processes in the sun, where only ν_e were thought to be produced. After running the experiment, only $\sim$1/3 of the expected flux of neutrinos was detected.

Future experiments showed similar discrepancies between predicted neutrino fluxes and observed neutrinos. These experiments studied neutrinos produced in the sun and through cosmic ray interactions in the upper atmosphere of the Earth [16, 17, 12, 11]. The first experiment to conclusively show evidence for neutrino oscillations was the Super-Kamiokande experiment. This experiment observed the flux of atmospheric neutrinos. Through cosmic ray interactions in the upper atmosphere, a flux of ν_e and ν_μ is expected at a well known ratio. However, observations showed that the ratio of ν_e to ν_μ was higher than expected, showing a hint of neutrino oscillation [46]. Another method used by Super-Kamiokande was to observe the flux of ν_μ as a function of the arrival direction. Since cosmic rays arrive at the Earth isotropically, the flux of ν_μ should be constant with respect to the angle from the zenith, however the flux of ν_μ did show a dependence on the angle from the zenith [47]. These discrepancies can be explained by neutrino oscillations, that is, the ν_μ "oscillated" into other types of neutrinos.

An independent confirmation of neutrino oscillations came from solar neutrino observations. Previous solar neutrino observatories had a common feature that they were all sensitive to only one type of neutrino. In 1999, an experiment was devised to look at the neutrinos produced within the sun called the Sudbury Neutrino Observatory (SNO). SNO was a unique experiment in that it was sensitive to all three types of neutrinos, and was also able to distinguish between the three neutrino types. The experiment showed that the total number of observed neutrinos was correct, but only a fraction of them were ν_e. The remaining neutrinos were of ν_μ and ν_τ type [48]. The only way these neutrinos could have come into existence was through neutrino oscillations. In order to have oscillations between different types of neutrinos, the neutrinos must have mass, contradicting the original assumption of the Standard Model.

2.2.4.2 Coupling Constants

Yet another characteristic that makes the Standard Model less attractive is that of the coupling constants. In the 19th century, James Clerk Maxwell was able to combine the seemingly unrelated forces of electricity and magnetism into one force called electromagnetism. Similarly, in the 1970's, physicists Abdus Salam, Steven Weinberg, and Sheldon Glashow formulated a theory to combine electromagnetism and the weak force into what became known as the electroweak force [49, 50, 51]. Since then, physicists have been working on unifying the electroweak force with the strong force in a Grand Unified Theory (GUT). From collider experiments, it has been seen that the coupling constants for the electromagnetic, strong, and weak Forces (the constants characterizing the relative strengths of the interactions) change with energy [52]. Collider experiments have only been able to probe up to several hundred GeV, and the change of the coupling constants has been seen in this energy range. The Standard Model predicts this change in the coupling constants up to the highest energies. Fig. 2.11 shows

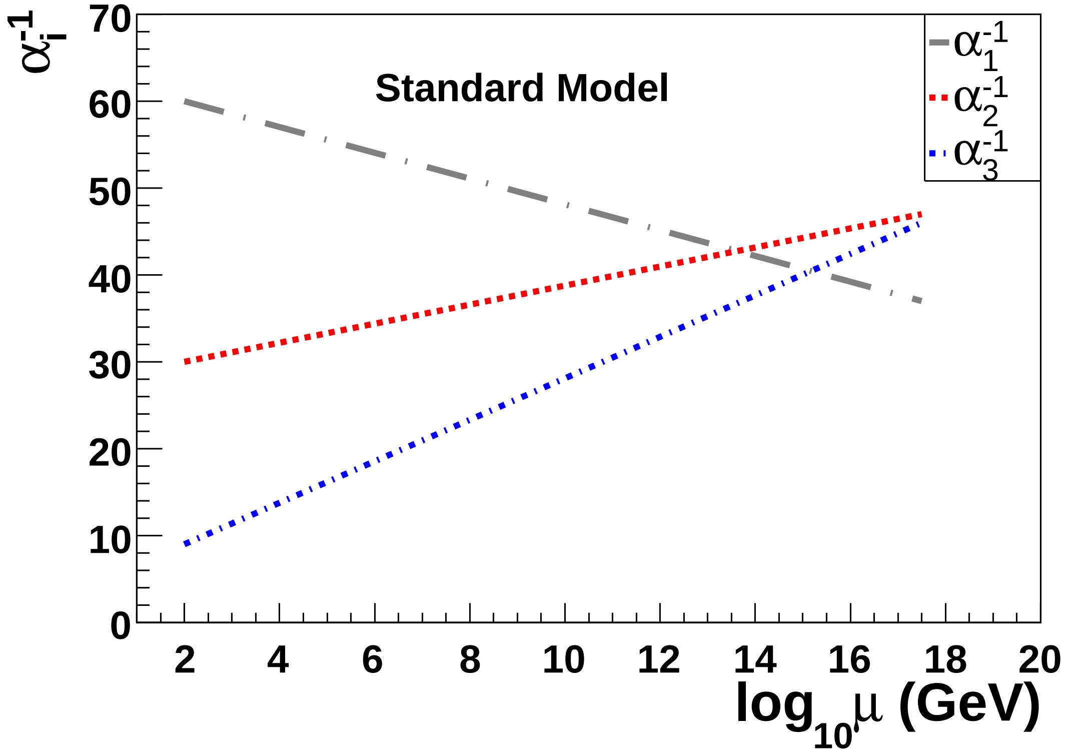

Figure 2.11: An extrapolation of the energy dependence of the coupling constants for the electromagnetic (α_1), weak (α_2), and strong (α_3) forces in the Standard Model. Note that they do not converge to a single point at the highest energies.

the running of the coupling constants with respect to energy for the Standard Model. Unfortunately, with the Standard Model, the three coupling constants do not meet at a single point, and unification is therefore not possible. Although unification is not required within the Standard Model, as new physics at higher energies may account for this, it would have been an attractive feature.

Another problem is that the point of "near unification" occurs at around 10^{14} GeV. Several experiments have been conducted and are ongoing searching for proton decay, which is a consequence of many of the GUTs. Although no experiment has observed proton decay, a lower limit has been set on the proton lifetime [44]. However, if unification did indeed occur at $\sim 10^{14}$ GeV, it would predict a proton lifetime much shorter than the current limit.

2.2.4.3 Hierarchy Problem

The Hierarchy Problem is yet another problem with the Standard Model [2]. The Higgs Boson is the only particle of the Standard Model that has been theorized but not yet observed experimentally. The Higgs couples to the gauge bosons to give their effective masses, m_b. Using rules given by the Standard Model, the quantum corrections to the masses of the fermions can be calculated. These corrections depend on a cut-off energy scale L logarithmically:

$$\delta m_f \sim m_f \ln\left(\frac{L^2}{m_f^2}\right) \tag{2.18}$$

The expected corrections to the mass of the Higgs particle can also be calculated, which turns out to be:

$$\delta m_H^2 \sim L^2 \tag{2.19}$$

The problem here is that the mass of the Higgs is sensitive to the scale of L. Since the masses of the gauge bosons couple to that of the Higgs, the L dependence of the Higgs mass would drive the masses of the gauge bosons to the Planck scale ($\sim 10^{19}$ GeV) [52]. This cannot be the case, as it is known that the electroweak interaction scale is 246 GeV, much lower than the Planck scale. The only possible solution within the Standard Model to account for this discrepancy is that there exists fine tuning that cancels out terms within the calculation of the Higgs mass. Such a solution is unfavorable as there is no reason for fine tuning to exist to such precision.

2.2.5 Supersymmetry

Several theories have been brought forth in order to solve the above stated problems with the Standard Model. Of these theories, one of the more prevailing theories is Supersymmetry. In Supersymmetry, the number of particles from the Standard Model is doubled. As shown in Fig. 2.12, every particle from the Standard Model will have a supersymmetric partner. These new particles will have the same properties as the original set of particles aside for the spins of the particles. Every particle with an integer spin will have a partner with half-integer spin, and every particle with half-integer spin will have a partner with integer spin [53]. In other words, for every boson there exists a partner fermion and every fermion has a partner boson. The supersymmetric particles will have the same names as the Standard Model counterparts, except that the supersymmetric boson partners to the Standard Model fermions have an ‘s’ place in front of the name (for example, fermions→sfermions, quarks→squarks, electrons→selectrons) while the supersymmetric fermion partners to the Standard Model bosons have an ‘ino’ placed at the end of the name (for example, bosons→bosinos, W→Wino, photon→photino).

Supersymmetry can be used to solve some of the problems with the Standard

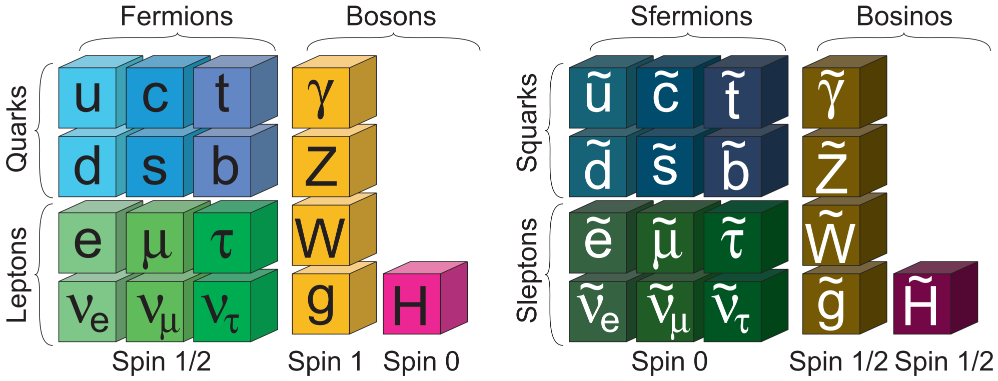

Figure 2.12: A diagram of all of the particles in the Standard Model along with their Supersymmetric partners. The spins of the Supersymmetric partners differ from those of the Standard Model by 1/2, and the masses of these particles must be greater than those of their Standard Model partners.

Model. Within the calculations of the mass of the Higgs particle, Supersymmetry naturally introduces terms that cancel out the largest contributions to the Higgs mass [54]:

$$\delta m_H^2 \sim (m_b^2 - m_f^2) \tag{2.20}$$

Here, m_b and m_f correspond to the masses of the bosons and fermions respectively. The fact that these masses enter into the corrections with opposite signs allows for the Higgs mass to be protected, and removes its dependence on L.

Furthermore, with the introduction of Supersymmetry, the coupling constants become modified at energies above several hundred GeV, and the constants do meet at a single point allowing for unification [52] as seen in Fig. 2.13. The point of unification in Supersymmetry is also at a higher energy than the point of “near unification” in the Standard Model. This then allows for the unification to be consistent with experimental limits of proton decay [44].

If Supersymmetry did indeed exist, the supersymmetric particles would have

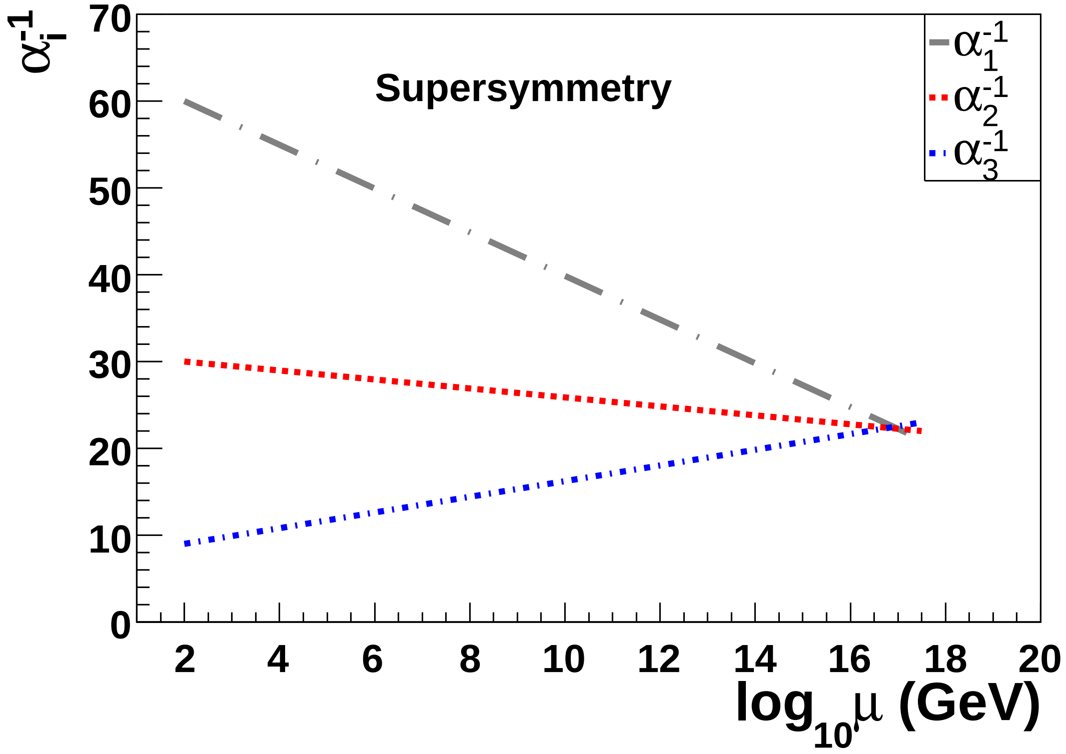

Figure 2.13: A prediction of the energy dependence of the coupling constants for the electromagnetic (α_1), weak (α_2), and strong (α_3) forces with the inclusion of Supersymmetry. In this case, the coupling constants do meet at a single point at the GUT scale.

already been observed. Since the new partners have the same characteristics (aside from spin), they should also have the same mass and would be within the realm of current experiments. These supersymmetric particles have not yet been discovered, and thus it is theorized that Supersymmetry is in fact a broken symmetry, with the new particles having masses heavier than their Standard Model partners. In order for Supersymmetry to solve the hierarchy problem as explained above, the supersymmetric particles should have masses on the order of ~TeV and the Higgs should have a mass $m_H < 130$ GeV [55, 56]. As a comparison, the mass of a proton is 938 MeV, and so the supersymmetric particles would have masses around 1000 times that of the proton.

2.3 The WIMP Miracle

Supersymmetry has become an intriguing theory for physics beyond the Standard Model. Supersymmetry in the most general form has 106 free parameters (along with 18 from the Standard Model). This makes Supersymmetry in this form less appealing, however the additional number of free parameters can be reduced to five using several constraints. This type of Supersymmetry is called the Minimal Supersymmetric Model (MSSM) [52].

The concept of R-Parity is introduced in the MSSM. R-Parity is a conserved quantity that is required in order for MSSM to be in agreement with the observed lepton number and baryon number conservation in the Standard Model. R-Parity is defined as $R = (-1)^{2s+3B+L}$ where s is the spin of the particle, B is the baryon number, and L is the lepton number [57]. All Standard Model particles have an R-Parity of 1, while all supersymmetric particles have an R-Parity of -1. If R-Parity is conserved, then all supersymmetric particles that can decay must decay into a Standard Model particle and a supersymmetric particle. Because of this, the Lightest Supersymmetric Particle (LSP) must be stable, as there are no lighter supersymmetric particles for it to decay into.

The MSSM predicts the LSP to have a mass on the order of the electroweak scale, that is, around several hundred GeV. If dark matter is in the form of WIMPs, cosmology predicts that the mass and cross section of these particles should also be around the electroweak scale. If dark matter is indeed WIMPs, there exists a point in time after the Big Bang where these WIMPs freeze-out. Early in the Universe, the temperature exceeded the WIMP mass allowing for WIMPs to be constantly created and annihilated, such that the WIMPs were in thermal equilibrium. As the Universe expanded and cooled below the WIMP mass, the creation of WIMPs ceased, while annihilation continued. Finally, the expansion of the Universe reached a point such that the number density of WIMPs were too low for them to effectively annihilate. The number of WIMPs then remained relatively constant after this "freeze-out." The freeze-out process is shown in Fig. 2.14. A simple way to describe the time evolution of the WIMP number density is [57]:

$$\frac{dn_\chi}{dt} + 3Hn_\chi = -\langle \sigma_A v \rangle \left[(n_\chi)^2 - (n_\chi^{eq})^2 \right] \tag{2.21}$$

Here, n_χ is the number density of WIMPs, H is the Hubble expansion rate of the Universe, σ_A is the annihilation cross section for WIMPs, v is the relative velocity, and n_χ^{eq} is the number density of WIMPs at equilibrium. The point at which freeze-out occurs, and thus the number density of WIMPs after freeze-out, depends on the annihilation cross section of the WIMPs, which in turn depends on the mass of the WIMPs. In order to have the expected number density of WIMPs in the Universe, the mass and interaction cross section of the WIMP turns out to be at the electroweak scale. The "miracle" therefore is that the LSP, which comes out of a theory to solve problems in particle physics, becomes a good

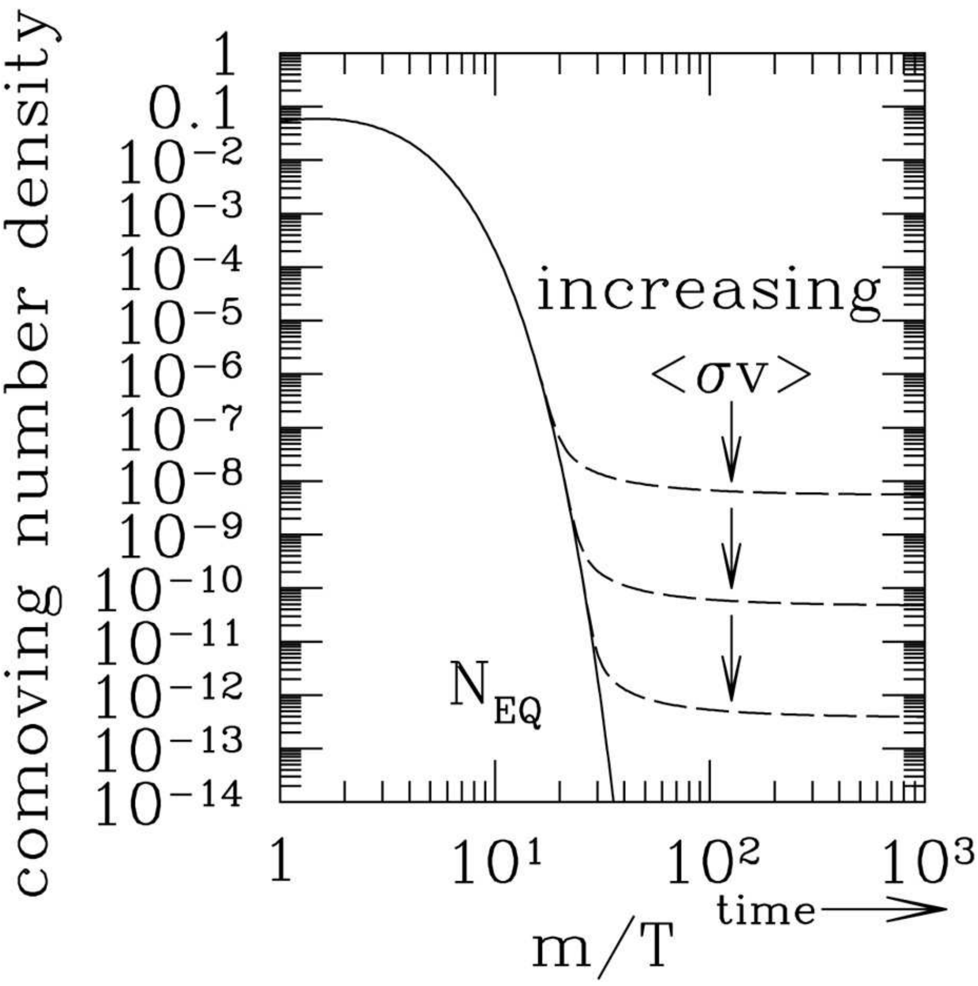

Figure 2.14: A plot of the comoving number density of WIMPs as a function of time. A comoving distance is a distance scale normalized such that the expansion of the Universe is factored out. That is, the distance does not change with the expansion of the Universe over time. Early in the Universe, the number density is relatively constant, as creation and annihilation of WIMPs occur in equilibrium. As the temperature of the Universe drops, the rate of creation of WIMPs drops, while annihilation continues, and so the number density begins to fall. As the Universe expands further, the number density of the WIMPs falls to such a level that the WIMPs can no longer annihilate at an appreciable rate. At this point, the comoving WIMP number density stays constant. This is known as freeze-out [58].

candidate for dark matter, which was theorized to solve problems in astrophysics and cosmology.

In order for the LSP to be a good candidate for dark matter, it should be a neutralino. A neutralino is a linear combination of the neutral supersymmetric fermions (Zino, photino, and Higgsino). These are the supersymmetric partners of the neutral Standard Model bosons (Z, γ, and H). Supersymmetry predicts four such linear combinations, resulting in four neutralinos labeled as $\tilde{\chi}_1^0$, $\tilde{\chi}_2^0$, $\tilde{\chi}_3^0$, and $\tilde{\chi}_4^0$. The lightest of these four neutralinos can then make up dark matter in the form of WIMPs.

2.4 Summary

Since dark matter makes up 23% of the Universe, yet the Standard Model of particle physics does not account for it, it is imperative to make every effort to understand and characterize dark matter so that a more complete model can be developed. The leading candidate for dark matter, WIMPs in the form of neutralinos, is attractive in that it simultaneously solves problems in cosmology and in particle physics, and the discovery of such neutralinos may allow for Supersymmetry to become the new model of particle physics. The following chapter will describe experiments which are currently searching for the existence of WIMPs.

CHAPTER 3

Current Generation Detectors

Although there is strong evidence for the existence of dark matter in the form of WIMPs, there has never been a positive detection of WIMPs. Several searches are underway to discover dark matter using different types of technologies. Dark matter searches can be characterized in three major groups, accelerator searches, indirect detection, and direct detection experiments.

3.1 Accelerator Searches

Accelerator searches for dark matter refer to the possibility of creating WIMPs through the collisions of particles in particle accelerators. Particle accelerators have been essential in the development of particle physics for many decades. Every generation of accelerator has proved to be useful in the discovery of new particles by achieving higher energies and thereby probing higher masses. Currently, the leading accelerator is the Large Hadron Collider (LHC) in CERN [59]. The LHC, when operating at full energy, will have a center of mass energy of 14 TeV, seven times higher than the next leading accelerator, the Tevatron.

Searching for the production of WIMPs at the LHC is not trivial. Although the energy may be high enough to produce WIMPs, the WIMPs will not interact with the detectors at the LHC and will simply exit the accelerator without being detected. In order to conclude that a WIMP was created at the LHC, one must look for "missing energy." By observing the energies and momenta of the particles detected from the collision, one can deduce whether or not a particle was created and simply exited the accelerator without being detected [60]. Along with this approach, one can also search for telltale signatures for the production of other supersymmetric particles. It can be possible that the LHC produces supersymmetric particles that are not necessarily the LSP. These particles may decay down to the LSP within the span of the detector, thereby creating Standard Model particles in proportions that would not be seen in Standard Model physics [61].

3.2 Indirect Detection

Another way of searching for dark matter is by looking for signatures of the annihilation of WIMPs in areas where an excess of dark matter is expected. Fig. 3.1 shows the simulated distribution of dark matter in a galaxy similar to our own. Because dark matter interacts gravitationally, it is expected that places in the Universe with greater mass than the surroundings may harbor clumps of dark matter [62]. The center of galaxies for example may have greater concentrations of WIMPs, and the sun itself, or the Earth may also have local excesses of dark matter. In these locations, WIMPs would be gravitationally bound to the large mass, and would lose angular momentum through weak interactions with either the surrounding matter or other WIMPs. This would cause the WIMPs to fall into the gravitational well and would create a local excess.

In many models of Supersymmetry, the LSP may be able to self annihilate, that is they may annihilate with one another [64]. If this is the case, the annihilation processes would occur more readily in areas with greater densities of dark matter (if the LSP is the main constituent of dark matter). Many different

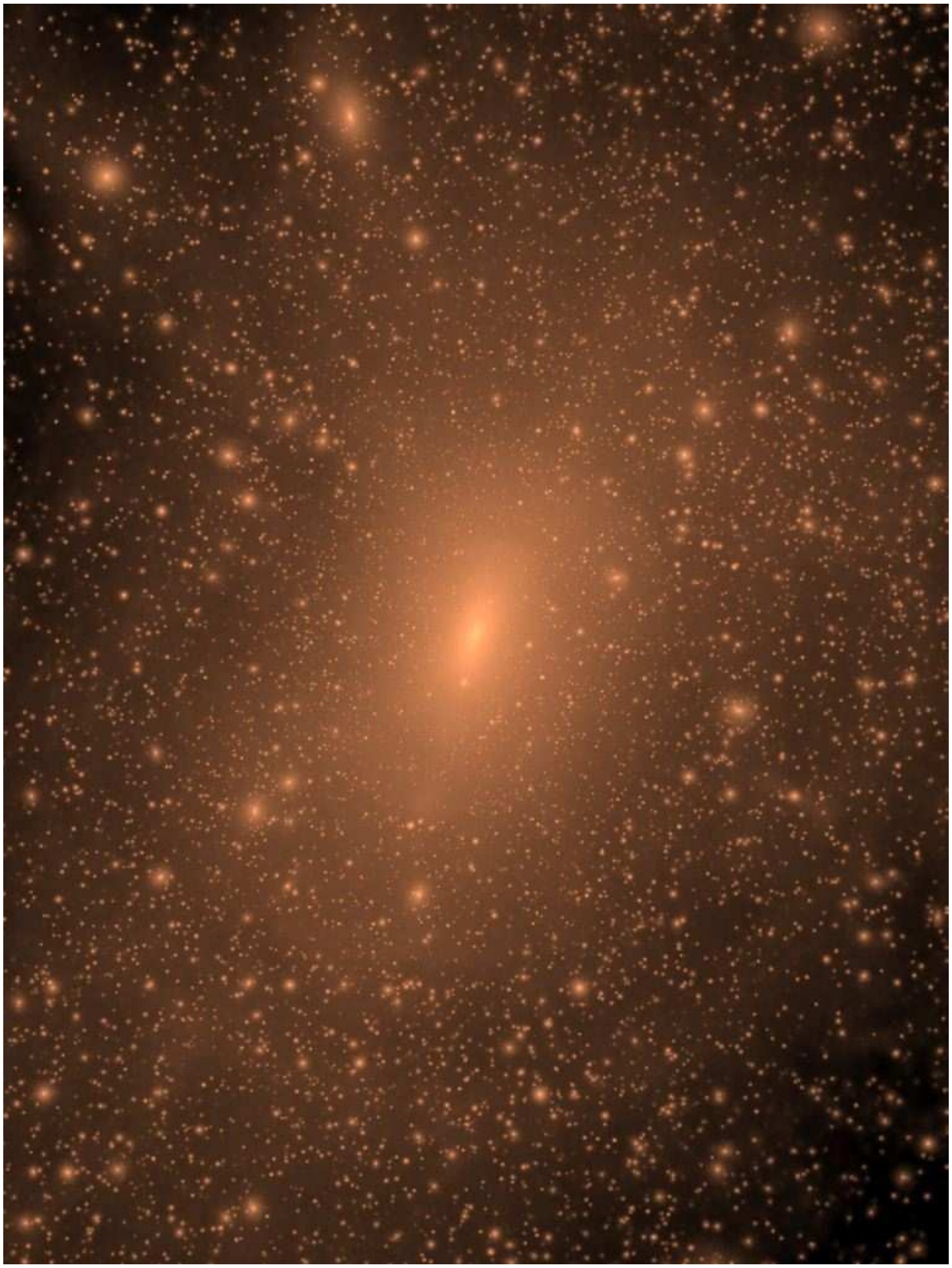

Figure 3.1: A simulation of the dark matter distribution of a galaxy similar to the Milky Way. This image corresponds to 800×600 kpc, going through a 600 kpc deep cube. Note the higher densities in the center and in clumps surrounding the galaxy [63].

models of Supersymmetry exist, and as such, many different possible annihilation processes may occur. It is thought that WIMPs would preferentially annihilate to heavy quarks, gauge bosons, or the Higgs Boson [65]. In either case, these particles will decay down to lighter particles. In order to distinguish an excess of these particles over backgrounds, indirect searches focus on certain distinct signatures. In the case of γ-ray annihilations, certain theories predict spectral shapes that constitute a “smoking gun” signature of dark matter. That is, no background would be able to reproduce a spectrum similar to that expected from WIMP annihilation. These experiments look at regions of high dark matter density, such as the galactic center or dwarf galaxies. Examples of indirect detection experiments searching for γ-ray signals are HESS, VERITAS, MAGIC, and Fermi-LAT [66, 67, 68, 69]. Other indirect searches are looking for excesses in neutrinos from the sun, as solar physics is understood quite well, and the only particles from WIMP annihilations that would be able to exit the sun would be neutrinos. Some examples of experiments using neutrinos for indirect dark matter detection are IceCube and AMANDA [70]. Finally, other experiments are searching for excesses of positrons, anti-protons, or anti-deuterons originating from the dark matter surrounding the Milky Way, such as PAMELA, AMS, BESS and GAPS [71, 72, 73, 74].

3.3 Direct Detection

Direct dark matter detection experiments search for interactions between WIMPs and ordinary matter. When a WIMP scatters off of an atom, it can deposit energy which may be detected through various methods. The leading direct dark matter search experiments search for energy deposits through either scintillation, ionization, phonons, or any combination of two out of these three. The method by which energy deposits are observed and characterized is dependent on the target materials used in the detector.

It is important to understand the expected spectrum of the deposited energy in the detector from WIMP interactions. The differential energy spectrum is expected to be [75]:

$$\frac{dR}{dE_R} = \frac{R_0}{E_0 r} e^{-E_R/E_0 r} \tag{3.1}$$

Here, E_R is the recoil energy of the target nucleus, E_0 is the mean incident kinetic energy of a WIMP of mass m_χ such that $E_0 = \frac{1}{2} m_\chi u_0^2$ with u_0 being the relative velocity of the WIMP, R is the event rate per unit mass of the target, R_0 is the total event rate, and r is given by

$$r = \frac{4 m_t m_\chi}{(m_t + m_\chi)^2} \tag{3.2}$$

where m_t is the mass of the target nucleus. The differential energy spectrum in Eq. 3.1 is thus featureless and smoothly decreasing with energy. If the WIMP mass is between 10 GeV and 1 TeV, a majority of the events would be expected to deposit energies < 100 keV.

The differential energy spectrum must also be corrected for the nuclear "Form Factor." The wavelength λ of the WIMP is defined as

$$\lambda = h/q \tag{3.3}$$

where h is the Plank constant, and q is the momentum transfer in the interaction:

$$q = \sqrt{2 m_t E_R} \tag{3.4}$$

For WIMP masses of 10 GeV $-$ 1 TeV, this wavelength is $\lambda \sim 10^{-14} - 10^{-15}$ m for low momentum transfers. This is comparable to the typical size of a nucleus, and so the interaction is with the nucleus as a whole. However, as q increases, λ

decreases and the finite size of the nucleus must be considered. This results in a correction to the event rate due to the Form Factor, which will be discussed in further detail in Sec. 5.1.

3.3.1 Noble Liquid Detectors

One common target material used in direct dark matter searches is noble liquids. Liquid xenon, argon, or neon are all scintillators, that is, when a particle deposits energy in the liquid, the atoms emit light in the form of UV photons. This scintillation light can be observed and characterized in order to determine the amount of energy deposited. Examples of experiments observing scintillation light from noble liquids are XMASS [76] which uses liquid xenon, and CLEAN [77] which uses liquid neon.

The deposited energy from the WIMP may also cause some of the atoms of the target material to become ionized. The liberated electrons can be drifted through the liquid in response to an applied electric field and read out. WARP [78] and ArDM [79] are examples of experiments searching for scintillation and ionization in liquid argon, while LUX [80], ZEPLIN-II and ZEPLIN-III [81, 82], and XENON10 and XENON100 [83, 84] are examples of experiments using liquid xenon to detect scintillation and ionization.

3.3.2 Solid State Germanium Detectors

Another common target material used in direct dark matter searches is germanium. An energy deposit due to WIMPs or other particles ionizes the germanium and liberates electrons. These electrons are drifted due to an electric field, similar to noble liquid detectors, and are read out through electrodes on one side of the germanium. When a WIMP interacts with the germanium, it also creates some phonons which heat the material slightly. The germanium is kept at millikelvin temperatures just below the transition temperature where the material becomes superconducting. The heating causes the germanium to cross the transition edge making it no longer superconducting. This way, these detectors can detect both ionization signals and phonons. The CDMS [85] and EDELWEISS [86] detectors both use germanium to detect these two signals.

3.3.3 Other Detectors

Various other target materials and detection techniques are employed by experiments worldwide. The DAMA/LIBRA [87] experiment uses sodium iodide (NaI) crystals that scintillate in response to an energy deposit to search for annual modulation of WIMP interactions. The event rate for WIMP interactions depends on the relative velocity of the WIMP with respect to the detector, as shown in Eq. 3.1. Since the WIMPs are effectively at rest in the galaxy, the relative velocity corresponds to the velocity of the Earth around the galactic center. The orbital axis of the Earth is tilted by ∼60° in relation to the orbit of the sun about the galactic center as seen in Fig. 3.2. For this reason, the relative velocity of WIMPs with respect to the Earth changes over the course of a year. This causes a modulation in the event rate which the DAMA/LIBRA experiment can measure. In fact, DAMA/LIBRA has seen an annual modulation [88] consistent with what is expected from WIMPs, however the results seem to be ruled out by other experiments.

CRESST [89] on the other hand uses calcium tungstate ($CaWO_4$) crystals to observe scintillation light and phonons from dark matter interactions, while experiments such as PICASSO [90] and COUPP [91] use superheated fluids. When a WIMP deposits energy in the fluid, a bubble is formed and can be

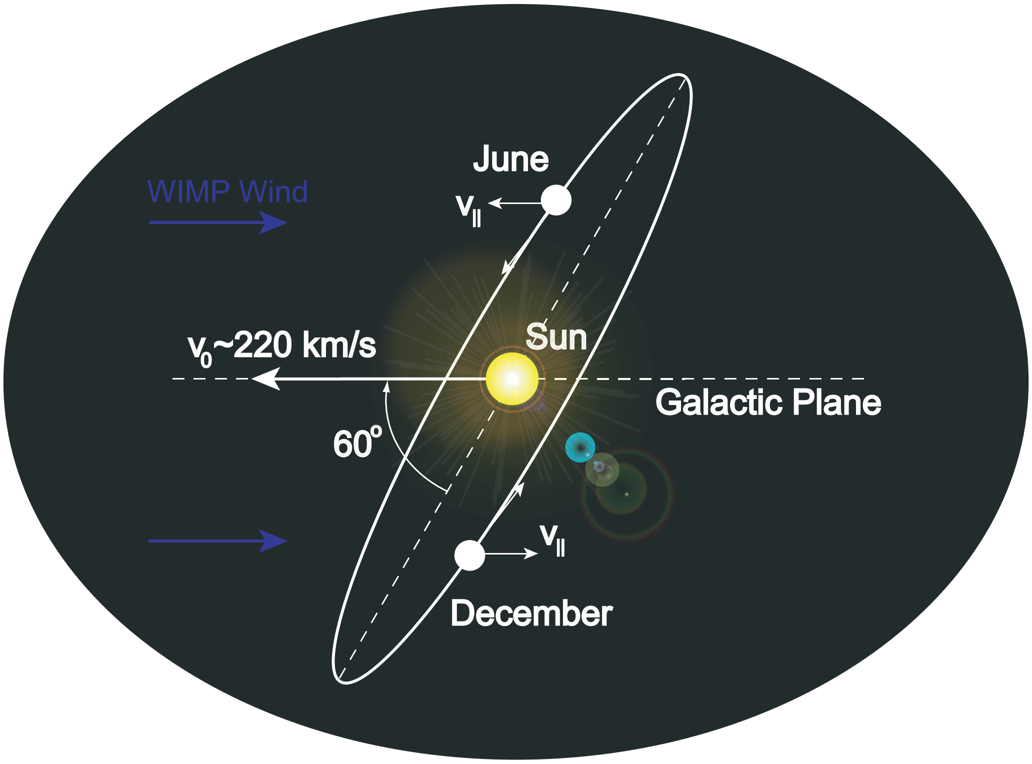

Figure 3.2: A diagram of the orbit of the Earth around the sun, and the motion of the sun through the galaxy. Because the orbital axis of the Earth is tilted by ∼60°, the relative velocity of the WIMPs with respect to the Earth varies throughout the course of a year.

observed with a camera and piezo-electric sensors. Finally, some direct dark matter searches such as DRIFT [92] use low pressure gas chambers to observe the ionization tracks from WIMP interactions, and use the directionality to confirm that the tracks are consistent with the direction the WIMPs are expected to be coming from.

3.4 Summary

The field of dark matter detection has been growing for the last two decades. The near future will prove to be an exciting time when these dark matter detectors will become large enough and sensitive enough to have a good chance of discovery. However, dark matter detection is not the only field searching for rare events due to physics beyond the Standard Model. Neutrinoless double beta decay is another process not accounted for in the Standard Model, and many experiments that work on the same principles as dark matter detectors are being built to search for these events.

CHAPTER 4

Double Beta Decay

Double beta decay is a process by which the nucleus of an atom releases two β-particles accompanied by two electron anti-neutrinos. For example, in ^{136}Xe:

$$^{136}_{54}\mathrm{Xe} \rightarrow ^{136}_{56}\mathrm{Ba} + 2e^- + 2\bar{\nu}_e \tag{4.1}$$

Although several isotopes are predicted to undergo double beta decay, many of these atoms also undergo ordinary beta decay with a much higher rate. This swamps any signal from double beta decay, making detection nearly impossible. In order to experimentally observe double beta decay, the single beta decay mode must be energetically suppressed in the given isotope. This can occur if the nucleus has an even mass number (A). In the case of an odd A, if one were to plot the mass of the nucleus as a function of the atomic number (Z), the various nuclei would follow an approximate parabola. In the case of an even A, the atomic number and number of neutrons (N) must either both be odd or both even. Plotting the mass of the nucleus as a function of Z, the two cases (even N-even Z or odd N-odd Z) follow two distinct parabolas. Depending on the positioning of the various nuclei in this plot, single beta decay may be forbidden while double beta decay is allowed [93]. Fig. 4.1 shows an example of an odd A nucleus and an even A nucleus, showing various possibilities for ordinary beta decay and double beta decay.

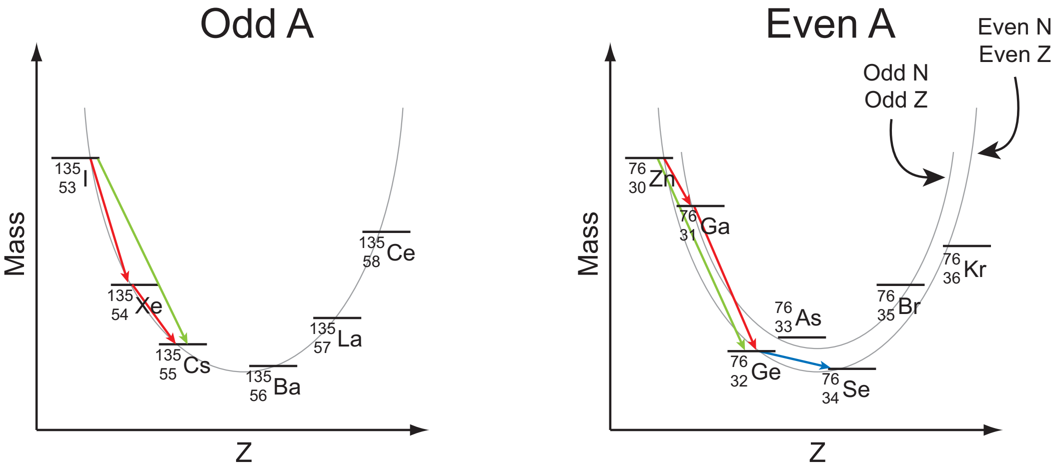

Figure 4.1: On the left, a plot of the masses of various nuclei as a function of Z for nuclei with an odd A. On the right, the same plot for nuclei with an even A. The red arrows show examples of ordinary beta decay, while the green arrows show examples of double beta decay where ordinary beta decay can occur. These double beta decays cannot be observed experimentally because of the overwhelming ordinary beta decay signal. The blue arrow shows an example of double beta decay which can be observed experimentally because ordinary beta decay is not energetically allowed [94].

4.1 Neutrinoless Double Beta Decay

As explained above, double beta decay of a nucleus releases two β-particles along with two electron anti-neutrinos. If the neutrino is its own antiparticle (that is, a Majorana particle), then the process of neutrinoless double beta decay can occur [95]. Here, an ordinary beta decay of a neutron occurs with the release of an electron anti-neutrino, which is then absorbed by a second neutron. This causes the release of a second β-particle. However, for this to occur, the neutrino must undergo a helicity flip, further suppressing this process. Feynman diagrams of the two neutrino double beta decay and neutrinoless double beta decay processes are shown in Fig. 4.2. In the case of two neutrino double beta decay, the energy difference between the parent and daughter nucleus (the Q-value) is split between the four outgoing particles (two β-particles and two electron anti-neutrinos), and so the effective detectable energy, which is the sum energy of the two β-particles, forms a spectrum spanning up to the Q-value. The energy spectrum of the summed β-particle energies is [94]:

$$\frac{dN}{dK} \sim K(Q-K)^5 \left(1 + 2K + \frac{4K^2}{3} + \frac{K^3}{3} + \frac{K^4}{30}\right) \tag{4.2}$$

Here, K is the summed β-particle energies, and Q is the Q-value of the decay. In neutrinoless double beta decay, since there are no neutrinos carrying away energy, the sum energy of the β-particles will form a line at the Q-value. The spectra of two neutrino double beta decay and for neutrinoless double beta decay is shown in Fig. 4.3.

Double beta decay has been predicted in a number of isotopes, and the two neutrino double beta decay mode has been experimentally observed in these isotopes. Neutrinoless double beta decay however has never been conclusively

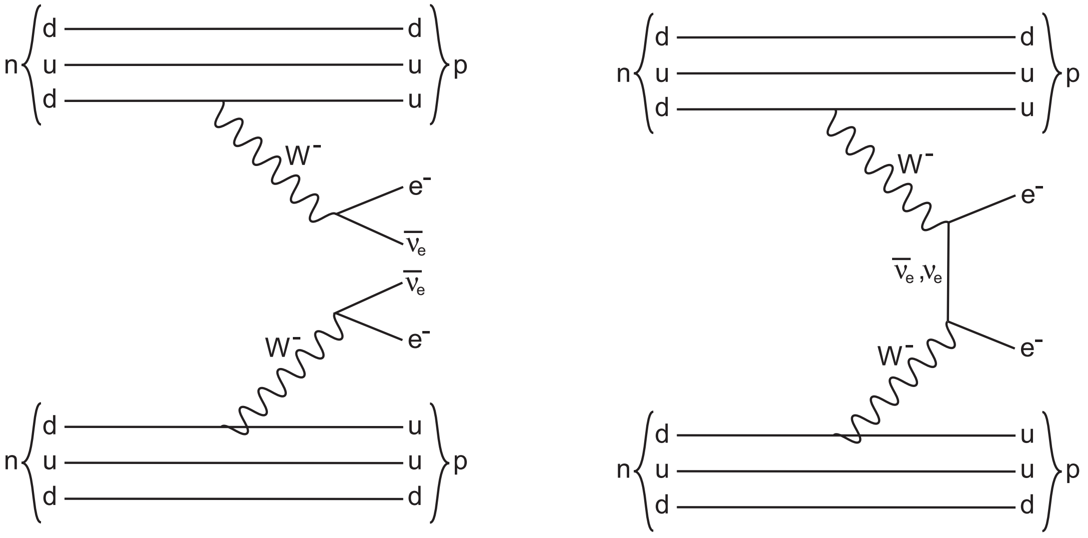

Figure 4.2: On the left, a diagram of ordinary double beta decay. Two neutrons decay into two protons through the emission of two electrons and two antineutrinos. On the right, a diagram of neutrinoless double beta decay. If the neutrino is a Majorana particle, the emitted neutrino can be reabsorbed within the nucleus and only two electrons are emitted. However, in order for this to occur, the neutrino must undergo a helicity flip, which further increases the lifetime of this decay mode.

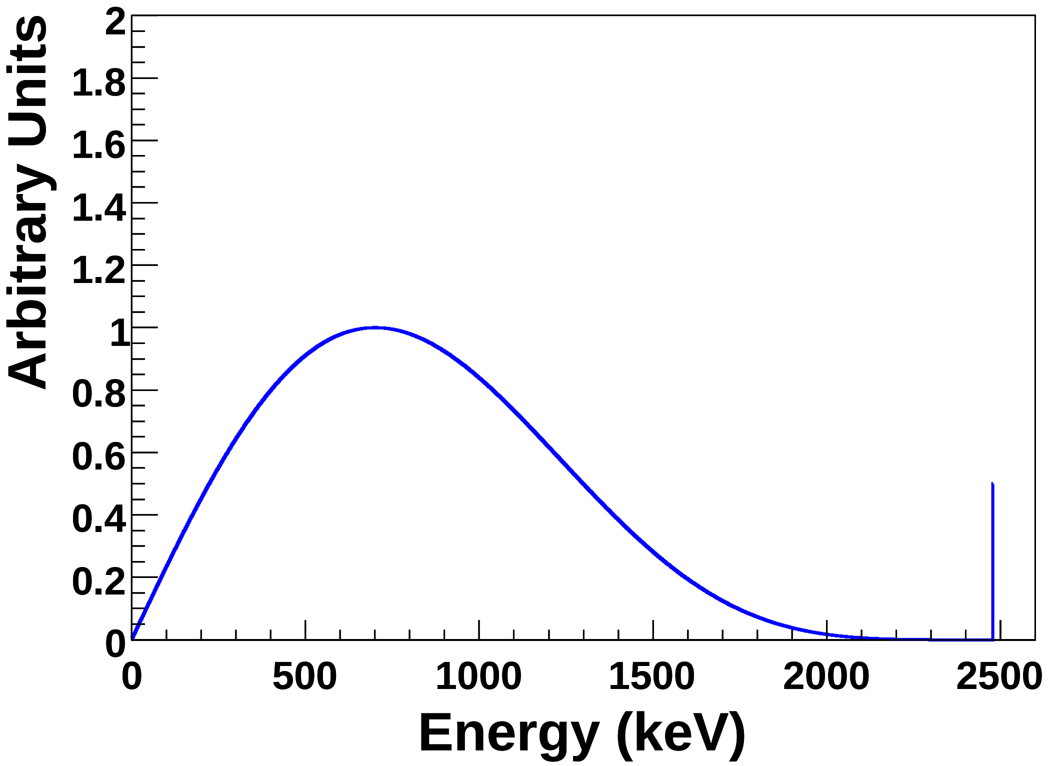

Figure 4.3: A plot of the energy spectrum of double beta decay for ^{136}Xe. Two neutrino double beta decay creates a smooth distribution up to the Q-value, 2.458 MeV in this case [96, 97]. Neutrinoless double beta decay creates a line at the Q-value. Note that the relative heights of the neutrinoless double beta decay and two neutrino double beta decay spectra are arbitrary in this case in order to illustrate the difference in the spectral shapes.

observed[1]. Tab. 4.1 lists all of these isotopes, along with their relative isotopic abundances, Q-values, half-lives, and the limits placed on the neutrinoless double beta decay mode.

Isotope	Q (MeV)	Isotopic Abundance	$2\nu\beta\beta$ Half-Life (yr)	$0\nu\beta\beta$ Half-Life Limit (yr)
^{48}Ca	4.272	0.187	$4.4^{+0.6}_{-0.5} \times 10^{19}$ [99]	$> 5.8 \times 10^{22}$ [100]
^{76}Ge	2.039	7.8	$(1.5 \pm 0.1) \times 10^{21}$ [99]	$> 1.9 \times 10^{25}$ [101]
^{82}Se	2.996	9.2	$(0.92 \pm 0.07) \times 10^{20}$ [99]	$> 3.6 \times 10^{23}$ [102]
^{96}Zr	3.350	2.8	$(2.3 \pm 0.2) \times 10^{19}$ [99]	$> 9.2 \times 10^{21}$ [103]
^{100}Mo	3.034	9.6	$(7.1 \pm 0.4) \times 10^{18}$ [99]	$> 1.1 \times 10^{24}$ [102]
^{116}Cd	2.805	7.5	$(2.8 \pm 0.2) \times 10^{19}$ [99]	$> 1.7 \times 10^{23}$ [104]
^{130}Te	2.528	34.5	$6.8^{+1.2}_{-1.1} \times 10^{20}$ [99]	$> 2.8 \times 10^{24}$ [105]
^{136}Xe	2.458	8.9	$(2.11 \pm 0.21) \times 10^{21}$ [106]	$> 1.2 \times 10^{24}$ [107]
^{150}Nd	3.367	5.6	$(8.2 \pm 0.9) \times 10^{18}$ [99]	$> 1.8 \times 10^{22}$ [108]

Table 4.1: Table of various isotopes known to undergo double beta decay, including the Q-value of the decay, isotopic abundance, and two neutrino double beta decay half-life. The lower limits for the neutrinoless double beta decay for each isotope is given in the last column.

Two neutrino double beta decay, being a second order weak process, is one of the rarest processes that has been observed experimentally. As seen in Tab. 4.1, the half-lives of two neutrino double beta decay are on the order of $10^{18} - 10^{21}$ years, which is up to 10^{11} times the age of the Universe. Since two neutrino double beta decay is predicted from the standard model, it is not surprising that this process has been observed. More interesting is the prospect of observing neutrinoless double beta decay.

One of the fundamental conservation parameters in the Standard Model is the "Lepton Number Conservation." According to the Standard Model, all leptons have a lepton number $L = 1$, while the antiparticle equivalents have a lepton num-

---

[1] Klapdor-Kleingrothaus et al. have claimed to have observed neutrinoless double beta decay in germanium [98], however this claim has not been confirmed by other experiments.

ber $L = -1$ and all other particles have a lepton number $L = 0$. In any process, the total lepton number, and in particular the individual lepton flavor numbers (which is electron-type, μ-type, and τ-type leptons) must be conserved[2] [109]. For example, in two neutrino double beta decay

$$\underbrace{2n}_{L_e=0} \rightarrow \underbrace{2p}_{L_e=0} + \underbrace{2e^-}_{L_e=2} + \underbrace{2\bar{\nu_e}}_{L_e=-2} \tag{4.3}$$

and the lepton numbers are conserved. However, in neutrinoless double beta decay, the process is:

$$\underbrace{2n}_{L_e=0} \rightarrow \underbrace{2p}_{L_e=0} + \underbrace{2e^-}_{L_e=2} \tag{4.4}$$

In this case, the lepton numbers are not conserved. If neutrinoless double beta decay is observed, it would show a violation of one of the basic conservation laws of the Standard Model.

As explained in Sec. 2.2.4, the Standard Model is known to be incomplete. One aspect that is known to be incorrect is the fact that the neutrinos in the Standard Model are considered to be massless. Neutrino oscillation experiments have shown that the neutrinos do have mass [17, 16, 11], however the absolute mass scale is at present not known. The oscillation experiments are only able to give differences in the squared masses of the neutrinos $\Delta m_{ij}^2 = \left|m_i^2 - m_j^2\right|$. Since only the squared mass differences can be inferred from these experiments, the overall hierarchy cannot be determined, that is it is impossible to know which neutrino is the heaviest and which the lightest. This leads to two possibilities, a normal hierarchy or an inverted hierarchy. Fig. 4.4 shows the relative masses of the three neutrinos in the normal and inverted hierarchies.

---

[2] Neutrino oscillation, a phenomenon which is not possible in the realm of the Standard Model but is observed, violates individual lepton flavor number conservation, however lepton number is still conserved.

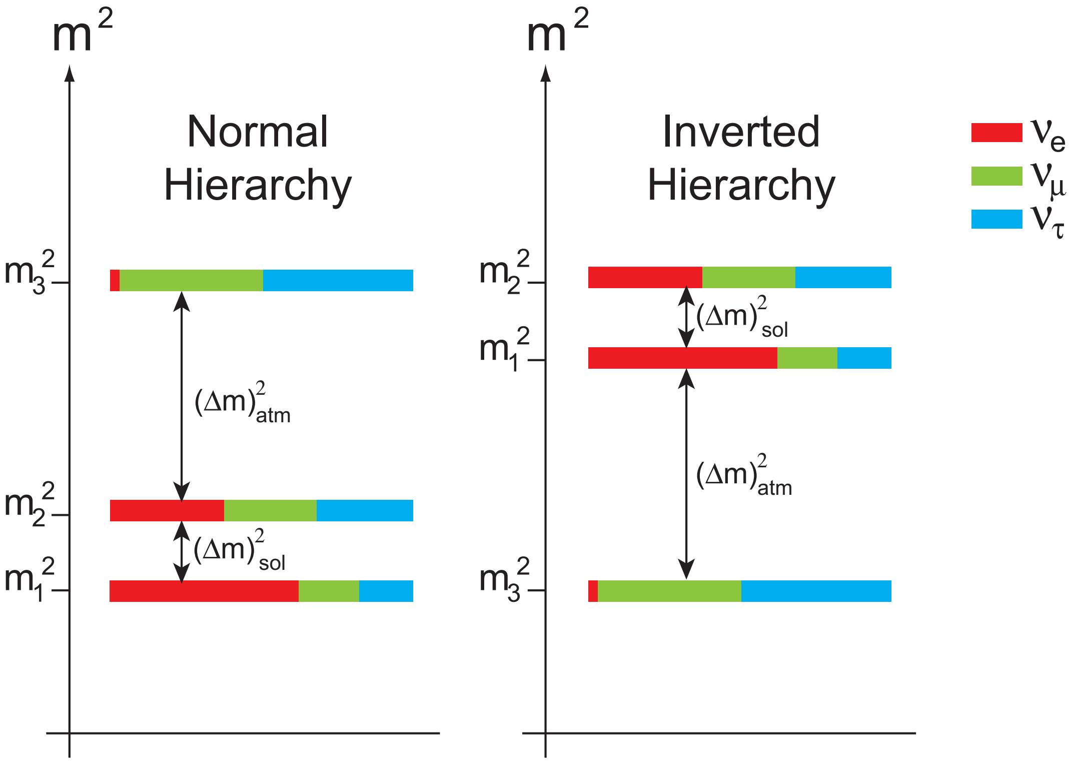

Figure 4.4: On the left, a plot of the relative masses of the neutrinos for the normal hierarchy. On the right, the same plot for the inverted hierarchy. The values are for the mass eigenstates of the neutrinos (ν_1, ν_2, ν_3) and the contributions from the weak eigenstates (ν_e, ν_μ, ν_τ) are shown as different colors. The squared mass difference between ν_1 and ν_2 can be deduced from oscillations of solar neutrinos, while the squared mass difference between ν_2 and ν_3 can be found through oscillations of atmospheric neutrinos. The absolute mass scale cannot be determined from such oscillation experiments.

Observations of neutrinoless double beta decay however can be used to set an absolute mass scale for the neutrino. If neutrinoless double beta decay is observed, the half-life of this process will be [93]:

$$[T^{0\nu}_{1/2}(0^+ \rightarrow 0^+)]^{-1} = G^{0\nu}(E_0, Z) \left| M^{0\nu}_{GT} - \frac{g_V^2}{g_A^2} M^{0\nu}_F \right|^2 \langle m_\nu \rangle^2 \tag{4.5}$$

Eq. 4.5 shows the half-life from an initial spin and parity 0^+ state to a final 0^+ state, as this is nearly always the case. Here, $G^{0\nu}$ is an exactly calculable phase space integral, E_0 is the available energy where the sum electron kinetic energy peak is at $Q = E_0 - 2m_e$, Z is the atomic number of the parent nucleus, g_V and g_A are the vector and axial vector coupling constants respectively, $\langle m_\nu \rangle$ is the effective neutrino mass (see Eq. 4.9), and $M^{0\nu}_{GT}$ and $M^{0\nu}_F$ are the Gamow-Teller and Fermi nuclear matrix elements. The nuclear matrix elements can currently be determined through two methods, the Quasiparticle Random Phase Approximation (QRPA) and the Nuclear Shell Model (NSM). A full treatment of these methods can be found in Ref. [93]. The phase space integral, $G^{0\nu}$ is proportional to [93]:

$$G^{0\nu} \sim \int F(Z, \epsilon_1) F(Z, \epsilon_2) p_1 p_2 \epsilon_1 \epsilon_2 \delta(E_0 - \epsilon_1 - \epsilon_2) d\epsilon_1 d\epsilon_2 \tag{4.6}$$

Here, ϵ_1 (ϵ_2) and p_1 (p_2) is the energy and momentum of the first (second) outgoing β-particle respectively, while $F(Z, \epsilon)$ is the Fermi function describing the Coulomb effect on the outgoing β-particle.

Assuming there are N massive Majorana neutrinos ν_i ($i = 1, ..., N$), the weak eigenstate neutrinos (ν_e, ν_μ, ν_τ) would be a linear superposition of them. For example, the ν_e would be:

$$\nu_e = \sum_i^N U_{ei} \nu_i \tag{4.7}$$

Where U_{ei} is the $3 \times N$ neutrino mixing matrix, such that:

$$\begin{bmatrix} \nu_e \\ \nu_\mu \\ \nu_\tau \end{bmatrix} = \begin{bmatrix} U_{e1} & U_{e2} & \cdots & U_{eN} \\ U_{\mu 1} & U_{\mu 2} & \cdots & U_{\mu N} \\ U_{\tau 1} & U_{\tau 2} & \cdots & U_{\tau N} \end{bmatrix} \begin{bmatrix} \nu_1 \\ \nu_2 \\ \vdots \\ \nu_N \end{bmatrix} \tag{4.8}$$

In this case, the effective Majorana neutrino mass would be defined as:

$$\langle m_\nu \rangle^2 = \left| \sum_i^N U_{ei}^2 m_i \right|^2 = \left| \sum_i^N |U_{ei}|^2 e^{\alpha_i} m_i \right|^2, (\text{all } m_i \geq 0) \tag{4.9}$$

As seen in Eq. 4.9, $\langle m_\nu \rangle^2$ depends on the phases (α_i) of the neutrino mixing matrix, and as such can cause cancellations in the sum, however the maximum and minimum values of $\langle m_\nu \rangle^2$ depend only on the absolute value of the mixing angles:

$$\langle m_\nu \rangle_{max} = \sum_i^N |U_{ei}|^2 m_i \tag{4.10}$$

$$\langle m_\nu \rangle_{min} = \max[(2 |U_{ei}|^2 m_i - \langle m_\nu \rangle_{max}, 0] \tag{4.11}$$

The values for the mixing matrix can be deduced through neutrino oscillation experiments independent of neutrinoless double beta decay searches. As such, if neutrinoless double beta decay is observed, and the half-life is determined, $\langle m_\nu \rangle$ can be calculated, leading to a range of values for the individual neutrino masses. Fig. 4.5 shows the relationship between $\langle m_\nu \rangle$ and the mass of the lightest neutrino for the two mass hierarchies using the current values for the neutrino mixing matrix.

4.2 Double Beta Decay Experiments

There is much motivation to observe neutrinoless double beta decay. As explained above, the observation of such decays can lead to physics beyond the Standard

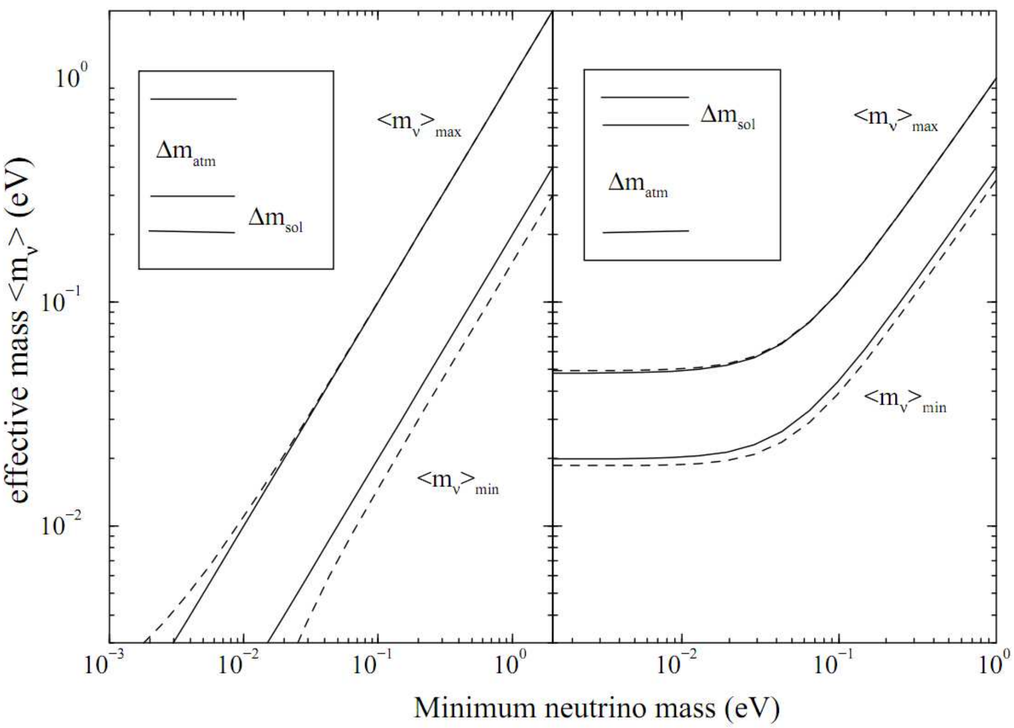

Figure 4.5: On the left, a plot of $\langle m_\nu \rangle$ as a function of the lightest neutrino mass for a normal hierarchy. On the right, the same plot for an inverted hierarchy. These plots use the experimentally determined values for the neutrino mixing matrix parameters. The solid lines show the upper and lower limits on $\langle m_\nu \rangle$ for the matrix element $U_{e3} = 0$, while the dashed lines show the same contours for $|U_{e3}|^2 = 0.025$, the maximum value allowed by the CHOOZ and PALO VERDE reactor experiments [110, 111, 93].

Model and will allow for the determination of the absolute scale of neutrino masses. Many ongoing experiments are searching for neutrinoless double beta decay in different elements, including EXO (^{136}Xe), GERDA (^{76}Ge), COBRA (^{116}Cd and ^{130}Te), and NEMO (^{100}Mo) [112, 113, 114, 115]. As seen in Fig. 4.3, the summed energies of the two emitted β-particles creates a broad spectrum up to the Q-value of the decay for the two neutrino mode, however for neutrinoless double beta decay, the summed energy forms a peak exactly at the Q-value. For this reason, nearly all of the neutrinoless double beta decay experiments are searching for a line in the energy spectrum at the Q-value of the respective decay.

The current and future neutrinoless double beta decay experiments are focusing on one or more of the following key parameters of the detectors:

- The rate of background events in the detector
- The number of atoms of the isotope being observed
- The energy resolution of the detector

It is imperative that all neutrinoless double beta decay experiments achieve as low of a background rate as possible since the rate of neutrinoless double beta decay is so low. Any background near the Q-value of the decay can swamp the signal from neutrinoless double beta decay. This can be done by constructing the detector with materials which have very low intrinsic radioactivity and by using shielding to block from external sources of background. Also, increasing the amount of the candidate isotope will allow for a better chance to detect neutrinoless double beta decay. This can be done by increasing the total mass of the element used in the detector, or by enriching the material with the candidate isotope. Finally, improving the detector energy resolution will help to ultimately claim a discovery

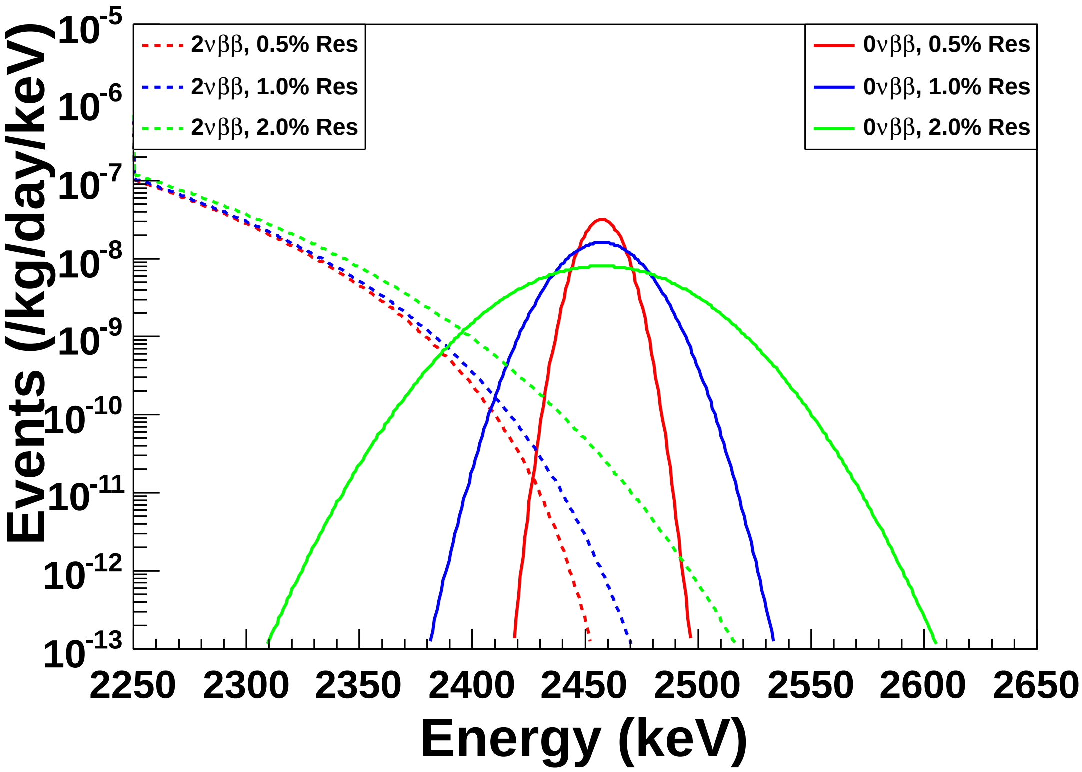

Figure 4.6: The energy spectrum of two neutrino double beta decay (dotted lines) and neutrinoless double beta decay (solid lines) in ^{136}Xe, which has a Q-value of 2.458 MeV. This plot assumes a half-life of 2.11×10^{21} years for the two neutrino mode and 10^{27} years for the neutrinoless mode. The different curves represent the observed energy spectrum for various values of the detector resolution. Note that as the resolution gets worse, more of the two neutrino events leak into the energy range of interest for neutrinoless double beta decay.

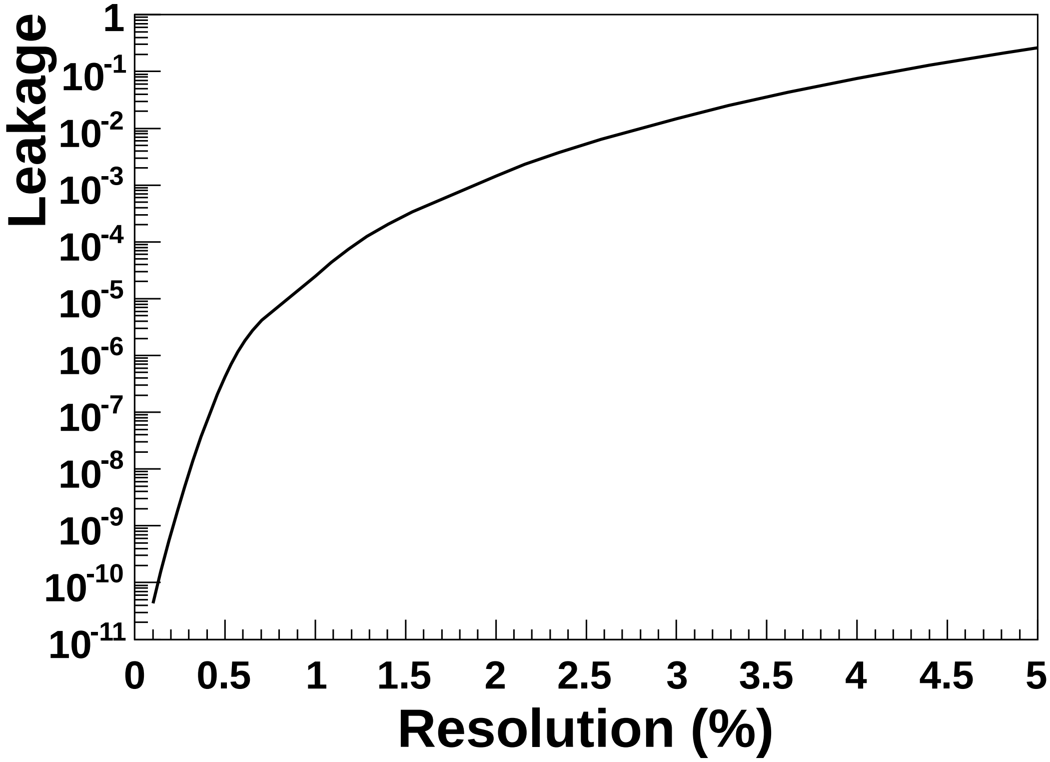

Figure 4.7: A plot of the fraction of two neutrino double beta decay events leaking into the energy range of interest for neutrinoless double beta decay as a function of resolution of the detector. This is defined as the number of two neutrino decays divided by the number of neutrinoless decays in the energy range. The energy range considered is between the Q-value of the neutrinoless double beta decay and the half maximum to the right. Once again, this plot is for ^{136}Xe, with assumed half-lives of 2.11×10^{21} years for the two neutrino mode and 10^{27} years for the neutrinoless mode. It is important to see that the fraction of two neutrino leakage events are strongly dependent on the detector resolution.

of neutrinoless double beta decay. The energy spectrum of two neutrino double beta decay ends at the Q-value of the decay, however a poor energy resolution will allow for these events to appear to extend beyond the Q-value. At the same time, the line due to neutrinoless double beta decay will become a broad Gaussian if the resolution is too low. This way, the two neutrino double beta decay events will effectively become a background for the neutrinoless mode. Fig. 4.6 shows the effect of different energy resolutions on the energy spectra near the Q-value. A good energy resolution will minimize the leakage of two neutrino decay events into the energy range chosen to observe neutrinoless decays. Fig. 4.7 shows the leakage for ^{136}Xe, highlighting the need for very good energy resolution. The EXO collaboration has shown the capability to reach energy resolutions of 1.6% at the Q-value of ^{136}Xe [116].

Many of the detectors currently operational or under construction have several similarities to dark matter detectors. In fact, some of the target materials in dark matter detectors are also candidates for double beta decay. For example, some of the leading direct dark matter detectors use liquid xenon as a target material. Natural xenon contains 8.9% ^{136}Xe, which can undergo double beta decay. Similarly, germanium is a commonly used target for dark matter detectors, and ^{76}Ge is known to undergo double beta decay. Because of the same target materials, similar detector designs are used in double beta decay detection, and similar background reduction techniques are employed in both experiments. This is discussed in further detail for liquid xenon detectors in Sec. 5.3.

CHAPTER 5

The XENON100 Detector

The XENON100 dark matter detector is a state of the art liquid xenon time projection chamber (TPC) used to detect small energy deposits from WIMPs. As explained in Ch. 3, several different target materials are employed in many experiments searching for dark matter. However, noble liquids, particularly liquid xenon, have proved to be capable of setting competitive limits on the mass and cross section of WIMP interactions.

5.1 Liquid Xenon as a Target

Liquid xenon is an effective target material for the detection of dark matter. Xenon is a scintillator and is transparent to its own scintillation light. The scintillation process occurs when an energy deposit excites the xenon atoms, which then de-excite and create 178 nm photons that can be detected by photomultiplier tubes. Synthetic silica, a material commonly used in the windows of photomultiplier tubes, is transparent to this wavelength, and so photomultiplier tubes can be used to detect this scintillation light without modification (the photomultiplier tube and concept will be explained in further detail in Ch. 7). Free electrons are also able to drift within the liquid xenon. These properties allows for liquid xenon to be used in a TPC (the TPC concept will be described further in Sec. 5.2). Tab. 5.1 shows a comparison between the properties of various noble liquids that are often employed in dark matter detection.

Compared to other direct detection experiments, liquid xenon is operated at a relatively high temperature. The boiling point of xenon is -100° C at 1.5 bar, whereas the boiling points of argon and neon (two other materials often used in dark matter detectors) are -180° C and -245° C respectively at 1.5 bar. Other solid state dark matter detectors use transition edge sensors made of germanium or silicon which must be cooled down to ∼100 mK. Thus, the cryogenics required for liquid xenon detectors are simple in comparison to other cryogenic dark matter detectors.

	Unit	Neon	Argon	Xenon
Z		10	18	54
A		20	40	131
Liquid Density	g/cm^3	1.21	1.4	2.95
Energy Loss (dE/dx)	MeV/cm	1.4	2.1	3.8
Radiation Length	cm	24	14	2.8
Boiling Point (1.5 bar)	°C	-245	-180	-100
Scintillation Wavelength	nm	85	125	178
Scintillation Yield	photons/keV	30	40	46
Ionization Yield	e^-/keV	46	42	64
Decay Time (Fast)	ns	19	7	4
Decay Time (Slow)	ns	1500	1600	26
Radioactive Isotopes		None	^{39}Ar	None

Table 5.1: Summary of the key parameters of various noble liquids used in direct dark matter detection experiments.

Liquid xenon has a relatively high density of 2.95 g/cm^3. Because of this, a

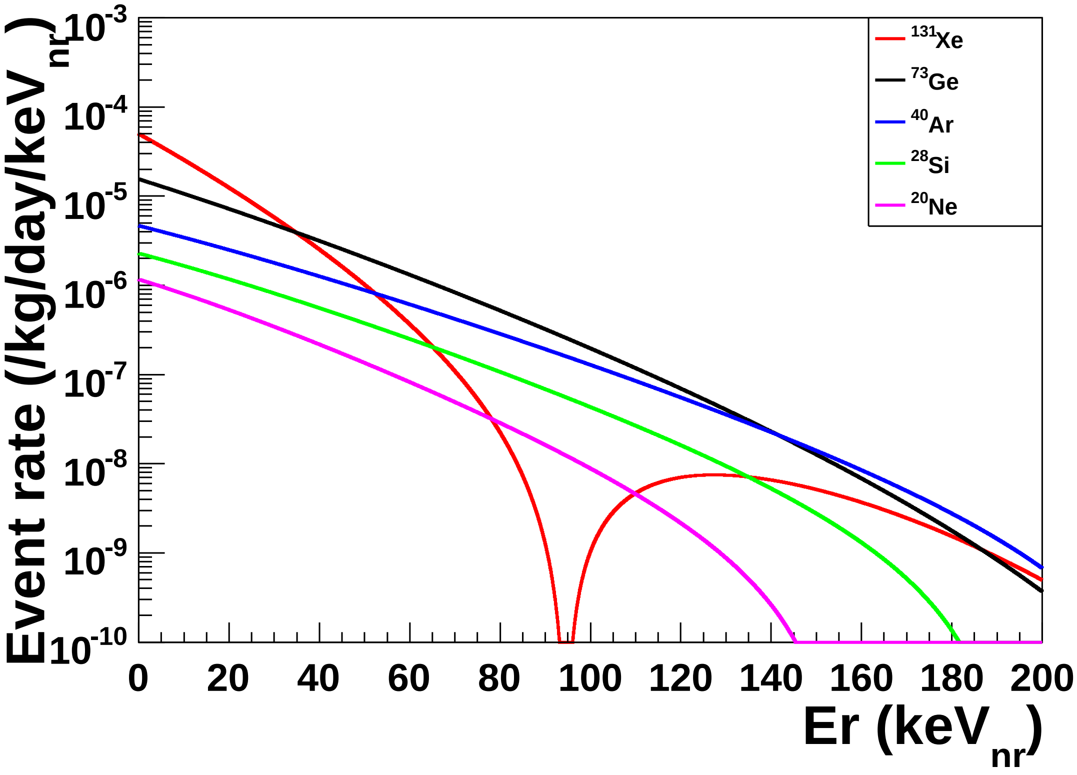

Figure 5.1: The energy spectrum of a 100 GeV WIMP with a WIMP-nucleon cross section of 10^{-45} cm^2 interacting with various target materials. At the lowest energies, xenon has the highest event rate due to the A^2 dependence of the WIMP-nucleus cross section. The dip in the spectrum of ^{131}Xe is due to a form factor correction. The notation "keV$_{nr}$" will be explained in further detail in Sec. 5.4.1.

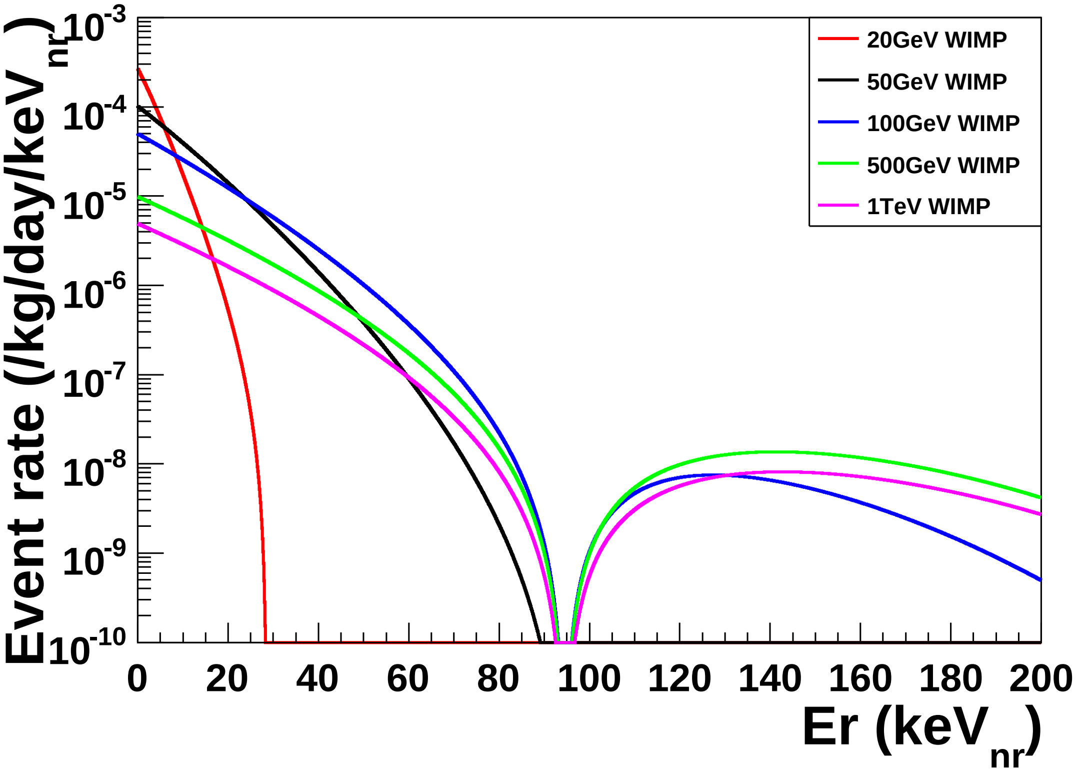

Figure 5.2: The energy spectrum of WIMPs of various masses with a WIMP-nucleon cross section of 10^{-45} cm^2 interacting with a xenon target.

large target mass can be contained in a small volume. The high density, along with a high atomic number of 54, makes xenon very effective at self shielding as well. Particles entering the xenon from outside, particularly γ-rays, are attenuated within the first few centimeters of liquid xenon. The outer few centimeters of the xenon can then act as a shield for external radioactivity, and events occurring in this region can be discarded [117].

Another advantage of xenon is that natural xenon contains no long-lived radioactive isotopes[1]. Any radioactivity within a dark matter experiment will create energy deposits within the target material that can become a form of background. Natural argon for example contains the radioactive isotope ^{39}Ar with a half-life of 269 years. Since the radioactivity from ^{39}Ar is a background within the liquid argon dark matter detectors, either the argon must be depleted of ^{39}Ar or a method must be developed to remove ^{39}Ar events during data analysis. Although xenon does not have the problem of long-lived radioactive isotopes, there is radioactive ^{85}Kr present in small quantities in commercially available xenon gas, which undergoes β-decay with a half-life of 10.8 yr and a maximum β energy of 687 keV. The ^{85}Kr contamination can be reduced by using a krypton distillation column [118]. By taking advantage of the different boiling points of xenon and krypton, the column can separate the krypton from the xenon gas such that only ppt (part per trillion) levels of krypton remain in the xenon.

Finally, the large atomic mass of xenon ($A = 131$) allows for greater sensitivity for WIMP detection. Fig. 5.1 shows the spectra of a 100 GeV WIMP interacting with different target materials, while Fig. 5.2 shows the spectra of different mass

---

[1] Although ^{136}Xe is predicted to undergo double beta decay, the half-life is much too long to affect the experiment

WIMPs interacting with a xenon target. The WIMP-nucleus cross section is [9]:

$$\sigma = F(Q)\frac{4m_r^2}{\pi}\left(Zf_p + (A-Z)f_n\right)^2 \tag{5.1}$$

Here, Z and A are the atomic number and atomic mass respectively, m_r is the reduced mass of a nucleon, while f_p and f_n are the WIMP couplings to protons and neutrons respectively. $F(Q)$ is the Woods-Saxon form factor, defined as [119]:

$$F(Q) = \left(\frac{3j_1(qR_1)}{qR_1}\right)^2 e^{-(qs)^2} \tag{5.2}$$

$$R_1 = \sqrt{R^2 - 5s^2} \tag{5.3}$$

$$q = \sqrt{sm_nQ} \tag{5.4}$$

In Eq. 5.2, j_1 is the first Spherical Bessel Function, $R \approx 1.2A^{1/3}$ fm, $s \approx 1$ fm, m_N is the mass of a nucleon, and Q is the energy transferred from the WIMP to the target nucleus. Of particular importance is the fact that Eq. 5.1 shows an A^2 dependence of the cross section if the WIMP couplings to protons and neutrons are comparable. For this reason, using a target material with a higher atomic mass greatly increases the expected interaction rate. Because of the high atomic mass of xenon, the rate of events is higher in the xenon than other materials at the lowest energies.

Noble liquid dark matter detectors are also easily scalable. Every generation of dark matter detector should be larger than the last, and noble liquid detectors are able to be scaled up without a dramatic increase in cost. Solid state detectors using germanium and silicon however can become expensive at larger masses. Because these detectors use solid state crystals, the crystals must be grown to larger sizes with minimal impurities, making the process difficult and expensive.

Figure 5.3: A picture of the XENON100 TPC. The walls of the TPC are made of PTFE (polytetrafluoroethylene or Teflon), and the photomultiplier tubes used for the outer veto are seen on the top and bottom of the TPC. The wires surrounding the PTFE maintain the electric field inside the TPC.

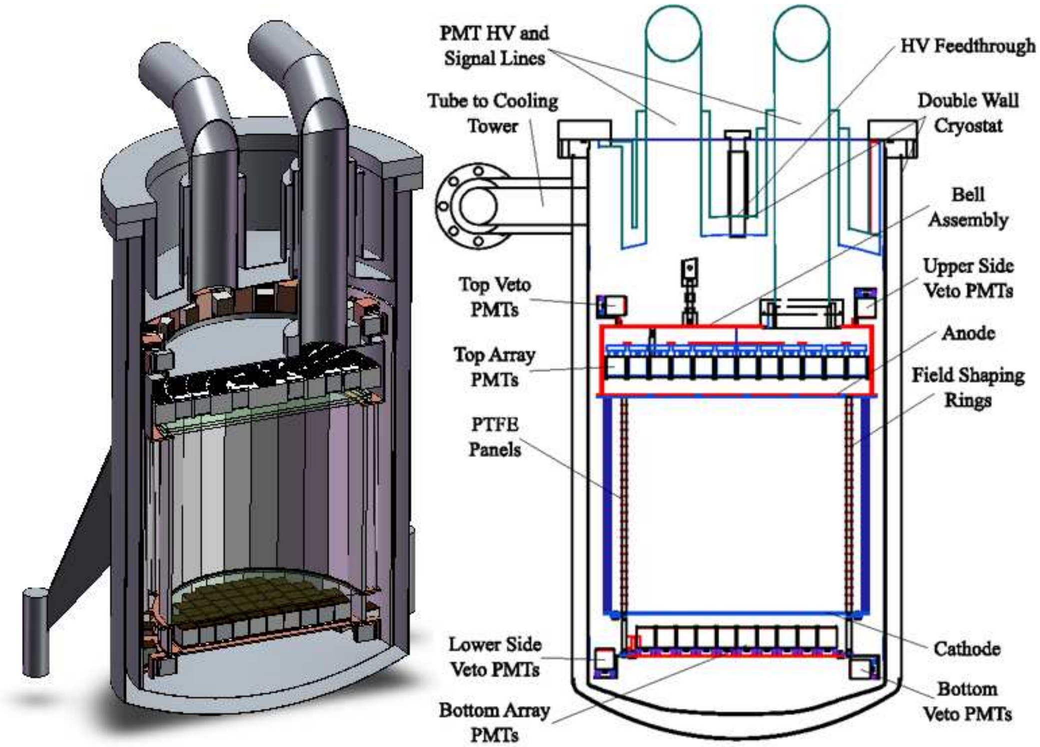

Figure 5.4: On the left, a CAD (computer-aided design) of the internals of the XENON100 TPC. On the right, a schematic diagram of the TPC. The top, bottom, top veto, and bottom veto PMT arrays can be seen in both drawings.

5.2 The XENON100 Time Projection Chamber

The XENON100 detector uses liquid xenon and two arrays of photomultiplier tubes (PMTs) in order to detect energy deposits from particle interactions and to determine the location of the energy deposit. The detector itself is a vacuum insulated cryostat and is filled with 170 kg of liquid xenon. Fig. 5.3 and 5.4 show a picture and diagrams of the internals of the XENON100 detector. A PTFE (polytetrafluoroethylene or Teflon) cylinder with 30 cm inner diameter and 30 cm height creates the body of the TPC. At the bottom of the TPC is a cathode mesh held at -15 kV, and at the top is a mesh held at ground level ∼2.5 mm below the liquid level. A set of rings surround the PTFE cylinder and are held at potentials increasing from ground level to -15 kV from the top to the bottom of the TPC. These rings and meshes create a uniform electric field within the TPC. An anode mesh is located ∼2.5 mm above the liquid surface and is held at +5 kV, creating a stronger field at the liquid-gas interface. Below the cathode mesh is an array of 80 PMTs facing into the xenon, and above the anode mesh in the gas layer is an array of 98 PMTs looking downwards at the liquid xenon.

When a particle enters the TPC, it interacts with the xenon atoms and deposits energy. This energy excites a xenon atom, which in turn combines with another xenon atom to create a Xe_2^* excited dimer (excimer). The excimer de-excites into two ground state xenon atoms, releasing 178 nm scintillation photons. The initial energy deposit may also ionize some of the xenon atoms, releasing free electrons. Part of the electrons recombine with the xenon ions, once again creating Xe_2^* excimers which release scintillation light. An energy deposit in the liquid xenon can follow one of two pathways [120, 121]:

$$\begin{aligned} E + \mathrm{Xe} &\rightarrow \mathrm{Xe}^* \\ \mathrm{Xe}^* + \mathrm{Xe} &\rightarrow \mathrm{Xe}_2^* \\ \mathrm{Xe}_2^* &\rightarrow 2\mathrm{Xe} + h\nu \end{aligned} \tag{5.5}$$

Here, all of the energy goes into exciting the xenon and eventually creating scintillation photons.

$$\begin{aligned} E + \mathrm{Xe} &\rightarrow \mathrm{Xe}^+ + e^- \\ \mathrm{Xe}^+ + \mathrm{Xe} &\rightarrow \mathrm{Xe}_2^+ \\ \mathrm{Xe}_2^+ + e^- &\rightarrow \mathrm{Xe}^{**} + \mathrm{Xe} \\ \mathrm{Xe}^{**} &\rightarrow \mathrm{Xe}^* + \mathrm{heat} \\ \mathrm{Xe}^* + \mathrm{Xe} &\rightarrow \mathrm{Xe}_2^* \\ \mathrm{Xe}_2^* &\rightarrow 2\mathrm{Xe} + h\nu \end{aligned} \tag{5.6}$$

In this case, the energy deposit ionizes the xenon, and the electron eventually recombines creating scintillation light, while a fraction of the electrons are drifted and cannot recombine. A diagram of these pathways is shown in Fig. 5.5.

The primary scintillation photons are detected by the PMTs and are called the S1 signal. This S1 signal has a width of $\lesssim 50$ ns. The remaining free electrons which did not recombine drift upwards in the liquid xenon due to the supplied electric field. At the liquid-gas interface, the stronger electric field extracts the electrons into the gas layer. The electrons drifting within the strong electric field in the gas xenon create proportional scintillation light via electroluminescence. That is, the number of photons produced is proportional to the number of electrons drifting in the xenon gas. The electrons accelerating across the higher potential excite the xenon gas which in turn releases scintillation light. This secondary scintillation within the gas layer is called the S2 signal and is also detected by the PMTs. S2 signals are longer than the corresponding S1, with a width of ~2 μs in the case of XENON100. The S2 width is dependent on several factors including the size of the gas phase and electric field strength. Fig. 5.6 shows a diagram of the energy deposition process in a liquid xenon TPC.

Inside the liquid xenon, the free electrons drift in response to the applied electric field of 0.5 kV/cm with a constant velocity of ~2 mm/μs. By measuring the time difference between the S1 and S2 signals, it is possible to obtain a vertical (z) position of the energy deposit to within a few mm accuracy (the term Time Projection Chamber comes from the fact that the time difference in the two signals allows for accurate determination of the event location along the drift axis). The pattern of photon hits on the top array of PMTs from the S2 signal allows for reconstruction of the horizontal (x-y) position of the energy deposit also to within a few mm accuracy. Since the S2 physically occurs very close to the top PMTs, a majority of the photons hit the PMTs directly above the S2 location. An example of the hit patterns on the PMT arrays for an actual energy deposit are shown in Fig. 5.7 while Fig. 5.8 shows pictures of the top and bottom arrays. By counting the number of photons detected in the S1 signal, a value for the actual energy deposit can be inferred. One can also use an anticorrelation between the S1 and S2 signals to obtain a better energy resolution. This way, the S1 and S2 signals provide the energy of the event and its three dimensional position [84].

In order to achieve the highest yield for S1 and S2 signals, it is imperative that any contaminants are removed from the parts within the detector and that the xenon is purified. Contaminants within the detector and outgassing from parts inside the detector will decrease the purity of the xenon, and so a circulation system with a heated getter is used. Gaseous xenon is pumped out of the detector,

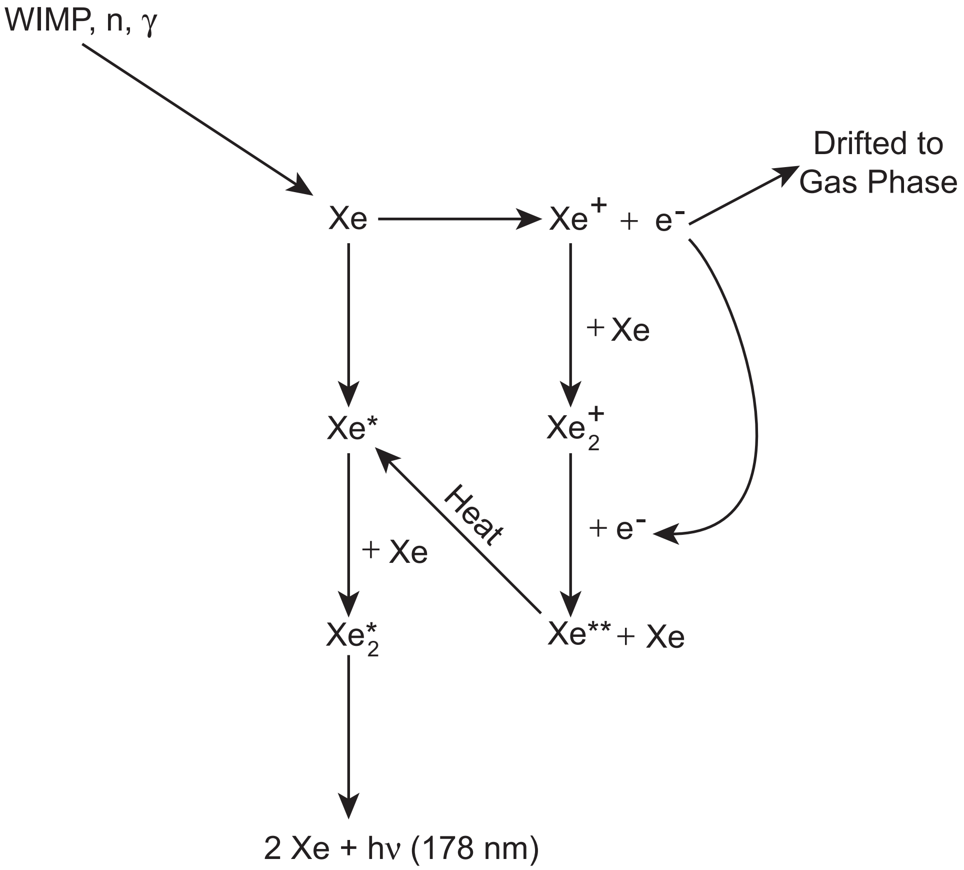

Figure 5.5: A diagram showing the different paths that produce scintillation and ionization within a liquid xenon TPC after a particle deposits energy. In some cases, the energy only excites a xenon atom eventually creating scintillation light. In other cases, the energy ionizes the xenon atoms, and the ionized electrons may either drift to the gas phase or recombine with a Xe_2^+ ion.

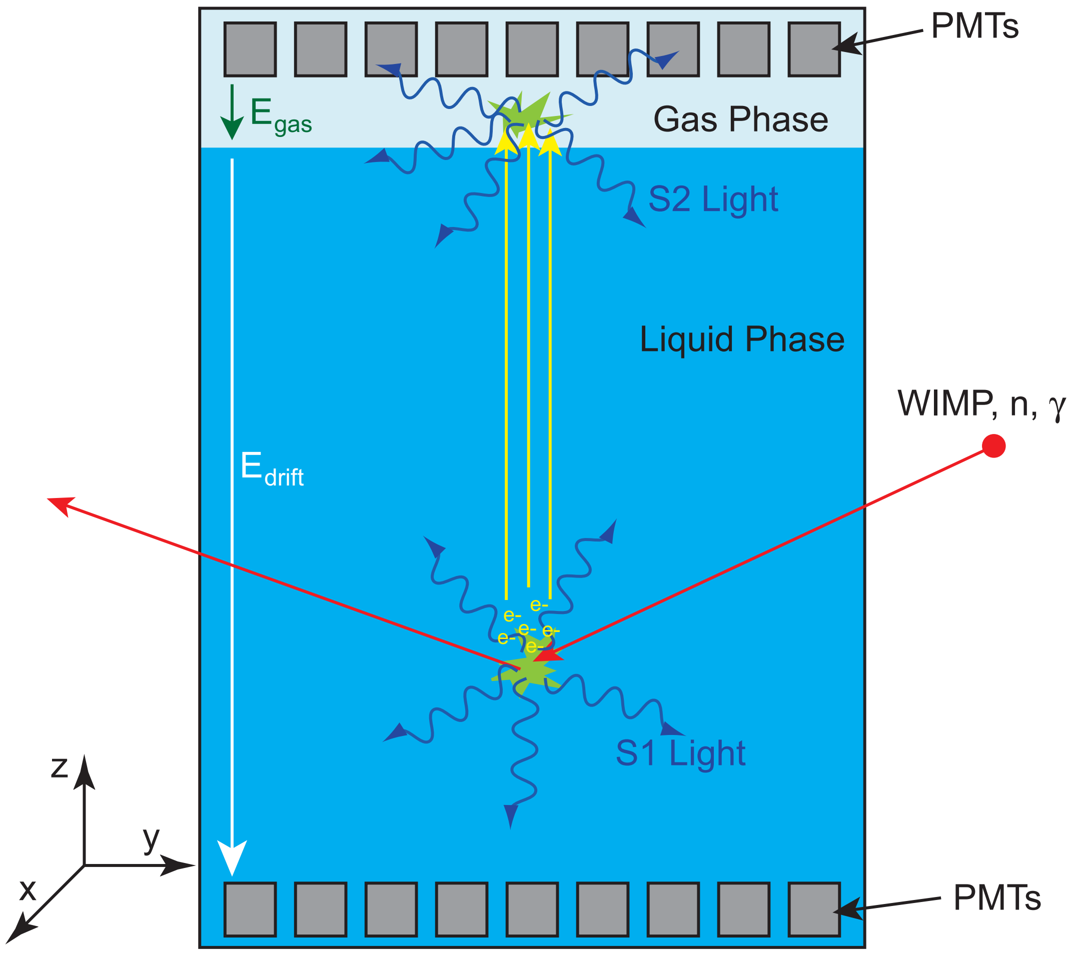

Figure 5.6: A diagram of a liquid xenon TPC. An energy deposit by a WIMP, neutron, γ-ray, or other particle creates 178 nm scintillation light (S1) that is detected by the PMTs. The energy deposit also ionizes electrons, which are then drifted to a gas phase due to a drift field (E_{drift}). In the gas phase, a stronger electric field (E_{gas}) allows for the electrons to create proportional scintillation light (S2) that is also detected by the PMTs. The time difference between the S1 and S2 signals gives the z position of the event, whereas the PMT hit pattern from the S2 allows for the reconstruction of the x-y position of the event.

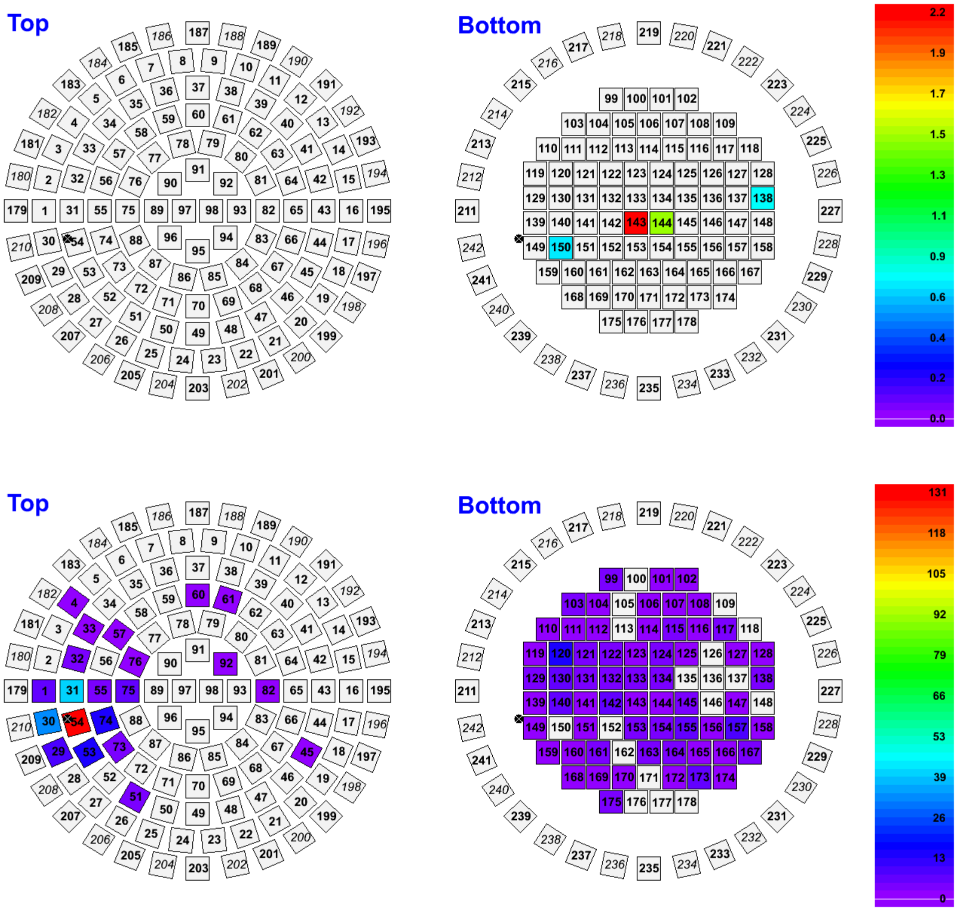

Figure 5.7: On the top, the PMT hit patterns on the top and bottom arrays from the S1 signal of an event. The total number of photoelectrons measured during the S1 signal provides the energy information of the event. On the bottom, the PMT hit patterns on the top and bottom arrays from the S2 signal of the same event. The hit pattern on the top array of PMTs from the S2 signal provides the x-y position of the event, marked as a ⊗ near PMT 54 and 149. The time difference between the S1 and S2 signals gives the z position of the event.

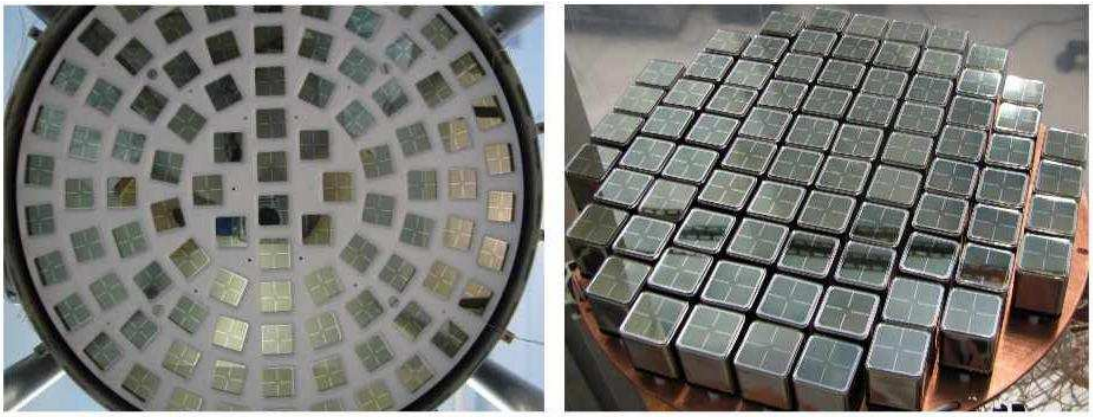

Figure 5.8: On the left, a picture of the top PMT array within the XENON100 detector. On the right, a picture of the bottom PMT array. The dense packing of PMTs on the bottom are to ensure maximum photon collection from the S1 signals.

through a heated getter[2] that removes impurities from the xenon. The clean xenon gas is then pumped back into the detector, and a pulse tube refrigerator[3] is used to maintain liquid temperature. Impurities such as water will decrease the S1 signals by absorbing the UV photons emitted during scintillation while other highly electronegative impurities such as oxygen will attract the drifting electrons, thereby decreasing the electron lifetime in the xenon and reducing the S2 signals. By constantly circulating the xenon through the heated getter, one can achieve a high S1 light yield and a good electron lifetime for S2 signals.

---

[2] SAES Model PS4-MT3/15-R/N-1/2 Mono-torr Getter

[3] Iwatani Model PC-150 Pulse Tube Refrigerator

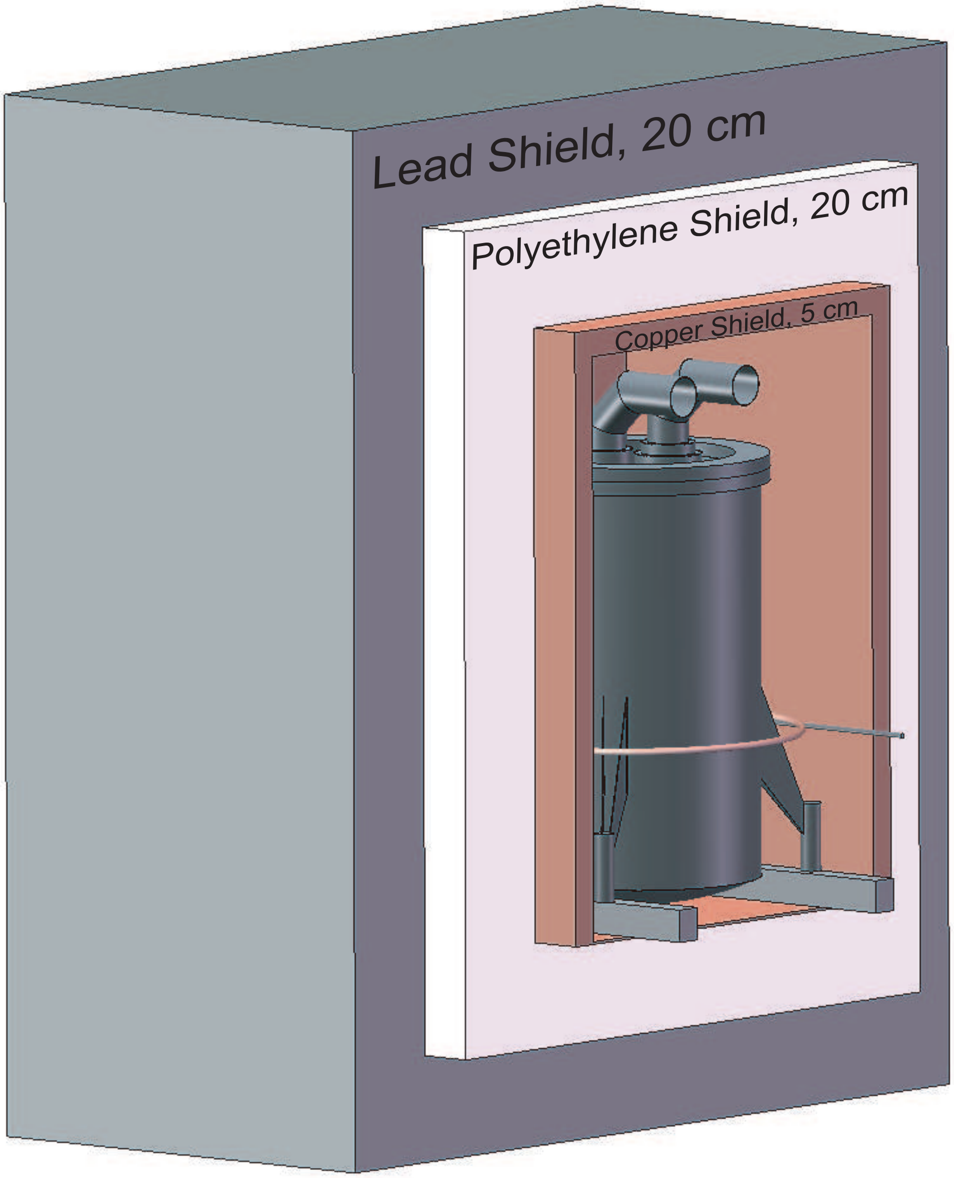

Figure 5.9: A cross section of the external shielding with the XENON100 detector inside. The shield consists of 20 cm of lead (the inner 5 cm being lead with low radioactivity) surrounding 20 cm of polyethylene, which in turn surrounds 5 cm of high purity copper. The tube surrounding the detector is used to introduce radioactive sources for calibrations.

5.3 Backgrounds and Background Reduction Techniques

5.3.1 Shielding Cosmic Rays

In searching for WIMP interactions, great care must be taken to reduce and reject any background events. Cosmic rays are constantly bombarding the Earth's atmosphere, and if these were to reach the detector, they would constantly be depositing energy and creating backgrounds in the detector. In order to shield from cosmic rays, the XENON100 detector was placed in the Laboratori Nazionali del Gran Sasso (LNGS), a laboratory deep under the Gran Sasso mountain in Italy. The mountain itself acts as a shield and attenuates the cosmic rays. WIMPs on the other hand will pass through the mountain unabated due to their weakly interacting nature.

5.3.2 External Shield

Another background to consider is the radioactivity produced from the surrounding rock and materials. This radioactivity will create γ-rays and neutrons which can be mistaken for WIMP events in the detector. Similarly, cosmic muons interacting in the rock surrounding the laboratory can also create neutrons. In order to attenuate these γ-rays and neutrons, a multilayer shield was constructed around the XENON100 detector. A drawing of the shielding structure is shown in Fig. 5.9. The outermost layer is made of 20 cm of lead to shield from the γ-rays originating from external sources. The inner 5 cm of this lead contains very low ^{210}Pb contamination, making it cleaner than the outer 15 cm. The next layer is 20 cm of polyethylene, used mainly to slow down and attenuate neutrons. The innermost layer is 5 cm of high purity copper. This also helps to shield from γ-rays originating from external sources or from the polyethylene shield. The shield itself is finally flushed with high purity nitrogen gas, in order to ensure that no radon gas remains in the shield cavity.

5.3.3 Active Veto and Multiple Scatter Cuts

Within the XENON100 detector is an active veto layer to shield from γ-rays and neutrons originating from the external shield or detector materials. Outside the PTFE cylinder of the TPC, there is a layer of liquid xenon on all sides. PMTs are placed above and below the TPC, facing into this veto layer. If a particle enters the veto layer, it can create scintillation light, and any event within the TPC that coincides with an event in the veto is rejected as having come from an external source, since a WIMP will very rarely scatter twice within the detector. Fig. 5.10 shows a diagram of the veto in XENON100 and events that scatter within the veto and the target volume.

A further technique for background reduction is known as a "multiple scatter" cut. Since WIMPs by definition interact weakly and have an incredibly small interaction cross section, it is nearly impossible for a WIMP to deposit energy in multiple locations within a detector. Neutrons and γ-rays however are likely to have multiple scatters. By examining the S2 PMT hit pattern, it is possible to distinguish single scatters from multiple scatters, and thereby remove multiple scatter events. Similarly, an S1 signal followed by two separate S2 signals signifies an event which interacted in two different z-locations and can be removed.

5.3.4 Screening and Fiducialization

The external shielding structure and internal active veto are effective at shielding from external radioactivity, but the components used within the XENON100 detector itself can also be a source for backgrounds. The stainless steel cryostat,

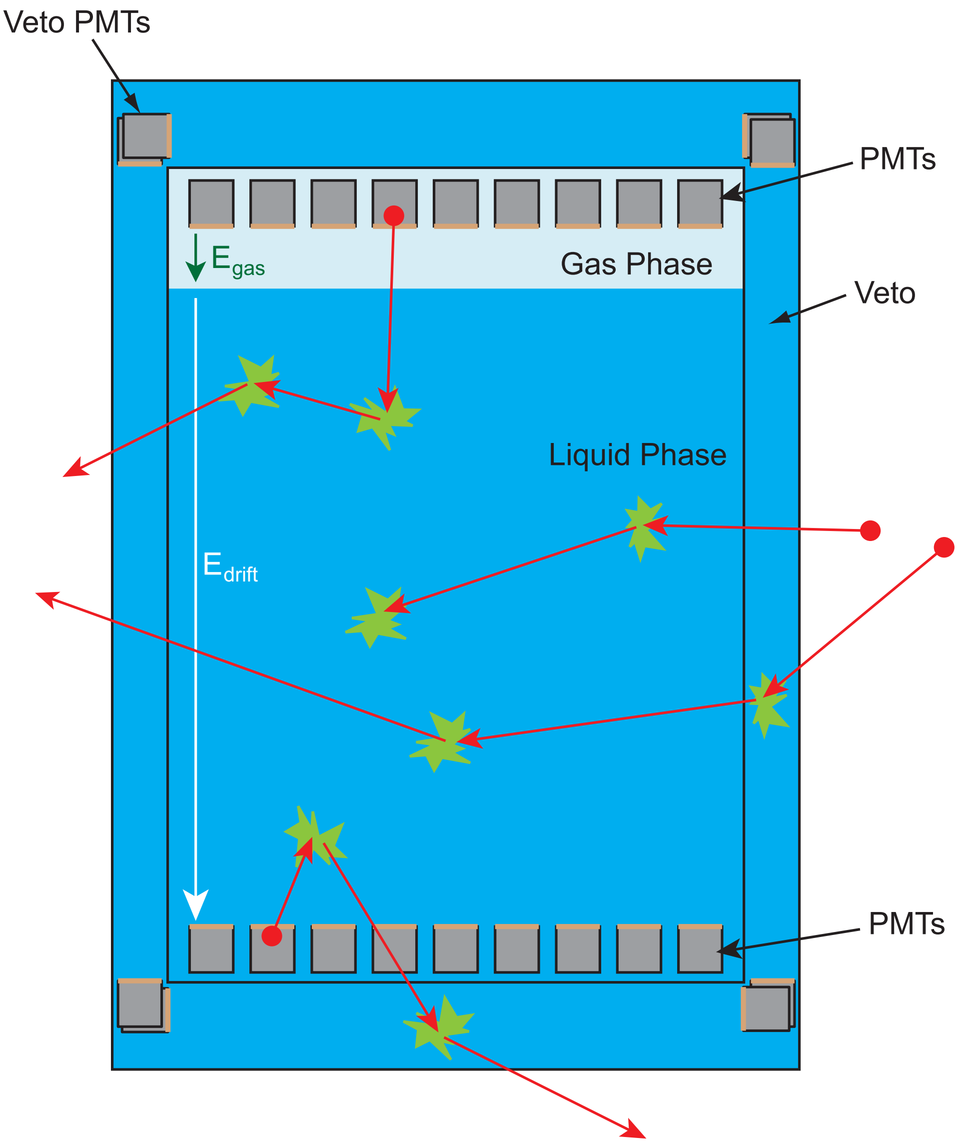

Figure 5.10: A diagram of the XENON100 TPC with the surrounding active veto. This figure includes examples of events that can be removed due to interactions within the veto, or through multiple scatters.

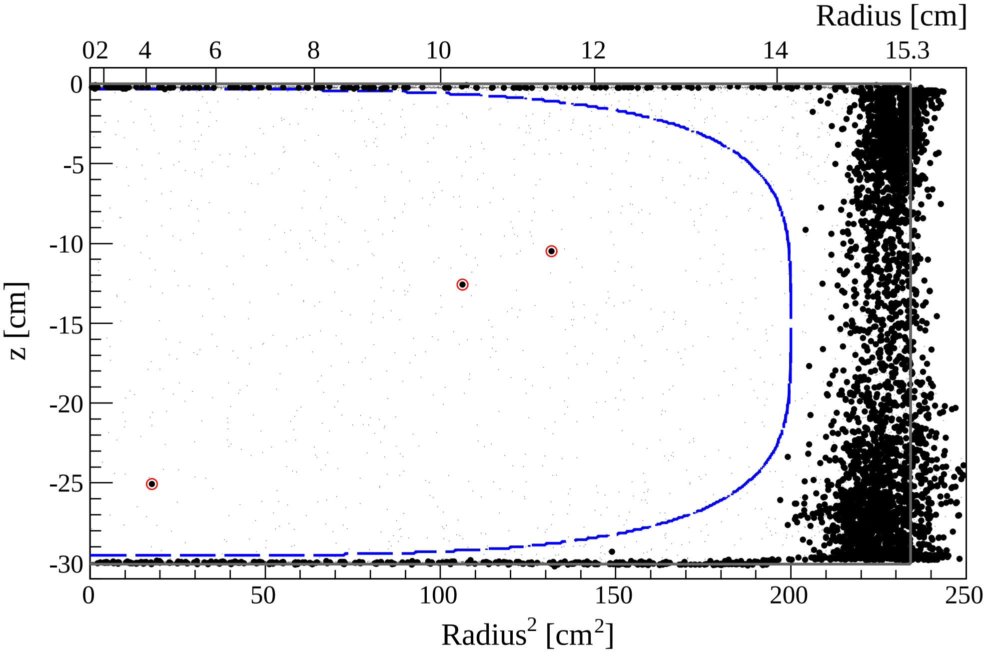

Figure 5.11: Location of events in the XENON100 detector from the latest science run. The light gray dots are the locations of events that pass all of the cuts aside from the $\log_{10}(S2/S1)$ discrimination, while the large black dots have passed all cuts including the $\log_{10}(S2/S1)$ cut. The blue line represents the border of the defined fiducial volume cut for 48 kg of liquid xenon. A majority of of the events occur near the top, bottom, and side of the detector, demonstrating the power of the fiducial volume cut. The red circled events are three events which passed all cuts and are located within the fiducial volume [123].

PTFE used for the TPC, cabling, PMTs and PMT bases all contain some radioactive impurities. In order to minimize the backgrounds from these components, all materials used in the construction of XENON100 were screened for radioactivity at the Gator screening facility at LNGS (see Sec. 8.4 for a more detailed description of the Gator test facility). Only the materials with the lowest radioactivity were chosen to be used in the detector [122]. Monte Carlo simulations were also performed to predict the amount of neutron background expected through (α,n) reactions within the detector materials. As explained in Sec. 5.1, the liquid xenon used in the detector is excellent at self shielding. γ-rays emitted by radioactivity within the detector only travel a short distance within the liquid xenon. By using the S1 and S2 signals, a precise location of the interaction can be determined, and events occurring within a few centimeters from the top, bottom, and side of the TPC can be removed. The innermost mass of xenon (called the "fiducial volume") is thus mostly free of external backgrounds, and only events occurring in this inner fiducial volume are considered in the data analysis. Fig. 5.11 shows the effectiveness of fiducialization in the actual data of the XENON100 experiment.

5.3.5 Log(S2/S1) Discrimination

When γ-rays or electrons enter the TPC and deposit energy, they interact with the electrons of the xenon atoms. The electron recoils and causes scintillation and ionization of the xenon atoms. A neutron or WIMP however interacts with the nucleus of the xenon atom, which in turn recoils and deposits energy in the xenon. A recoiling nucleus has a shorter path in xenon for a given energy than a recoiling electron. For this reason, the nuclear recoil events (WIMP and neutron interactions) have dense energy deposition, whereas electron recoil events (γ-rays and electrons) have sparse energy deposition. When the energy deposited is in a smaller physical volume, the ionized electrons have a greater possibility of recombining with a xenon ion. This lowers the S2 signal and increases the S1 signal for a given energy. Because nuclear recoils have dense energy deposition and electron recoils have sparse deposition, it is possible to distinguish between the two using the ratios of the S2 to S1 signals for each event. By using this rejection technique, it is possible to reject up to 99.75% of the electronic recoil events.

In order to distinguish between the electronic recoil and nuclear recoil events based on the S1 and S2 signals, $\log_{10}$(S2/S1) is plotted versus the S1 for all of the events. A ^{60}Co γ-ray source was used to establish the location of the electronic recoil band in $\log_{10}$(S2/S1) space, while an AmBe source was used to determine the nuclear recoil band. Fig. 5.12 shows the distribution of events from the γ-ray and neutron calibration sources. It can be seen that the nuclear recoil events and electronic recoil events populate two distinctly separate bands.

5.4 XENON100 Results

The background estimation, data analysis, and overall maintenance of the detector were performed by the entire XENON collaboration. I was involved in simulations of the backgrounds originating from radioactive contaminants in the detector materials. During the testing phases of the detector before the science run, I took several shifts in order to ensure that the detector was behaving properly and to help with the calibration runs. I also took shifts during the xenon distillation phase, where the xenon gas was run through the krypton distillation column to remove any krypton contamination. Finally, I personally designed a lead shield used to block γ-rays from the AmBe source used for neutron calibration. A simple copper tube circling the detector is used to introduce a γ-ray source

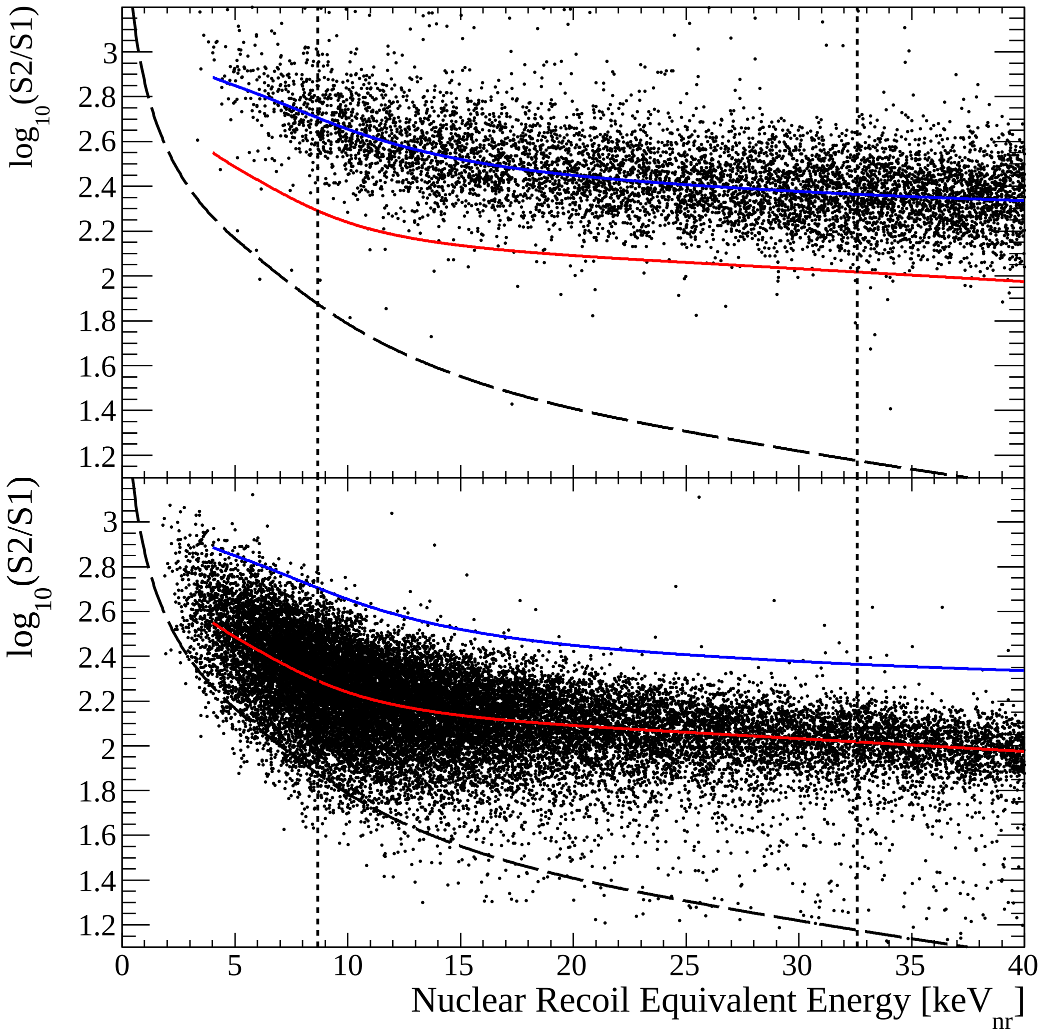

Figure 5.12: On the top, a plot of the events from a ^{60}Co γ-ray calibration source in log$_{10}$(S2/S1) space. On the bottom, a plot of the events from an AmBe neutron calibration source. The blue curve in both plots shows the mean of the electronic recoil band, whereas the red curve shows the mean of the nuclear recoil curve. The nuclear recoil and electronic recoil bands are separated, and so this parameter can be used for discrimination.

during an electronic recoil calibration run. However, for the neutron calibration, any γ-rays entering the detector from the source will affect the calibration. For this reason, I designed a lead shield to be placed around the copper tube in the correct location to ensure that only the neutrons from the source would enter the detector. A picture of the lead shield is shown in Fig. 5.13.

5.4.1 Detector Behavior

The XENON100 detector was run for 100.9 live days in order to search for WIMP interactions. A Monte Carlo simulation was performed before this run in order to understand the γ-ray backgrounds originating from radioactivity from detector materials. The measured radioactivity values from Ref. [122] were used in a `Geant4` Monte Carlo simulation [124], and the results are shown in Fig. 5.14 and 5.15. The actual data from a short run before the WIMP search is also presented in the same figure. It can be seen that the data and simulation match well across most of the energy range. A deviation is apparent at the highest energies, which can be attributed to nonlinearity in the PMTs (the nonlinearity of PMTs will be discussed further in Sec. 7.1.5). Fig. 5.15 shows the same data and Monte Carlo comparison at low energies.

During the WIMP search, weekly ^{137}Cs calibrations were performed to characterize the electron lifetime and the S2 response as a function of position. ^{137}Cs emits a 662 keV γ-ray which was used to understand the response of the XENON100 detector by measuring the difference in S2 signals based on the location of interaction. A similar procedure was used to characterize the S1 response of the detector using the 40 keV line from inelastic scatters of neutrons on ^{129}Xe.

It is important to note that due to the different processes for scintillation light from electronic and nuclear recoil events, the energy inferred from the number

Figure 5.13: A picture of the XENON100 detector outside of the shielding. The copper tube encircling the detector is used to introduce calibration sources, and the lead shield surrounding part of the copper tube is used to stop γ-rays from the AmBe neutron source.

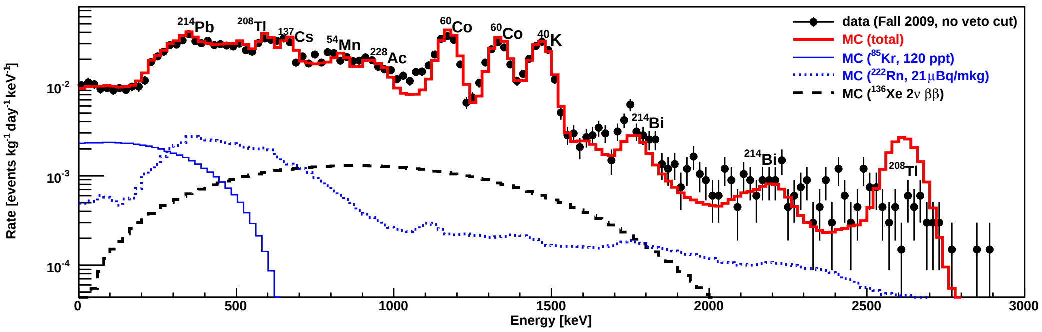

Figure 5.14: A plot comparing the Monte Carlo simulated electronic recoil background spectrum to actual data taken before the WIMP search [125]. The Monte Carlo and real data match well up to high energies. A deviation between the data and Monte Carlo at the highest energies is due to nonlinearities in the PMTs.

of photoelectrons in the S1 signal of an event can differ whether the event is an electronic or nuclear recoil event. The nuclear recoil energy is defined as:

$$E_{nr} = \left(\frac{S1}{L_y}\right)\left(\frac{1}{\mathcal{L}_{eff}}\right)\left(\frac{S_{ee}}{S_{nr}}\right) \tag{5.7}$$

In Eq. 5.7, $S1$ is the number of photoelectrons (pe) from the S1 signal of the event, L_y is the light yield in pe/keV$_{ee}$ for 122 keV γ-rays, and S_{ee} and S_{nr} are the electric field scintillation quenching factors for electronic recoil and nuclear recoil events respectively. Since electronic recoil events and nuclear recoil events produce different numbers of photoelectrons for the same amount of energy deposited, the convention of keV$_{ee}$ and keV$_{nr}$ is used to distinguish between an electronic recoil energy deposit and a nuclear recoil energy deposit respectively. Values of S_{ee}=0.58 and S_{nr}=0.95 were used in the analysis as taken from Ref. [126]. $\mathcal{L}_{eff}$ in Eq. 5.7 is the scintillation efficiency of nuclear recoil events relative to the 122 keV γ-ray interactions. This value has been measured by several groups, and the parameterization used is shown in Fig. 5.16 [127, 123].

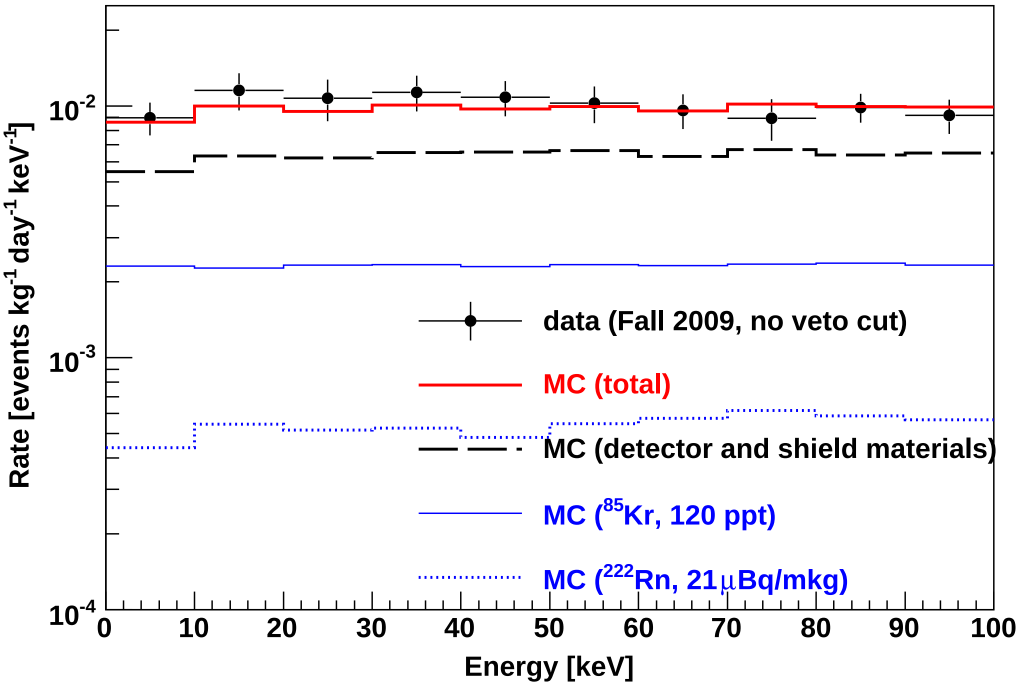

Figure 5.15: A plot of the low energy background from data and Monte Carlo [125]. This is a zoom of the lowest energies from Fig. 5.14.

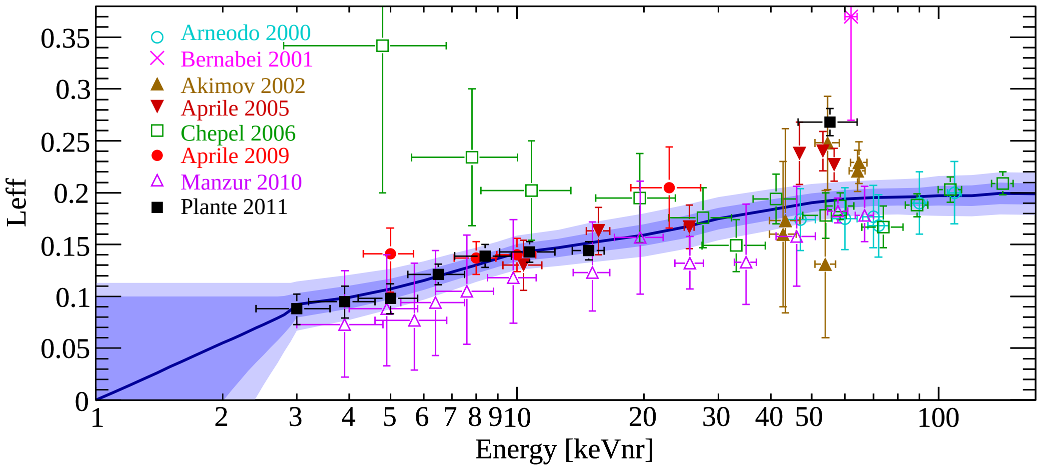

Figure 5.16: A plot of the scintillation efficiency factor ($\mathcal{L}_{eff}$) as measured by various groups. The best fit curve (solid black line) was used in the XENON100 analysis, which was logarithmically extrapolated to zero at 1 keV$_{nr}$ [123].

During data taking, the data was blinded under the 90% quantile of the electronic recoil band in the $\log_{10}$(S2/S1) space, and for S1 signals less than 160 photoelectrons. A set of quality cuts were established before unblinding the data in order to maintain a high acceptance of WIMP-like events. A software threshold was established such that only events with S2 signals above 300 photoelectrons were recorded, while cuts required that the S1 signals be above 4 photoelectrons and must have at least a two-fold PMT coincidence within ±20 ns.

As mentioned in Sec. 5.3, various techniques were used for background rejection. A multiple scatter cut was used in order to remove any events that interact more than once within the liquid xenon target. Also, any event which had a coincidence between an S1 and an energy deposit in the veto was tagged and removed. A fiducial cut was applied to the events such that interactions only within the inner 48 kg were considered. Finally, a $\log_{10}$(S2/S1) cut was applied to the data. This ensures that the events that are below the 99.75% quantile of the electronic recoil band and above the lower 3σ nuclear recoil quantile were considered to be WIMP-like signals.

While checking the performance of XENON100 during the WIMP search, it became apparent that the electronic recoil background rate was higher than expected. This increase in rate was attributed to a higher than expected krypton contamination. Comparison between Monte Carlo and the data outside of the blinded region showed that the ^{nat}Kr contamination during this run was 700 ± 100 ppt, higher than was anticipated from previous data. It was deduced that the high krypton contamination resulted from an air leak in the recirculation system during maintenance. The contribution from this excess ^{85}Kr was then added to the Monte Carlo simulations.

5.4.2 Background Estimation

There are three main types of background events that may enter the WIMP search region, Gaussian leakage of electronic recoil events, non-Gaussian leakage of electronic recoils, and nuclear recoil events from neutrons. The number of neutron events in the search region was estimated with a Monte Carlo which considered $(\alpha$,n) reactions and spontaneous fission of radioactive nuclei. In addition, the rate of muon-induced neutrons from the material in the laboratory was also simulated, and a total number of nuclear recoils of $0.11^{+0.08}_{-0.04}$ was expected in the region of interest. For the electronic recoil events, a ^{60}Co source was used to characterize the electronic recoil band. This band was flattened in $\log_{10}(S2/S1)$ space by subtracting the mean as a function of the energy. Afterwards, the band was characterized as a Gaussian distribution in $\log_{10}(S2/S1)$. By observing the number of events outside of the blinded region during data taking, an estimate was made for the number of events leaking into the WIMP search region of 1.14 ± 0.48 events assuming a Gaussian leakage. In this run, the electronic recoil events were dominated by the ^{85}Kr contamination.

The non-Gaussian leakage of electronic recoil events into the WIMP region of interest is due to a separate class of events known as "Gamma-X" events. In these events, a γ-ray enters the detector and deposits energy in the target volume, creating scintillation light ($S1$) and ionization electrons ($S2$). However, a second scatter occurs in a "charge insensitive" region, that is, a location within the detector where the γ-ray can create a scintillation light ($S1'$) but no ionization electrons are drifted. This may occur below the cathode for example, where there is no drift field. For this reason, the scintillation signal is artificially greater than expected as both the $S1$ and $S1'$ are observed, and so the discrimination parameter is decreased:

$$\log_{10}\left(\frac{S2}{S1+S1'}\right) < \log_{10}\left(\frac{S2}{S1}\right) \tag{5.8}$$

The expected number of non-Gaussian leakage events was estimated using a ^{60}Co calibration to be $0.56^{+0.21}_{-0.27}$ events. Combining this number with the expected Gaussian leakage of electronic recoils and the nuclear recoils expected in the region of interest gives a total expected background of 1.8 ± 0.6 events.

5.4.3 Results

After applying all necessary cuts, the WIMP region of interest was unblinded, and an unexpected population of noise events at the lowest energies was seen. These events occurred due to a coincidence of an S1 signal on a single PMT with a noise spike on a different PMT. A post-blinding cut was devised and applied to all of the data in order to remove these events. After the noise events were removed, three candidate events remained in the signal region. These events are shown as

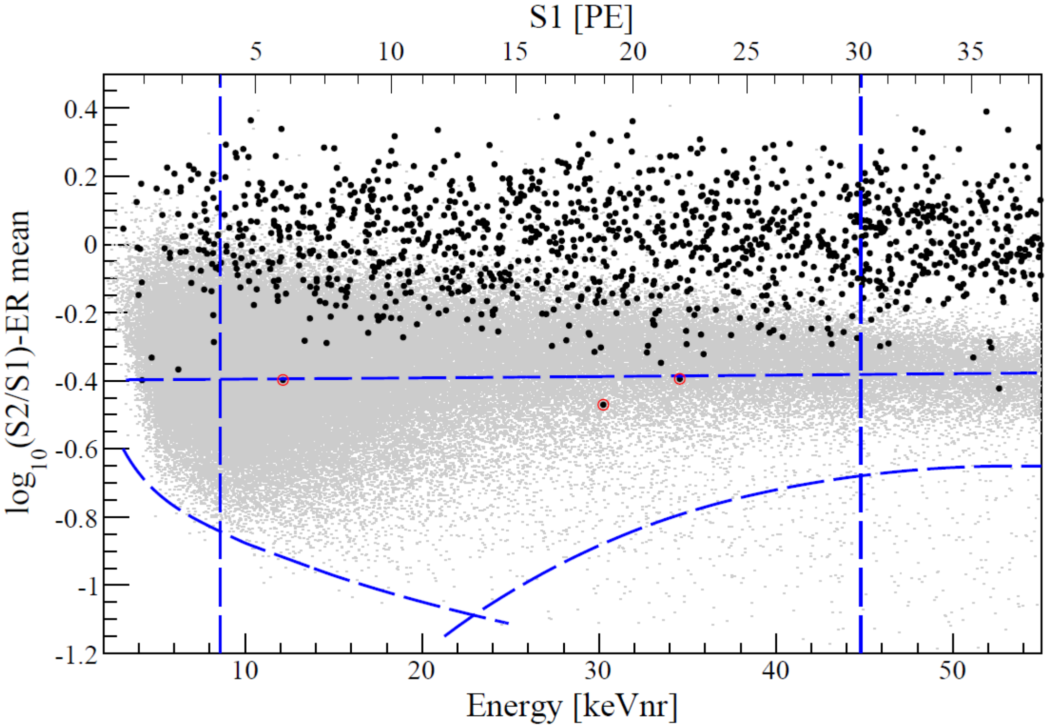

Figure 5.17: The actual data from the XENON100 experiment after running for 100.9 days. The y-axis in this plot is the $\log_{10}$(S2/S1) parameter flattened by subtracting the mean of the electronic recoil band. The gray points are neutron calibration points to show the nuclear recoil band. The black points are all the data left after applying the quality cuts and the fiducial volume cut. The energy range chosen for the signal region was $4-30$ photoelectrons, corresponding to $8.4-44.6$ keV$_{nr}$, as signified by the two vertical lines. The horizontal line is the 99.75% quantile of the electronic recoil band, the bottom left line corresponds to a software threshold of 300 photoelectrons for S2 signals, and the bottom right line is the 3σ contour of the nuclear recoil band. Together, these five lines define the WIMP search region, and three events fell within this region, shown with red circles, with an expected background of 1.8 ± 0.6 [123].

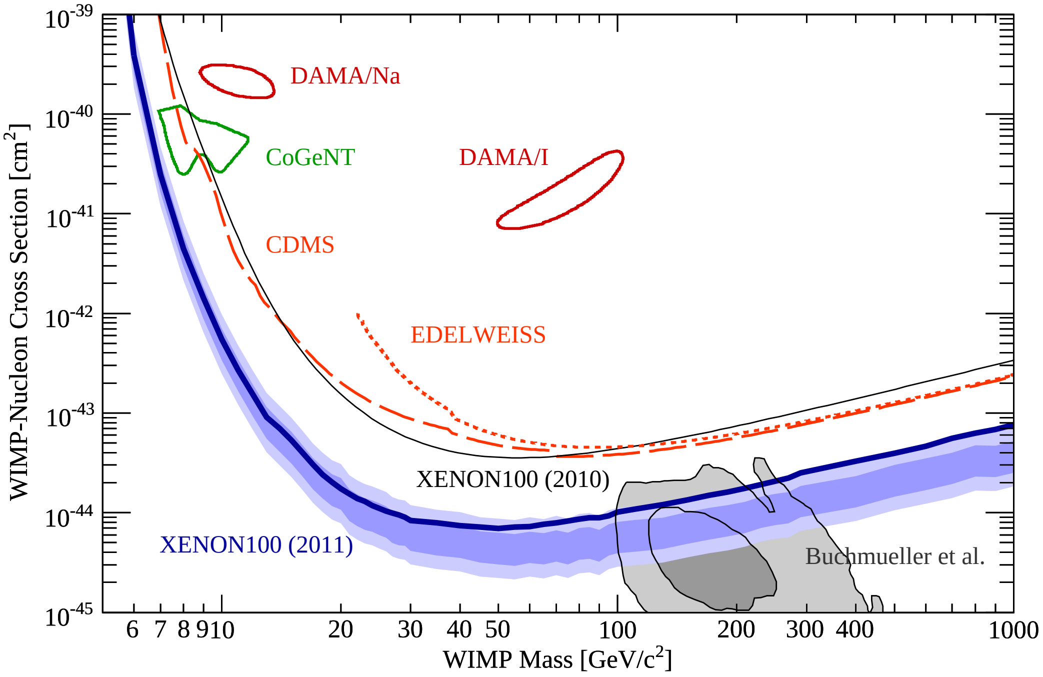

Figure 5.18: Limits produced by the latest science run of the XENON100 experiment (shown as a thick blue line), along with the limits and allowed regions from competing experiments and a previous run of XENON100 [129]. The gray shaded area is the theoretical prediction for WIMPs [130], while the dark (light) blue regions correspond to the 1σ (2σ) sensitivity of the run. The limits from EDELWEISS [86] and CDMS [85] are shown in dotted orange and dashed orange respectively, while the 90% confidence level regions favored by CoGeNT [131] and DAMA [88] are shown as solid green and solid red curves respectively [123].

red circled dots in Fig. 5.17. With an expected background of 1.8 ± 0.6 events, a discovery cannot be claimed. Using Poisson statistics, there is a 28% chance that the three events were merely fluctuations of the expected number of backgrounds. Instead, a limit was placed on the WIMP cross section as seen in Fig. 5.18 using the Profile Likelihood method [128]. An upper limit of 7.0×10^{-45} cm^2 was placed on the WIMP-nucleon cross section σ for a 50 GeV WIMP. As a comparison, the cross section of solar neutrino scattering off of electrons is $\sim 10^{-45}$ cm^2.

5.5 Summary

XENON100, being the largest and cleanest dark matter detector currently in operation, was able to set the lowest limit on the mass and cross section of WIMP interactions. By using the virtues of liquid xenon, including the powerful self shielding effect, the backgrounds in the detector were reduced to a point where only 1.8 ± 0.6 backgrounds were expected. XENON100 is now in the process of taking data for a second run with lower ^{85}Kr contamination to further enhance this limit. However, the data taken with XENON100 can also be used to search for two neutrino double beta decay in ^{136}Xe.

CHAPTER 6

Double Beta Decay in XENON100

Double beta decay in ^{136}Xe has recently been observed in the EXO-200 detector with a half-life of $2.11 \pm 0.04(\mathrm{stat}) \pm 0.21(\mathrm{sys}) \times 10^{21}$ yr [106], however neutrinoless double beta decay, which has not yet been detected, is of great importance because it will show physics beyond the Standard Model. XENON100, which has been developed specifically for dark matter detection, is optimized for low energy events, and such high energies as those seen in neutrinoless double beta decay cannot be detected properly. This is due to nonlinearity of the PMTs occuring at energies $\gtrsim$ 1700 keV. The light yield calibrations for XENON100 were performed at lower energies of 40 keV, 80 keV, 164 keV, and 662 keV [84], below the energy of neutrinoless double beta decay (2.458 MeV). For this reason, XENON100 cannot detect neutrinoless double beta decay, however there is potential for the two neutrino mode. The analysis in this chapter, including the Monte Carlo background estimation and setting a limit on the double beta decay half-life, was performed by myself and the results have not been aproved by the XENON100 collaboration.

6.1 Background Reduction

In order to provide a limit on the half-life of double beta decay in ^{136}Xe, the backgrounds in the experiment must be decreased as much as possible. Many of

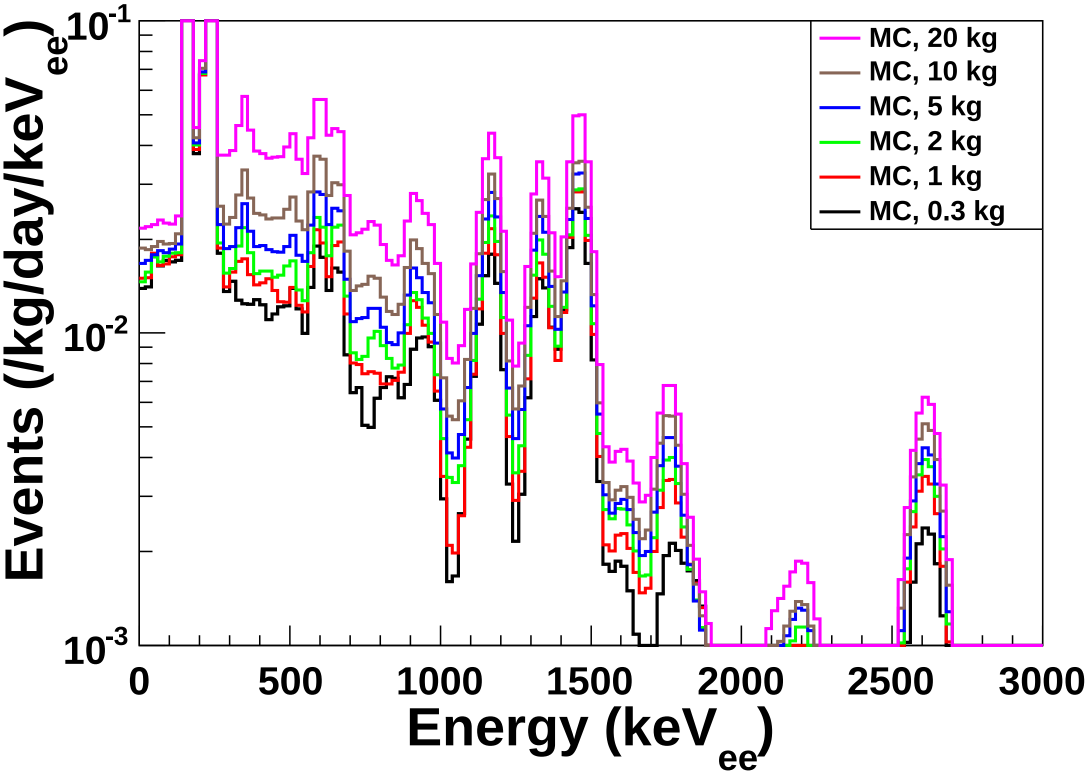

Figure 6.1: A plot of the `Geant4` simulated electronic recoil background spectrum based on the known radioactive contaminants in the detector materials. These spectra have already been scaled to match the spectra of the actual data. The effects of fiducialization are seen, as a smaller fiducial volume decreases the differential background rate. However, the smallest fiducial volumes have similar differential event rates, due to the small size of the detector. Backgrounds originating from outside the detector can penetrate deeply and create a uniform background with respect to the fiducial volume.

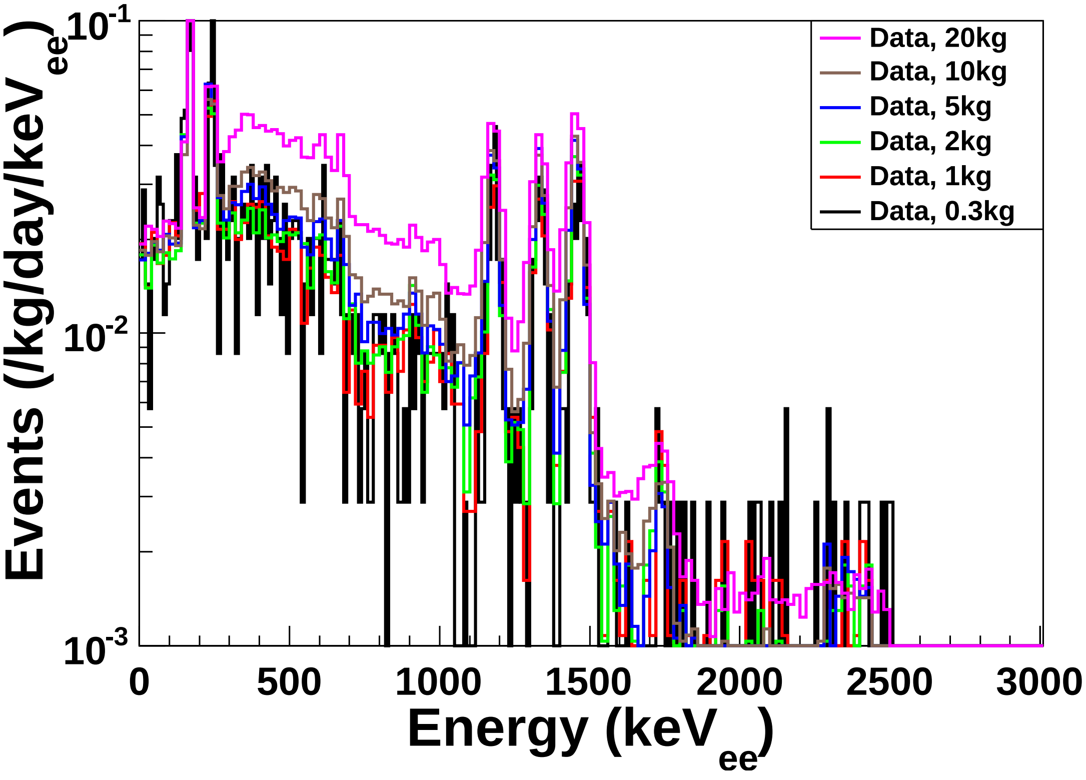

Figure 6.2: The same plot as Fig. 6.1 for the actual data. The effects of fiducialization can be seen once again, and a similar trend as the Monte Carlo spectrum can be seen with the differential event rate remaining relatively constant at the smallest fiducial volumes.

the same background reduction techniques used in the XENON100 dark matter search (see Sec. 5.3) are applied for the double beta decay search as well. Since the same detector is used, the materials have already been chosen to have low radioactive contamination. A multiple scatter cut is also used, as the emitted β-particles will remain in a small volume and appear to be a single scatter. The same quality cuts are used as for the dark matter search as well. Since the energy deposits are due to the emitted β-particles, the interactions will all be electromagnetic, and so the $\log_{10}(\mathrm{S2}/\mathrm{S1})$ cut is not applied for this data analysis.

A fiducial volume cut is used to reduce the external backgrounds as much as possible. Since the spectrum of double beta decay in ^{136}Xe spans up to 2.458 MeV, the external γ-rays which make up a majority of the background are more penetrative, and so a smaller fiducial volume is used than in the dark matter search. Fig. 6.1 shows the effects of various fiducial volume cuts on the expected backgrounds by using a `Geant4` Monte Carlo simulation and considering the radioactive contaminants in all of the relevant detector materials (see Ref. [125]). Similarly, Fig. 6.2 shows the effect of fiducialization on the actual data from XENON100.

6.2 Data Analysis and Results

The Monte Carlo generated background spectrum includes contributions from ^{238}U, ^{232}Th, ^{60}Co, ^{137}Cs, and ^{40}K from the detector materials, along with ^{222}Rn from the shield cavity and ^{85}Kr in the liquid xenon. Two peaks in the spectrum at 1.17 MeV and 1.33 MeV correspond to ^{60}Co contamination in detector materials, while a third peak exists at 1.46 MeV from ^{40}K. Upon observing the actual data, the entire Monte Carlo spectrum was scaled up by a factor dependent on the fiducial volume chosen. This was done to match the data at the

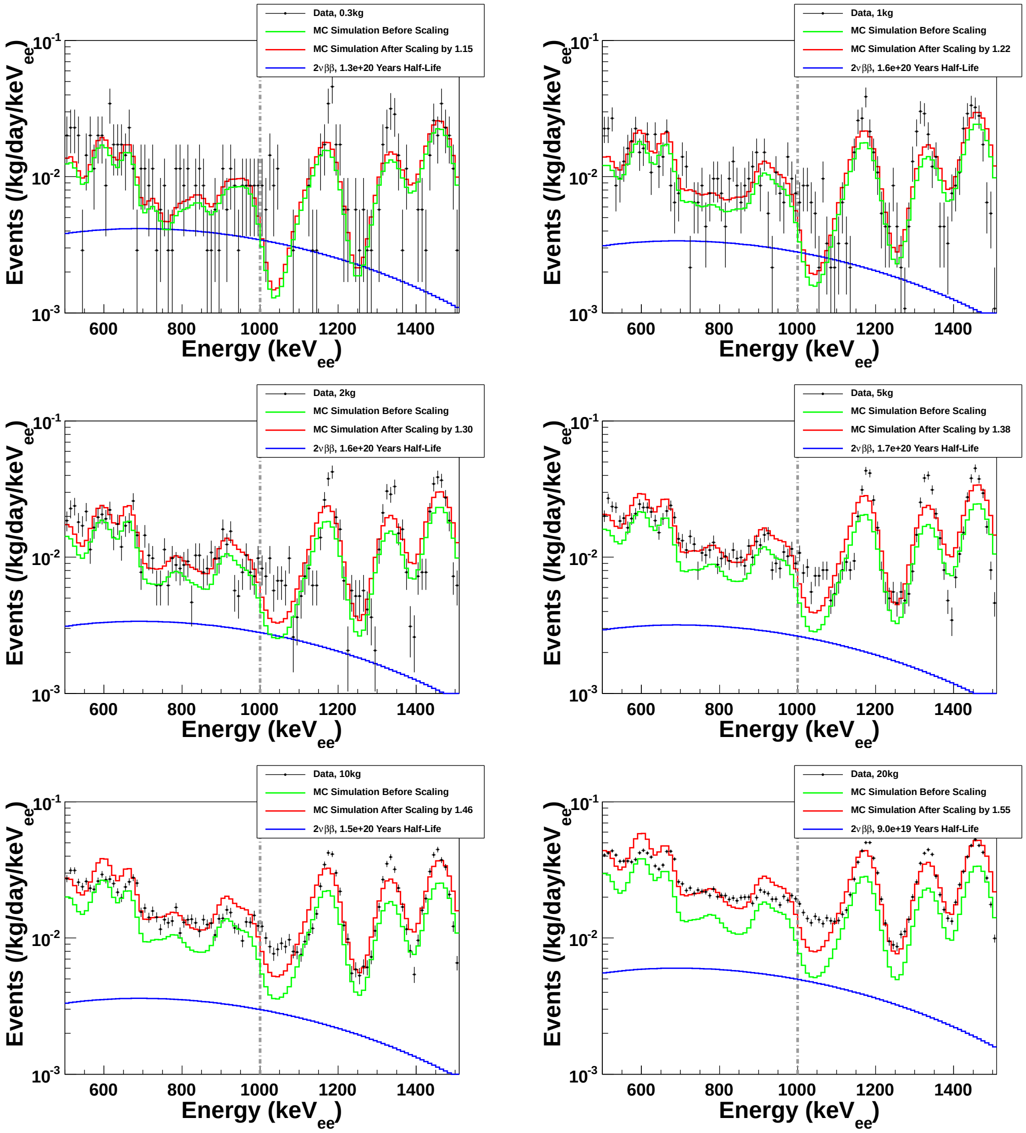

Figure 6.3: A comparison between real data and Monte Carlo for various fiducial volumes. The black points are the actual data, with error bars corresponding to Poisson fluctuations of the data. The green and red curves correspond to the Monte Carlo generated spectra before and after scaling respectively, with the scaling factor shown in the legends. The blue curve corresponds to the double beta decay spectrum with the half-life limit determined from the given fiducial volume. Finally, the gray vertical line shows the maximum energy used for the data analysis.

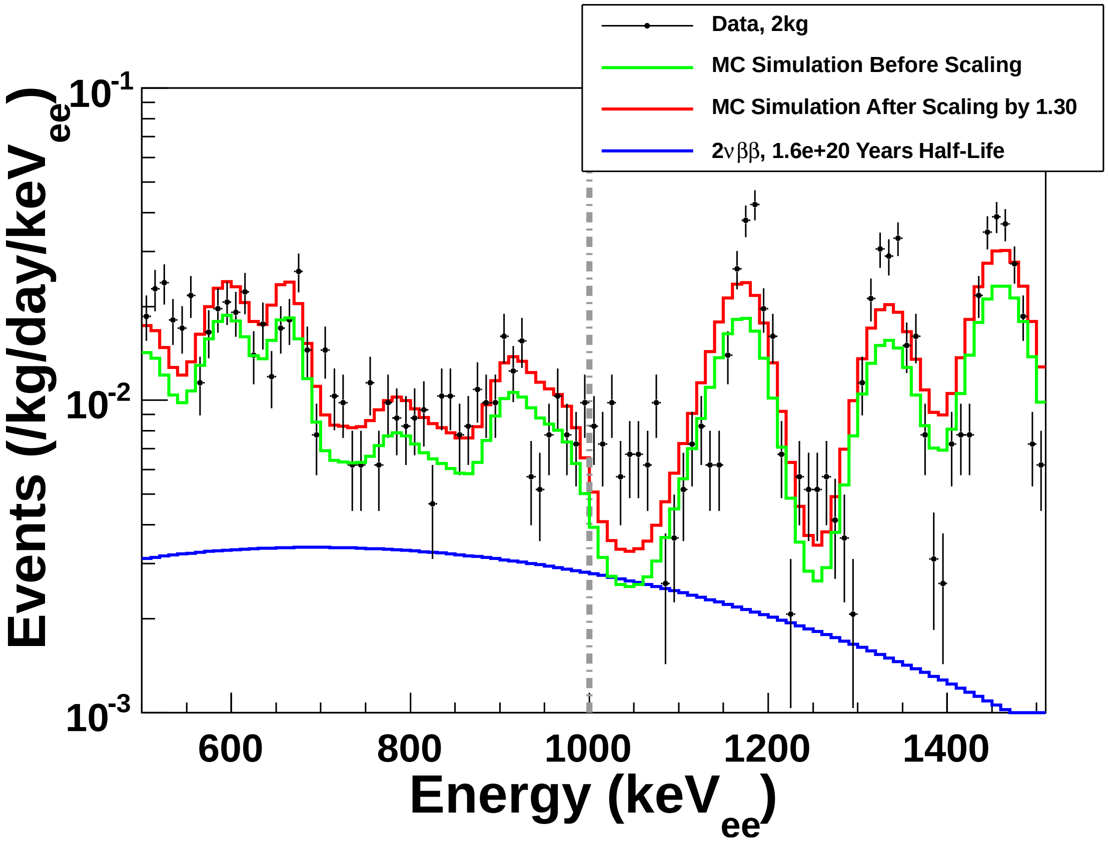

Figure 6.4: A comparison between real data and Monte Carlo for the case of a 2 kg fiducial. This is the same as the plot in Fig. 6.3.

three prominent peaks. The integral number of events between 1.1 MeV and 1.5 MeV was compared between the data and Monte Carlo, and the Monte Carlo spectrum was scaled such that the two values agreed. For example, in the case of a 2 kg fiducial volume, the entire Monte Carlo spectrum was multiplied by 1.30. Two other peaks not in the Monte Carlo spectrum at 164 keV and 236 keV correspond to the activated ^{131m}Xe and ^{129m}Xe respectively. These peaks exist in the real data as a neutron calibration was done just before data taking, causing the activation of xenon, and were also added into the Monte Carlo results. As explained in Sec. 5.4.1, the XENON100 detector had a high ^{85}Kr contamination, which accounts for a large portion of the backgrounds at energies < 500 keV.

An energy range of $500 - 1000$ keV was chosen for the analysis in order to avoid the region used to determine the scaling factor for the spectrum and the region with ^{85}Kr contamination. This energy range also includes the maximum of the two neutrino double beta decay spectrum at $\sim$700 keV (see Fig. 4.3). Comparisons between the data and Monte Carlo generated differential energy spectra before and after scaling are shown in Fig. 6.3 for various fiducial volumes and Fig. 6.4 shows the same plot for the case of a 2 kg fiducial volume. The error bars in the data include only the statistical error determined through Poisson fluctuations such that $\sigma = \sqrt{N}$ where σ is the error used and N is the number of events in the given bin. No error bars were included for the Monte Carlo generated spectra, as the number of events simulated is very large and the statistical fluctuations are negligible. The plots include the amount by which the simulated spectrum was scaled, and the spectrum of two neutrino double beta decay for half-lives determined using the given fiducial mass (the method for determining the half-lives is described in further detail below).

The mismatch in the simulated spectrum and actual data above $\gtrsim 1700$ keV as seen in Fig. 6.1 and 6.2 was traced to nonlinearity effects of the PMTs which caused the events to be incorrectly reconstructed in both position and energy. This same effect caused the difference in the overall normalization in the energies of interest. Because of the incorrect position reconstruction, events occuring outside of the fiducial volume considered were reconstructed into the fiducial volume, causing an increase in the event rate over what was expected. Other unknown effects may also cause the difference in the overall event rate. By comparing the data and Monte Carlo for various sizes and shapes of the fiducial volume, it became apparent that the incorrect position and energy reconstruction was causing the differences between the data and Monte Carlo. Larger fiducial masses require greater scaling to account for the difference, which shows that the incorrect position and energy determination is dependent on the proximity of the event to the outter edges of the TPC.

The ratio between the actual number of events seen and the predicted number from the scaled Monte Carlo simulation are shown in Fig. 6.5 for different fiducial volumes, while Fig. 6.6 focuses on the case of a 2 kg fiducial volume. The error bars in these plots are from statistical fluctuations of the data and were calculated by $\sigma = \frac{N_{Data}}{N_{MC}}\sqrt{\left(\frac{\sigma_{Data}}{N_{Data}}\right)^2 + \left(\frac{\sigma_{Sim}}{N_{Sim}}\right)^2}$ where N_{Data} and N_{Sim} are the number of data points and the number of Monte Carlo simulated events respectively, N_{MC} is the number of events predicted by the Monte Carlo, and σ_{Data} and σ_{Sim} are the Poisson fluctuations of the data and Monte Carlo such that $\sigma_{Data} = \sqrt{N_{Data}}$ and $\sigma_{Sim} = \sqrt{N_{Sim}}$. Since the number of Monte Carlo simulated events is very large, the error reduces to $\sigma = \frac{N_{Data}}{N_{MC}}\frac{\sigma_{Data}}{N_{Data}} = \frac{\sqrt{N_{Data}}}{N_{MC}}$.

From the plots in Fig. 6.5, the mean of the ratio between the real data and Monte Carlo spectrum was calculated over the energy range of interest (500 − 1000 keV) and the Root Mean Square (RMS) difference from the mean were

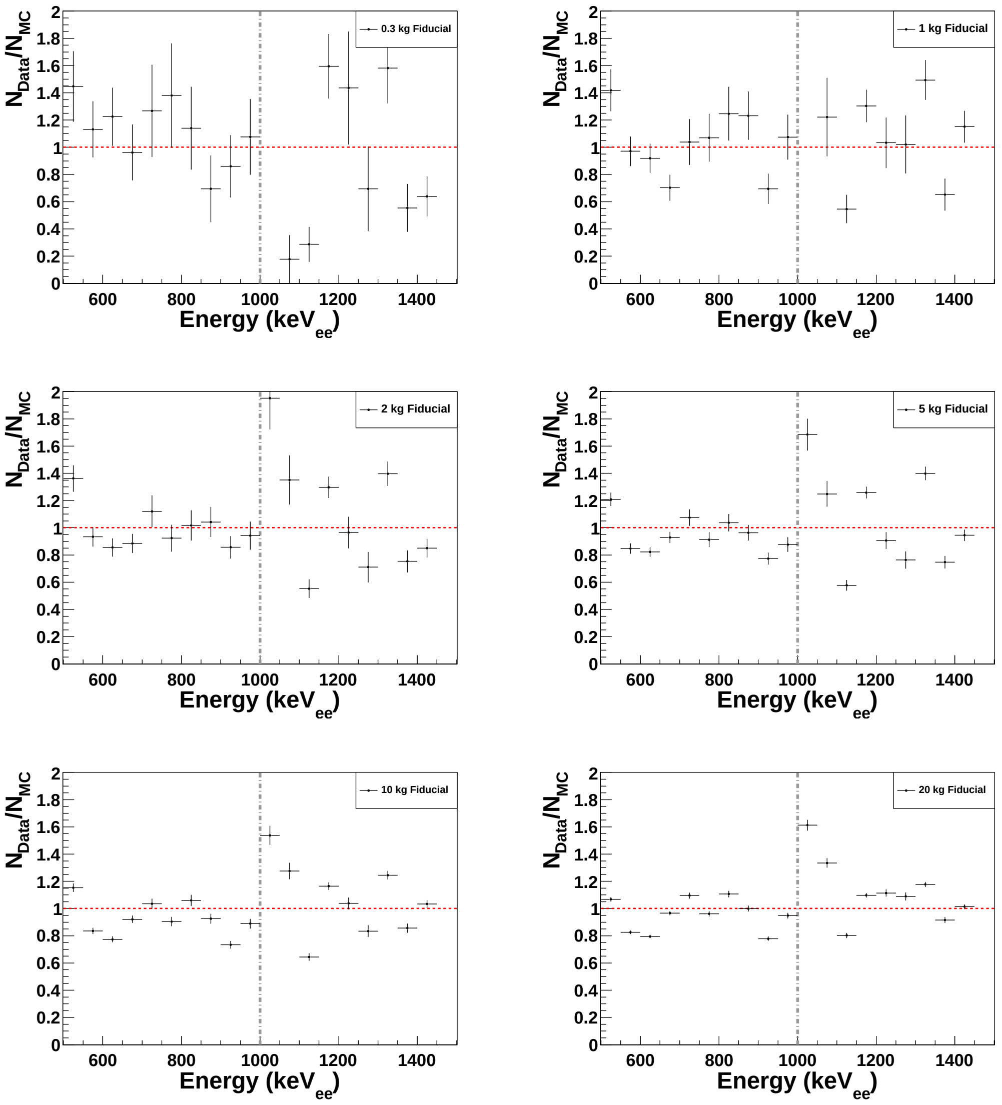

Figure 6.5: A plot of the ratio between the number of events predicted by the Monte Carlo after scaling and the actual number of events observed for various fiducial volumes. The error bars in this plot are due to Poisson fluctuations, explained further in the text. The horizontal red line corresponds to a perfect match between the data and Monte Carlo, and the vertical gray line shows the maximum energy used for the analysis. In the $500 - 1000$ keV energy range of interest, the ratios from all fiducial volumes have a mean near 1 and an RMS difference from the mean $< 25\%$.

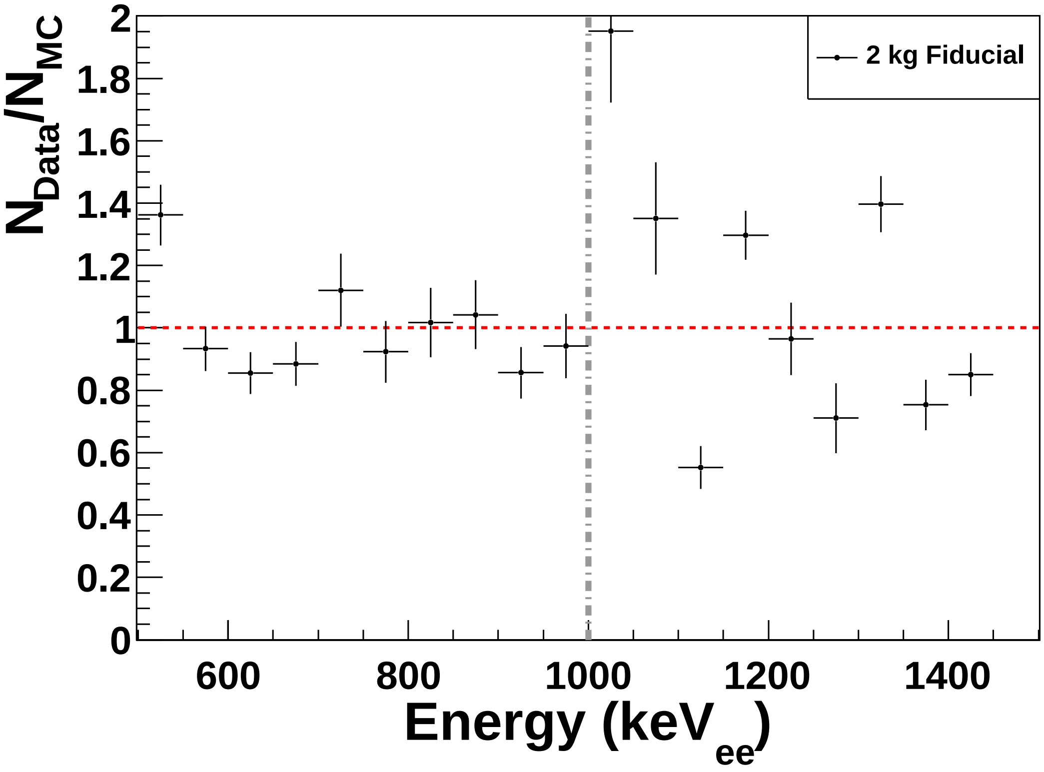

Figure 6.6: A plot of the ratio between the number of events predicted by the Monte Carlo after scaling and the actual number of events observed for the case of a 2 kg fiducial volume. This is the same as the plot in Fig. 6.5.

calculated for all of the fiducial volumes. These values are shown in Tab. 6.2, along with the scaling factor used for the Monte Carlo, the number of events predicted by the Monte Carlo and the observed number of events. All of the fiducial volumes shown have mean values near 1 and RMS differences from the mean $< 25\%$. The RMS differences from the mean show how the shapes of the Monte Carlo generated spectrum and real data spectrum differ. From these values, and from the values for scaling the Monte Carlo, an estimate for the systematic uncertainty of 20% was determined as a conservative value for all of the fiducial volumes and was used in further calculations.

As the size of the fiducial volume was increased, the amount of scaling required also increased, however the RMS difference from the mean of the ratio between the Monte Carlo and real data decreased as seen in Tab. 6.2. For this reason, the analysis focuses on a 2 kg fiducial volume, however the same analysis was performed for all fiducial volumes considered. Within the 2 kg fiducial volume and in the energy range of $500 - 1000$ keV, a number of events $n = 1260$ was observed. The Monte Carlo simulation provided a background estimate of $b = 1290 \pm 36(\text{stat}) \pm 258(\text{sys})$ events. A one-sided 90% C.L. limit on the expected number of background events was calculated as $1290 - 1.3 \times \sqrt{36^2 + 258^2} = 951$. It should be noted that since the systematic error is much larger than the statistical fluctuations, the statistical error has very little impact on the final number. The difference between the data and 90% C.L. expected background, 309 events, was then attributed to double beta decay events in the given energy range. Based on the energy resolution and considering the fact that natural xenon contains 8.86% ^{136}Xe, 309 events in 2 kg of natural xenon in the energy range of $500 - 1000$ keV corresponds to a half-life of:

$$T_{1/2}^{2\nu} > 1.6 \times 10^{20}\text{yr} \tag{6.1}$$

As shown in Tab. 6.2, the same analysis was performed for various other fiducial volumes, and the resulting limit was relatively independent of the fiducial volume due to the large systematic error. The value for the lower limit on the half-life of two neutrino double beta decay found here is consistent with the recently published value from EXO-200 as seen in Tab. 6.1. Other experiments have released lower limits on the half-life that are inconsistent with the EXO-200 results. These experiments had higher background rates and larger systematic errors than EXO-200 and could not have seen double beta decay as clearly as EXO-200 has. The following section discusses the recent positive identification of two neutrino double beta decay in ^{136}Xe by the EXO-200 collaboration, showing that the systematic uncertainties and number of background events can be reduced to a level where detection of double beta decay is possible.

Reference	Year	Half-Life (yr)
E. Bellotti, et al. [134]	1991	$> 6.0 \times 10^{19}$
J. L. Vuilleumier, et al. [132]	1993	$> 2.1 \times 10^{20}$
R. Luescher, et al. [135]	1998	$> 3.6 \times 10^{20}$
R. Bernabei, et al. [107]	2002	$> 1.0 \times 10^{22}$
Ju. M. Gavriljuk, et al. [136]	2005	$> 8.5 \times 10^{21}$
N. Ackerman, et al. [106]	2011	$2.11 \pm 0.04(\text{stat}) \pm 0.21(\text{sys}) \times 10^{21}$
This Work	2011	$> 1.6 \times 10^{20}$

Table 6.1: Table of the limits on two neutrino double beta decay of ^{136}Xe, as found by various groups.

6.3 Observation of Two Neutrino Double Beta Decay in EXO-200

The EXO collaboration recently released results showing a discovery of two neutrino double beta decay in ^{136}Xe from the EXO-200 detector [106]. The EXO-200 detector consists of an enriched liquid xenon TPC with a 40 cm diameter and 44 cm length. A cathode grid in the center of the detector and two anode grids at each end divides the TPC into two sections. The anode grids provide a charge readout for detection of ionization signals, and 250 large area avalanche photodiodes (LAAPDs) detect the primary scintillation light. Fig. 6.7 shows a schematic of the EXO-200 detector.

The xenon used in EXO-200 was enriched to 80% ^{136}Xe. Data was collected for 752.66 hours with a fiducial mass containing 63 kg of ^{136}Xe. This allowed for the discovery of two neutrino double beta decay with a half-life of $2.11 \pm 0.04(\text{stat}) \pm 0.21(\text{sys}) \times 10^{21}$ yr [106]. The discovery was able to be made due to the fact that all materials used in the construction of EXO-200 were screened and only the materials with lowest radioactivity were used in the detector [137]. The materials used in the detector were also kept to a minimum. Of particular importance is the fact that the radioactivity associated from the LAAPDs are lower than that of conventional PMTs. Fig. 6.8 shows a plot of the spectrum from EXO-200, along with a fit which includes various background components and two neutrino double beta decay.

The energy resolution obtained by EXO-200 was $\sigma = 4.5\%$ at 2615 keV [106]. As illustrated in Fig. 4.6 and 4.7, such a value for the resolution is not sufficient for a search for neutrinoless double beta decay. With a resolution of 4.5%, 10% of the events detected between the Q-value and the half-maximum of the neutrinoless

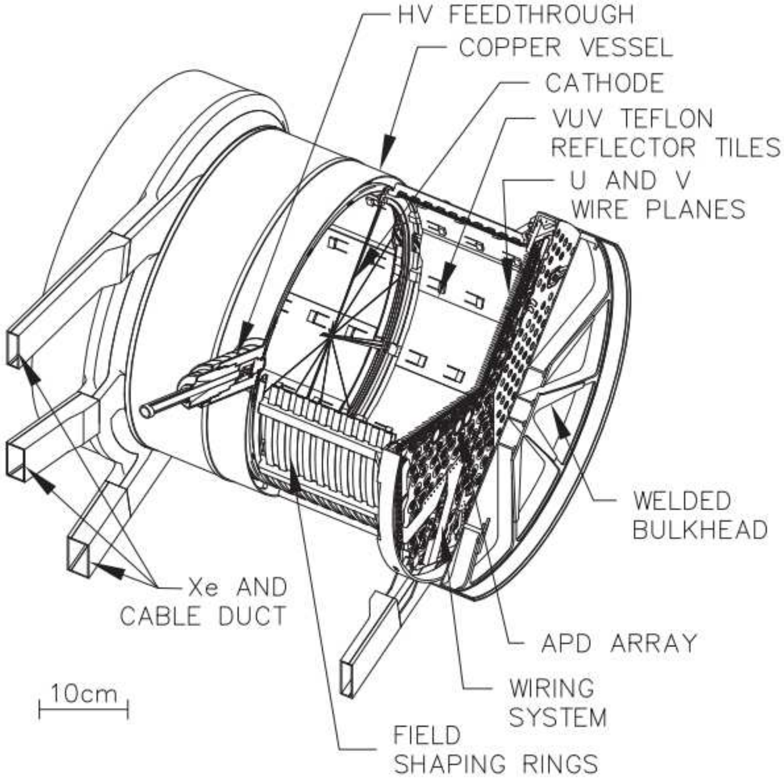

Figure 6.7: A schematic of the EXO-200 detector. The detector consists of an enriched liquid xenon TPC with 40 cm diameter and 44 cm length [106].

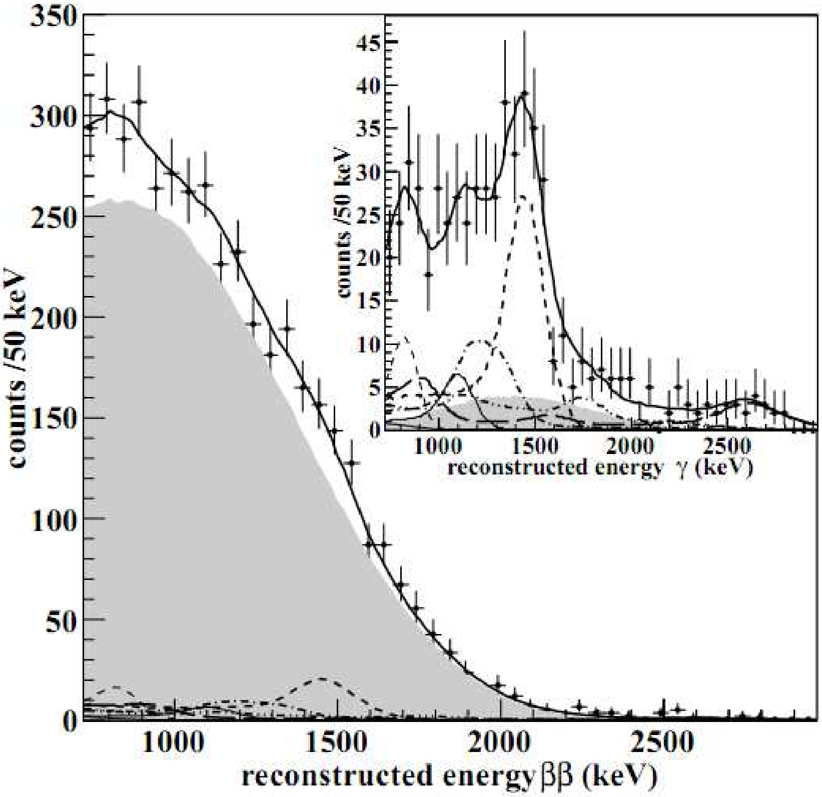

Figure 6.8: A plot of the energy spectrum from 752.66 hr exposure of EXO-200. The main plot includes the single scatter events, while the inset shows the multiple scatter events. The fit to several backgrounds along with two neutrino double beta decay is shown as a solid line, while the shaded region is the contribution from two neutrino double beta decay. The background components shown include ^{232}Th (long dash), ^{40}K (dash) and ^{60}Co (dash-dot) [106].

double beta decay peak will be from two neutrino double beta decay. This leakage drops to 0.01% at a resolution of 1.5%. A better resolution will also distinguish between a line from neutrinoless double beta decay and nearby peaks in the background from radioactive contamination. The low resolution of EXO-200 is due to the fact that only the ionization signal is read out through the anode grids. An anticorrelation of the primary scintillation light and the ionization signal can increase the resolution to a level that would allow for a neutrinoless double beta decay search. The fact that the LAAPDs have a gain of ∼100 [138], compared to a gain of $10^6 - 10^7$ for conventional PMTs, means that the primary scintillation signal cannot be used in the energy determination. Similarly, the low gain of the LAAPDs causes the EXO-200 detector to have an energy threshold of 720 keV, and the LAAPD signals are only used for timing information to determine the location of an event.

The EXO-200 detector demonstrates the importance of low radioactive contamination and minimal use of materials. Future double beta decay detectors must follow this example in order to achieve a low background rate that would allow for the discovery of neutrinoless double beta decay. Unlike EXO-200 however, the energy resolution must be $\lesssim 1.5\%$ in order for the line from neutrinoless double beta decay to be detected. This can be achieved through the use of photodetectors with higher gains than the LAAPDs. By replacing the LAAPDs with high gain photodetectors in future experiments, the threshold can also be lowered, and the same detector can be used for both double beta decay detection and dark matter detection. However, as demonstrated by the XENON100 detector, the linearity of the photodetectors must also be improved for a future combined experiment in order to decrease the systematic effects to a level below the statistical fluctuations.

6.4 Summary

Although XENON100 was designed for dark matter detection, the detector also provided insight into two neutrino double beta decay in ^{136}Xe. Similar background reduction techniques were used for this analysis as for dark matter, except that a smaller fiducial mass was used and a higher energy range was analyzed. With the systematic errors in the detector, a discovery cannot be made, however a lower limit was placed on the half-life of two neutrino double beta decay which is lower than the recent positive identification from EXO-200.

Future dark matter detectors can also be used for similar double beta decay analyses, however to improve the quality of double beta decay data, and to allow for the possibility of neutrinoless double beta decay searches and detection, the photodetectors used in these experiments must have lower radioactivity and a higher linearity range. The EXO-200 detector has shown the capability to decrease the backgrounds in double beta decay experiments to such levels that two neutrino double beta decay is conclusively observed by using large area avalanche photodiodes. However, this detector has a high energy threshold due to the low gain of LAAPDs and poor energy resolution from the fact that only the ionization signal is used for energy determination. By combinind the virtues of XENON100 and EXO-200, a future liquid xenon TPC can be developed with proper photodetectors to allow for a combined neutrinoless double beta decay and dark matter search. These photodetectors must have the single photon sensitivity of conventional PMTs for dark matter detection, along with low radioactivity and high linearity offered by the LAAPDs to detect double beta decay. The TPC must also have the capability of using both the scintillation and ionization signals to have better energy resolution.

A new photodetector concept called the QUartz Photon Intensifying Detector (QUPID) developed at UCLA can satisfy all of these requirements. This photodetector will be implemented in the future dark matter detectors to allow for a combined dark matter and double beta decay search. The following chapter will discuss the concept of the PMT and the properties which are important to characterize in order to fully understand the response of the dark matter and double beta decay detectors up to the highest energies, while Ch. 8 will discuss the development and testing of the QUPID.

Fiducial Mass	Scaling Factor	MC Prediction	Data	Mean of $\frac{\mathrm{N_{Data}}}{\mathrm{N_{MC}}}$	RMS Difference from Mean of $\frac{\mathrm{N_{Data}}}{\mathrm{N_{MC}}}$	90% C.L. Number of $2\nu\beta\beta$ Events	90% C.L. Lower Limit Half-Life
0.3 kg	1.15	176	197	1.12	0.22	69	1.3×10^{20} yr
1 kg	1.22	547	551	1.04	0.22	149	1.6×10^{20} yr
2 kg	1.30	1290	1260	0.99	0.15	308	1.6×10^{20} yr
5 kg	1.38	4235	3950	0.94	0.12	819	1.7×10^{20} yr
10 kg	1.46	10412	9476	0.92	0.12	1774	1.5×10^{20} yr
20 kg	1.55	32280	30035	0.95	0.11	6151	0.9×10^{20} yr

Table 6.2: A table of the various parameters used for the calculation of the lower limit of the half-life for two neutrino double beta decay in different fiducial volumes. The half-life calculations had a weak dependence on the fiducial mass.

CHAPTER 7

Photomultiplier Tube Concept

As explained in Ch. 5, noble liquid detectors operate by observing scintillation light from the target material. This scintillation light is detected by photomultiplier tubes placed on the top and bottom of the detector, facing into the target volume. Because of the size of the detector and the low energy deposited by WIMP interactions, the photons originating from the initial scintillation light are sparsely distributed on the PMTs, and often only single photons strike the surface of a PMT. For this reason, it is essential that these PMTs be sensitive to single photons. The XENON100 detector uses Hamamatsu[1] R8520 1” square PMTs, however future ton-scale dark matter detectors will require larger PMTs in order to achieve effective coverage with a manageable number of PMTs. The Hamamatsu R11065 and R11410 3” round PMTs are currently being considered for use in future detectors. This chapter will introduce the basic parameters of PMTs, while a full treatment on the methods of characterization will follow in Ch. 8. This chapter also includes the results of some basic tests which I performed on the R11065 3” PMT and the R8520 1” PMT.

A photomultiplier tube consists of a transparent window coated with a photocathode material made of a mixture of various alkali metals, followed by a focusing electrode, several electron multiplication stages (dynodes), and finally an anode, all contained within a vacuum. A diagram of a conventional PMT is

---

[1] Hamamatsu Photonics K.K., 314-5 Shimokanzo, Iwata City 438-0193, Shizuoka, Japan

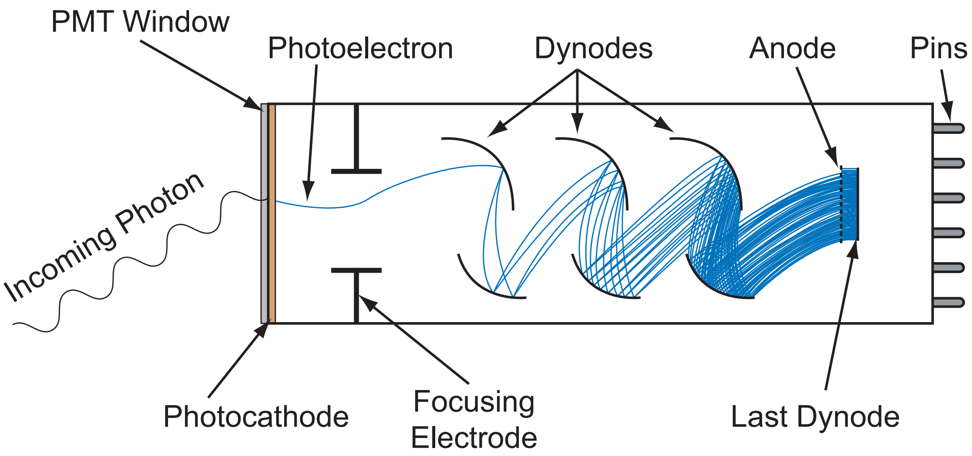

Figure 7.1: A simplified diagram of a photomultiplier tube and the basic theory of operation. A photon passes through the window of the PMT and strikes the photocathode, ejecting a photoelectron. The photoelectron is then accelerated onto the first dynode, and several secondary electrons are released. These electrons are then accelerated and multiplied on the next dynode and so on, until reaching the anode.

shown in Fig. 7.1. The photocathode is held at a high negative potential, and every successive dynode is held at a lower negative potential, with the anode being at ground level. A photon passes through the window and strikes the photocathode. If the energy of the incident photon is great enough, an electron will be ejected from the photocathode via the photoelectric effect with a maximum kinetic energy of

$$K_{max} = h\nu - \psi \tag{7.1}$$

where h is the Plank constant, ν is the frequency of the photon, and ψ is the work function, defined as

$$\psi = h\nu_0 \tag{7.2}$$

with ν_0 being the minimum frequency a photon can have in order to eject an electron. The ejected electron is called a "photoelectron." The potentials applied to the photocathode, focusing electrode, and dynodes creates an electric field that accelerates and focuses the photoelectron onto the first dynode.

The dynodes themselves are coated with a material that emits secondary electrons when bombarded by an accelerated electron. The number of electrons ejected by the dynode for every primary electron is called the secondary emission ratio and is designated by δ. The value of δ increases with increasing primary electron energy. Each of the secondary electrons are then accelerated onto the next dynode, and the process continues for every dynode. The electrons are finally gathered on the anode and read out of the PMT.

In order to supply the voltages to the photocathode and dynodes, and to read out the final signal from the anode of the PMT, a base is required. The base itself contains a set of resistors arranged in a voltage divider that provides every dynode with a lower negative voltage than the last. A diagram of such a voltage divider is shown in Fig. 7.2.

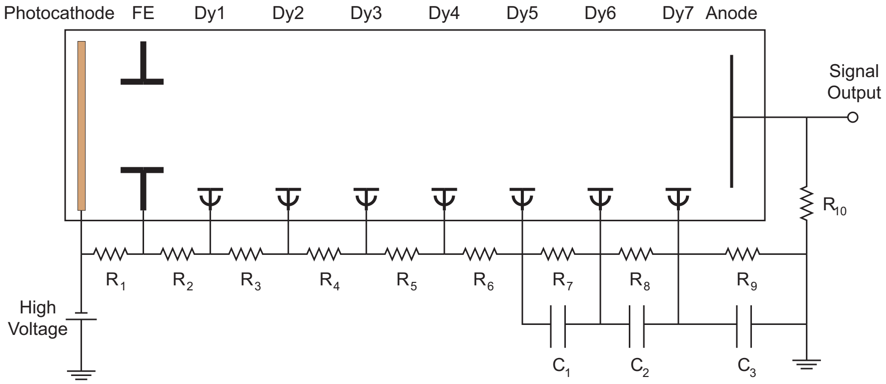

Figure 7.2: A schematic of a typical voltage divider used to supply varying potentials to the photocathode, dynodes, and anode of a PMT. In this figure, FE is the focusing electrode and Dy1−Dy7 are the dynodes. The resistor values are typically between 100 kΩ − 10 MΩ. The capacitors help to supply charge in pulsed mode operation in order to increase the anode linearity (see Sec. 7.1.5.2).

7.1 PMT Characteristics

7.1.1 Quantum Efficiency and Collection Efficiency

The quantum efficiency is a property of the photocathode defined as the percent chance that a photon which hits the photocathode will eject a photoelectron. This probability is a function of the wavelength of the incident photon. Before striking the photocathode, the photon must first pass through the window of the PMT. The window can also absorb the photon before it hits the photocathode, and thus the quantum efficiency includes the properties of the window as well. Fig. 7.3 shows a plot of the quantum efficiency for two PMTs with different types of photocathode. After photons hit the photocathode, the photoelectrons will be ejected isotropically, and so at most 50% of the photoelectrons will continue on in the electron multiplication process, while the other 50% will enter the PMT

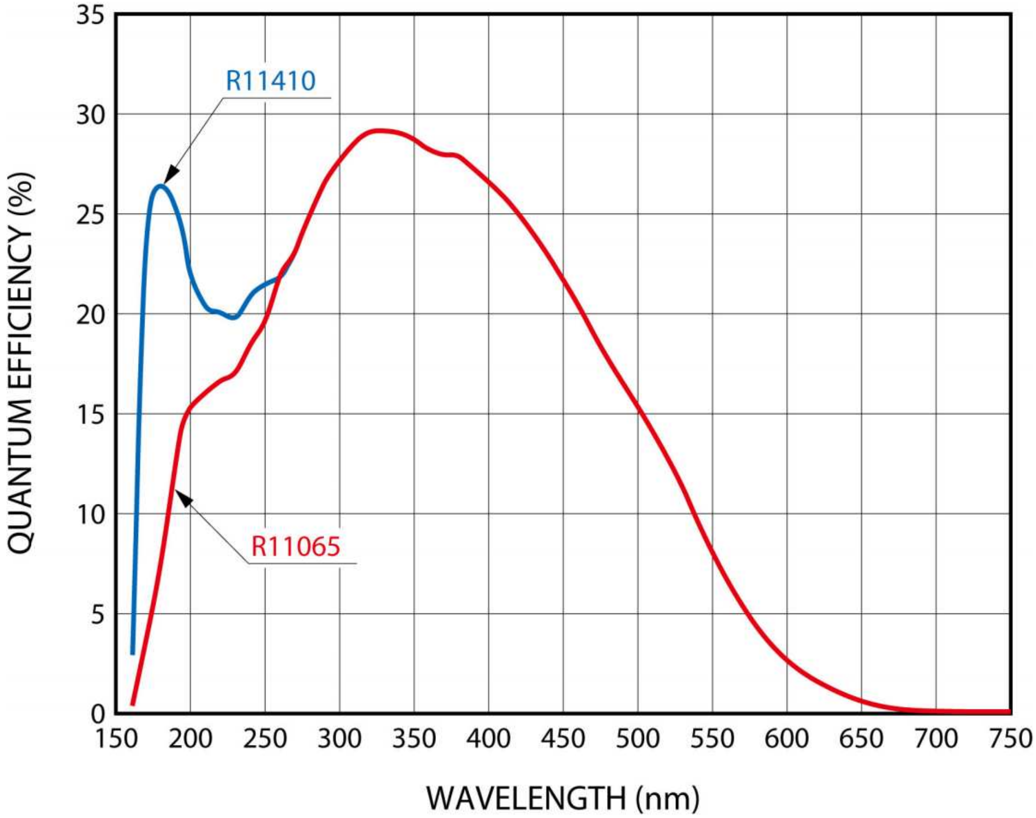

Figure 7.3: A plot of the quantum efficiency of the photocathode of two PMTs, a Hamamatsu R11410 3" PMT and a Hamamatsu R11065 3" PMT. The only difference between these two PMTs is the type of photocathode used. The data for this plot was taken at Hamamatsu.

window and stop. The probability that an ejected photoelectron will bombard the first dynode and undergo the multiplication process is defined as the collection efficiency and is dependent on the position of the photon hits along the photocathode.

7.1.2 Photocathode and Anode Uniformity

During the production of PMTs, a vacuum is pumped inside the PMT after the body and internals of the PMT are assembled. Once a vacuum is pumped, the photocathode material can be deposited onto the inner surface of the window. The photocathode material is introduced into the PMT and evaporated onto the window. The evaporation process is not necessarily uniform, and different parts of the window may have different amounts of photocathode material. The photocathode uniformity describes how evenly the photocathode material has been deposited onto the window.

When a photoelectron is ejected from the photocathode, it must hit the first dynode in order to continue with the electron multiplication process. However, depending on the initial position of the photon hit, there is a probability that the photoelectron might miss the first dynode. Subsequently, if the photoelectron hits the first dynode, there is a chance that not all of the secondary electrons strike the second dynode due to the initial photoelectron trajectory, and so on with the remaining dynodes. Because of these effects, the signal read out from the anode of the PMT may vary with the position of the light striking the photocathode. These variations in the anode signal are characterized by the anode uniformity of the PMT.

7.1.3 Gain

As explained above, a photoelectron that is emitted from the photocathode is accelerated and focused onto the first dynode, and the secondary electrons ejected from the first dynode are accelerated and focused onto the second dynode, and so on until reaching the anode. At each stage, the electrons are multiplied by a factor δ, where [139]:

$$\delta = aE^k \tag{7.3}$$

In Eq. 7.3, E is the potential difference between the dynodes, a is a constant, and k is a constant between 0.6 and 0.8 which depends on the coating of the dynodes. From this, the total gain for a PMT with n stages is then:

$$G = \prod_{m=1}^{n} \delta_m \tag{7.4}$$

If the potential difference between every set of two consecutive dynodes are the same, namely E, then one can substitute Eq. 7.3 into Eq. 7.4 to get:

$$G = \left(aE^k\right)^n = a^n \left(\frac{V}{n+1}\right)^{kn} = AV^{kn} \tag{7.5}$$

$$A = \frac{a^n}{(n+1)^{kn}} \tag{7.6}$$

Here, a supply voltage of V is provided, which is equally divided amongst the dynodes. Thus, from Eq. 7.5 it is apparent that the gain of the PMT is proportional to V^{kn}. Fig. 7.4 shows the gain curve of the Hamamatsu R11065 3" PMT. Generally, PMTs are able to achieve a gain $> 10^6$, and this PMT can be operated at a gain $\sim 10^7$.

The gain curve of a PMT is achieved by observing the single photoelectron signal of the PMT at various voltages. The PMT is placed in a dark box, and a light source is pulsed at a dim enough level so that only a very small number

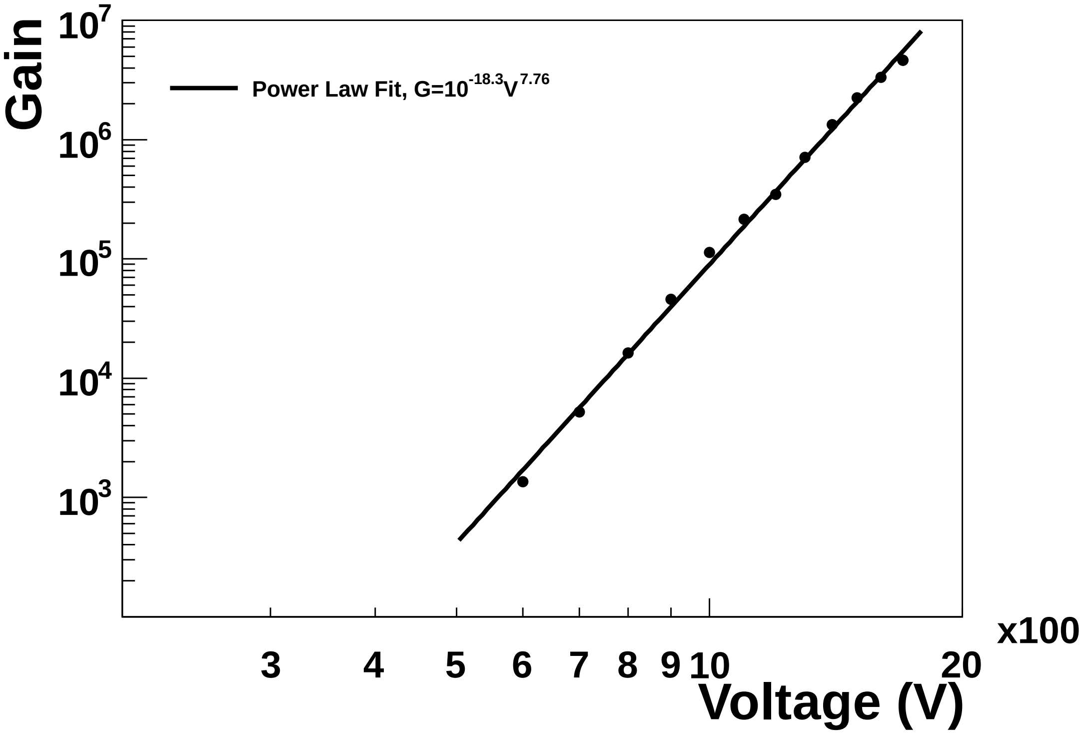

Figure 7.4: Gain curve of a Hamamatsu R11065 3" PMT with 12 dynode stages. The gain follows a power law dependence on the applied voltage and reaches a maximum of $\sim 10^7$.

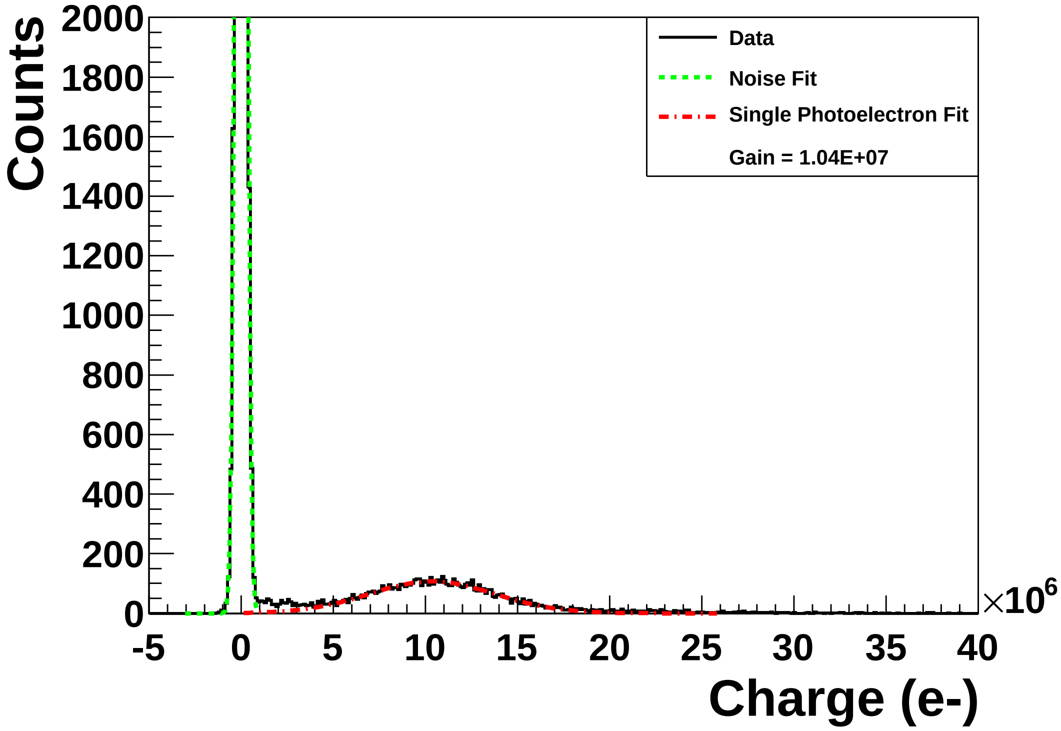

Figure 7.5: Single photoelectron spectrum of a Hamamatsu R11065 3" PMT. The noise pedestal is fit with the green Gaussian, while the single photoelectrons create the smaller, red Gaussian to the right. The PMT was operated at 1.7 kV for this spectrum.

of photoelectrons are observed, either zero, one, or two. At this point, since the number of photoelectrons is so low, the probability of observing n photoelectrons is given by Poisson statistics:

$$f(n, \lambda) = \frac{\lambda^n e^{-\lambda}}{n!} \tag{7.7}$$

where λ is the mean of the Poisson distribution, and $f(n, \lambda)$ gives the probability of observing n photoelectrons. If the light source is tuned such that 90% of the time no photoelectrons are observed, the mean of the distribution would be found by

$$f(0, \lambda) = 0.9 = e^{-\lambda} \tag{7.8}$$

$$\lambda = 0.105 \tag{7.9}$$

Then, the probability of observing one, two, or three photoelectrons would be:

$$f(1, 0.105) = \frac{0.105e^{-0.105}}{1!} = 0.09 \tag{7.10}$$

$$f(2, 0.105) = \frac{0.105^2 e^{-0.105}}{2!} = 0.005 \tag{7.11}$$

$$f(3, 0.105) = \frac{0.105^3 e^{-0.105}}{3!} = 0.0001 \tag{7.12}$$

This way, one can assure that 9% of the time, only one photoelectron is observed, and 1% of the time a higher number of photoelectrons are seen. Once the light is tuned to this level, the pulses from the PMT are integrated on an oscilloscope, and the total charge is placed in a histogram, as seen in Fig. 7.5. This histogram should have a noise pedestal corresponding to triggers with zero photoelectrons, and a smaller Gaussian from the single photoelectrons. The mean of this Gaussian curve is then the gain of the PMT.

7.1.4 Dark Counts

When using PMTs for the detection of small signals, it is important to consider the dark count rate of the PMT. The dark count rate is defined as the rate of single photoelectron pulses observed from the PMT when no light is present. The electrons within a photocathode have some thermal energy proportional to the temperature of the photocathode. It is possible that the thermal energy of an electron exceeds the work function of the photocathode. In such a case, the electron will be ejected from the photocathode. The electron then is accelerated to the first dynode and behaves just as a single photoelectron would. As the temperature of the photocathode is decreased, the thermal energy of the electrons also decreases. For this reason, it is less likely that these electrons have an energy above the work function, and thus the dark count rate decreases with decreasing temperature. The dark current due to thermal electron emission as a function of temperature is [139]:

$$I_{DC} = CT^{5/4}e^{-\frac{q_e\psi}{kT}} \tag{7.13}$$

Here, I_{DC} is the current from the thermally emitted electrons, C is a constant, T is the temperature, q_e is the charge of the electron, ψ is the work function of the photocathode, and k is the Boltzmann Constant.

7.1.5 Linearity

The linearity of a PMT is a measure of how the output current of the PMT behaves with a changing light source. Ideally, the PMT should be perfectly linear, that is, the output current of the PMT should be directly proportional to the incident light intensity. However, in real PMTs, the output current is only proportional to the incident light intensity up to a certain output current, above which the PMT becomes nonlinear. When considering the linearity of a PMT, it is important to distinguish between the photocathode linearity and the anode linearity.

7.1.5.1 Photocathode Linearity

The photocathode itself is susceptible to nonlinearity. As the light hitting the photocathode is increased, there will come a point where the ejected photoelectron current is no longer proportional to the input light intensity. The current at which this nonlinearity occurs is strongly dependent on the temperature of the photocathode. As the temperature of the photocathode is decreased, the resistivity of the photocathode itself begins to increase. Because of the higher resistivity, fewer electrons can be supplied to the photocathode in response to a bright light. For this reason, the photocathode will become nonlinear at smaller photocathode currents as the temperature is decreased. Generally, the photocathode linearity is not a concern for room temperature operation, however care must be taken when operating at low temperatures in order to avoid the nonlinear range of the photocathode. Fig. 7.6 shows a plot of the photocathode linearity of the Hamamatsu R11065 3" PMT.

7.1.5.2 Anode Linearity

A different effect governs the linearity of the anode current of a PMT. As the electrons travel from dynode to dynode, they are multiplied at every stage and a larger bunch of electrons develops. At the very last stage, the number of electrons in the bunch can become so large, while in such a small volume, that the electrons begin to repel each other. This is called the "space-charge" effect. Because of this space-charge effect, the physical size of the electron bunch begins to increase, and some of the electrons may miss the last dynode. Increasing the potential between

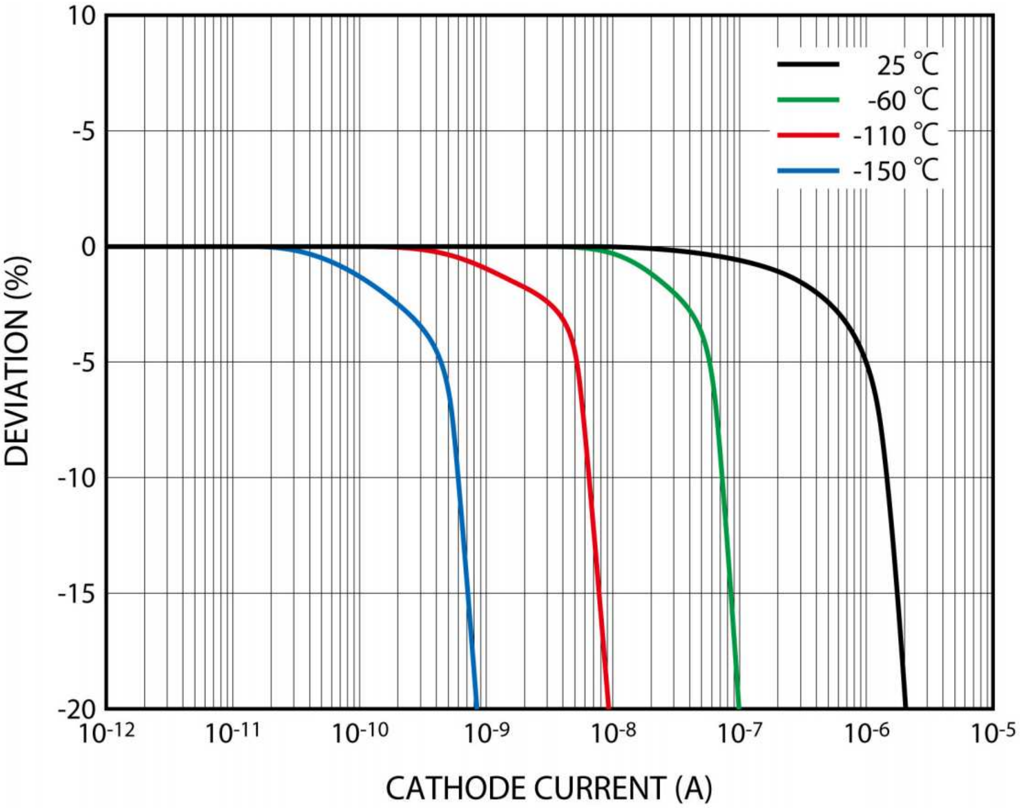

Figure 7.6: Photocathode linearity of a Hamamatsu R11065 3” PMT. A strong temperature dependence is seen in the saturation current. This data was taken at Hamamatsu.

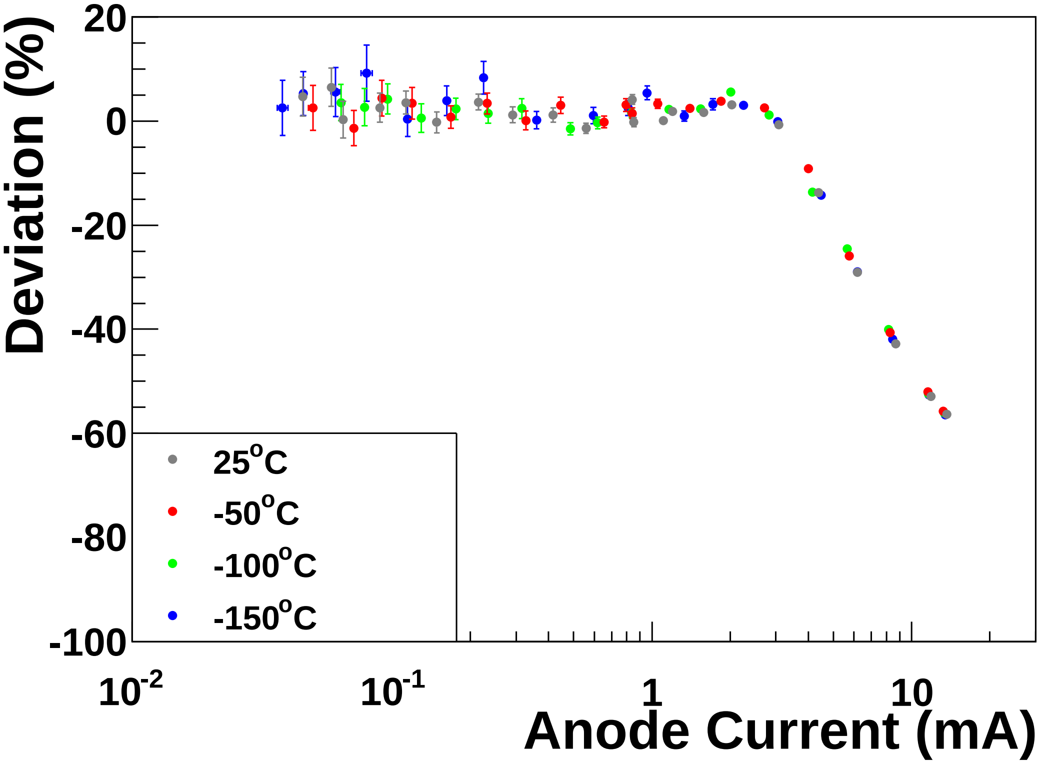

Figure 7.7: Anode linearity of a Hamamatsu R11065 3" PMT. The PMT was operated at a gain of 10^7, and saturation is observed around 2 mA anode current. No temperature dependence was observed in the anode linearity.

the dynodes in the last stages can help to increase the anode linearity range by providing a stronger electric field, while different dynode geometries can also be optimized for high linearity. Fig. 7.7 shows the anode linearity of the 3" R11065 PMT. Since the nonlinearity of the anode current is dominated by the space-charge effect, little temperature dependence is seen in the anode linearity curves.

7.1.6 Timing Properties

PMTs are often employed in experiments where timing of signals is critical. For this reason, it is important to understand the timing properties of the PMTs themselves. This depends on the finite time it takes for photoelectrons emitted from the photocathode to undergo the multiplication process and eventually reach the anode, which can be affected by the dynode structure of the PMT and the applied voltage. There are four main timing parameters measured for PMTs:

i) Rise Time: Defined as the time difference between 10% and 90% of the output pulse from the PMT.

ii) Fall Time: Similarly defined as the time difference between the 90% and 10% level.

iii) Pulse Width: The full width at half maximum (FWHM) of the pulse, that is, the time difference between the 50% level of the rising edge and the 50% level of the falling edge.

iv) Transit Time Spread: The FWHM of the spread of the transit time of the signal, which is defined as the time difference between the moment a photon strikes the photocathode and the time that the peak of the signal appears at the anode of the PMT.

These values were measured for the R11065 3" PMT and the R8520 1" PMT as shown in Tab. 7.1.

PMT	Rise Time	Fall Time	Pulse Width	Transit Time Spread
R11065	4.2 ± 1.1 ns	10.0 ± 1.0 ns	8.0 ± 0.6 ns	7.4 ± 0.5 ns
R8520	1.9 ± 0.2 ns	2.9 ± 0.2 ns	4.4 ± 0.1 ns	1.1 ± 0.1 ns

Table 7.1: Table of the timing parameters for the R11065 3” PMT and R8520 1” PMT.

7.2 Summary

Understanding and characterizing PMTs is an important first step in the design of a dark matter and double beta decay detector. The properties of the PMT must match the requirements for detection of these rare processes, including the gain, linearity, dark counts, and timing properties. Although many types of PMTs may be used successfully in dark matter detectors, a new photodetector called the QUartz Photon Intensifying Detector is showing promise of not only having lower radioactivity than all previous PMTs, but also being superior in all relevant properties.

CHAPTER 8

Characterization of the QUPID

Future generations of dark matter detectors must be larger and cleaner than previous generations to ensure a detection of WIMPs. The larger mass provides a greater amount of target material for the WIMPs to interact with, and materials with lower radioactivity must be used to ensure that the backgrounds in the experiments are minimized. The photodetectors used in the dark matter experiments are of particular importance; since they are placed directly adjacent to the target material, any radioactivity within the photodetectors proves to be a major background. A new photodetector concept called the QUartz Photon Intensifying Detector or QUPID has been developed jointly by UCLA and Hamamatsu Photonics in order to be used in future dark matter detectors. The QUPID proves to be an ideal replacement for conventional PMTs by offering several advantages over the photodetectors used in present dark matter experiments.

Similarly, liquid xenon TPCs searching for double beta decay require extremely low backgrounds originating from detector materials, due to the rarity of these processes. Along with the low radioactivity, PMTs used in double beta decay experiments require high linearity in order to observe signals up to several MeV. The QUPID can thus be effectively used as a replacement for conventional PMTs in double beta decay searches as well. This chapter includes detailed discussions of the test setups and methods used to measure the various parameters of the QUPIDs. I personally designed and built the liquid nitrogen cooldown system to be discussed in Sec. 8.6, and I was responsible for taking the gain, leakage current, timing, and dark count measurements. I also helped in the design and construction of the liquid xenon system, and was involved in the data taking for the scintillation measurements (Sec. 8.10). Other tests, such as the uniformity and anode linearity measurements, were performed by other members of the UCLA group while I provided help in the assembly and debugging of these systems. Finally, the quantum efficiency and photocathode linearity measurements were performed by Hamamatsu, while the screening of the radioactivity was done at the Gator test facility by the Zurich[1] group.

8.1 Photodetector Requirements

In order to improve the performance of the next generation experiments, the photodetectors must meet the following requirements:

- Intrinsic radioactivity significantly lower than the current generation PMTs. A majority of the background events in current generation experiments are due to the radioactivity of the PMTs since these devices are placed in close proximity to the target volume.
- Quantum efficiency $> 30\%$ to maximize the number of photoelectrons from a given energy deposit. Current generation PMTs have quantum efficiencies of $\sim$30%, and newer photodetectors should at least match this number.
- High gain $> 10^5$ so that single photoelectrons can be detected above the readout noise level.

---

[1] Physics Institute, University of Zürich, Winterthurerstrasse 190, CH-8057, Zürich, Switzerland

- Good timing performance with a pulse width < 10 ns, to provide accurate time information. This can be useful for pulse shape discrimination techniques.

- Good collection efficiency and uniformity along the photodetector surface. This ensures that no biases are introduced based on where a photon hits on the photodetector surface.

- A large dynamic range with superior linearity, for precise measurement of energy depositions in the regions of interest. Dark matter detectors observe events depositing low energies ($\lesssim 100$ keV), however it is important to observe a large energy range (up to several MeV) in order to properly understand the backgrounds of the experiment. Similarly, double beta decay experiments require a dynamic range up to $\sim$3 MeV.

- A low dark count rate in order to avoid any accidental coincidences that could be mistaken for WIMP interactions.

Since these experiments use liquid xenon or liquid argon, it is imperative that the photodetectors be able to operate at cryogenic temperatures. For this reason, many of the tests done on the QUPID were performed down to -100° C or lower. The following sections describe in detail the tests performed that prove the capability for the QUPID to satisfy the requirements stated above.

8.2 QUPID Concept

The QUPID is based on the Hybrid Avalanche Photodiode (HAPD) design. In HAPDs, photons hit a photocathode causing the emission of photoelectrons, which are then accelerated onto an Avalanche Photodiode (APD) due to a high

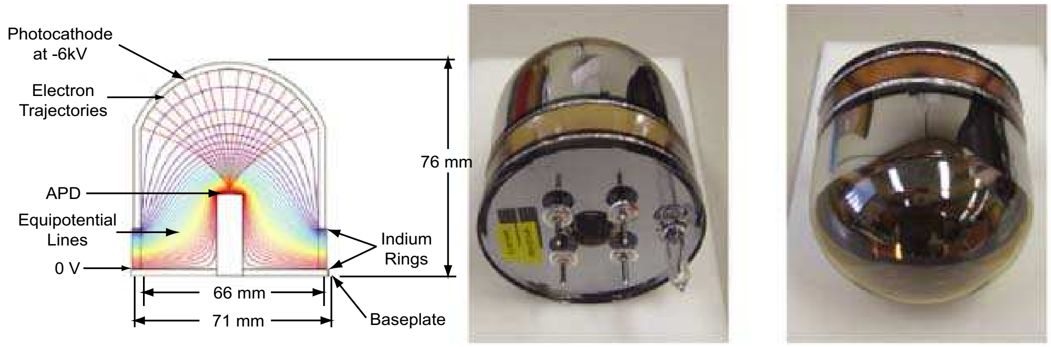

Figure 8.1: On the left is a drawing of the Qupid showing the electric field and the electron trajectory simulations. The photoelectrons are focused onto the APD due to the electric field within the Qupid. In the center and on the right are back and front views of the Qupid. Two indium rings, one used to provide -6 kV to the photocathode and the other for grounding, can be seen. The same rings bond the quartz cylinder, ring, and baseplate together.

potential difference (several kV) between the photocathode and the APD. The kinetic energy of the electrons creates hundreds of electron-hole pairs within the APD. The APD is reverse biased to several hundred volts, which creates an electric field within the APD. The electrons and holes created in the APD are separated and accelerated due to this electric field, and the accelerated electrons collide with other electrons creating further electron-hole pairs, thereby undergoing an avalanche effect [140, 141, 142].

The Qupid is made of a cylindrical quartz tube with a hemispherical photocathode window, a baseplate, and an intermediate quartz ring. The quartz cylinder, ring, and baseplate are bonded together using indium (see Fig. 8.1 center and right). The outer diameter of the cylinder is 71 mm, with the hemispherical photocathode window having a radius of 37 mm. The photocathode has an effective diameter of 64 mm (for vertical incident photons). The inner

Figure 8.2: A comparison between a Hamamatsu R8520 1" PMT (left), a Hamamatsu R11065 3" PMT (center) and the Qupid (right). The R8520 is currently being used in the XENON100 detector, while the R11065 and Qupid are candidates for future dark matter detectors.

part of the cylinder is coated with aluminum and the hemispherical cap is coated with a photocathode material. The baseplate on the opposite end supports a solid cylindrical quartz pillar with a 3 mm silicon APD at the top. The APD (with a capacitance of 11 pF) has been specifically developed and manufactured by Hamamatsu Photonics for use in the QUPIDs.

On the left of Fig. 8.1, a drawing of the QUPID is presented, showing a simulation of the electric field equipotential lines and of the photoelectron trajectories from the photocathode onto the APD. Fig. 8.1 center shows the QUPID seen from the baseplate, and on the right from the hemispherical photocathode. Fig. 8.2 shows a comparison between the QUPID and two conventional PMTs, the Hamamatsu R8520 1" PMT used in XENON100 and the Hamamatsu R11065 3" PMT, which is being considered for future dark matter detectors.

A negative high voltage, up to -6 kV, is applied to the photocathode of the QUPID through the indium sealing ring, while ground level is maintained on the baseplate and APD from the second indium ring. As in conventional HAPDs, the high potential difference creates an electric field which focuses the photoelectrons ejected from the photocathode onto the APD. The QUPID design has been optimized such that the photoelectron focusing is independent of the voltage applied to the photocathode. The baseplate of the QUPID has four pins, two of which are for the APD anode and cathode, while the other two are used during production for activating an internal getter. Finally, a quartz tube on the baseplate is used for pulling a vacuum during assembly of the QUPID and for evaporating the photocathode material onto the inner surface of the hemispherical cap.

Figure 8.3: A comparison between old versions of the Qupid and the current version. Note that the new version (top-right) has an intermediate quartz ring and a small quartz pipe, while the old versions do not.

8.3 Evolution of the QUPID

The design of the QUPID has gone through several different iterations. The original design did not have an intermediate quartz ring. The upper hemisphere and cylindrical body were made as one piece and fused directly onto the baseplate using indium (see Fig. 8.3) which was then used for supplying the photocathode voltage. This design was not satisfactory because sparking would occur within the QUPID if the photocathode voltage was placed above -4 kV. The addition of the intermediate quartz ring allowed for the photocathode voltage to be ramped up to -6 kV without any sparking.

For the first set of QUPIDs, a vacuum transfer system was used for production. In this system, the various parts of the QUPID were placed in a vacuum chamber. The photocathode was evaporated onto the hemisphere, and only afterwards the hemisphere and baseplate were brought together and fused, while still within the vacuum. This process was both costly and time intensive and could not have been used for the mass production of QUPIDs. In order to decrease the production time and costs, a system was designed at Hamamatsu that followed the production line of conventional PMTs. In this mass production system, the separate parts of the QUPID were assembled in ordinary conditions, and afterwards a vacuum was pulled through the small quartz tube at the base. After pulling a vacuum, the photocathode was evaporated onto the window of the QUPID, and the quartz tube was sealed.

Although this method greatly simplified the production of the QUPIDs, it added an unforeseen problem. Since the photocathode was evaporated within the QUPID after the entire structure was assembled, some of the photocathode material was deposited onto the APD itself. This caused unstable behavior of the APD after a short period of operation. In order to overcome this prob-

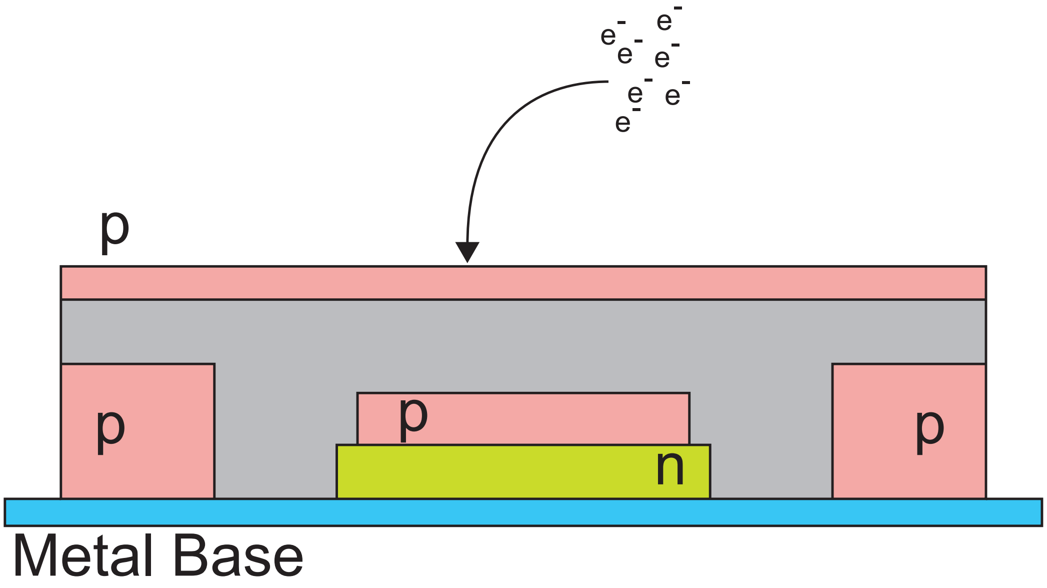

Figure 8.4: A drawing of the back-illuminated APD used in the QUPID, outlining the n-type and p-type regions of the APD [143].

lem, Hamamatsu changed the configuration of the APD to be back-illuminated, as the original design included a front-illuminated APD. Fig. 8.4 shows a layout of the back-illuminated APD. In the case of a back-illuminated APD, the photoelectrons strike the surface of the APD with p-type material, whereas the front-illuminated version has the photoelectrons bombarding the n-type material (a back-illuminated APD is merely a front-illuminated APD flipped over). The new back-illuminated APD used in this version of the QUPID was a 5 mm APD, whereas the initial front-illuminated APD was only 3 mm. The larger APD had a greater capacitance, and therefore the rise time, fall time, and pulse width of the signals increased.

The latest version of the QUPID uses a 3 mm, back-illuminated APD. The QUPID is produced using the production line method, similar to conventional

PMTs, and includes the intermediate quartz ring. This is still not the final, mass-production version of the QUPID, as more changes are to be expected (this will be explained in further detail in Sec. 8.7.1, 8.7.2, and 8.9).

8.4 Radioactivity

One of the main motivations for the QUPID is the fact that the synthetic fused silica (quartz) used in a majority of the QUPID has low radioactive contaminants. Aside from the quartz, the only other materials used in the production are indium for the sealing rings, Kovar pins, and a small silicon APD in the center of the QUPID. Fig. 8.5 shows the contributions to the γ-ray background in XENON100 from various detector materials, highlighting the need for low radioactivity photodetectors.

The radioactivity of the QUPIDs has been measured in the Gator screening facility, operated by the University of Zurich at LNGS. A diagram of Gator is shown in Fig. 8.6. The facility consists of a high-purity, p-type coaxial germanium (HPGe) detector with a 2.2 kg sensitive mass, operated in an ultra-low background shield continuously flushed with boil-off nitrogen gas to suppress radon diffusion. With an integral background rate of 0.16 events/min in the $100 - 2700$ keV region, Gator is one of the world's most sensitive Ge spectrometers [144].

Two batches of five QUPIDs were tested at the Gator facility. To determine the specific activities for the ^{238}U and ^{232}Th chains, as well as for ^{60}Co and ^{40}K, the most prominent γ-lines of the respective decays are analyzed using the efficiencies determined by a detailed Monte Carlo simulation of the detector, shield, and QUPID samples. The latest background run of Gator had been taken

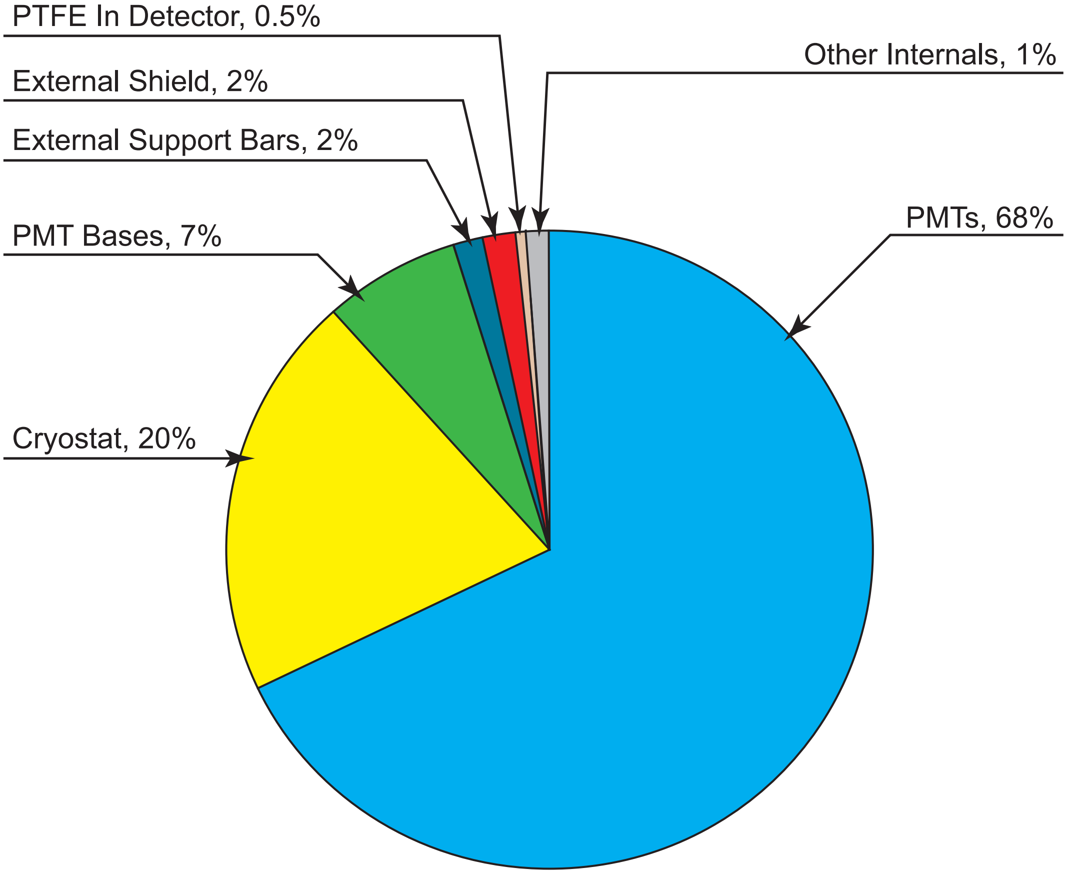

Figure 8.5: A plot of the contributions to the γ-ray background of the XENON100 experiment due to internal and external sources. A majority of the background comes from the PMTs and their bases, as seen in the light blue and green sections of the pie chart [125].

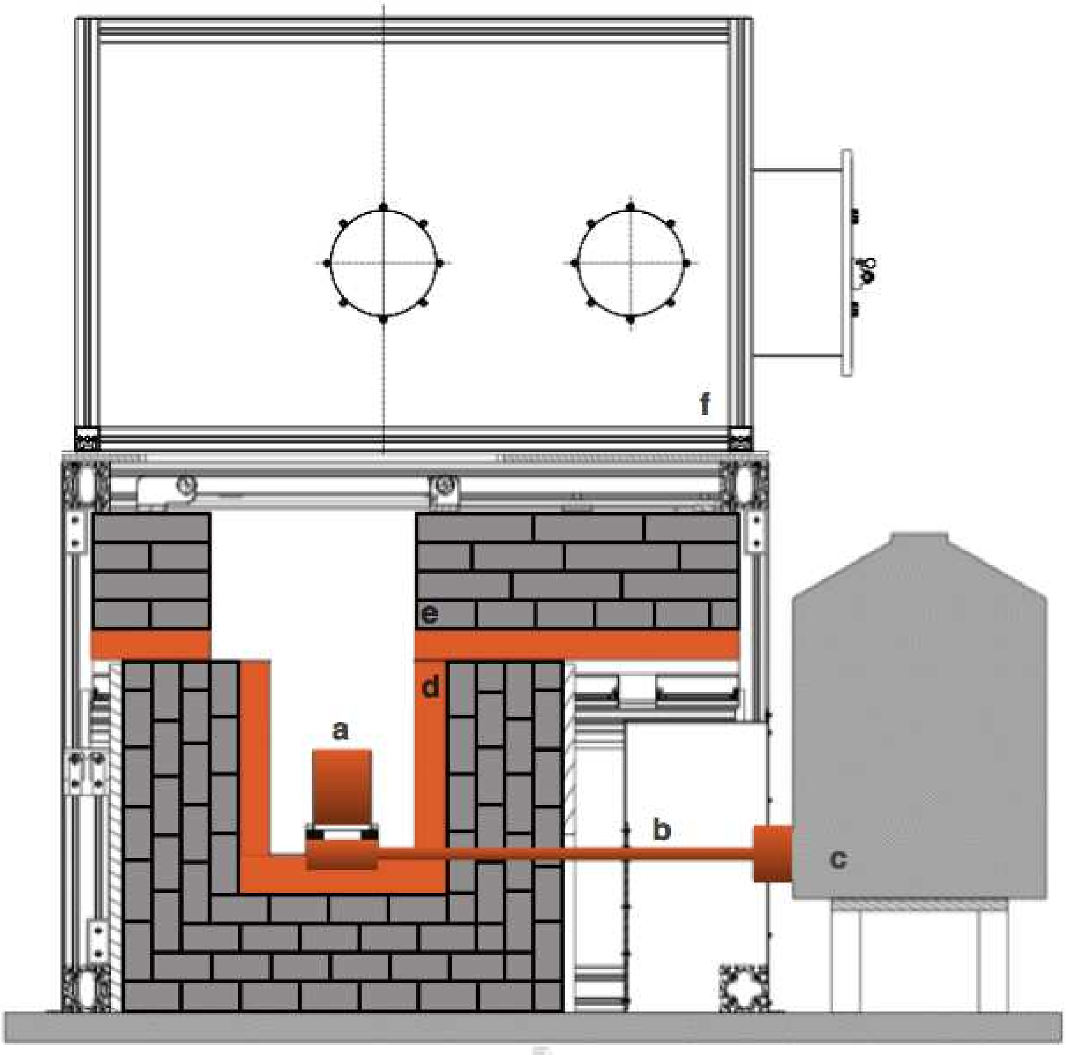

Figure 8.6: A diagram of the Gator screening facility, located at LNGS. Gator consists of a HPGe detector (a) cooled by a cold finger (b) using a dewar of liquid nitrogen (c). The sample is placed on the HPGe detector, and is shielded by copper (d) and lead (e) with a sliding door. The entire detector is operated in a glove box (f) that is continually flushed with boil-off nitrogen gas [144].

for a duration of two months prior to the QUPID screening. In the case in which no events were detected above the background, upper limits on the specific activities were calculated according to the method proposed in Ref. [145].

Contaminant	Activity (mBq/QUPID)	Events/year in Fiducial Cut, Target Mass (after fiducial cut), Energy $[2-18]$ keV$_{ee}$		
		0 cm, 2.3 ton	5 cm, 1.6 ton	10 cm, 1.1 ton
^{238}U	< 17.3	< 560	< 0.5	0
^{226}Ra	0.3 ± 0.1	23	0.14	0.01
^{232}Th	0.4 ± 0.2	35	0.24	0.02
^{40}K	5.5 ± 0.6	55	0.32	0.02
^{60}Co	< 0.18	< 4.9	< 0.21	< 0.02
Total	< 23.7	< 678	< 1.41	< 0.07

Table 8.1: First column: Contaminants present in the QUPID divided into the active chains. Second column: Measured intrinsic radioactivity of the QUPIDs. Remaining columns: Radioactive background from the QUPID in a ton-scale detector for different fiducial volume cuts in the $2-18$ keV$_{ee}$ energy range. The relatively high contamination arising from ^{238}U, of about 17 mBq/QUPID, does not affect the region of interest as γ-rays from this chain do not penetrate deeply inside the liquid xenon. It can be easily cut out, down to zero events per year, by increasing the fiducial cut to 10 cm from each side.

The radioactivities for each QUPID are < 17.3 mBq/QUPID for ^{238}U, 0.3 ± 0.1 mBq/QUPID for ^{226}Ra, 0.3 ± 0.1 mBq/QUPID for ^{232}Th, 0.4 ± 0.2 mBq/QUPID for ^{40}K and < 0.18 mBq/QUPID for ^{60}Co. Although ^{226}Ra belongs to the ^{238}U chain with a half-life of 1600 years, it bonds easily with electronegative elements and can be absorbed in strong thermal and/or chemical processes, generating a break in the equilibrium of the chain. In order to account for the possibility of a break in equilibrium, the two parts of the chain (i.e. ^{238}U and ^{226}Ra) have been treated separately in the analysis. These results are reported in the first column of Tab. 8.1, while Tab. 8.2 shows the radioactivity levels of standard PMTs used in current dark matter detectors and considered for future experiments [122].

Photodetector	Effective Area	Contamination (mBq/cm^2)				
		^{238}U	^{226}Ra	^{232}Th	^{40}K	^{60}Co
R8520	6.5 cm^2	< 1.0	0.039 ± 0.006	0.077 ± 0.015	1.2 ± 0.1	0.12 ± 0.01
R11410-MOD	32 cm^2	< 3.0	< 0.12	< 0.081	0.41 ± 0.13	0.11 ± 0.02
QUPID	32 cm^2	< 0.541	0.010 ± 0.004	0.012 ± 0.006	0.17 ± 0.02	< 0.0056

Table 8.2: Comparison of the radioactivity levels of various photomultiplier tubes used in current dark matter detectors, and being considered for future detectors [122].

To verify whether the electronic recoil background originating from the QUPIDs match the requirements of future detectors, a preliminary design of a ton-scale liquid xenon detector has been studied using the `Geant4` Monte Carlo software package. A diagram of the detector geometry used for the simulation is shown in Fig. 8.7. The simulation considers:

i) A liquid xenon TPC, with a diameter of 1 m and a height of 1 m (corresponding to a total mass of 2.3 ton)

ii) Two arrays of 121 QUPIDs each placed at the top and bottom of the TPC

iii) All the main detector materials, including the cryostat and PTFE support structure

To estimate the background level arising from the QUPIDs, the radioactive contamination from the Gator data was implemented in the code.

The simulation used the standard analysis cuts implemented by the XENON collaboration [129, 146], with a conservative assumption of 99% rejection power on the electronic recoil background from the $\log_{10}$(S2/S1) cut. The study has

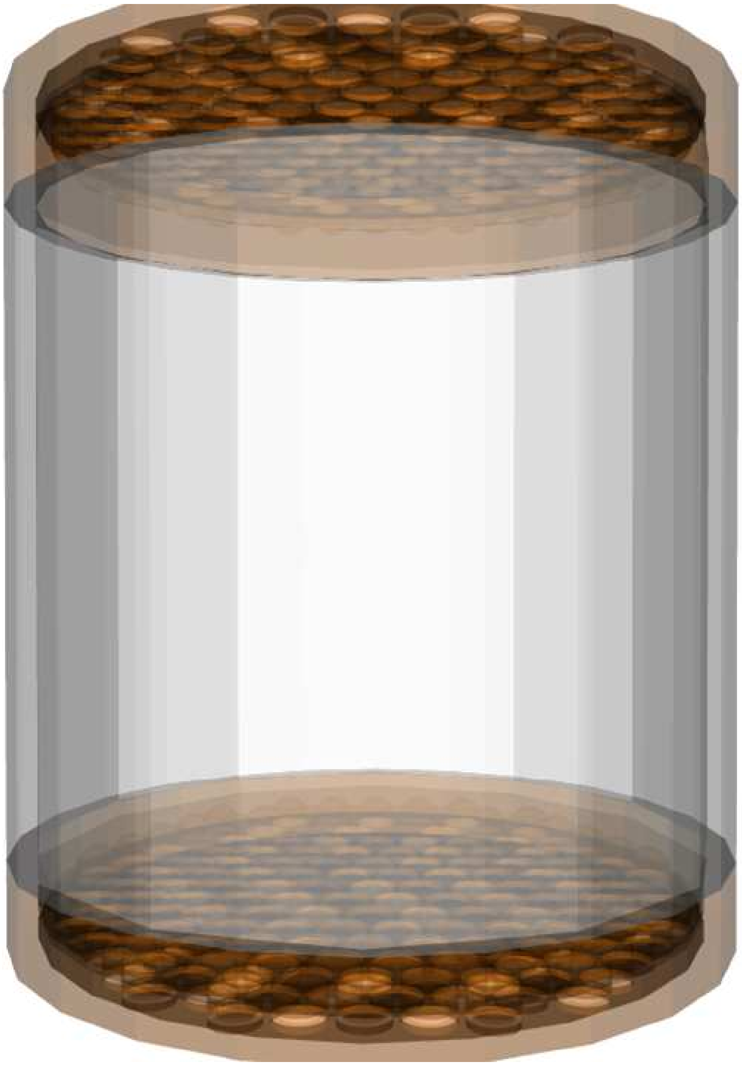

Figure 8.7: A diagram of the detector geometry used in the Monte Carlo simulations for a 1 ton detector. The geometry includes the QUPIDs, along with detector materials and support structures.

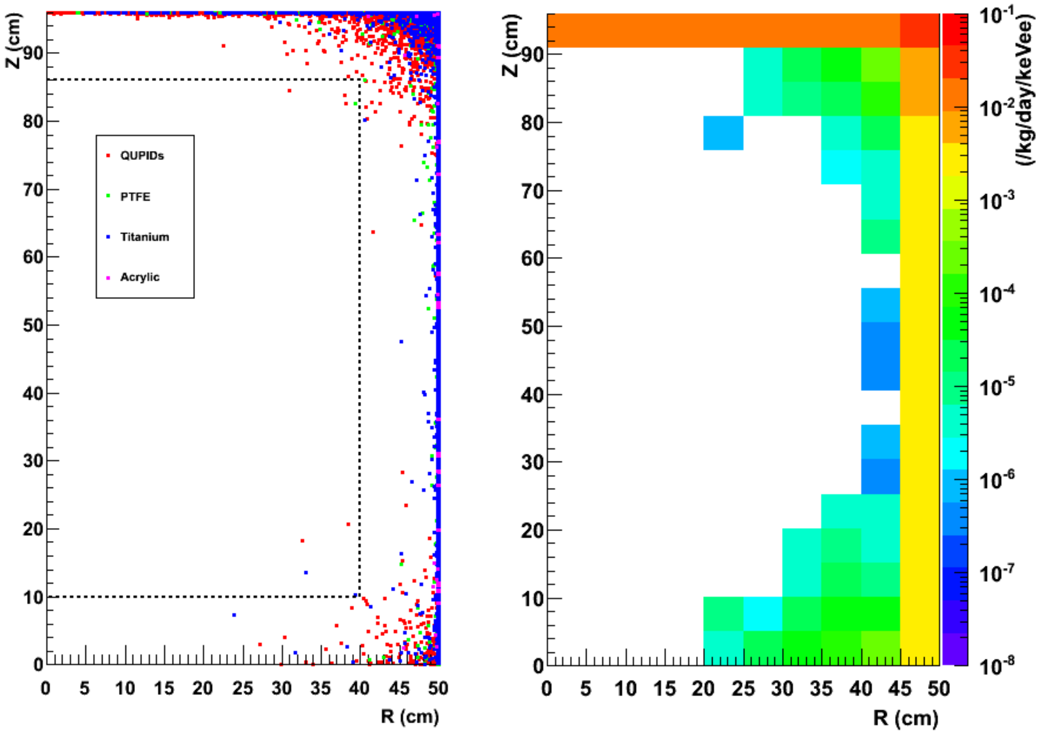

Figure 8.8: On the left, a scatter plot of the electronic recoil background events in the $2 - 18$ keV$_{ee}$ energy range in a 1 ton xenon detector from various detector materials. On the right, a 2D plot of the background rates in the same detector. These plots do not include the $\log_{10}$(S2/S1) rejection. Of particular importance is the simulated contribution from the QUPIDs, which appears as red dots in the plot on the left.

been repeated for different fiducial volumes, that is, cutting the top, bottom and sides of the liquid xenon and considering only the inner cylindrical volume as the target material and region of interest for any energy deposit. In Tab. 8.1 the results of the Monte Carlo simulation for fiducial volume cuts of 0, 5, and 10 cm are presented, along with the results of the screening for each chain. The indium used in the construction of the QUPIDs is known to undergo β-decay, and this radioactivity was also included in the Monte Carlo simulation. Due to the short attenuation length of β-particles in liquid xenon, no energy deposits were observed in the inner volumes of the target.

In a 1 m × 1 m liquid xenon detector with 10 cm fiducial volume cuts (corresponding to a target mass of 1.1 ton) 242 QUPIDs would give a total γ-ray background rate < 0.07 events/year, in the energy range between 2 and 18 keV$_{ee}$. The outcome of the simulation without the $\log_{10}$(S2/S1) cut can be seen in Fig. 8.8. This result, unachievable using the standard PMTs, would perfectly satisfy the requirements of the next generation dark matter experiments [147, 148].

8.5 Photocathode

8.5.1 Quantum Efficiency

The energy deposits expected from WIMP interactions in the target material of dark matter detectors is on the order of tens of keV. For this reason, it is important to detect as many of the photons as possible. Maximizing the number of detected photons also improves the energy resolution of the detector, which is a vital parameter for neutrinoless double beta decay searches. A high quantum efficiency assures that a maximum number of photons are detected by the photodetectors. The photocathode used in the QUPID has been specifically de-

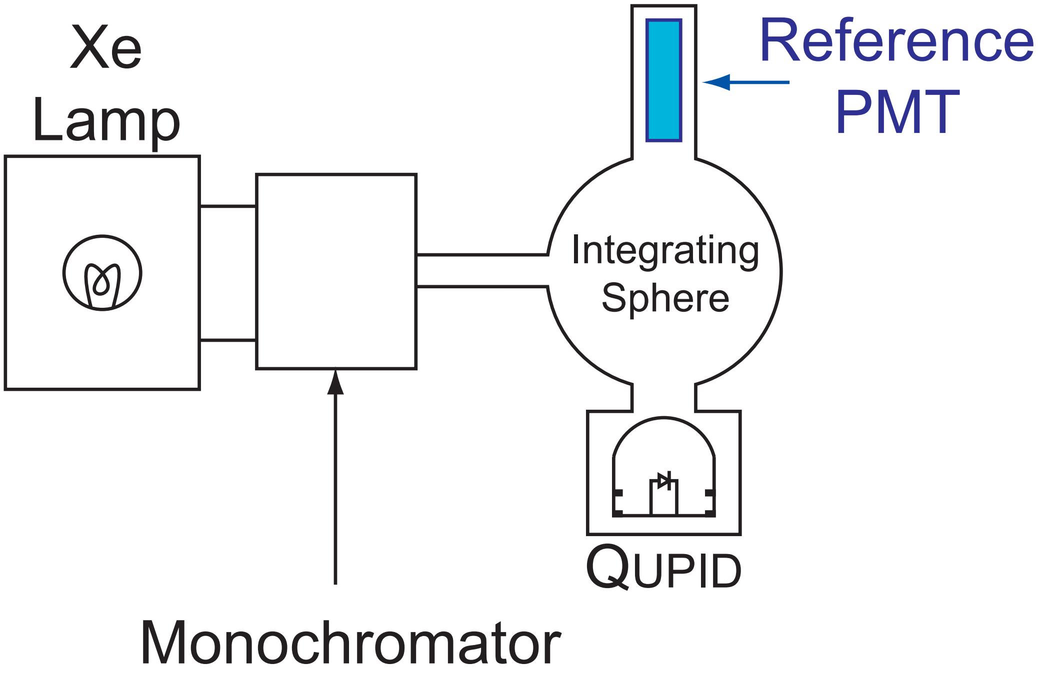

Figure 8.9: A drawing of the system used to check the quantum efficiency of the QUPID. Light from a xenon lamp is passed through a monochromator and to an integrating sphere. The integrating sphere ensures that equal light reaches the QUPID and a reference PMT with a known quantum efficiency. The response, as characterized by the photocathode current read out by a picoammeter, was compared between the QUPID and the reference PMT. Finally, the monochromator scans various wavelengths to check the quantum efficiency at all necessary wavelengths.

veloped [149] by Hamamatsu Photonics to achieve the highest quantum efficiency for 178 nm photons, corresponding to the xenon scintillation light.

The quantum efficiency has been measured at room temperature by comparing the response of the QUPID to a standard PMT, calibrated by means of a NIST standard UV sensitive photodiode [139]. Fig. 8.9 shows a diagram of the quantum efficiency test setup, while Fig. 8.10 shows the quantum efficiency measurements for different QUPIDs measured at Hamamatsu. All of the tested QUPIDs show a maximum quantum efficiency $> 30\%$ around 178 nm. The quantum efficiency shows a sharp cutoff below 170 nm because the quartz window of the QUPID is opaque to light of such short wavelengths.

Since the QUPIDs may be used in future liquid argon detectors, the quantum efficiency must be matched to the wavelengths expected in such detectors. The wavelength of argon scintillation light is 128 nm, and since this value is below the cutoff wavelength of the quartz window of the QUPID, a wavelength shifter must be used in liquid argon dark matter detectors. A possible wavelength shifter being considered is Tetraphenyl Butadiene (TPB). The wavelength shifter would be coated onto the walls of the TPC, or onto a quartz or acrylic plate in front of the photodetectors. The scintillation light from the argon will then be absorbed by the TPB, and re-emitted at visible wavelengths, which can be detected by the QUPIDs. A photocathode version optimized for operation in liquid argon is under development. A comparison of the quantum efficiencies of the standard xenon operation QUPID and a preliminary argon operation QUPID is shown in Fig. 8.11. The quantum efficiency for the argon version has the highest value around the wavelengths of visible light.

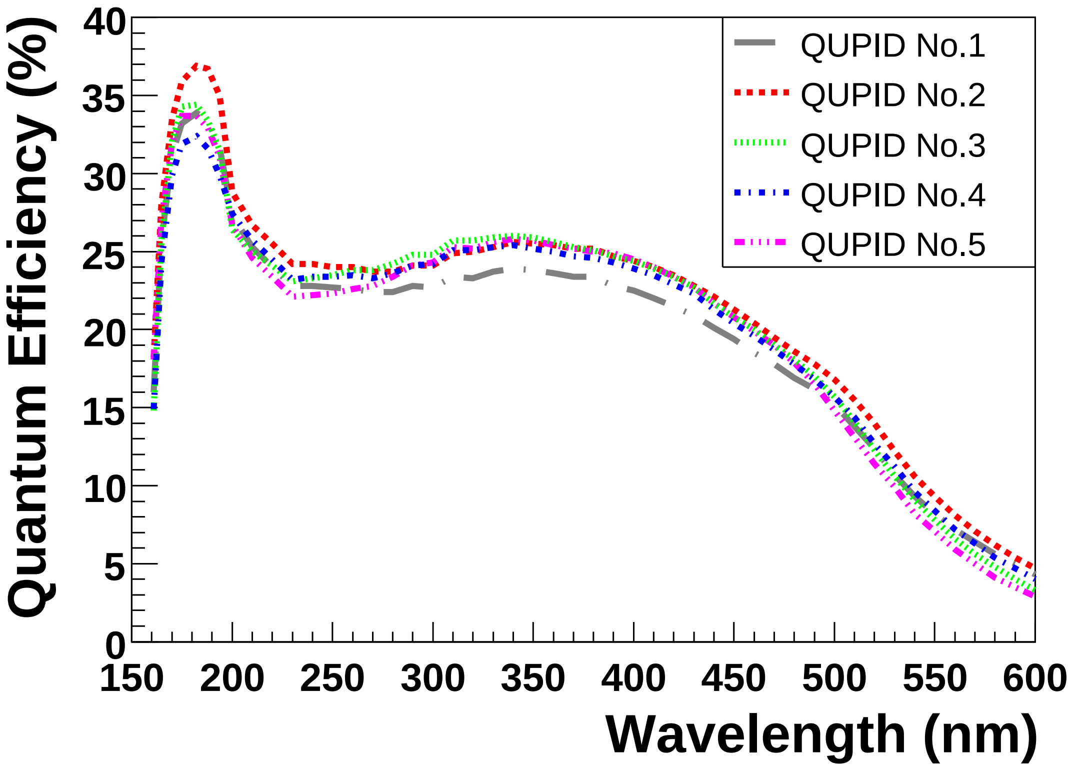

Figure 8.10: Quantum efficiency measured for various QUPIDs, optimized for liquid xenon operation, with the maximum value at 178 nm being $34 \pm 2\%$. The numbering of the QUPIDs are arbitrary and do not follow the production numbers.

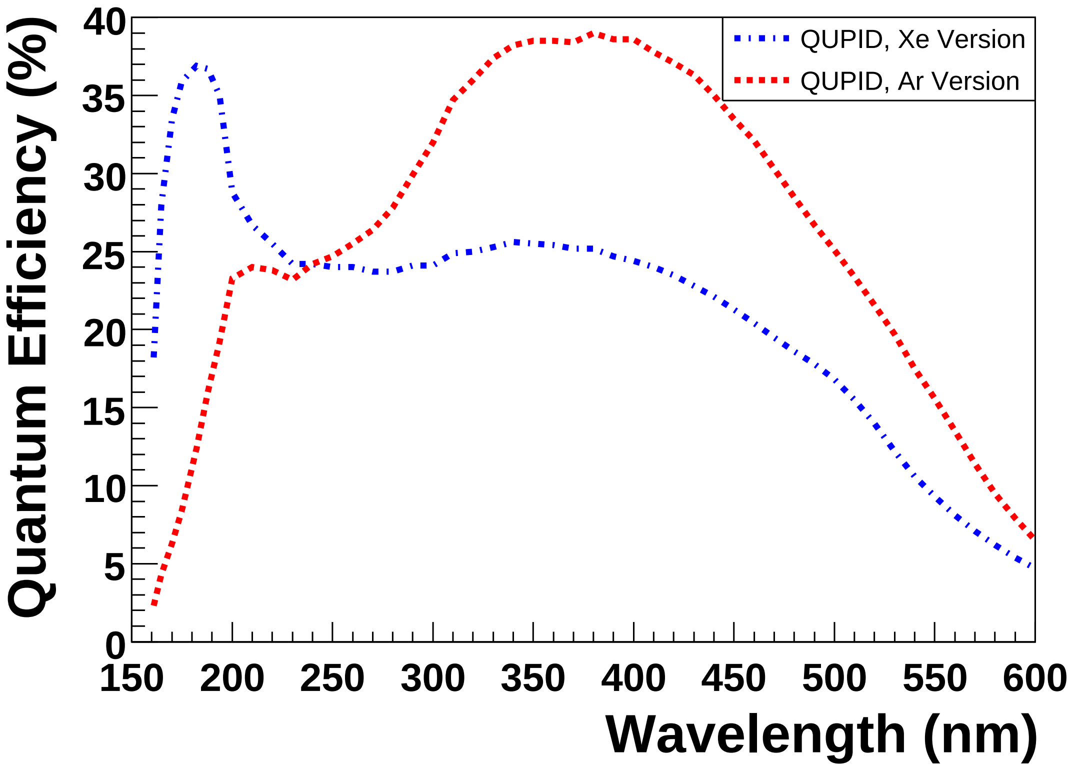

Figure 8.11: Quantum efficiency comparison between the xenon and argon versions of the QUPID. Both have a maximum quantum efficiency of > 35%, with the xenon version peaking at ∼180 nm and the argon version peaking at ∼370 nm.

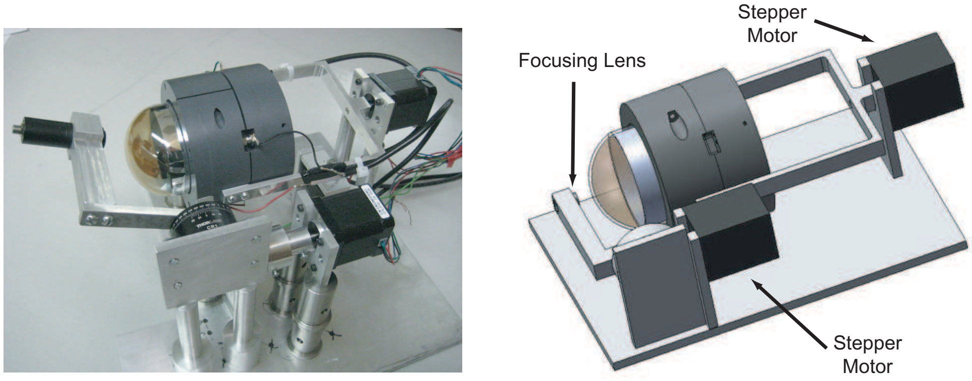

Figure 8.12: On the left, a photograph of the Qupid setup for uniformity measurements. On the right, its 3D rendering. In this system, the Qupid is rotated along the ϕ axis, and the light from the LED scans along the θ axis.

8.5.2 Uniformity

The uniformity of the Qupid photocathode is also an important parameter to measure. Photons from scintillation light can strike anywhere on the surface of the Qupid, and a non-uniform photocathode deposition can create systematic uncertainties in the energy and position reconstruction of events in the TPC. The uniformity of the photocathode was measured at room temperature. Light from a 405 nm LED[2] was brought to the Qupid through an optical fiber and focused onto the photocathode. The light was then scanned over the entire surface of the photocathode. The LED provided a spot of 1 mm focused on the spherical surface of the Qupid, while two stepper motors controlled independently:

i) the location of the focused light along the θ axis (i.e. moving from the top of the photocathode towards the indium rings, in steps of 1°)

ii) the position of the Qupid along the ϕ axis (i.e. moving the Qupid around

---

[2] Thorlabs Model LED405E 405 nm LED

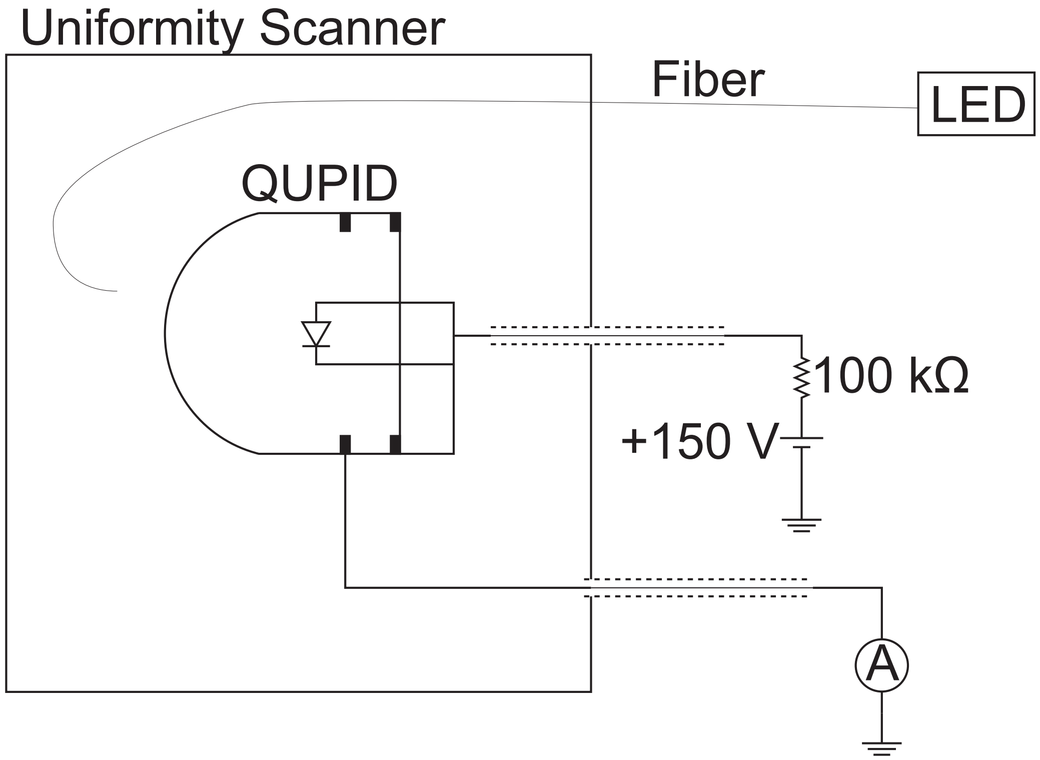

Figure 8.13: A schematic of the readout system used for the photocathode uniformity measurements. +150 V was applied to the grounding ring, APD anode, and APD cathode, and the photocathode current was read out through a picoammeter.

its main rotation axis, in steps of 10°)

A photograph and a drawing of the setup are shown on the left and right of Fig. 8.12 respectively.

The uniformity was tested by measuring the current from the photocathode by means of a picoammeter while applying +150 V to the grounding ring and to both the anode and the cathode of the APD shorted together. This maintains an electric field that attracts the photoelectrons ejected from the photocathode. A schematic drawing of the readout for the photocathode uniformity is shown in

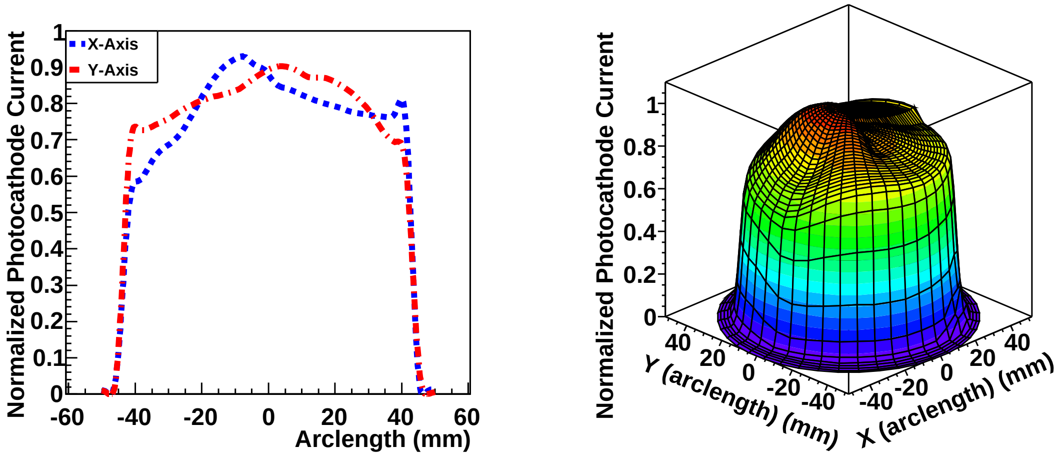

Figure 8.14: Photocathode uniformity results for QUPID No. 7 showing X and Y slices (on the left), and a 3D plot (on the right). The QUPID is uniform to ∼80% across the entire face.

Fig. 8.13, and the results of the scan are shown in Fig. 8.14. The photocathode is uniform to about 80% across the entire face.

8.5.3 Photocathode Linearity

The Low Temperature Bialkali photocathode (Bialkali-LT) developed by Hamamatsu Photonics and employed in the QUPIDs is optimized for linearity over a wide dynamic range at low operating temperatures [149]. Common photocathodes become nonlinear at lower temperatures because the resistivity increases as the temperature is lowered.

For neutrinoless double beta decay in ^{136}Xe, the expected energy deposited is 2.458 MeV and the largest signals come from the S2s. While S1 signals have a light yield of 3 pe/keV$_{ee}$, corresponding to about 7,400 photoelectrons, the S2

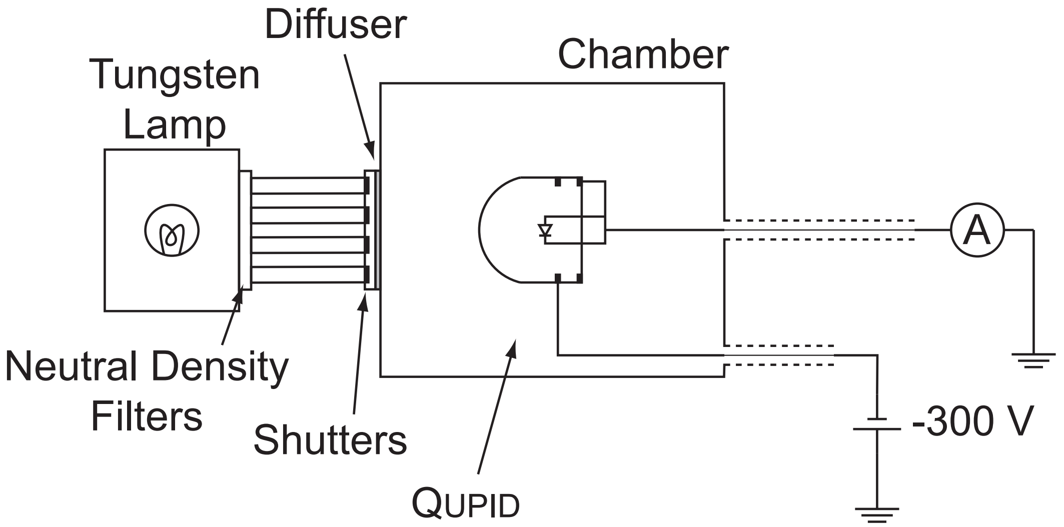

Figure 8.15: Photocathode linearity system. A tungsten lamp, neutral density filter wheel, and diffuser, along with four shutters, control the illumination of the photocathode of the Qupid. The photocathode is supplied with -300 V while the APD and the grounding ring are read out by a picoammeter.

signals have 200 times the number of photoelectrons spread out over 2 μs. The S2 signal is distributed over several photodetectors, and at most 10% of the signal can be expected on a single Qupid. This results in a maximum photocathode current of about 12 nA. The photocathode response of the Qupid must then be linear up to at least this current so that it may be used for neutrinoless double beta decay searches.

The linearity of the photocathode of the Qupid was tested at Hamamatsu Photonics. To test the linearity of the photocathode, light from a tungsten lamp was passed through a neutral density filter wheel to a light guide. A set of four shutters and a diffuser were coupled to the end of the light guide, and the light illuminated the Qupid. The photocathode was supplied with a potential of -300 V and the APD (both the anode and the cathode) and the grounding ring

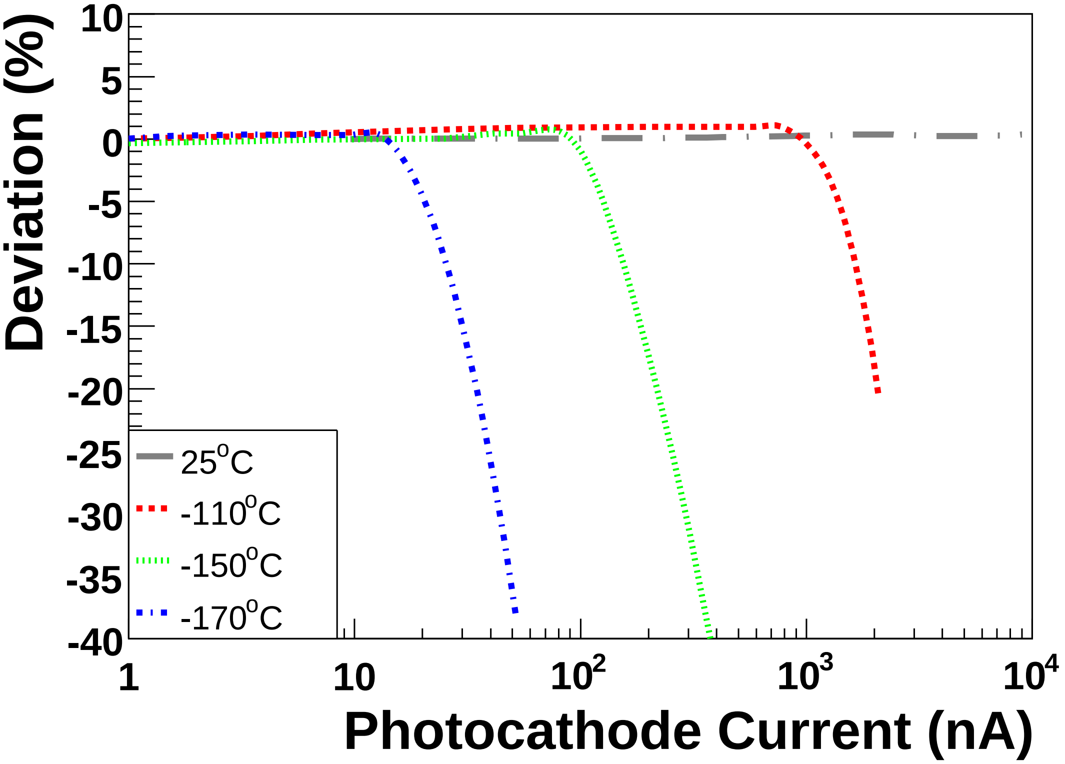

Figure 8.16: Photocathode linearity versus current at various temperatures of QUPID No. 3. The photocathode deviates from linearity at lower currents for lower temperatures due to the increased resistance of the photocathode. At liquid xenon temperature, saturation occurs above 1 μA, far exceeding the requirement of 12 nA.

were connected to a picoammeter. Fig. 8.15 shows a diagram of the testing system used for the photocathode linearity. The -300 V applied to the photocathode maintains the electric field within the QUPID, and the resulting photoelectron current is read through the picoammeter as the photoelectrons are accelerated to either the APD or the ground plane.

Each of the shutters were opened individually while keeping all the others closed, and the corresponding photocathode current was read out with the picoammeter (I_i, where $i = 1, 2, 3, 4$). The current with all the shutters opened was measured (I_{all}) as well. The same procedure was repeated with different light intensities by varying the position of the neutral density filter wheel, thereby increasing/decreasing the photocathode current in response to the changing light intensity. In such a configuration, the deviation from linearity can be defined as

$$\Delta Lin = \frac{I_{all} - \sum_{i=1}^{4} I_i}{\sum_{i=1}^{4} I_i} \tag{8.1}$$

which in the ideal case of perfect linearity must be equal to zero for all the filter configurations (as the sum of all photocathode currents with only one shutter open should be equal to the current with all the shutters open).

Fig. 8.16 shows ΔLin versus the photocathode current for different temperatures. At -110° C the linearity is well maintained up to 1 μA. This value largely overcomes the 12 nA dynamic range required for neutrinoless double beta decay detection in liquid xenon.

8.6 Cooldown System

The QUPIDs will mainly be used in noble liquid detectors. For this reason, most of the tests performed on the QUPID must be done at cryogenic temperatures. Fig. 8.17 shows a picture and a drawing of the cryogenic system used for per-

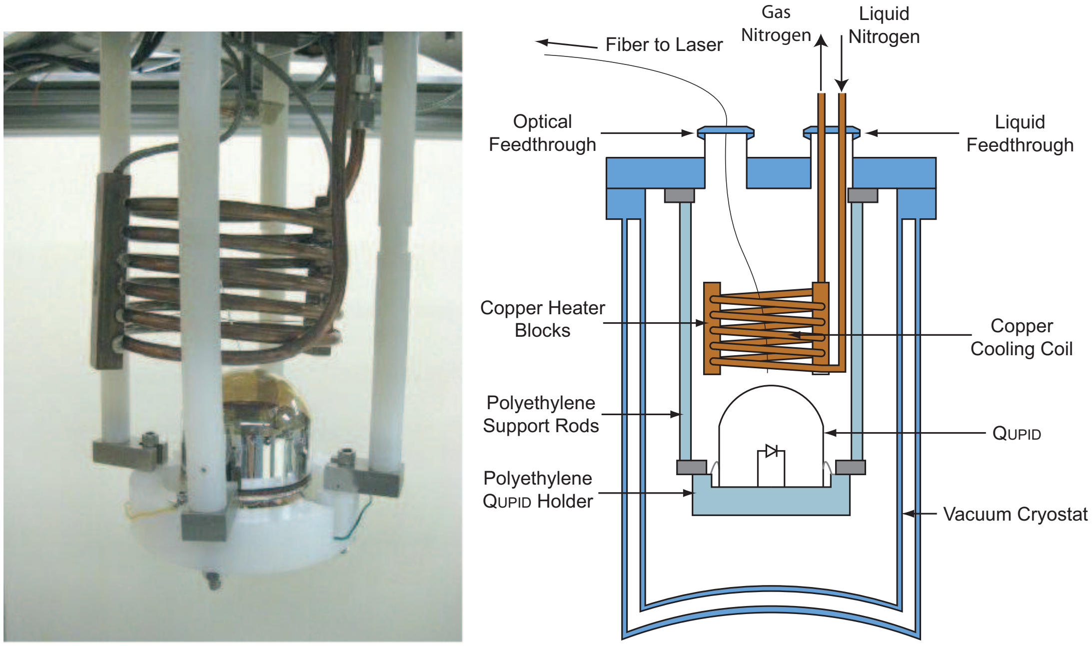

Figure 8.17: On the left is a photograph of the liquid nitrogen cooling system and the QUPID support. On the right, a diagram of the nitrogen cooling system and the QUPID support with labels on the key components of the system.

forming tests on the QUPID at low temperatures.

In the low temperature system, the QUPID is held in a polyethylene support structure suspended from the top flange of a vacuum insulated cryostat by four polyethylene rods. A set of four stainless steel clips hold the QUPID to the polyethylene support and also provide connections for the photocathode voltage and the grounding ring. High voltage and coaxial feedthroughs on the cryostat are used to provide the photocathode voltage, bias voltage and readout. All of the readout electronics, along with the power supplies for operation of the QUPID are placed outside of the cryostat. An optical fiber feedthrough is placed on the cryostat, and a fiber is pointed towards the QUPID. This allows for light from a laser or LED to be shined at the QUPID for various tests without exposing the light source to low temperatures.

After positioning the QUPID in the cryostat, a vacuum is pumped using an oil free pumping station[3] and dry nitrogen gas is introduced. Liquid nitrogen is then flowed through a copper coil at a constant rate to cool the surrounding nitrogen gas, thereby cooling the QUPID. Two 100 W resistive heaters inserted into copper bars (soldered onto the copper coil) serve as temperature stabilizers, controlled by a Proportional-Integral-Derivative (PID) controller[4] and monitored by Resistance Temperature Detectors (RTDs). Near -100° C the temperature can be maintained within ±0.1° C of the setpoint temperature.

---

[3] The station (Pfieffer Vacuum Hi-Cube Eco-3 Pumping Station) consists of a diaphragm pump and a turbomolecular pump.

[4] Omega Model CN8201 Temperature Controller

8.7 Anode

8.7.1 Leakage Current

When a reverse bias voltage is applied onto an APD, a small leakage current develops. This leakage current is expected to increase linearly with the bias voltage following Ohm's Law until breakdown, above which the leakage current increases drastically. To measure the leakage current and breakdown voltage at low temperature, the QUPID was placed in the cryostat, tightly insulated from external light, with both the photocathode and grounding ring grounded. A negative voltage[5] was applied to the APD anode while the cathode was connected to a picoammeter. The leakage current was read out from the picoammeter for a given bias voltage, which was then scanned to just beyond the breakdown voltage. Fig. 8.18 shows a schematic diagram of the leakage current readout system.

Fig. 8.19 shows the leakage current curves for different temperatures as a function of the applied bias voltage. As expected, the leakage current followed a linear increase up to a breakdown voltage, after which it rose dramatically. The leakage current was seen to have a strong temperature dependence. As the temperature was lowered, the overall leakage current decreased and at liquid xenon temperature, the leakage current was < 1 nA for QUPID No. 6. Fig. 8.20 shows the behavior of the leakage current as a function of temperature for different QUPIDs while holding the bias voltage constant at -100 V. For all of the QUPIDs, the leakage current shows an approximately exponential increase with temperature.

The breakdown voltage also decreased with the temperature. Fig. 8.21 shows the temperature dependence of the breakdown voltage for various QUPIDs. It can be seen that the breakdown voltage follows a linear trend with the temperature,

---

[5] Stanford Research Systems Model PS350 +/- 5 kV Power Supply.

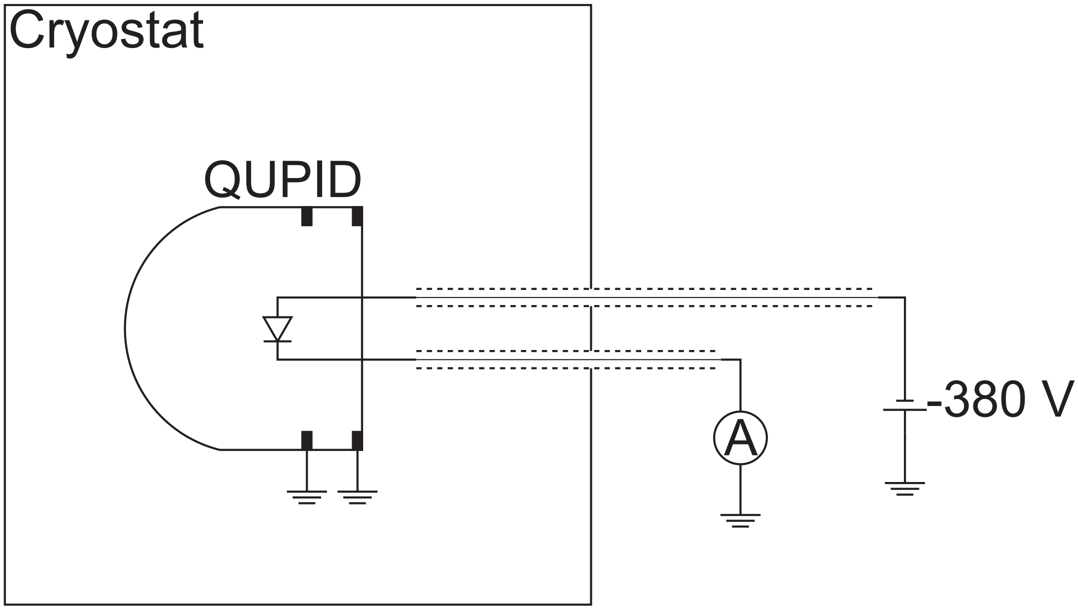

Figure 8.18: Schematic for the leakage current readout system. The photocathode and grounding rings are both grounded while a reverse bias voltage is applied to the anode of the APD. The leakage current is then read out through a picoammeter attached to the cathode of the APD.

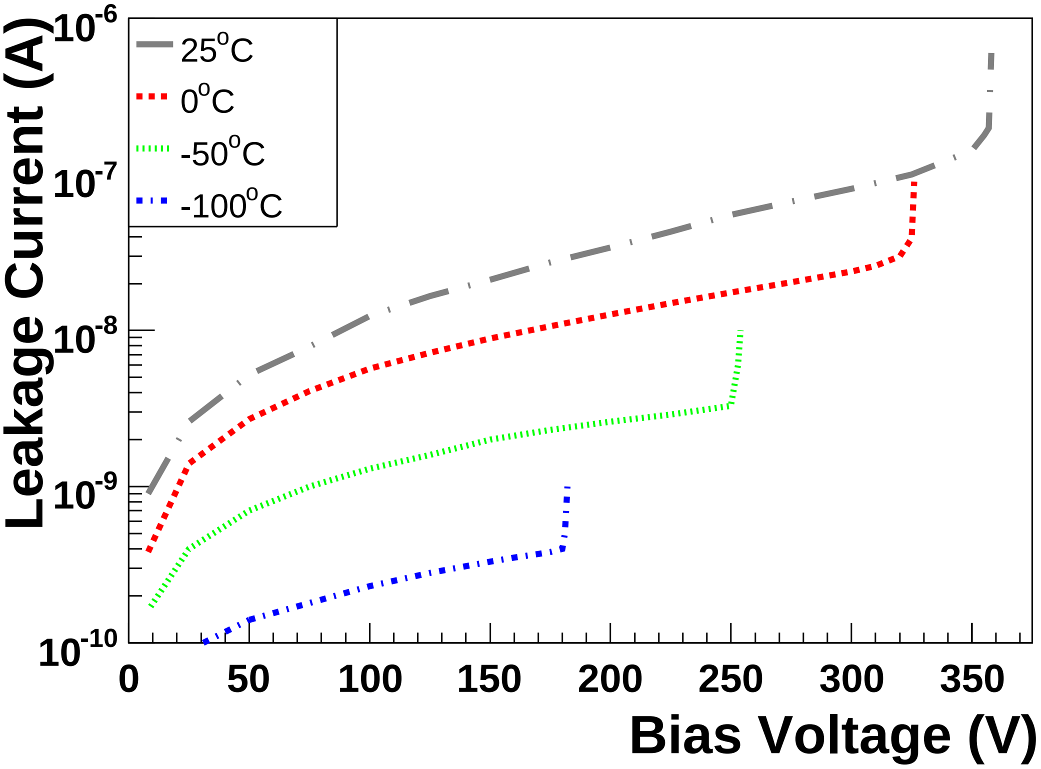

Figure 8.19: Leakage current versus the APD bias voltage at various temperatures for QUPID No. 6. As the temperature decreases, the overall leakage current decreases. Also, the breakdown voltage, recognizable from the dramatic increase of the slope of the leakage current curves, decreases with the temperature. At liquid xenon temperature, the leakage current is < 1 nA while breakdown occurs at 180 V.

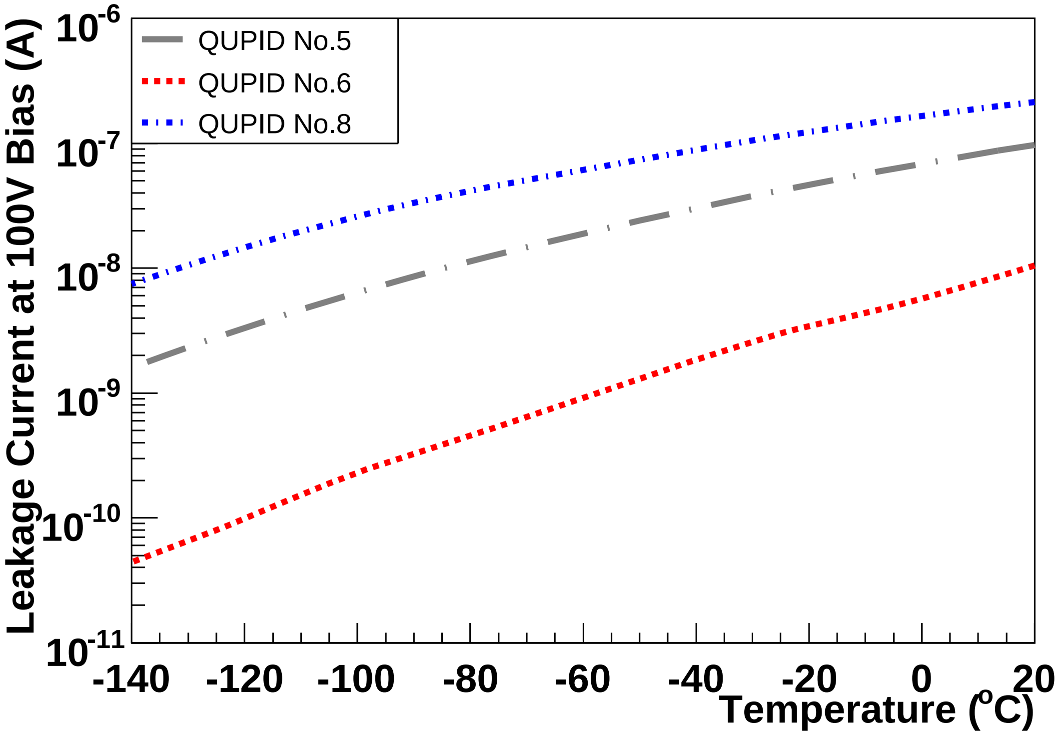

Figure 8.20: Temperature dependence of the leakage current for different QUPIDs while the APD is held at -100 V bias. The leakage currents show an approximately exponential trend with the temperature.

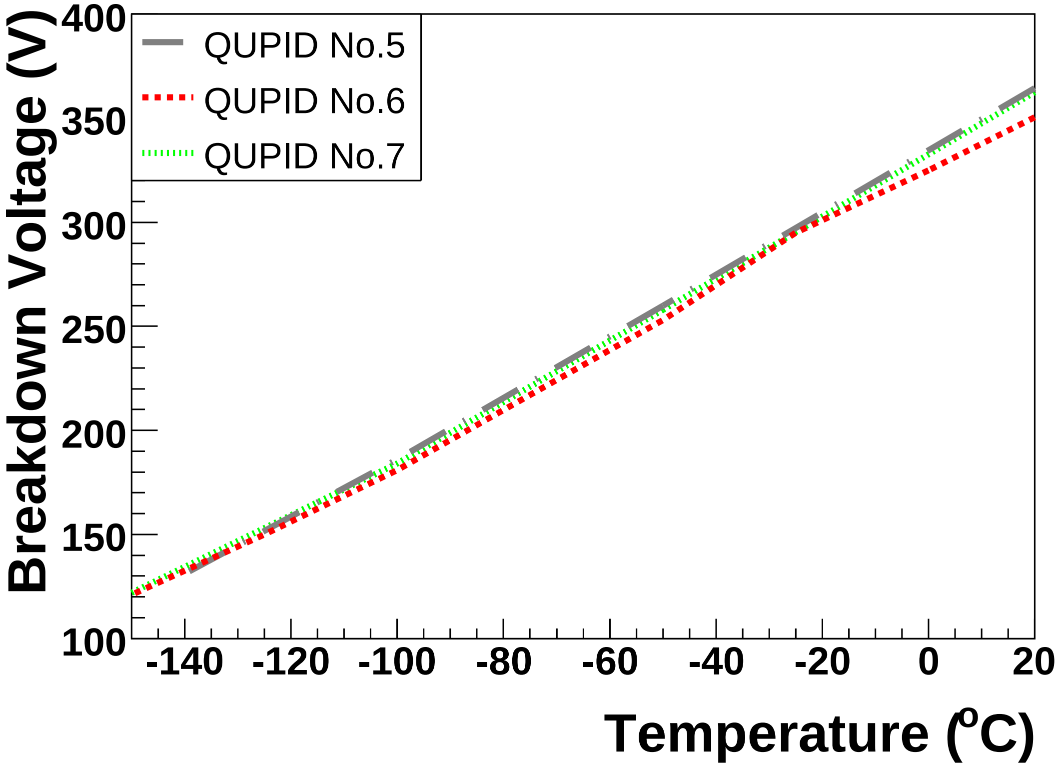

Figure 8.21: Temperature dependence of the breakdown voltage for different QUPIDs. The breakdown voltage shows a linear trend with the temperature.

and at -100° C the breakdown voltage was 180 V. By extrapolating the curve down to the temperature of liquid argon (-180° C), the breakdown voltage would be ∼90 V. Although the leakage current curves at various temperatures are well defined at all voltages up to the breakdown voltage, the APD does not operate properly below ∼120 V independent of temperature. This is due to the fact that the APD must be supplied with at least this voltage in order create an effective depletion region for the avalanche process. This version of the APD is thus not suitable for operation under liquid argon, as the breakdown voltage is reached before an effective depletion region is created.

A new version of the APD is being produced by Hamamatsu that will have a significantly higher breakdown voltage. This APD will be used in the next iteration of the QUPID and will be standard on both the xenon and argon versions.

8.7.2 Gain

Unlike conventional PMTs, the gain of an HAPD is a combination of two separate processes, the bombardment process and avalanche process. In an HAPD, a photoelectron is accelerated onto the APD due to a high potential applied to the photocathode, on the order of several kV. The kinetic energy of the photoelectron bombarding onto the APD creates hundreds of electron-hole pairs. The number of electron-hole pairs created within the APD due to the bombardment process from a single photoelectron is called the Bombardment Gain.

The APD itself is maintained at a high reverse bias voltage. When an electron-hole pair is created within the APD, the electric field due to the bias voltage pulls the electron and hole apart. The electron is accelerated across the field and will likely impact another electron within the APD, creating another electron-hole pair. These electrons are accelerated once again due to the field, and impact

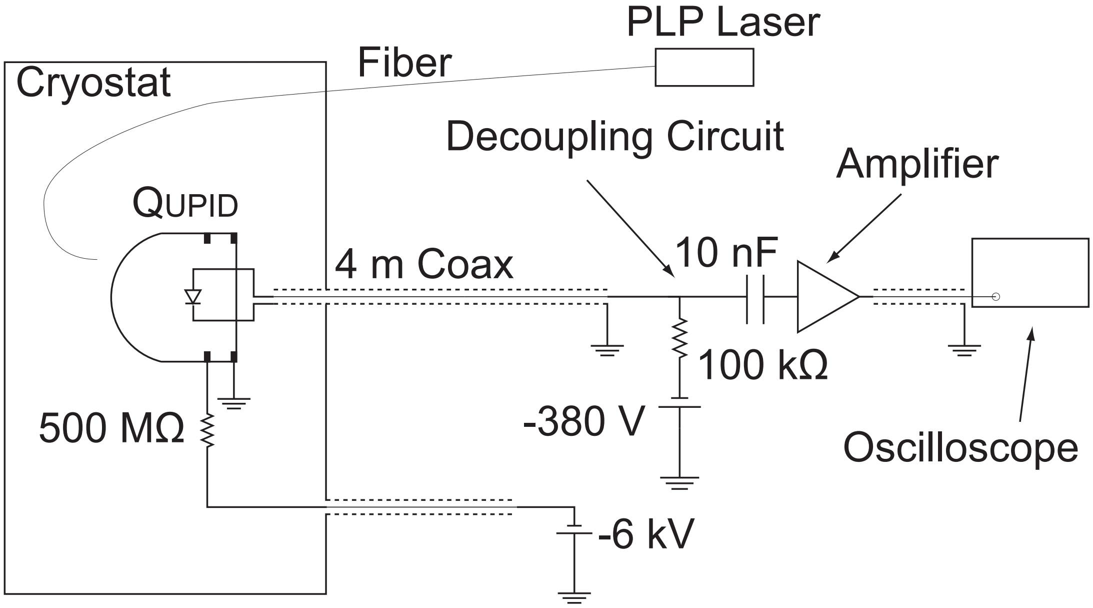

Figure 8.22: Schematic of the test setup with the pulsed laser light used for gain and anode linearity measurements. The photocathode is supplied with high voltage and a bias voltage is connected to the APD anode through a decoupling circuit. The output of the APD is passed through an amplifier to the readout system, an oscilloscope in this case.

further electrons. The same process occurs for the holes, and an overall avalanche effect is produced. Thus, a single electron-hole pair can produce several hundred electron-hole pairs through this avalanche process. The amount by which the initial electron-hole pair is multiplied is designated as the Avalanche Gain.

To measure the gain of the QUPID, a pulsed laser light of 405 nm wavelength and 70 ± 30 ps pulse width emitted at a rate of 100 kHz was used[6]. The photocathode voltage[7] was set to -6 kV and the APD bias voltage ∼10 V below the breakdown. In order to minimize the cabling within the cryostat, both the signal and the bias voltage were carried by the same coaxial cable. To supply the bias voltage and read out the signal, a decoupling circuit was placed outside of the cryostat, along with an amplifier[8] and an oscilloscope for data acquisition[9]. Fig. 8.22 shows the schematic of the readout used for the gain measurements, and for general QUPID operation.

8.7.2.1 Bombardment Gain

In order to measure the bombardment gain of the QUPID, the laser was pulsed at a fixed light intensity, and the APD was biased to a fixed voltage below the breakdown. The oscilloscope was triggered with a pulse from the laser synchronized to the light pulses, ensuring that the resulting pulses from the QUPID would occur at the same location on the oscilloscope. These signals were then integrated to obtain the total charge outputted by the QUPID. This output charge is equal to:

$$Q_{out} = G_b G_a N_{pe} C E \tag{8.2}$$

---

[6] Hamamatsu Model C10196 Laser Controller with Model M10306-30 PLP-10 Laser Head

[7] Stanford Research Systems Model PS355 -10 kV Power Supply

[8] RFBay Model LNA-1440 Amplifier, 40 dB gain, 1.4 GHz bandwidth

[9] LeCroy WaveRunner 204MXi-L Oscilloscope, 10 GS/s, 2 GHz bandwidth

where G_b is the bombardment gain, G_a is the avalanche gain, N_{pe} is the number of photoelectrons emitted from the photocathode, and CE is the collection efficiency of the QUPID. In order to extract G_b from this equation, it is important to note that in silicon, one electron-hole pair is created for every 3.6 eV of energy deposited by the impinging photoelectrons. For this reason, the bombardment gain curve should be linear and have a slope of $\frac{1}{3.6V} = 0.28\ V^{-1}$. Q_{out} is then plotted with respect to the photocathode voltage, and the curve is scaled by a factor in order to set the slope to $0.28\ V^{-1}$. The scale factor is equal to $\frac{1}{G_a N_{pe} CE}$ and the resulting curve is then the bombardment gain curve.

The outcome of this procedure is shown in Fig. 8.23, where the bombardment gain versus the photocathode voltage is reported for different temperatures. The bombardment gain follows the expected linear behavior above -4 kV. The non-linear trend at negative voltages smaller than -4 kV is due to a dead layer of the APD, which stops the photoelectrons that do not have enough energy to penetrate into the active area. At -6 kV, the QUPID achieves a bombardment gain of above 700, independent of the temperature.

In order to increase the bombardment gain achievable, Hamamatsu is in the process of making changes to the design of the QUPID. Currently, the QUPID cannot be operated at a photocathode voltage above -6 kV. Any voltage higher than this will cause sparking between the photocathode and grounding ring. Hamamatsu is developing a resistive coating and surface treatment for the intermediate quartz ring to allow for the photocathode voltage to safely reach -8 kV without any sparking. This would impart a greater kinetic energy onto the photoelectrons, which increases the bombardment gain and allows for the photoelectrons to more easily overcome the dead layer of the APD. At the same time, the APD is being changed to minimize the thickness of the dead layer. This will allow

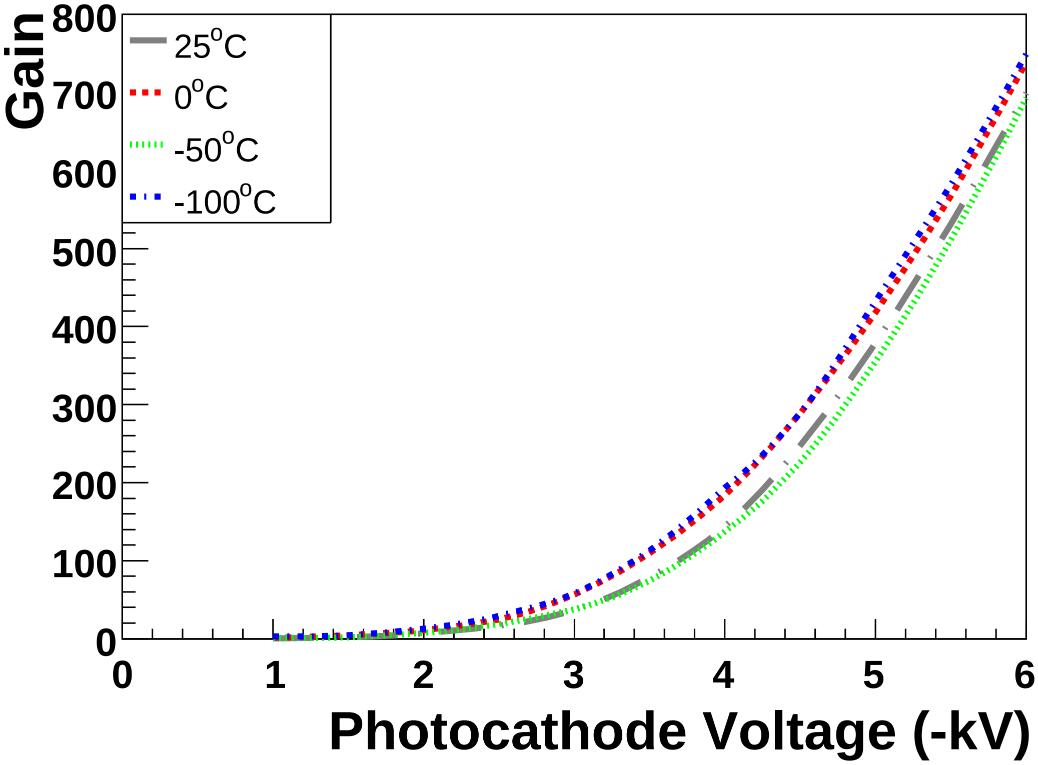

Figure 8.23: Bombardment gain of Qupid No. 6 for various temperatures. The curve follows a linear behavior above -4 kV as expected. The bombardment gain shows no temperature dependence and reaches a maximum of 750.

for more photoelectrons to pass through the dead layer without losing as much kinetic energy.

8.7.2.2 Avalanche Gain

The avalanche gain is measured in a similar fashion as the bombardment gain. The laser light is kept at a fixed intensity, and the photocathode is held at -6 kV. The APD bias voltage is scanned up to just below the breakdown voltage, and the output charge is measured. In order to obtain the absolute normalization for the avalanche gain, a single photoelectron spectrum is taken using the same procedure as for a conventional PMT at -6 kV photocathode voltage, and a set APD bias voltage (see Sec. 7.1.3). From the single photoelectron spectrum, the total gain can be calculated. The total gain is related to the avalanche gain and bombardment gain by

$$G_{tot} = G_b G_a \tag{8.3}$$

and since G_b is known at -6 kV from the bombardment gain calculations, G_a can be determined at this APD bias voltage. Using Eq. 8.2, $(N_{pe}CE)$ can be determined for the laser intensity used in the measurements. Finally, using the measured value of G_b and the calculated value of $(N_{pe}CE)$, G_a can be determined for any APD bias voltage.

Fig. 8.24 shows a single photoelectron spectrum of QUPID No. 5. In the case of the QUPID, the single photoelectron spectrum does not follow a Gaussian shape. When the photoelectron is bombarded upon the APD, there is a chance that the photoelectron may deposit a portion of its energy into the dead region of the APD. In this case, the full kinetic energy is not converted to electron-hole pairs, and a tail at the lower end of the single photoelectron spectrum develops. Similarly, the photoelectron may deposit a fraction of its energy into the APD, then scatter

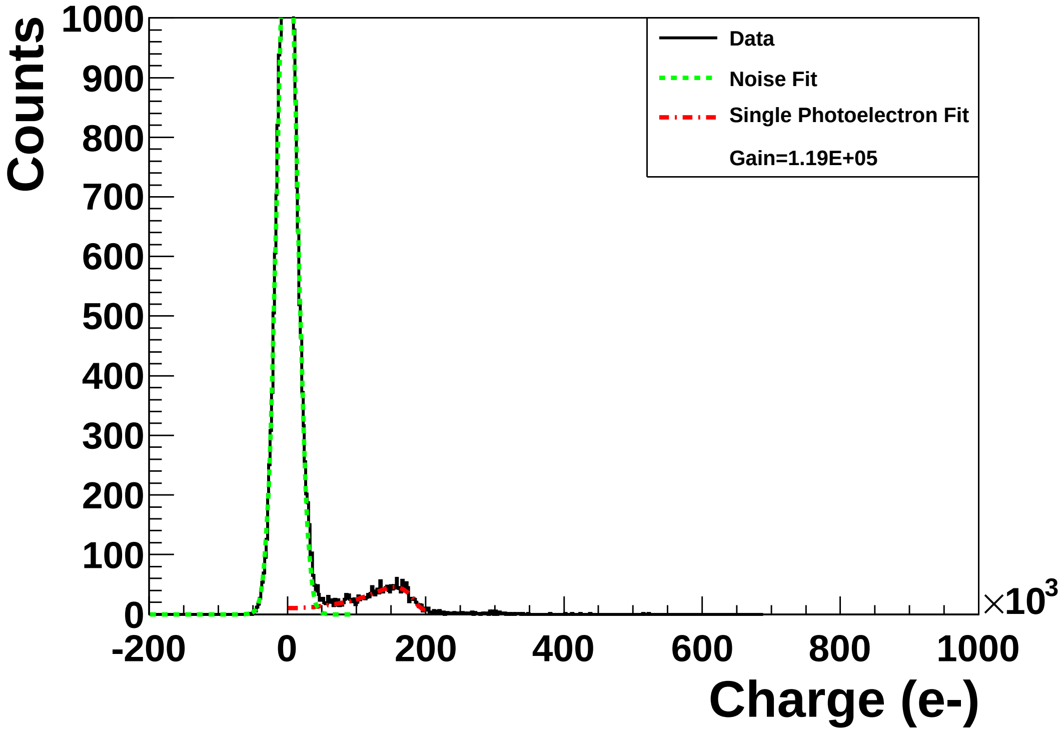

Figure 8.24: Single photoelectron spectrum of QUPID No. 5 operated at room temperature. For this single photoelectron spectrum, the photocathode voltage was placed at -6 kV and the APD bias voltage was held at -370 V. Unlike conventional PMTs, the single photoelectron spectrum of the QUPID is not a Gaussian.

out. Again, this process creates a tail at the lower end of the spectrum. The absolute gain as measured from the single photoelectron spectrum is then the centroid of this distribution.

Fig. 8.25 shows the avalanche gain versus bias voltage for the QUPID. A temperature dependence of the avalanche gain can be seen, with the gain increasing as the temperature decreases. A maximum avalanche gain of $200-300$ is reached at a lower bias voltage for lower temperatures.

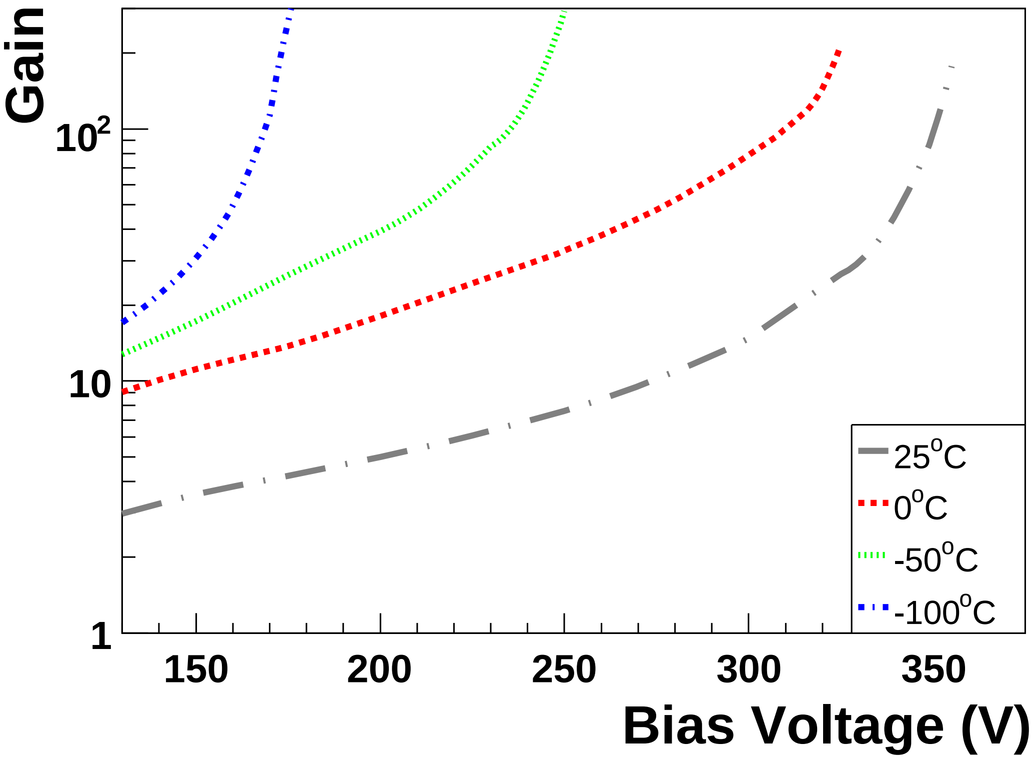

Figure 8.25: Avalanche gain of QUPID No. 6 for various temperatures. As the temperature decreases, the avalanche gain increases for a set bias voltage, and the maximum gain is achieved at a lower bias voltage. A maximum avalanche gain of 300 is seen at -100° C.

Combining the bombardment gain and avalanche gain using Eq. 8.4, the total gain of the QUPID is then $700 \times 200 \sim 10^5$ at -6 kV and near the maximum bias voltage, enough for single photoelectron detection.

8.7.3 Anode Linearity

As discussed in Sec. 8.5.3, the photocathode of the QUPID must be linear up to at least 12 nA in order to observe the largest expected signals, which arise from the S2s of neutrinoless double beta decay events, or high energy γ-rays from the decay of radioactive contaminants. The anode of the QUPID must then be linear up to this value multiplied by the gain. Thus, for a gain of 10^5, the QUPID anode should be linear to 1.2 mA.

The setup for the anode linearity characterization of the QUPID consists of two rotating neutral density filter wheels controlled by two stepper motors. One is a continuously variable filter wheel with a range of optical densities from 0 to 2.0, the other is a set of discrete filters with optical densities ranging from 0 to 5.0. The optical density OD is defined as:

$$OD = \log_{10}\left(\frac{I_0}{I}\right) \tag{8.4}$$

where I_0 and I are the intensities of the incoming and outgoing light respectively. An ultrabright LED[10] provides pulsed light which is attenuated through the filters and is brought to the QUPID through an optical fiber. Fig. 8.26 shows a photograph and a diagram of the test system.

For the measurement, the LED is pulsed at alternating light levels with a fixed brightness ratio of 1:4, resulting in alternating high and low currents from the APD of the QUPID. Each pulse has a width of 1 μs, comparable to the

---

[10] Nichia Model NS6B083T 470 nm LED

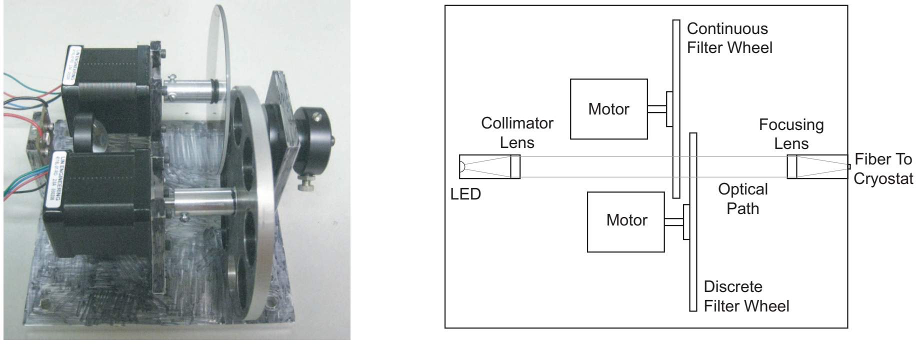

Figure 8.26: On the left, a photograph of the anode linearity pulsing system. On the right, a schematic diagram of the anode linearity pulsing system. A pulsed LED shines through two sets of filters and is passed into a fiber, which then carries the light to the Qupid.

S2 signals in a noble liquid TPC, and the dim and bright pulses alternate at a frequency of 600 Hz. The light from the LED is then attenuated through the two filter wheels. In this way, while the overall brightness is changed using different combinations of the filters, the 1:4 brightness ratio is maintained between the alternating pulses. The waveforms are then read out with an oscilloscope and integrated. The readout system used for these measurements was the same as for the gain measurements (see Fig. 8.22), however the amplifier was removed.

At low light levels for both dim and bright pulses, the anode current of the Qupid shows the same constant ratio of 1:4. As the light level increases (by decreasing the optical density of the filter wheels) the absolute value of the anode current increases, and the ratio of low and high anode current starts to deviate from the original 1:4, thereby showing nonlinear behavior. Fig. 8.27 shows the output current from the Qupid for the bright and dim light pulses at a given optical density, while Fig. 8.28 shows the measured anode linearity over the entire range.

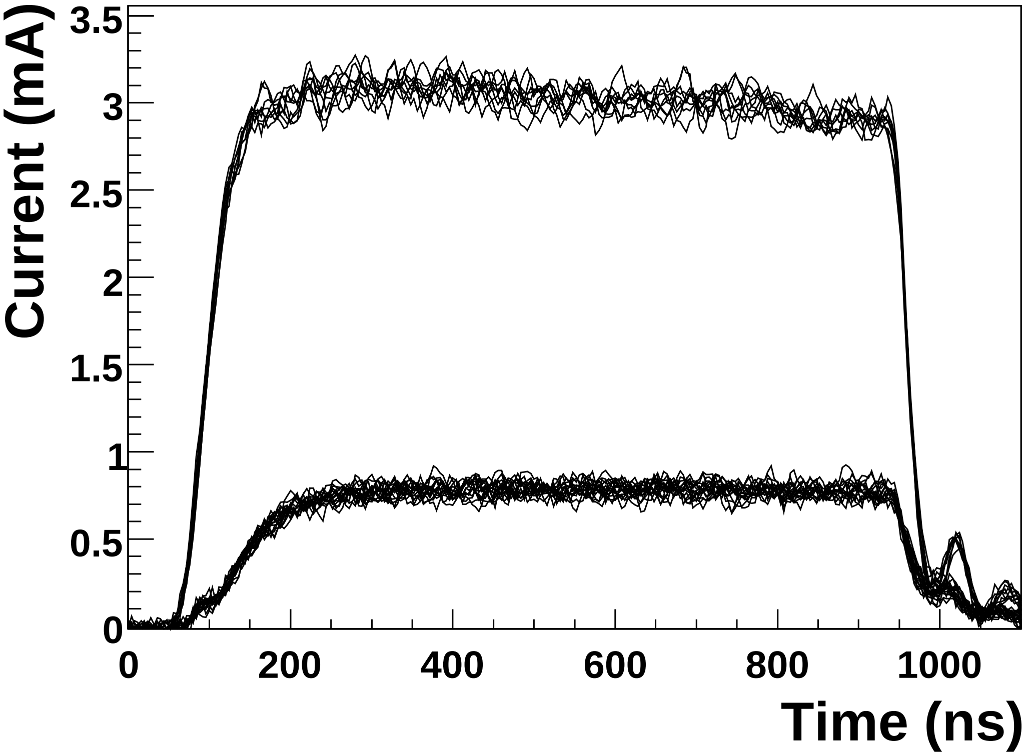

Figure 8.27: Waveforms from QUPID No. 5 at the bright and dim light levels from the LED of the linearity testing system. The waveforms from the bright pulses are at 3 mA, where the QUPID starts showing a deviation from linearity at the 5% level.

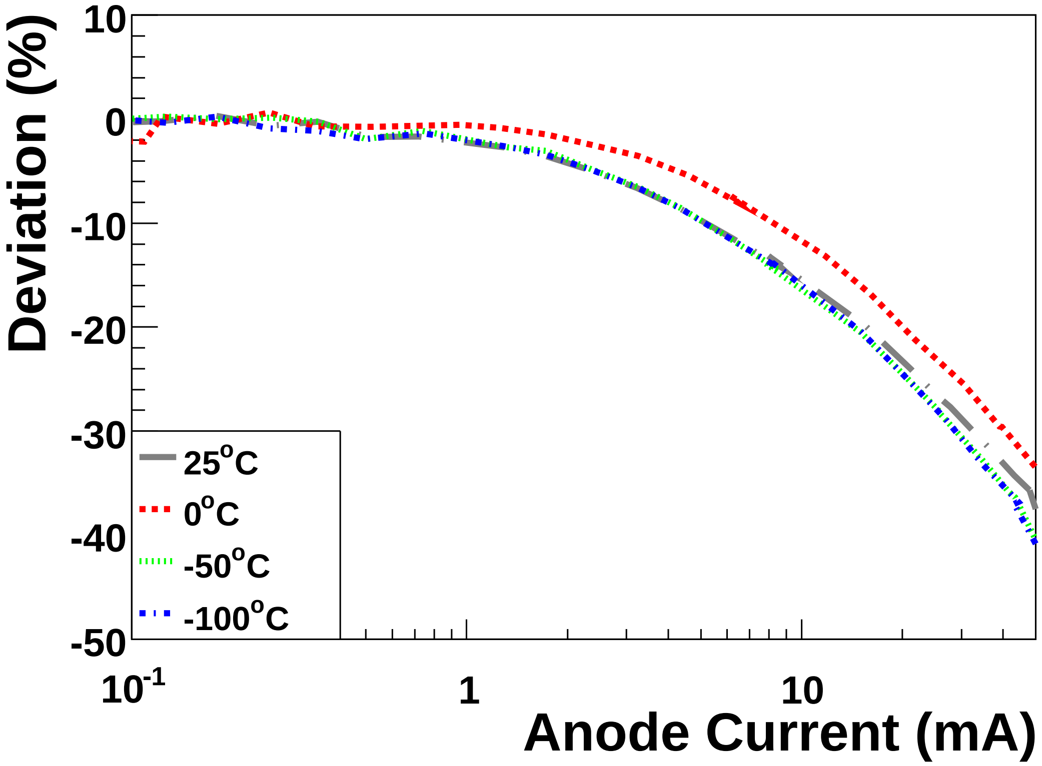

Figure 8.28: Anode linearity for various temperatures of Qupid No. 5. A 5% nonlinear behavior starting at an anode current of 3 mA is evident.

Although nonlinear behavior begins to appear at the 5% level from 3 mA peak anode current at a total gain of 10^5, the nonlinearity of the QUPID at these levels is gradual. This nonlinearity can be characterized as a function of the anode output current and corrected for high light levels, thereby increasing the effective dynamic range. The tests were performed at various temperatures down to -100° C in the cryogenic setup described above, and the linearity of the QUPID was seen to be independent of the temperature.

The nonlinearity of the APD arises from a space-charge effect similar to that in conventional PMTs. During the avalanche process within the APD, the number of electrons and holes increases dramatically. Because the electrons and holes are drifted apart, and the numbers are constantly multiplying, the charge of the electrons and holes can alter the electric field within the APD. This decreases the effective electric field in the APD and hinders the avalanche process, thereby causing nonlinear behavior.

8.7.4 Collection Efficiency

The same scanner for testing the photocathode uniformity (see Sec. 8.5.2 and Fig. 8.12) has also been used for the anode uniformity. In these measurements, the photocathode was held at -6 kV while a bias voltage of -250 V was applied to the anode of the APD. A constant light was shined onto a spot on the photocathode from the LED, and current was read through the cathode of the APD using a picoammeter. A schematic of the setup used for the anode uniformity measurements is presented in Fig. 8.29. The light was scanned across the entire face of the QUPID, just as it was done for the photocathode uniformity.

The photoelectron collection efficiency can be inferred from the ratio between anode uniformity and photocathode uniformity scaled by the total gain. Fig. 8.30

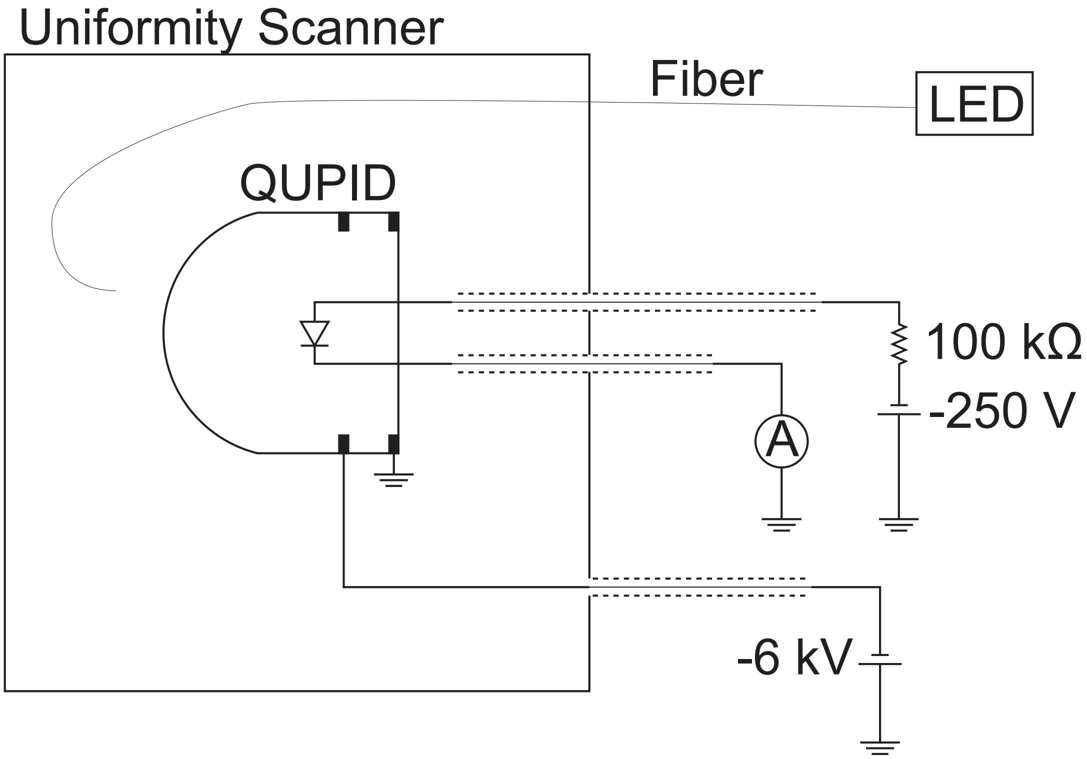

Figure 8.29: A schematic of the anode uniformity setup. The photocathode was held at -6 kV while the APD was held at a bias voltage of -250 V. The LED provided a constant light, focused onto the photocathode, and the current from the APD was read out through a picoammeter.

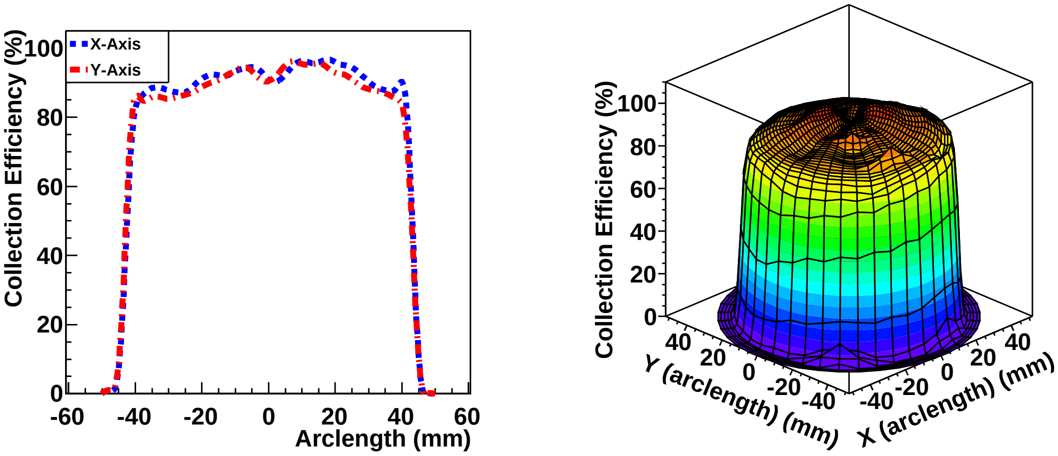

Figure 8.30: Photoelectron collection efficiency in X and Y slices (on the left), and in a 3D plot (on the right) for QUPID No. 7. The collection efficiency is $> 80\%$ across the entire face of the QUPID.

shows the photoelectron collection efficiency of QUPID No. 7. The collection efficiency is above 80% for a majority of the surface, and is uniform across the entire face.

8.8 Waveforms and Timing

In conjunction with the gain measurements, waveforms of the QUPID were also obtained at low light levels. With the QUPID in the same setup for gain measurements (see Fig. 8.22), the intensity of the picosecond laser was lowered such that only a small number of photoelectrons were observed. The picosecond laser controller provided a trigger output synchronized to the laser pulse. A narrow window was then chosen around this point for integration of the signal, and the resulting charge of the signals were plotted in a histogram. Fig. 8.31 shows the

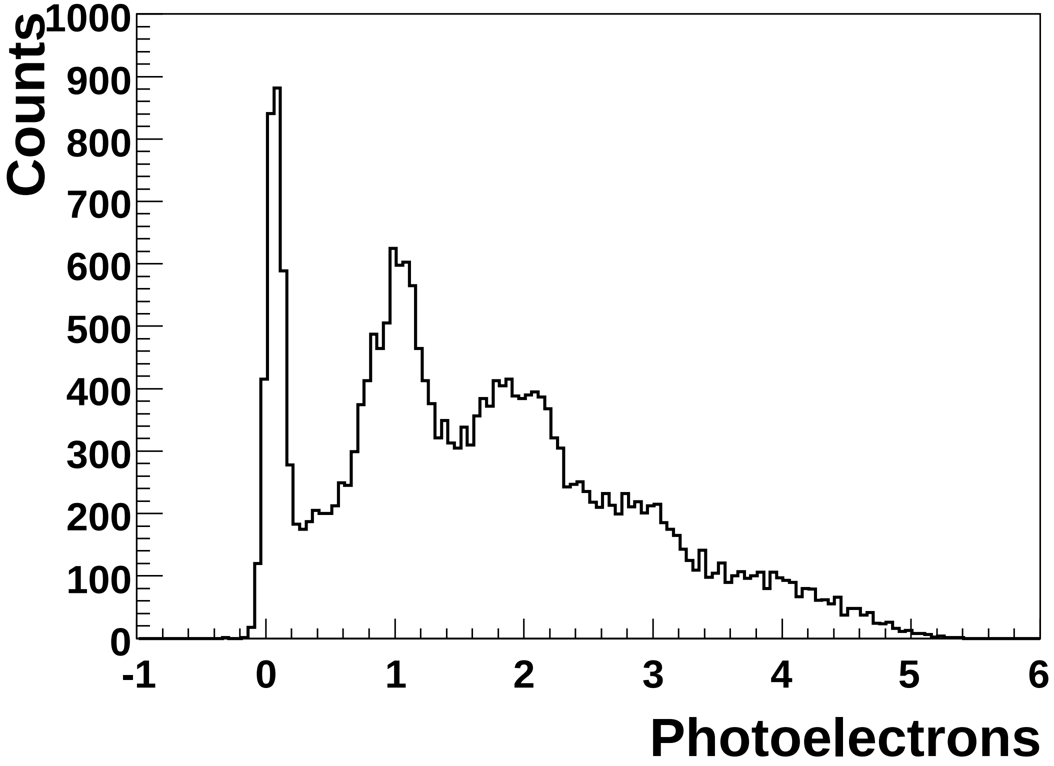

Figure 8.31: Charge distribution measured for dim laser pulses on QUPID No. 5. Peaks of 0, 1, 2, and 3 photoelectrons can be clearly seen. A narrow pedestal of width 0.09 photoelectrons is visible.

charge distribution of QUPID signals from 0, 1, 2, and 3 photoelectrons. A narrow pedestal of zero photoelectrons can be seen in the histogram, and clear peaks corresponding to integer numbers of photoelectrons are apparent. It is important to note that conventional PMTs do not show such clear separation between the different numbers of photoelectrons.

Much of the electronics used for reading out signals from the QUPID contain high levels of intrinsic radioactivity. Such devices should be placed as far from the target volume of a dark matter detector as possible to reduce backgrounds. Ton-scale dark matter detectors will require long cabling on the order of several meters to ensure that the readout electronics are far away. For this reason, a 4 m coaxial cable was inserted between the cryostat and the decoupling circuit. Fig. 8.32 shows 100 waveforms taken at -100° C in this setup. Even with such a long cable before amplifying the signal, there is little degradation of the waveform, and bands of 0, 1, and 2 photoelectrons can be seen.

Timing information of the waveforms was measured in the same setup. A rise time of 1.8 ± 0.1 ns and a fall time of 2.5 ± 0.2 ns were measured for the QUPID. The pulse width of the signal was 4.20 ± 0.05 ns, while the transit time spread of the QUPID was measured as 160 ± 30 ps. It is important to note that this value can be considered as an upper limit as it includes the uncertainties arising from the jitter of the laser trigger. Tab. 8.3 shows a comparison of the timing parameters of the QUPID to the Hamamatsu R8520 1" PMT and the Hamamatsu R11065 3" PMT. Compared to conventional PMTs, the timing characteristics of the QUPID are superior. This can be useful for identifying S1 signals over noise if a sufficient sampling frequency is used, or for time of flight measurements for position reconstruction.

PMT	Rise Time	Fall Time	Pulse Width	Transit Time Spread
R11065	4.2 ± 1.1 ns	10.0 ± 1.0 ns	8.0 ± 0.6 ns	7.4 ± 0.5 ns
R8520	1.9 ± 0.2 ns	2.9 ± 0.2 ns	4.4 ± 0.1 ns	1.1 ± 0.1 ns
QUPID	1.8 ± 0.1 ns	2.5 ± 0.2 ns	4.20 ± 0.05 ns	0.16 ± 0.03 ns

Table 8.3: Table of the timing parameters for the R11065 3" PMT, R8520 1" PMT, and the QUPID. This table is the same as Tab. 7.1 with the addition of the QUPID measurements.

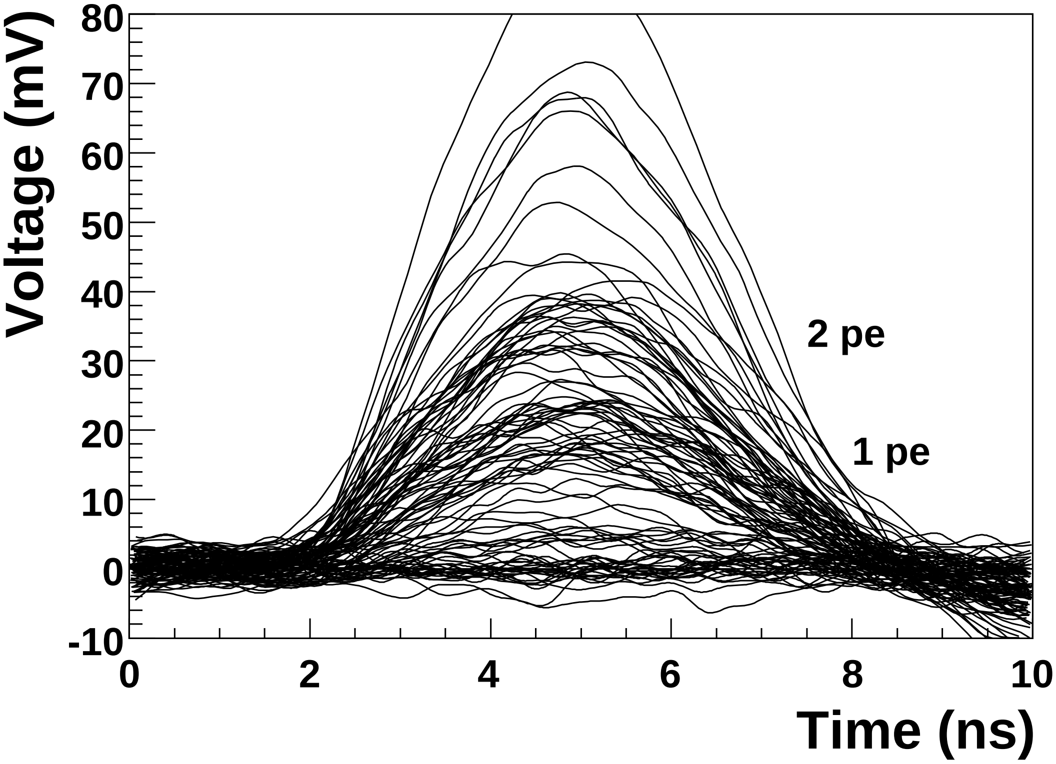

Figure 8.32: Waveforms for dim laser pulses at -100° C from QUPID No. 5. A 4 m coaxial cable was used between the cryostat and the decoupling circuit. Even with this long cable, clear bands corresponding to 0, 1, and 2 photoelectrons are well visible. The rise time and fall time were measured as 1.8 ± 0.1 ns and 2.5 ± 0.2 ns respectively, with a pulse width of 4.20 ± 0.05 ns.

The fast timing response, especially the transit time spread, allow for the possibility of pulse shape discrimination using the QUPIDs. As shown in Tab. 5.1, and further discussed in Sec. 8.10 and 9.2, noble liquids have distinct fast and slow decay times for scintillation light. Electronic recoil and nuclear recoil events have different ratios of fast to slow components, and by taking advantage of this fact, a further discrimination can be implemented based on the decay time of the S1 signals. For argon, the different decay times differ by over two orders of magnitude, but for xenon the two decay times are much more similar, differing only by a factor of six. However, with the low transit time spread of the QUPID coupled with fast digitization, pulse shape discrimination can be used in future xenon detectors. To be able to effectively take advantage of this, enough light must be detected, and so the threshold for S1 signals must be increased.

8.9 Dark Counts

The dark count rate of the QUPID is a very important parameter to characterize for future use in dark matter detection experiments. WIMP interactions in liquid xenon or argon produce small energy deposits. These energy deposits generate low numbers of photoelectrons. In order to ensure that events seen are not merely dark counts from the photodetectors, a coincidence cut is applied to the events such that only the energy deposits that produce signals on at least two photodetectors are accepted. These signals can be as low as a single photoelectron on each photodetector.

If the dark count rate of the QUPID is too high, there can be accidental coincidences when two QUPIDs generate a dark count within a short time of one another, thereby creating an event that passes the coincidence cut. In order to test the dark count rate, the QUPID was placed in the cryostat and connected

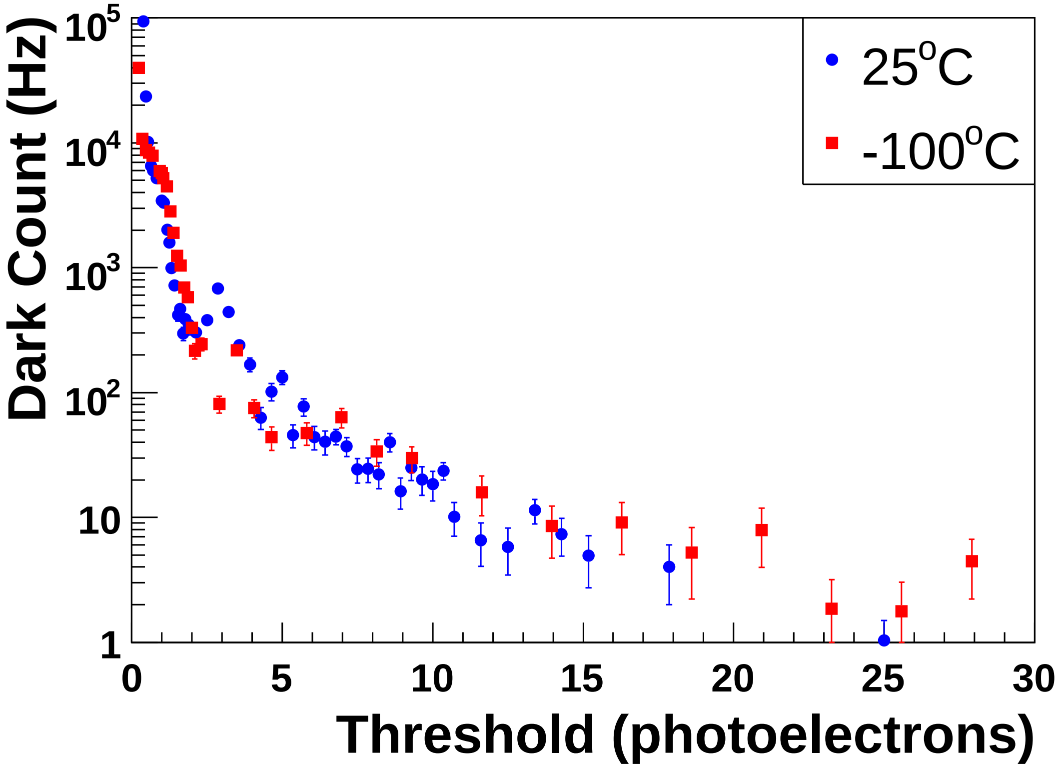

Figure 8.33: Dark counts from Qupid No. 7 as a function of threshold. The error bars in this figure are only due to statistical error. If the dark counts were solely due to thermal emission of electrons from the photocathode, the dark count rate would be negligible above a threshold of 1.5 photoelectrons and would drop considerably at low temperatures. This plot shows that the dark counts do not have a temperature dependence and are still high at a threshold greater than 1.5 photoelectrons. These dark counts must be due to some other process, in this case small sparks originating at the APD.

in the same way as standard operation (see Fig. 8.17 and Fig. 8.22). While in the cryostat, the QUPID was placed at the operational photocathode voltage and bias voltage, and the output of the QUPID was recorded for a 100 μs window. A threshold was set at a given voltage, and the number of times the output of the QUPID crossed this threshold was measured. This process was done several thousand times in order to obtain useful statistics. Finally, the entire procedure was repeated at various levels of the threshold voltage.

The results of the dark count analysis are shown in Fig. 8.33 for room temperature and for -100° C. If the dark counts are only due to thermal emission of electrons from the photocathode, one would expect the rate to drop to nearly zero at threshold levels above 1.5 photoelectrons, as the probability for two or more electrons being thermally emitted simultaneously is very low. However, it is apparent from the plots that although the dark count drops when the threshold is set to a level above one photoelectron, there is still an observable dark count rate. Above 10 photoelectrons a dark count rate of $1-10$ Hz is observed, while thermally emitted electrons should never create signals this large.

As explained in Sec. 7.1.4, the dark count rate should also decrease with temperature if it is due to the thermal emission of electrons. From Fig. 8.33, it is apparent that there is no temperature dependence in the dark count rate of the QUPID. From this observation, and from the fact that the dark counts still exist even at high thresholds, it was determined that these dark counts were not due to thermal emission of electrons from the photocathode. Instead, these dark counts were originating from sparking at the APD. This was due to the deposition of photocathode material onto the APD during the production process. Hamamatsu has agreed to address this problem and has made several advances in preventing sparking at the APD. It is expected that the dark count rate of the new version of the QUPID should be well below the values shown in Fig. 8.33, especially at the higher threshold values and lower temperatures.

8.10 QUPID in Liquid Xenon

Characterization of the various properties of the QUPID are important to understand its basic operation at room temperature and at low temperatures. It is imperative to also operate the QUPID under liquid xenon to ensure the functionality in such an environment. The QUPID has been tested extensively in a liquid xenon setup built at UCLA, which is shown in Fig. 8.34. The QUPID was placed inside a PTFE and aluminum holder (see Sec. 9.1.1) supported by a polyethylene structure inside a stainless steel chamber. The chamber was then placed inside a vacuum cryostat. A cryocooler[11] was used to liquefy the xenon and to maintain liquid xenon temperature during operation.

The PTFE housing was fully immersed in liquid xenon allowing for the QUPID to operate in single-phase mode, that is only under liquid xenon with no gas phase. The temperature and pressure were held constant at -100° C and 1.5 bar, and the system was operated under stable conditions for approximately two weeks. During this period, the xenon gas was purified with a hot metal getter[12] in a closed recirculation loop[13]. Gaseous xenon was pumped out from the top of the chamber and sent through the getter. In order to purify the gas, the getter heated the xenon to a high temperature. After the purification, the getter would cool the gas back to room temperature and the gas was then sent back to the chamber and flowed over the cooler. This created an efficient circulation loop by removing xenon gas from the chamber, purifying it, and sending it back to the chamber as

---

[11] Q-Drive Model 2S132K-WR Cryocooler

[12] SAES Model PS3MT3R1 Mono-torr Getter

[13] Q-Drive/UCLA Model 2S132K-UCLA Pump

clean liquid.

Gain calibration was performed while the QUPID was submerged in liquid xenon by measuring its response to light from the picosecond laser. The laser pulses were fed into the PTFE housing via an optical fiber. Following the gain calibration, internal ^{57}Co and ^{210}Po sources placed just above the QUPID were used to measure and monitor the QUPID response to the scintillation light of xenon. The readout setup used for measuring this scintillation was the same as for the gain measurements (Fig. 8.22), however no amplifier was used. The presence of impurities, out-gassing of the surrounding material, and a PTFE housing that was not fully optimized limited the achievable light detection efficiency, which was found to be dependent on the recirculation speed throughout the run. Fig. 8.35 shows the response of the QUPID to the ^{57}Co and ^{210}Po sources, including pulse shapes and energy spectra.

Tab. 8.4 summarizes the parameters measured from each of the sources. ^{57}Co decays through the emission of a 122 keV γ-ray with an 86% branching ratio, and a 136 keV γ-ray with 11% branching ratio. As seen in Fig. 8.35, these two lines are not separated but give a single peak whose weighted average energy of 123.6 keV was used for further calculations. The ^{57}Co light yield averaged over a few hours was found to be 2.0 ± 0.2 pe/keV$_{ee}$, with $10.4 \pm 1.2\%$ energy resolution. The stated errors are estimated from the fluctuations of the light yield for the measurements taken with different trigger threshold values over the span of a few hours.

Fig. 8.35 also shows the part of the measured spectrum dominated by the peak due to the ^{210}Po source. ^{210}Po decays by a 5.3 MeV α-particle, and from this a light yield of 1.6 ± 0.2 pe/keV$_{nr}$ was obtained with a resolution of $2.5 \pm 0.5\%$. These measurements were taken on a different date than the ^{57}Co data, and thus

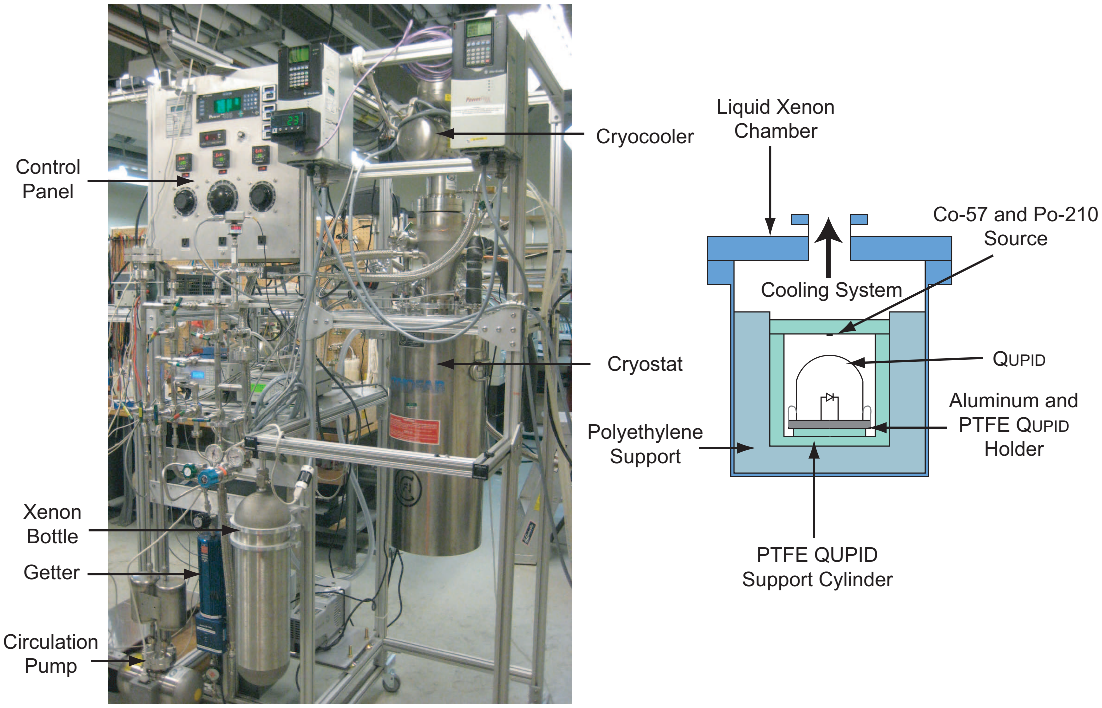

Figure 8.34: On the left, a photograph of the liquid xenon test system. The external cryostat, cryocooler, circulation pump, and getter can be seen in the photograph. On the right, a drawing of the liquid xenon cell inside the cryostat. The QUPID was held in a polyethylene, PTFE, and aluminum holder while in liquid xenon, and two radioactive sources, ^{210}Po and ^{57}Co, were placed inside to generate scintillation light.

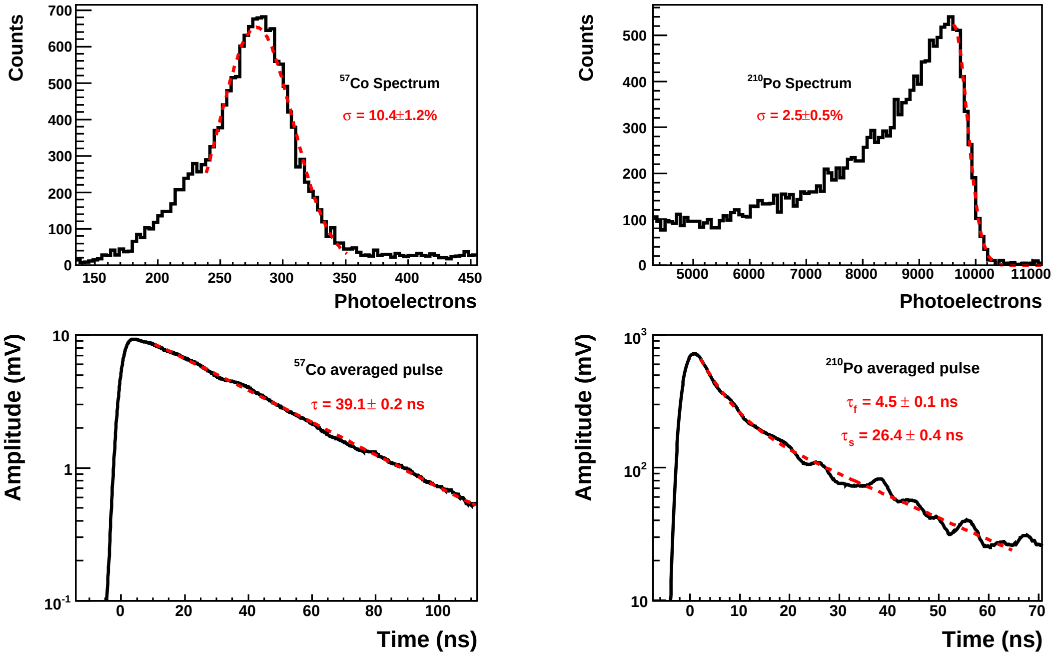

Figure 8.35: Clockwise from top left: ^{57}Co energy spectrum, ^{210}Po energy spectrum, ^{210}Po averaged waveform, ^{57}Co averaged waveform using Qupid No. 7. The average light yield from several data sets of ^{57}Co was 2.0 ± 0.2 pe/keV$_{ee}$ with a resolution of $10.4 \pm 1.2\%$. The average light yield obtained from the ^{210}Po source was 1.6 ± 0.2 pe/keV$_{nr}$ with a resolution of $2.5 \pm 0.5\%$. The average waveforms also show exponential fits in red. A decay time of 39.1 ± 0.2 ns was found from the ^{57}Co pulses, and a fast and slow decay time of 4.5 ± 0.1 ns and 26.4 ± 0.4 ns are seen in the ^{210}Po waveforms.

Source	Type	Energy	Light Yield	Resolution	Decay Time	Previously Measured Decay Time [150, 151]
^{57}Co	γ	122 keV, 86% 136 keV, 11%	2.0 ± 0.2 pe/keV$_{ee}$	$10.4 \pm 1.2\%$	39.1 ± 0.2 ns	34 ± 2 ns
^{210}Po	α	5.3 MeV	1.6 ± 0.2 pe/keV$_{nr}$	$2.5 \pm 0.5\%$	4.5 ± 0.1 ns, fast (71%) 26.4 ± 0.4 ns, slow (29%)	4.3 ± 0.6 ns, fast (69%) 22.0 ± 2.0 ns, slow (31%)

Table 8.4: Parameters for the sources observed in liquid xenon, including light yield, resolution, and decay times. The obtained values for the decay times from both α-particle and γ-ray interactions are similar to previously published values. This particular QUPID had a lower quantum efficiency of 20% at 178 nm.

the conditions, such as xenon purity, changed between the data sets. This can account for the difference in the obtained light yields between the ^{57}Co and ^{210}Po data.

The scintillation light from liquid xenon has two decay components due to the de-excitation of the singlet and triplet states of the excited dimer Xe_2^* [152]. The averaged pulse shape for ^{210}Po α-particle and ^{57}Co γ-ray interactions, together with the fit of their overall decay profiles, are shown in Fig. 8.35 (bottom). The α-particle interactions from ^{210}Po had measured fast and slow decay times of 4.5 ± 0.1 ns and 26.4 ± 0.4 ns respectively, with an intensity ratio of the fast to slow components being 71% fast and 29% slow. The ^{57}Co pulses had a single decay time of 39.1 ± 0.2 ns. These decay time constants are similar to the previously published values of 4.3 ± 0.6 ns and 22.0 ± 2.0 ns for the α-particle fast and slow components, with a ratio of 69% fast and 31% slow, and to 34 ± 2 ns for γ-interactions [150, 151]. The ability to observe a difference in the pulse shapes of α-particle and γ-ray interactions allows for the possibility of pulse shape discrimination in dark matter detectors [153, 154, 155, 156].

8.11 Summary

The QUPIDs, the new low radioactivity photodetectors developed and evaluated jointly by Hamamatsu Photonics and UCLA, show optimum characteristics for use in the next generation of dark matter and double beta decay detectors aside from the dark count rate. This chapter has described the test setups and performance of several QUPIDs. Tab. 8.5 shows a summary of the most relevant results.

QUPIDs have lower radioactivity than conventional PMTs as measured at the Gator screening facility. Simulations of ton scale detectors including QUPIDs show that they satisfy the low background level requirement for dark matter detectors. The quantum efficiency, higher than 30% at the xenon scintillation wavelength, is competitive with standard photodetectors, and can easily be tuned for operation in liquid argon. A total gain of 10^5, and the capability of single photon counting, fit well with the detection of low intensity signals coming from WIMP interactions. A wide linear dynamic range, up to 3 mA of anode current at liquid xenon temperature, allows the QUPID to cover an energy range large enough for neutrinoless double beta decay detection. The QUPID uniformity has been measured to be above 80% over the entire surface, and it also has a good timing response of 1.8 ± 0.1 ns rise time, 2.5 ± 0.2 ns fall time, 4.20 ± 0.05 ns (FWHM) pulse width, and 160 ± 30 ps (FWHM) transit time spread. In a liquid xenon environment, the QUPIDs capability to detect scintillation light from γ-ray and α-particle interactions has also been demonstrated

These characteristics make the QUPID an ideal replacement for PMTs in future experiments, such as DARKSIDE50, XENON1Ton, MAX, DARWIN, and XAX [157, 148, 147, 158, 159], and will represent a major contribution for the next generation of ton scale dark matter and double beta decay detectors. Further improvements on the QUPID are expected in order for the APD to operate down to liquid argon temperatures, and for the photocathode voltage to be raised to -8 kV. The following chapter will discuss in further detail the upcoming DARKSIDE50 and XENON1Ton experiments, and how the QUPID will be integrated in these detectors.

Qupid Parameters			
Dimensions	Outer Diameter	71 mm	
	Effective Photocathode Diameter	64 mm	
	Radius of Hemispherical Photocathode	37 mm	
	Total Height	76 mm	
Radioactivity	^{238}U	< 17.3 mBq	
	^{226}Ra	0.3 ± 0.1 mBq	
	^{232}Th	0.4 ± 0.2 mBq	
	^{40}K	5.5 ± 0.6 mBq	
	^{60}Co	< 0.18 mBq	
Performance		25° C	-100° C
Photocathode	Material	Bialkali-LT	
	Quantum Efficiency at 178 nm	$34 \pm 2\%$	–
	Linearity	$> 10\ \mu$A	$> 1\ \mu$A
Electron Bombardment	Acceleration Voltage	6 kV	
	Typical Gain	750	
	Maximum Gain	800	
APD	Diameter	3 mm	
	Capacitance	11 pF	
	Leakage Current	200 nA	0.3 nA
	Breakdown Voltage	360 V	180 V
	Typical Gain	200	
	Maximum Gain	300	
Anode Output	Typical Total Gain	1.5×10^5	
	Maximum Total Gain	2.4×10^5	
	Linearity	3 mA	
Timing Properties	Rise Time (10%-90%)	1.8 ± 0.1 ns	
	Fall Time (90%-10%)	2.5 ± 0.2 ns	
	Pulse Width (50%-50%)	4.20 ± 0.05 ns	
	Transit Time Spread (FWHM)	160 ± 30 ps	

Table 8.5: Summary of the key parameters of the Qupid.

CHAPTER 9

The Future of the QUPID

The QUPID is being considered for use in the upcoming DARKSIDE50 detector, a 50 kg depleted argon TPC, and the XENON1Ton detector, a 2.4 ton liquid xenon TPC that will be the successor to the XENON100 experiment. DARKSIDE50 will use two arrays of 19 QUPIDs each, at the top and bottom of the detector, whereas XENON1Ton will have two arrays of 121 QUPIDs each. It is imperative that the QUPIDs are able to function in close proximity to one another while in liquid and gas xenon. Furthermore, there is a possibility that one or more of the QUPIDs will fail to function properly in the experiment. These QUPIDs must be switched off and brought to ground level. Since all the neighboring QUPIDs will be at -6 kV, one must be sure that sparking will not occur between the grounded QUPID and nearby QUPIDs. Simultaneously, it is important to have the QUPIDs as close as possible to one another in order to ensure maximum photocathode coverage, thereby maximizing the light yield of the TPC.

In the near future, the QUPID will be mass produced for the DARKSIDE50 and XENON1Ton detectors. These QUPIDs must all be characterized and must meet the set requirements before being employed in the dark matter detectors. An efficient test system is needed in order to characterize several QUPIDs at once. This will speed up the process of characterizing and accepting the QUPIDs for final operation. In order to both test the operation of several QUPIDs in close proximity to one another and to characterize many QUPIDs at once, I have

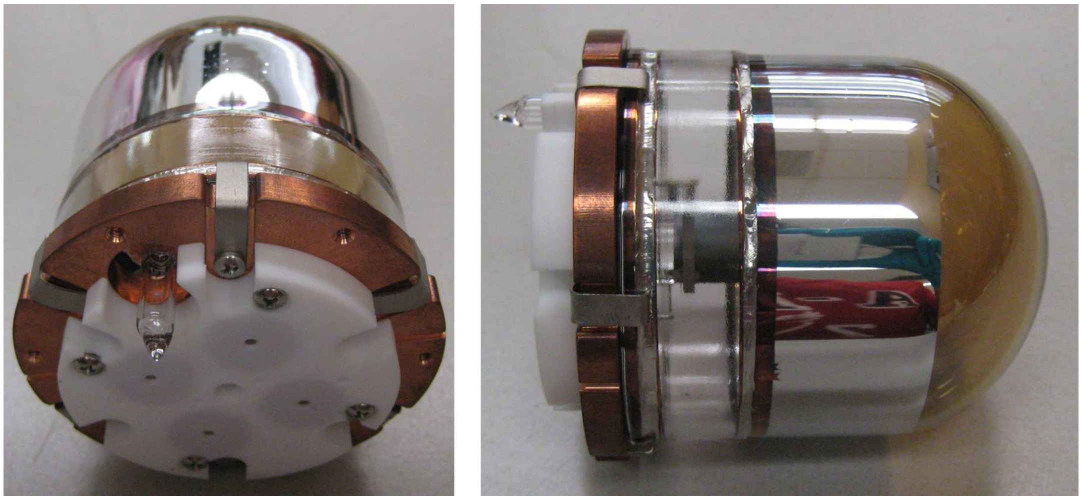

Figure 9.1: On the left, a back view of the Qupid attached to an individual holder. On the right, a side view of the same setup. The Qupid is held onto an OFHC (Oxygen Free High Conductivity) copper plate with six titanium clips. A PTFE piece attached to the back holds the connections for the APD. The coaxial bulkhead connector was not attached in this photograph.

designed a holder for the Qupid which will be installed into a 7-Qupid support structure which I also have designed. These holders were made to be modular for ease of use, and scalable up to the size of the proposed dark matter detectors.

9.1 7-QUPID System

9.1.1 Individual QUPID Holders

In order to have an effective design for a Qupid support structure, the design must be modular such that the Qupids can be inserted and removed one at a time and so that the same support can be used for any number of Qupids. To achieve this, I have developed a holder for a single Qupid. This single Qupid holder can then be attached to any large support structure by a simple method.

The holder must include all the relevant connections to the QUPID itself. Connections must be made to the APD cathode and anode via the pins at the bottom of the QUPID, and the ground and photocathode voltage must be supplied through the indium rings.

Finally, it is imperative that all parts of the holder be made of materials with low intrinsic radioactivity. Since one of the main advantages of the QUPID is its low radioactivity, any and all components placed near the QUPID must also have low radioactive contaminants.

Fig. 9.1 shows an individual QUPID holder which I have developed to satisfy all of these requirements. The base of the QUPID is held onto an Oxygen Free High Conductivity (OFHC) copper plate using six clips made with high purity (CP-1 grade) titanium. The clips grip the QUPID from the lower indium ring, and thereby provide both the structural support and grounding required for the QUPID. A PTFE piece is attached onto the bottom of the copper plate using a set of four #4-40 screws[1]. The PTFE holds two conical springs made of CP-1 titanium, each of which has an OFHC copper contact that is used to make the connections to the APD pins of the QUPID. Fig. 9.2 shows a cross section view of the holder with the springs and copper contacts visible. Two short wires from the copper contacts connect the APD pins to an SMA[2] bulkhead connector at the bottom of the QUPID holder. Finally, a CP-1 titanium wire insulated with a 1/16" PTFE tube is routed between the copper plate and PTFE piece and maintains pressure on the top indium ring of the QUPID. This wire is used to provide the photocathode voltage. The copper plate of the holder has a set of

---

[1] The screws currently used are made of stainless steel, however for the actual detector, a material with low radioactivity will be used, such as CP-1 titanium or OFHC copper.

[2] SMA (SubMiniature version A) is a type of coaxial connector designed for high frequency signal transmission.

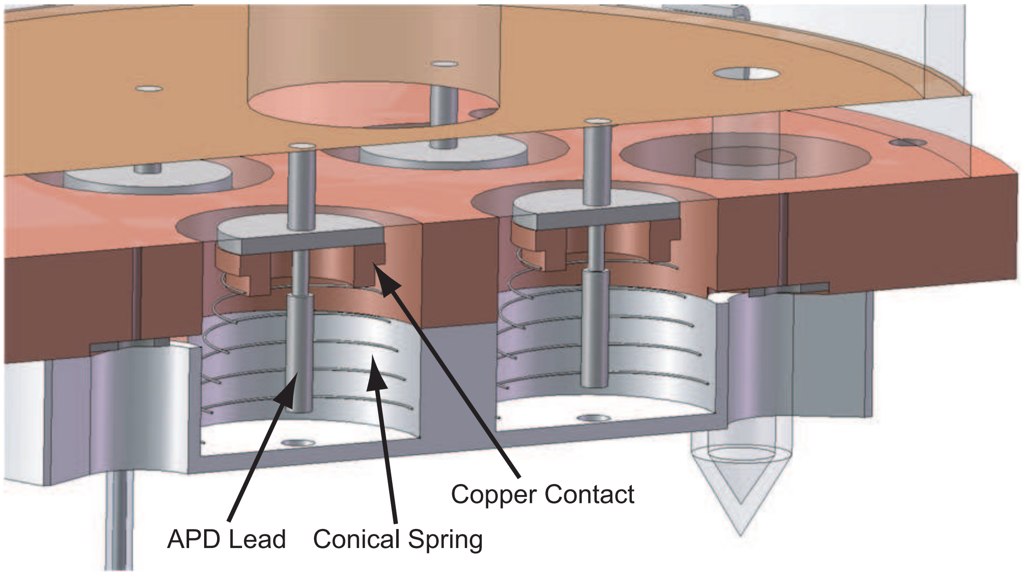

Figure 9.2: A cross section view of the Qupid holder. The conical springs and copper contacts are visible, along with the APD leads.

six #4-40 tapped holes. which can be used to screw the individual Qupid holder onto any support structure.

The Qupid holder is made entirely out of materials with low intrinsic radioactivity. OFHC copper, PTFE, and CP-1 titanium are all known to be very clean [122, 80]. The holder itself makes all of the connections needed for the Qupid, and a simple SMA cable is needed for the APD bias voltage and readout. The SMA bulkhead connector on the holder is not made of low radioactivity materials and is only used here to simplify the operation and increase the speed of characterizing a large number of Qupids. The final design to be implemented in the future dark matter detectors will have a coaxial cable for the signal and APD bias voltage connected directly onto the two wires which connect to the APD contacts. A high voltage cable can be attached via a pin and socket to the titanium wire used for the photocathode voltage. These features allow for the individual QUPID holder to be modular, simple to use, and practical. In case of a malfunction of the QUPID, or for characterizing mass produced QUPIDs, the holder and QUPID can easily be inserted and removed from any system it is integrated in.

9.1.2 7-QUPID Support Structure

The support structure for a 7-QUPID system should be designed with future dark matter detectors in mind. Since the individual holders for each QUPID were made to be modular, a support structure must be able to accommodate the individual holders in such a way that the insertion and removal of the QUPIDs can be done with relative ease. This support must also be made of materials with low radioactivity. My design for the support structure is shown in Fig. 9.3. The structure will be made entirely of OFHC copper to reduce radioactive contamination, however an aluminum version has been made for testing purposes at UCLA. The individual QUPIDs and their holders will be inserted from the top and screwed onto the support structure from the bottom. The centers of each QUPID will be separated by 80 mm in a hexagonal pattern, providing enough space between adjacent QUPIDs for the photocathode voltage connections, and ensuring that they are as tightly packed as possible to increase the photocathode coverage in the detector.

The support structure is also designed to accommodate for a set of PTFE reflectors, as seen in Fig. 9.4. The QUPIDs are of a cylindrical geometry, and will thus not be able to provide 100% photocathode coverage within the TPC. PTFE reflectors can be placed in the spaces between the QUPIDs such that any photons that do not encounter a QUPID will be reflected back into the TPC.

The support structure will be used for tests of the QUPIDs under liquid xenon,

Figure 9.3: The support for the 7-Qupid system, with seven Qupids installed in their individual holders. Here, the individual holders and the 7-Qupid support are made of aluminum for ease of machining. The version that will be used in future dark matter detectors will be made of OFHC copper.

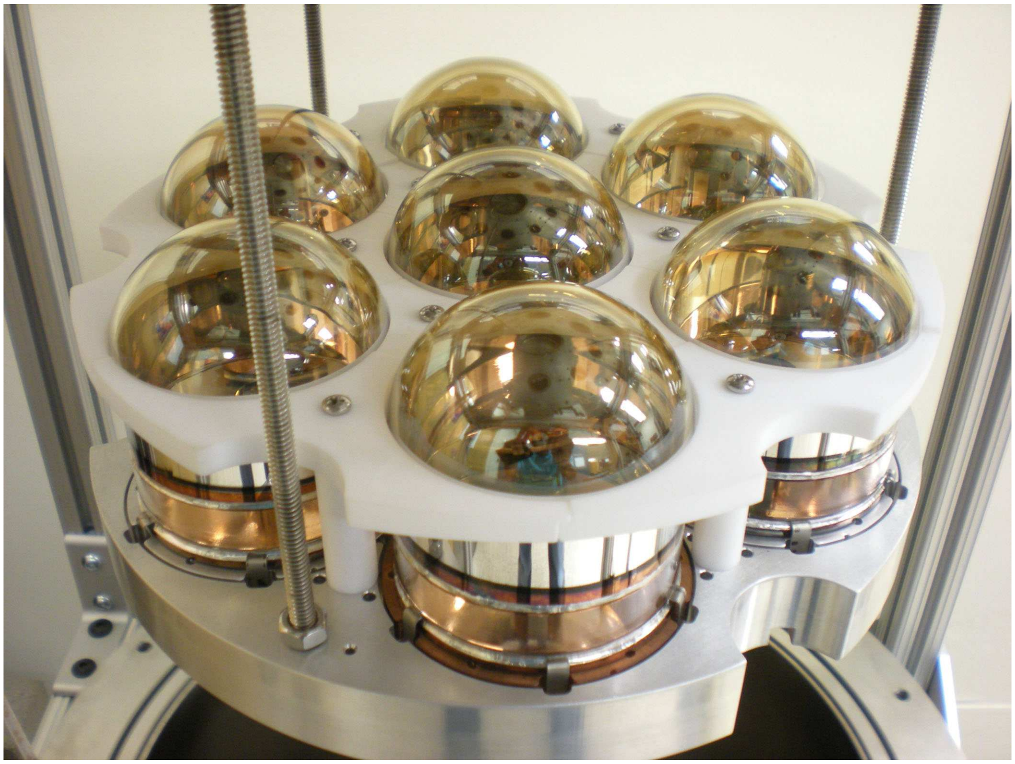

Figure 9.4: The 7-QUPID system, including the PTFE reflectors.

liquid argon, and for tests at various temperatures down to that of liquid argon. For the cooldown tests not involving noble liquids, a method for cooling must be integrated onto the support structure. A cylindrical copper block will be attached to the bottom of the support structure via a set of six 1/4”-20 bolts with cryogenically rated thermal grease providing good thermal contact between the copper block and the support structure. A 1/4” copper tube soldered onto the copper block in a spiral will provide liquid nitrogen which will be flowed through the copper tube with a constant rate of 50 slm[3]. This will cool down the copper block, which in turn will cool the support structure and the seven QUPIDs. Three 100 W resistive heaters inserted into the copper block will provide for temperature control. A PID controller[4] will be used to cycle the resistive heaters and maintain a stable temperature.

9.2 The DARKSIDE50 Detector

The DARKSIDE50 detector is an upcoming direct dark matter detection experiment. One key difference between DARKSIDE50 and XENON100 is that DARKSIDE50 will be using depleted argon as opposed to xenon. A liquid argon TPC works under the same principles as a liquid xenon TPC. Two phases of argon are maintained, a liquid phase and a gas phase, an electric field is applied to the liquid phase, and a stronger field is applied in the gas phase (see Fig. 5.6). Just as in a liquid xenon TPC, a WIMP deposits energy in the liquid argon target and creates scintillation light (S1). The energy deposit also liberates electrons which are drifted to the gas phase and undergo proportional scintillation (S2). Fig. 9.5 shows a drawing of the DARKSIDE50 detector.

---

[3] The unit “slm” stands for standard liters per minute, where a standard liter is the mass equivalent to 1 liter of gas at standard temperature and pressure.

[4] Omega Model CN8201 Temperature Controller

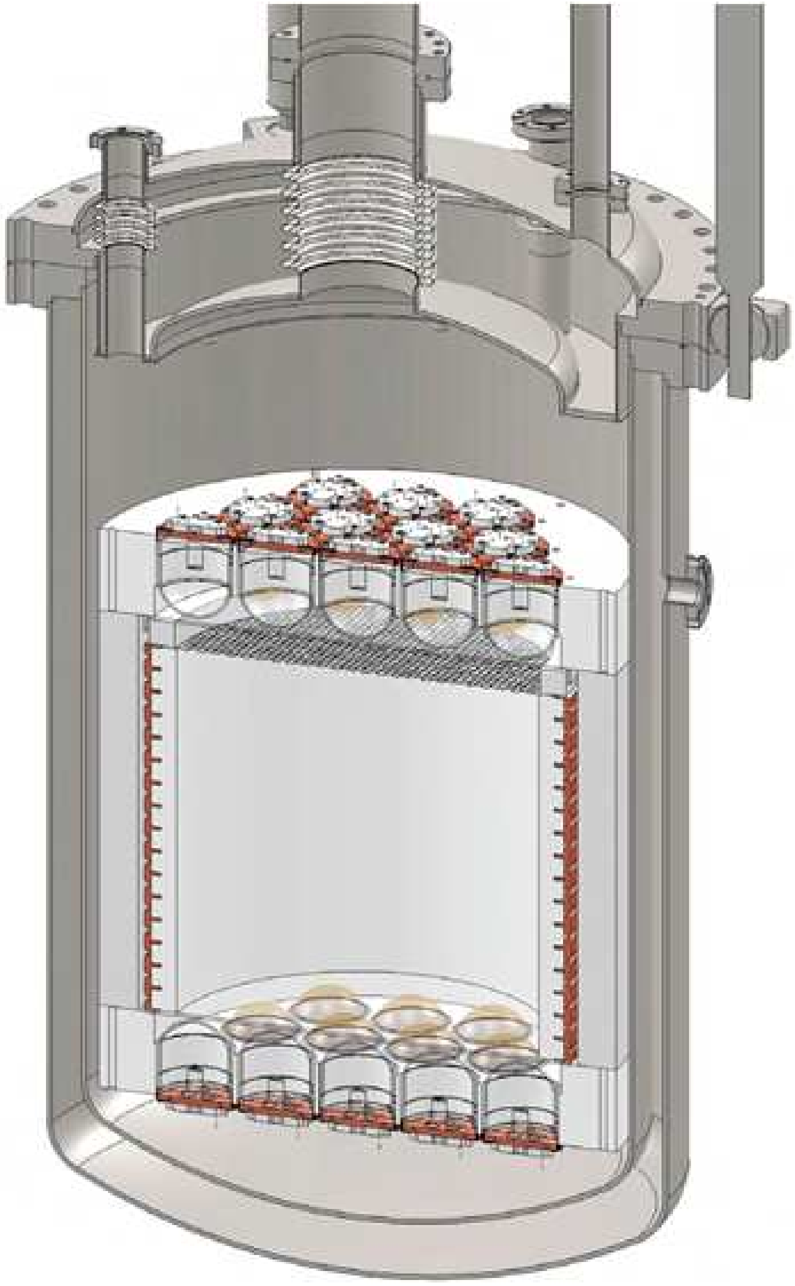

Figure 9.5: A CAD drawing of the internals of the future DarkSide50 Detector. The detector will use 19 Qupids at the top and 19 Qupids at the bottom. The total mass of depleted liquid argon will be 50 kg.

Liquid argon dark matter detectors use many of the same background reduction techniques as liquid xenon TPCs. A similar $\log_{10}$(S2/S1) cut can be applied, along with multiple scatter cuts and fiducial volume cuts. However, an important advantage of liquid argon TPCs is the fact that they can also use a pulse-shape discrimination cut. The fast and slow decay times in argon differ by two orders of magnitude (see Tab. 5.1). Because of this difference in the decay times, the pulse shape can be used to reject electronic recoil events by a factor of 10^7 in a signal region between 52 and 110 keV$_{nr}$ [155]. In order to use the pulse shape discrimination, a large number of photons are needed, and this requires a larger energy deposit. Due to the energy spectrum of WIMP interactions, the rate of interactions at the higher energies are much lower than the rate at lower energies. Similarly, since the mass number of argon is lower than that of xenon, the interaction rate (which goes as A^2) will be less than that of xenon. For these reasons, although the discrimination between nuclear and electronic recoil events is much better than liquid xenon TPCs, the liquid argon TPCs have lower sensitivity than a comparable mass liquid xenon TPC.

Natural argon also contains a fraction of ^{39}Ar which undergoes beta decay with a half-life of 269 years. This creates a background within the whole of the detector that cannot be removed through fiducialization or shielding. The $\log_{10}$(S2/S1) and pulse-shape discrimination can help to decrease this background, however the most effective way would be to remove the ^{39}Ar isotope from the argon used in the experiment. DarkSide50 will be using argon that has been depleted in ^{39}Ar to effectively remove as much of this background as possible [160].

The DarkSide50 detector, having a target of 50 kg of depleted liquid argon, and using the background rejection techniques explained above, is expected to reach a sensitivity of 10^{-45} cm^2 for the WIMP-nucleon cross section after running for 3 years [157]. This can only be achieved with the successful implementation of the QUPIDs as the low radioactivity photodetectors for the TPC. Thus, it is imperative that the QUPID be finalized and mass produced for use in DARKSIDE50. Although the sensitivity of DARKSIDE50 will not reach the levels achieved by other dark matter detectors, it will be used to demonstrate the capabilities of pulse-shape discrimination, QUPID operation in liquid argon, and the ability to deplete argon of ^{39}Ar. Once these have been proved successful, a larger detector will be built with sensitivities comparable to the leading dark matter detectors.

9.3 The XENON1Ton Detector

The XENON1Ton detector will be the successor to the XENON100 experiment. It will be a scaled up version of XENON100 with a few differences between the two. As explained in Ch. 5, XENON100 is a liquid xenon TPC with two arrays of Hamamatsu R8520 1" PMTs on the top and bottom, and an active volume of liquid xenon that is 30 cm tall with a 15 cm radius. The entire detector is placed inside a shield with a 20 cm layer of lead surrounding a 20 cm layer of polyethylene which in turns surrounds a 5 cm layer of copper (see Fig. 5.9) to help block external radioactivities. The future XENON1Ton detector will be larger than XENON100. The TPC will be 1 m in height with a 0.5 m radius, leading to a total active xenon mass of 2.4 tons. This larger mass allows for greater self shielding capabilities through fiducialization, and since the total fiducial mass will be larger, a lower WIMP-nucleon cross section can be probed. Fig. 9.6 shows a mechanical design of XENON1Ton. To decrease the effects of external radiation, the XENON1Ton detector will be placed inside a water tank with a 10 m height and 5 m radius. Furthermore, while the cryostat of XENON100 was made of stainless steel, the XENON1Ton cryostat will be made with high

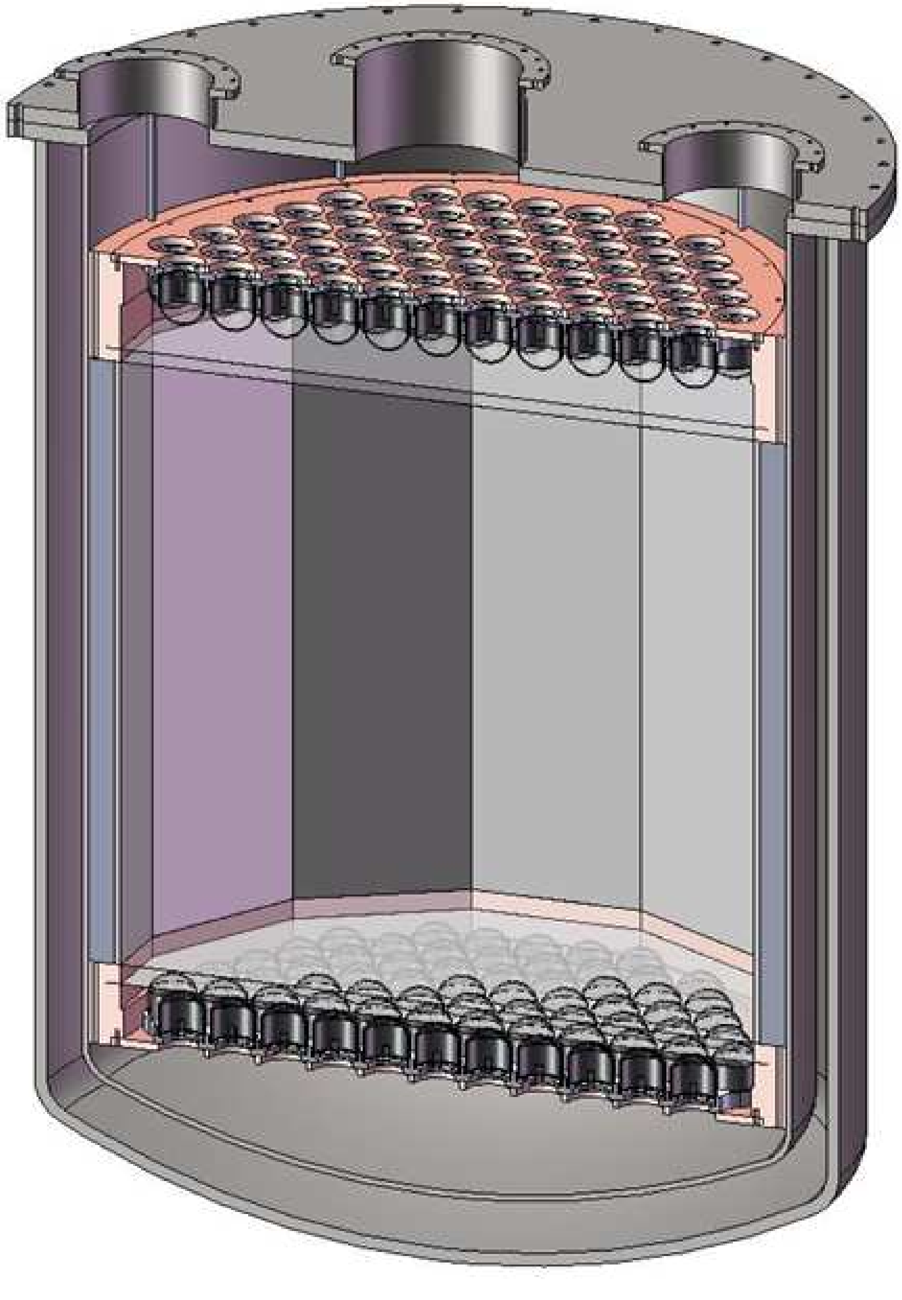

Figure 9.6: A CAD drawing of the internals of the future XENON1Ton Detector. The detector will use 121 QUPIDs at the top and 121 QUPIDs at the bottom. The total mass of liquid xenon will be 2.4 tons.

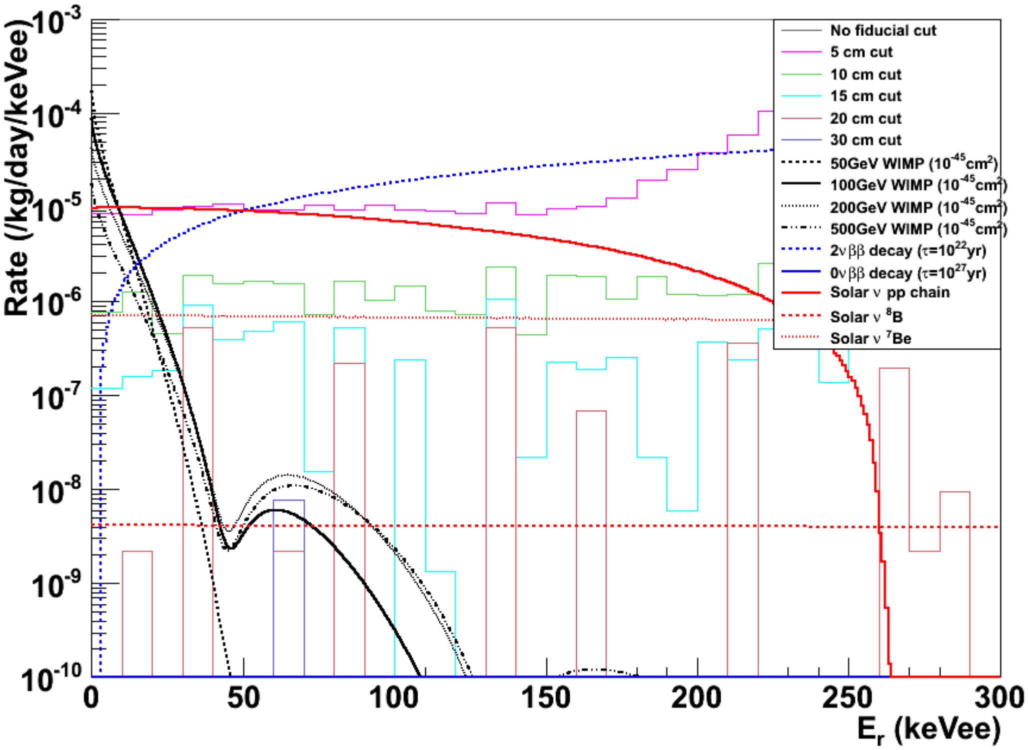

Figure 9.7: A plot of the simulated electronic recoil background spectrum in the XENON1Ton detector, showing the effects of self shielding. No $\log_{10}$(S2/S1) cut is used in this simulation. The expected signals from various masses of WIMPs are shown, along with a contribution from solar neutrinos and double beta decay. The background rate for no fiducial cut is above the upper limit of the plot. For a fiducial cut greater than 5 cm, the dominant backgrounds are expected to be from solar neutrinos and double beta decay.

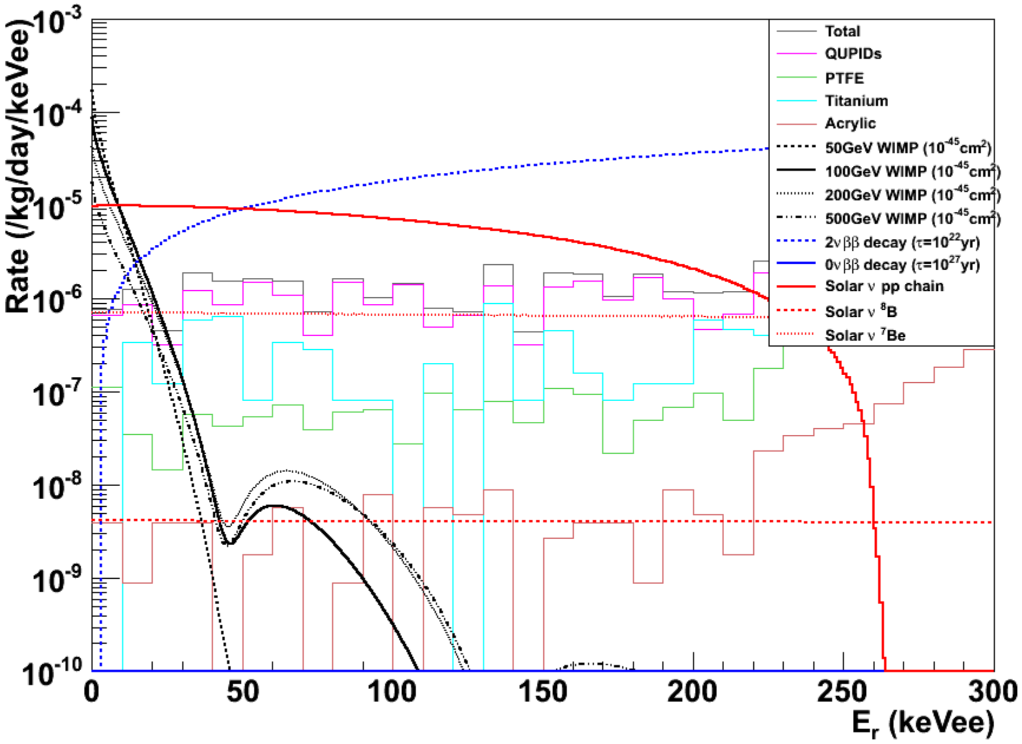

Figure 9.8: A plot of the simulated electronic recoil background spectrum in the XENON1Ton detector, showing the contributions from various detector materials. This plot assumes a fiducial cut of 10 cm and no $\log_{10}$(S2/S1) rejection.

purity titanium, to further decrease the radioactive contaminants. Finally, two arrays of 121 QUPIDs each will be used for the top and bottom photodetector arrays in the TPC, which will provide a lower background than conventional PMTs. Fig. 9.7 and 9.8 show simulations of the electronic recoil background in the XENON1Ton detector. By increasing the mass of the xenon, and by using materials and photodetectors with lower intrinsic radioactivity, the WIMP-nucleon cross section sensitivity of XENON1Ton should reach 10^{-47} cm^2 after one year of operation [147]. Based on the simulations shown in Tab. 8.1 and Fig. 8.8, 9.7, and 9.8 <0.07 events/year are expected from the QUPIDs, and a total of ~ 0.1 events from all detector materials are expected after a $\log_{10}(S2/S1)$ cut. Using the Feldman-Cousins analysis [133], a single observed event over an expected background of 0.1 events will constitute a discovery.

The recent results of two neutrino double beta decay detection in EXO-200 [106] show the importance of a low background experiment for detecting double beta decay. By performing comprehensive screening results, choosing only the materials with the lowest radioactivities, and minimizing detector materials, EXO-200 was able to conclusively detect double beta decay. A similar strategy can be employed in the XENON1Ton detector by using QUPIDs in order to decrease the radioactive backgrounds to levels comparable to those seen in EXO-200 by using a 20 cm fiducial cut. At the same time, by using QUPIDs with a gain of $\sim 10^5$, a lower energy threshold and higher resolution can be expected over the EXO-200 detector. With the high linearity range of the QUPID, signals up to the Q-value of double beta decay can be detected without compromising position and energy reconstruction. This will lower the overall systematic errors, and the detector can be used for dark matter and double beta decay detection.

9.4 Multi-Target Detectors for the Long Term Future

The future of dark matter detection is dependent on being able to successfully scale up every generation of detector. In the near future, the dark matter community will see the XENON1Ton detector, with 1 ton of liquid xenon, however a plan for the long term future must also be devised. As explained in Ref. [161], the UCLA dark matter group has demonstrated the effectiveness of a staged, multi-ton, multi-target system of detectors for dark matter, neutrinoless double beta decay, solar neutrino, and supernova neutrino detection and characterization. This would include three generations of detectors, G2, G3, and G4, each having a fiducial mass ten times larger than the last generation (G1 is designated as the current generation of dark matter experiments). There would be two detectors per generation, one using liquid xenon, and the other having liquid argon at about five times the mass of the corresponding liquid xenon detector. This ensures that the number of WIMP recoils expected in each detector will be comparable. All of the detectors will use the QUPID photodetectors in order to ensure a low background rate. Tab. 9.1 shows the relevant parameters of each generation of detector. Unlike the XENON100 TPC, these future detectors may have photodetectors on the sides as well as on the top and bottom, in order to increase the light yield. In the near future, a larger 6" QUPID may also be developed to be integrated into the largest dark matter detectors, and that possibility is reflected in the table.

After WIMPs have been detected, the mass and interaction cross section of the WIMPs must be determined. However, a degeneracy in the calculated mass and cross section of the WIMPs may arise based on the actual mass of the WIMP. Using two target materials can help to effectively determine the two values. This effect is demonstrated in Fig. 9.9 for several WIMP masses. Another advantage

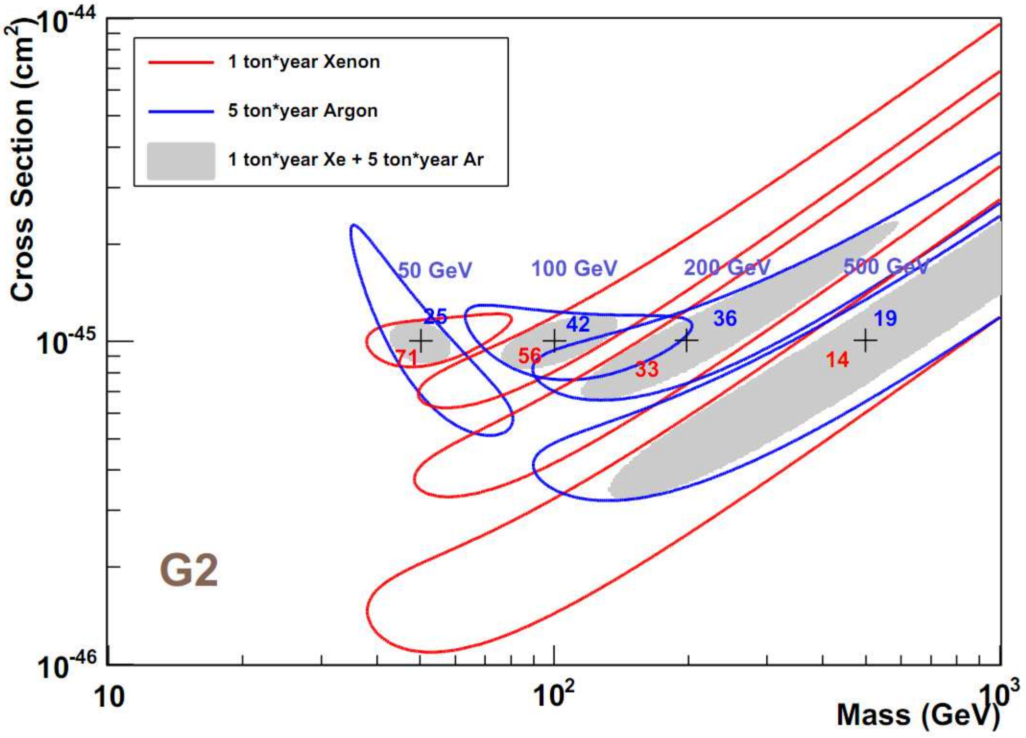

Figure 9.9: A plot of 1σ contours from the xenon and argon detectors for a WIMP of $50 - 500$ GeV mass and 10^{-45} cm^2 cross section in a 1 ton xenon detector or 5 ton argon detector with 1 year of exposure. The numbers indicate the number of signal events observed, and the gray areas show the degeneracy after combining the argon and xenon signals.

		G2		G3		G4	
		Xe	Ar	Xe	Ar	Xe	Ar
Dimensions	Diameter × Height (m)	1 × 1	2 × 2	2 × 2	4 × 4	4 × 4	8 × 8
	Total Target Mass (ton)	2.2	9	18	73	146	580
	Nominal Fiducial Mass (ton)	1	5	10	50	100	500
No. of Qupids	Top	120 (3”)	600 (3”)	600 (3”)	670 (6”)	670 (6”)	2000 (6”)
	Side (if instrumented)	520 (3”)	670 (6”)	670 (6”)	2400 (6”)	2400 (6”)	8000 (6”)
	Bottom	120 (3”)	160 (6”)	160 (6”)	670 (6”)	670 (6”)	2000 (6”)

Table 9.1: Table of the various properties for the next generations of multi-ton, multi-target dark matter detectors. This assumes that a larger, 6” Qupid will eventually be developed in order to reduce the number of photodetectors in the largest experiments.

of the two target materials is that in each subsequent generation, only one new detector must be made. The liquid argon detector from the previous generation can be reused with liquid xenon, while a new larger detector will be constructed for liquid argon.

Fig. 9.10 and 9.11 show drawings of the possible G2 and G3 detectors, along with their sizes. Following the successful implementation of these detectors, and assuming a WIMP discovery, a G4 phase may be commissioned to fully characterize the mass and cross section of the WIMPs. At the same time, these large detectors will have a large enough mass of xenon, and the possibility for a strong fiducial volume cut to provide for competitive limits on the neutrinoless double beta decay half-life of ^{136}Xe, and will allow for the observation of solar neutrinos. A full treatment of these possibilities is available in Ref. [161].

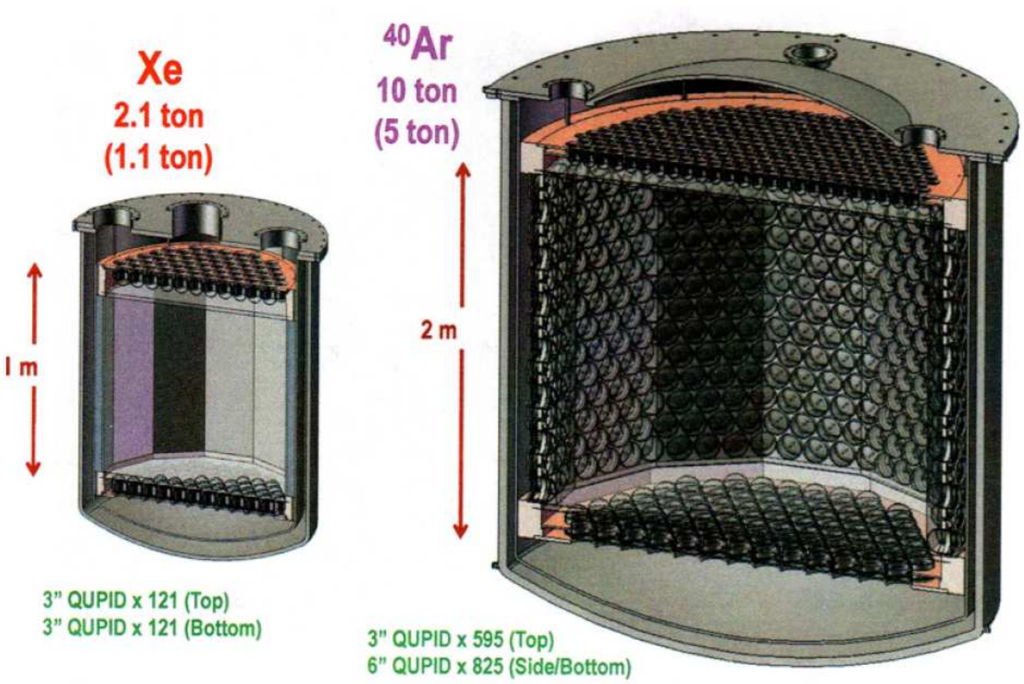

Figure 9.10: A drawing of a possible layout of the G2 detectors, along with their sizes and the number of QUPIDs used in each.

Figure 9.11: A drawing of a possible layout of the G3 detectors, along with their sizes and the number of QUPIDs used in each.

CHAPTER 10

Conclusion

Dark matter and double beta decay detection are two complementary fields as both are searching for very rare signals using similar techniques. The XENON100 experiment has been able to place the best limit on the mass and cross section of WIMPs, and I have also used the data to set a limit on the half-life of two neutrino double beta decay at $> 1.6 \times 10^{20}$ yr at the 90% C.L. Future dark matter experiments however will require new technology in the form of photodetectors with much lower radioactivity and with a wide linearity range.

The QUPID has been developed for this purpose. With a gain of $> 10^5$, excellent photoelectron collection efficiency, and an anode linearity range up to 3 mA, the QUPID can be used in future dark matter and double beta decay experiments. The QUPID was specifically developed to have a low radioactivity, and screening results show that it does have lower radioactive contaminants per unit area compared to conventional PMTs. An added advantage is that the QUPID has excellent timing response, with a pulse width of 4.20 ± 0.05 ns, a rise time of 1.8 ± 0.1 ns, and a fall time of 2.5 ± 0.2 ns, along with a transit time spread of 160 ± 30 ps. With the QUPID, the future XENON1Ton experiment can achieve a total background of $\sim$0.1 events/year in a 1.1 ton fiducial volume. Based on Feldman-Cousins analysis, 1 observed event is needed to claim a discovery over an expected background of 0.1 events.

For the XENON100 experiment, I have personally taken several shifts at the

Gran Sasso laboratory in order to ensure the correct operation of the experiment and to help with the monitoring of the krypton distillation process. At the same time, I was involved in Monte Carlo simulations of the backgrounds in the XENON100 detector using `Geant4`, and also performed the analysis needed for setting the limit on the half-life of double beta decay. I also designed the lead shield used for neutron calibration sources to ensure that no γ-rays originating from the source would enter the detector.

At UCLA, I was solely responsible for designing, building, and testing the liquid nitrogen cooldown system explained in Sec. 8.6. I also helped in the design and construction of the liquid xenon test system from Sec. 8.10, along with several previous prototypes for xenon liquefication systems. I personally performed nearly all of the QUPID and PMT testing described in Ch. 7 and 8, including the gain, leakage current, dark count, and timing property measurements. I also helped with the design of the uniformity and anode linearity test systems and was involved in these tests, while Hamamatsu performed the quantum efficiency and cathode linearity measurements. Finally, I designed and assembled the individual QUPID holders, 7-QUPID support structure, and the cooling for the 7-QUPID system introduced in Ch. 9, which will eventually be used as a scaled up version in the DARKSIDE50 and XENON1Ton experiments.

References

[1] A. Teymourian, et al., "Characterization of the QUartz Photon Intensifying Detector (QUPID) for noble liquid detectors" (2011), doi:10.1016/j.nima.2011.07.015.

[2] D. Griffiths, *Introduction to Elementary Particles.* John Wiley & Sons, 1987.

[3] G. Börner. *The Early Universe.* Springer, 2003.

[4] M. V. Berry. *Principles of Cosmology and Gravitation.* Institute of Physics Publishing, 1989.

[5] D. W. Sciama. *Modern Cosmology and the Dark Matter Problem.* Cambridge University Press, 1993.

[6] G. Gamow, Nature 162 (1948) 680.

[7] A. A. Penzias and R. W. Wilson, Astrophysical Journal Letters 142 (1965) 419.

[8] P. J. E. Peebles and H. Ratra, Reviews of Modern Physics 75 (2003) 559.

[9] G. Bertone, et al., Physics Reports 405 (2005) 279.

[10] R. Davis, et al., Physical Review Letters 20 (1968) 1205.

[11] M. H. Ahn, et al., Physical Review D 74 (2006) 072003.

[12] D. G. Michael, et al., Physical Review Letters 97 (2006) 191801.

[13] A. Riess, et al., Astronomical Journal 116 (1998) 1009.

[14] S. Perlmutter, et al., Astrophysical Journal 517 (1999) 565.

[15] M. Drinkwater, et al., Monthyl Notices of the Royal Astronomical Society 401 (2010) 1429.

[16] Y. Fukuda, et al., Physical Review Letters 81 (1998) 1158.

[17] T. Araki, et al., Physical Review Letters 94 (2005) 081801.

[18] F. Zwicky, Helvetica Physica Acta 6 (1933) 110.

[19] V. Rubin and W. K. Ford, Jr., Astrophysical Journal 159 (1970) 379.

[20] M. Girardi, et al., Astrophysical Journal 404 (1993) 38.

[21] M. Fich, et al., Astrophysical Journal 342 (1989) 272.

[22] K. M. Ashman, Publications of the Astronomical Society of the Pacific 104 (1932) 1109.

[23] A. Einstein, Science 84 (1936) 506.

[24] NASA, A. Fruchter and the ERO (STScI), STScI-PRC00-08.

[25] *Wilkinson Microwave Anisotropy Probe*. B. Griswold. 2010. NASA. <http://map.gsfc.nasa.gov/>.

[26] E. Gawiser and J. Silk, Physics Reports 333 (2000) 245.

[27] D. Larson, et al., Astrophysical Journal Supplemental Series 192 (2011) 16.

[28] S. Dodelson. *Modern Cosmology*. Academic Press, 2003.

[29] M. Boylan-Kolchin, et al., Monthly Notices of the Royal Astronomical Society 398 (2009) 1150.

[30] D. Clowe, et al., Astrophysical Journal 648 (2006) L109.

[31] M. Milgrom, Astrophysical Journal 270 (1983) 365.

[32] J. R. Brownstein and J. W. Moffat, Astrophysical Journal 636 (2006) 721.

[33] D. N. Spergel, et al., Astrophysical Journal Supplement Series 170 (2007) 377.

[34] *Constraining the Cosmological Parameters*. 2011. European Southern Observatory. <http://www.eso.org/public/images/eso0419d/>.

[35] J. Tonry, et al., Astrophysical Journal 594 (2003) 1.

[36] A. Riess, et al., Astrophysical Journal 607 (2004) 665.

[37] A. Gould, Publications of the Astronomical Society of the Pacific 113 (2001) 903.

[38] N. Palanque-Delabrouille, New Astronomy Reviews 45 (2001) 395.

[39] *Big Bang Nucleosynthesis*. E. L. Wright. 2011. UCLA. <http://www.astro.ucla.edu/∼wright/BBNS.html>.

[40] R. I. Epstein, et al., Nature 263 (1976) 198.

[41] D. Kirkman, et al., Astrophysical Journal Supplement 149 (2003) 1.

[42] P. Bonifacio, et al., Astronomy and Astrophysics 390 (2002) 91.

[43] J. M. Overduin and P. S. Wesson. *Dark Sky, Dark Matter*. Institute of Physics Publishing, 2003.

[44] W. B. Rolnick. *The Fundamental Particles and Their Interactions*. Addison-Wesley Publishing Company, 1994.

[45] G. Arnison, et al., Physics Letters B 126 (1983) 398.

[46] Y. Fukuda, et al., Physical Review Letters 81 (1998) 1562.

[47] Y. Fukuda, et al., Physics Letters B 436 (1998) 33.

[48] Q. R. Ahmad, et al., Physical Review Letters 87 (2001) 071301.

[49] S. L. Glashow, Nuclear Physics 22 (1961) 279.

[50] A. Salam, Physical Review 127 (1962) 331.

[51] S. Weinberg, Physical Review Letters 19 (1967) 1264.

[52] S. P. Martin, A Supersymmetry Primer. In Gordon L. Kane, editor, *Perspectives on Supersymmetry. Advanced Series on Directions in High Energy Physics*, Volume 18, World Scientific, 1998.

[53] H. Dreiner, "Hide and Seek with Supersymmetry" (1999), arXiv:hep-ph/9902347.

[54] D. Ross. The Standard Model. In P. M. Watkings, editor, *Proceedings of the School for Young High Energy Physicists*, Council for the Central Laboratory of the Research Councils, 2000. RAL Technical Report *RAL-TR-2000-008*.

[55] J. Ellis. Supersymmetry for alp hikers. In N. Ellis and J.D. March-Russell, editors, *Proceedings of the European School of High Energy Physics, Beatenburg, Switzerland, 16 Aug - 8 Sept 2001,* pages 157-204. *CERN-2002-002*.

[56] K. S. Ganezer, International Journal of Modern Physics A 16 (2001) 855.

[57] G. Jungman, et al., Physics Reports 267 (1996) 195.

[58] P. Gondolo, "Introduction to Non-Baryonic Dark Matter" (2004), arXiv:astro-ph/0403064.

[59] G. Herten, Modern Physics Letters A 26 (2011) 843.

[60] D. S. M. Alves, et al., "Where the Sidewalk Ends: Jets and Missing Energy Search Strategies for the 7 TeV LHC" (2011), arXiv:1102.5338.

[61] B. C. Allanach, Physical Review D 83 (2011) 095019.

[62] J. Diemand, et al., Nature 454 (2008) 735.

[63] J. Diemand, et al., Astrophysical Journal 657 (2007) 262.

[64] F. Boudjema, et al., Physical Review D 72 (2005) 055024.

[65] G. Jungman and M. Kamionkowski, Physical Review D 51 (1995) 328.

[66] A. Abramowski, et al., Physical Review Letters 106 (2011) 161301.

[67] R. G. Wagner, et al., "Indirect Dark Matter Searches with VERITAS" (2009), arXiv:0910.4563.

[68] S. Lombardi, et al., "Search for Dark Matter signatures with MAGIC-I and prospects for MAGIC Phase-II" (2009), arXiv:0907.0738.

[69] M. Ackermann, et al., Journal of Cosmology and Astroparticle Physics 05 (2010) 025.

[70] D. Hubert, et al., Nuclear Physics B Proceedings Supplements 173 (2007) 87.

[71] M. Boezio, et al., New Journal of Physics 11 (1009) 105023.

[72] A. Kounine, "Status of the AMS Experiment" (2010), arXiv:1009.5349.

[73] J. W. Mitchell, et al., Advances in Space Research 35 (2005) 135.

[74] Ph. von Doetinchem, et al., "The General Antiparticle Spectrometer (GAPS) - Hunt for dark matter using low-energy antideuterons" (2010), arXiv:1012.0273.

[75] J. D. Lewin and P. F. Smith, Astroparticle Physics 6 (1996) 87.

[76] H. Sekiya for the XMASS Collaboration, Journal of Physics: Conference Series 308 (2011) 012011.

[77] D. N. McKinsey and K. J. Coakley, Astroparticle Physics 22 (2005) 355.

[78] N. Ferrari, et al., Journal of Physics: Conference Series 39 (2006) 111.

[79] C. Regenfus, et al., Journal of Physics: Conference Series 203 (2010) 012024.

[80] D. N. McKinsey, et al., Journal of Physics: Conference Series 203 (2010) 012026.

[81] G. J. Alner, et al., Astroparticle Physics 28 (2007) 287.

[82] T. J. Sumner, New Astronomy Reviews 49 (2005) 277.

[83] E. Aprile, et al., New Astronomy Review 49 (2005) 289.

[84] E. Aprile, et al., "The XENON100 Dark Matter Experiment" (2011), arXiv:1107.2155

[85] Z. Ahmed, et al., Science 327 (2010) 1619.

[86] E. Armengaud, et al., "Final results of the EDELWEISS-II WIMP search using a 4-kg array of cryogenic germanium detectors with interleaved electrodes" (2011), arXiv:1103.4070.

[87] R. Bernabei, et al., Nuclear Instruments and Methods in Physics Research A 482 (2002) 728.

[88] C. Savage, et al., Journal of Cosmology and Astroparticle Physics 0904 (2009) 010.

[89] G. Angloher, et al., Astroparticle Physics 23 (2005) 325.

[90] M. Barnabé-Heider, et al., Nuclear Instruments and Methods in Physics Research A 555 (2007) 184.

[91] W. J. Bolte, et al., Nuclear Instruments and Methods in Physics Research A 577 (2007) 569.

[92] G. J. Alner, et al, Nuclear Instruments and Methods in Physics Research A 555 (2005) 173.

[93] S. R. Elliot and P. Vogel, Annual Review of Nuclear and Particle Science 52 (2002) 115.

[94] F. Boehm and P. Vogel. *Physics of Massive Neutrinos*. Cambridge University Press, 1987.

[95] A. Faessler and F. Simkovic, Journal of Physics G 24 (1998) 2139.

[96] M. Redshaw, et al., Physical Review Letters 98 (2007) 053003.

[97] F. T. Avignone, et al., New Journal of Physics 7 (2005) 6.

[98] H. V. Klapdor-Kleingrothaus, et al., Modern Physics Letters A 16 (2001) 2409.

[99] A. S. Barabash, Physical Review C 81 (2010) 035501.

[100] S. Umehara, et al., Physical Review C 78 (2008) 058501.

[101] H. V. Klapdor-Kleingrothaus, et al., European Physical Journal A 12 (2001) 147.

[102] A. S. Barabash and V. B. Brudanin, Physics of Atomic Nuclei 74 (2011) 312.

[103] J. Argyriades, et al., Nuclear Physics A 847 (2010) 168.

[104] F. A. Danevich, et al., Physical Review C 68 (2003) 035501.

[105] E. Andreotti, et al., Astroparticle Physics 34 (2011) 822.

[106] N. Ackerman, et al., "Observation of Two-Neutrino Double-Beta Decay in ^{136}Xe with EXO-200" (2011), arXiv:1108.4193.

[107] R. Bernabei, et al., Physics Letters B 546 (2002) 23.

[108] J. Argyriades, et al., Physical Review C 80 (2009) 032501(R).

[109] D. H. Perkins. *Introduction to High Energy Physics*. Cambridge University Press, 2000.

[110] M. Apollonio, et al., Physics Letters B 466 (1999) 415.

[111] F. Boehm, et al., Physical Review D 64 (2001) 112001.

[112] EXO Collaboration, "EXO: The Enriched Xenon Observatory for Double Beta Decay" (2002), arXiv:hep-ph/0210186.

[113] I. Abt, et al., "A New 76Ge Double Beta Decay Experiment at LNGS" (2004), arXiv:hep-ex/0404039.

[114] K. Zuber, Physics Letters B 519 (2001) 1.

[115] R. Arnold, et al., Physical Review Letters 95 (2005) 182302.

[116] E. Conti, et al., Physical Review B 68 (2003) 054201.

[117] A. Minamino, et al., "Self-shielding effect of a single phase liquid xenon detector for direct dark matter search" (2009), arXiv:0912.2405.

[118] K. Abe, et al., Astroparticle Physics 31 (2009) 290.

[119] J. Engel, Physics Letters B, 264 (1991) 114.

[120] S. Kubota et al, Physical Review B 17 (1978) 2762.

[121] T. Doke et al, Jpn. J. Appl. Phys. 41 (2002) 1538.

[122] E. Aprile, et al., "Material screening and selection for XENON100" (2011), arXiv:1103.5831.

[123] E. Aprile, et al., "Dark Matter Results from 100 Live Days of XENON100 Data" (2011), arXiv:1104.2549.

[124] S. Agostinelli, et al., (GEANT4 Collaboration), Nuclear Instruments and Methods in Physics Research A 506 (2003) 250.

[125] E. Aprile, et al., Physical Review D 83 (2011) 082001.

[126] E. Aprile, at al., Physical Review Letters 97 (2006) 081302.

[127] G. Plante, et al., "New Measurement of the Scintillation Efficiency of Low-Energy Nuclear Recoils in Liquid Xenon" (2011), arXiv:1104.2587.

[128] E. Aprile, et al., "Likelihood Approach to the First Dark Matter Results from XENON100" (2011), arXiv:1103.0303.

[129] E. Aprile, et al., Physical Review Letters 105 (2010) 131302.

[130] O. Buchmueller, et al., "Implications of Initial LHC Searches for Supersymmetry" (2011), arXiv:1102.4585.

[131] C. E. Aalseth, et al., Physical Review Letters 106 (2011) 131301.

[132] J. L. Vuilleumier, et al., Physical Review D 48 (1993) 1009.

[133] G. J. Feldman and R. D. Cousins, Physical Review D 57 (1998) 3873.

[134] E. Bellotti, et al., Journal of Physics G: Nuclear and Particle Physics 17 (1991) S231.

[135] R. Luescher, et al., Physics Letters B 434 (1998) 407.

[136] Ju. M. Gavriljuk, et al., Physics of Atomic Nuclei 69 (2005) 2129.

[137] D. S. Leonard, et al., Nuclear Instruments and Methods in Physics Research A 591 (2008) 490.

[138] R. Neilson, et al., “Characterization of large area APDs for the EXO-200 detector” (2009), arXiv:0906.2499.

[139] Photomultiplier Tubes, Basics and Applications, Hamamatsu Photonics K.K., Iwata City 438-0193, Shizuoka, Japan, 2006.

[140] M. Suyama, et al., Nuclear Instruments and Methods in Physics Research A 523 (2004) 147.

[141] H. Nakayama, et al., Nuclear Instruments and Methods in Physics Research A 567 (2006) 172.

[142] M. Hayashida, et al., Nuclear Instruments and Methods in Physics Research A 567 (2006) 180.

[143] Y. Kawai, et al., Nuclear Instruments and Methods in Physics Research A 579 (2007) 42.

[144] L. Baudis, et al., “Gator: a low-background counting facility at the Gran Sasso Underground Laboratory” (2011), arXiv:1103.2125.

[145] C. Hurtgen, et al., Applied Radiation and Isotopes 53 (2000) 45.

[146] Confidential communications with the XENON100 analysis group.

[147] XENON1Ton Collaboration, XENON1Ton at LNGS, Technical Design Report, Oct 2010.

[148] K. Arisaka, et al., Astroparticle Physics 31 (2009) 63.

[149] K. Nakamura, et al., Nuclear Instruments and Methods in Physics Research A 623 (2010) 276.

[150] A. Hitachi, et al., Physical Review B 27 (1983) 5279.

[151] S. Kubota, et al., Journal of Physics C 11 (1978) 2645.

[152] E. Aprile, T. Doke, Reviews of Modern Physics 82 (2010) 2053.

[153] F. A. Danevich, et al., Physical Review C 67 (2003) 014310.

[154] M. G. Boulay, et al., “Measurement of the scintillation time spectra and pulse-shape discrimination of low-energy beta and nuclear recoils in liquid argon with DEAP-1” (2009), arXiv:0904.2930.

[155] W. H. Lippincott, et al., Physical Review C 78 (2008) 035801.

[156] P. Benetti, et al., Astroparticle Physics 6 (2008) 495.

[157] DarkSide Collaboration, Collaborative Research: A Depleted Argon Detector for a Dark Matter Search, Proposed Oct 2009.

[158] L. Baudis (DARWIN Consortium), “DARWIN: Dark Matter WIMP Search with Noble Liquids” (2010), arXiv:1012.4764.

[159] MAX Collaboration, Multi-ton Argon and Xenon TPCs, proposed Jan 10 2009.

[160] C. Galbiati, et al., Journal of Physics: Conference Series 120 (2008) 042015.

[161] K. Arisaka, et al., “Studies of a three-stage dark matter and neutrino observatory based on multi-ton combinations of liquid xenon and liquid argon detectors” (2011), arXiv:1107.1295.